Electromagnetic Manipulation of Individual Nano- and Microparticles

D i s s e r t a t i o n

zur Erlangung des akademischen Grades

d o c t o r r e r u m n a t u r a l i u m
(Dr. rer. nat.)

im Fach Physik

eingereicht an der

Mathematisch-Naturwissenschaftlichen Fakultät
der Humboldt-Universität zu Berlin

von

Dipl.-Phys. Alexander Kuhlicke

Präsidentin der Humboldt-Universität zu Berlin:
Prof. Dr.-Ing. Dr. Sabine Kunst

Dekan der Mathematisch-Naturwissenschaftlichen Fakultät:
Prof. Dr. Elmar Kulke

Gutachter/innen:
1. Prof. Dr. Oliver Benson
2. Prof. Dr. Beate Röder
3. Prof. Dr. Romain Quidant

Tag der mündlichen Prüfung: 04.10.2017

Abstract

The topic of the present thesis is the investigation of single nano- and microsized particles for the understanding and design of novel nanooptical elements as light sources and sensors, as well as light collecting and guiding structures. In addition to particle characterization, the focus is on different methods for electromagnetic particle manipulation aimed at controlling the particle's position or geometry. The specific manipulations are used for isolation, modification and transfer of preselected particles, enabling combination of particles into more complex photonic systems, which exceed the functionalities of the individual constituents.

The main part of this work deals with experiments on levitated particles in linear Paul traps. Due to the spatial isolation in the electrodynamic quadrupole field, particles can be investigated with reduced environmental interaction. Different nano- and microparticles are characterized in the trap by fluorescence or white-light scattering spectroscopy: optically active particles (dye-doped polystyrene nanobeads, clusters of nanodiamonds with nitrogen vacancy defect centers, clusters of colloidal quantum dots) as well as particles with optical resonances (plasmonic silver nanowires, spherical silica microresonators). A method is presented that enables deposition of single particles from the trap onto the facet of an optical fiber for subsequent characterization with an atomic force microscope. This technique can also be used to functionalize fragile photonic structures, which is demonstrated by the deposition of spherical microresonators and quantum dots on a tapered optical fiber. Segmentation of the linear trap geometry allows for separation as well as transport of several particles along the one-dimensional trap center. This capability is the basis for another new method to combine single particles in the trap, which is used to assemble optically active particles and spherical microresonators. The resulting particle composites remain stable in the trap and show electromagnetic coupling effects.

In a further part of this work a method to manipulate the geometry of plasmonic nanoparticles is presented. Single gold nanospheres on a coverslip are melted and shaped with a focused laser beam. The localized surface plasmons can be influenced specifically by controlled changes of the particle symmetry. In addition to optical fluorescence and white-light spectroscopy, changes of the particles are monitored with an atomic force microscope and a scanning electron microscope. The technique can be carried out step by step and is reversible, which enables fine-tuning of the resonances of a plasmonic nanoparticle.

Zusammenfassung

Gegenstand der vorliegenden Dissertation ist die Untersuchung von einzelnen nano- und mikrometergroßen Partikeln, zum Verständnis und zur Entwicklung von neuartigen nanooptischen Elementen, wie Lichtquellen und Sensoren, sowie Strukturen zum Aufsammeln und Leiten von Licht. Neben der Charakterisierung stehen dabei verschiedene Methoden zur elektromagnetischen Manipulation im Vordergrund, die auf eine Kontrolle der Position oder der Geometrie der Partikel ausgerichtet sind. Die gezielten Manipulationen werden verwendet, um vorausgewählte Partikel zu isolieren, modifizieren und transferieren. Dadurch können Partikel zu komplexeren photonischen Systemen kombiniert werden, welche die Funktionalität der einzelnen Bestandteile übertreffen.

Der Hauptteil der Arbeit behandelt Experimente mit freischwebenden Partikeln in linearen Paul-Fallen. Durch die räumliche Isolation im elektrodynamischen Quadrupolfeld können Partikel mit reduzierter Wechselwirkung untersucht werden. Spektroskopisch werden unterschiedliche Nano- und Mikropartikel in der Falle anhand ihrer Fluoreszenz oder des an ihnen gestreuten Lichts charakterisiert: optisch aktive Partikel (farbstoffdotierte Polystyrol-Nanokügelchen, Cluster aus Nanodiamanten mit Stickstoff-Fehlstellen-Zentren, Cluster aus kolloidalen Quantenpunkten) sowie optische Resonatoren (plasmonische Silber-Nanodrähte, sphärische Siliziumdioxid-Mikroresonatoren). Es wird eine Methode vorgestellt, mit der einzelne Partikel aus der Falle auf der Facette einer optischen Faser abgelegt und anschließend mit einem Rasterkraftmikroskop ausgemessen werden können. Das Verfahren erlaubt außerdem fragile photonische Strukturen gezielt zu funktionalisieren, was mit der Ablage von sphärischen Mikroresonatoren und Quantenpunkten auf einem optischen Fasertaper demonstriert wird. Eine Segmentierung der linearen Fallengeometrie ermöglicht es, mehrere Teilchen entlang des eindimensionalen Fallenzentrums sowohl getrennt voneinander zu halten als auch zu bewegen. Diese Fähigkeit ist die Grundlage für eine weitere, neu entwickelte Methode zur Kombination von einzelnen Partikeln in der Falle, die dazu genutzt wird, optisch aktive Partikel mit sphärischen Mikroresonatoren zusammenzufügen. Die sich daraus ergebenden Komposite bleiben stabil in der Falle und zeigen elektromagnetische Kopplungseffekte.

In einem weiteren Teil der Arbeit wird eine Methode zur Manipulation der Geometrie von plasmonischen Nanopartikeln vorgestellt. Dabei werden einzelne Goldkugeln auf einem Deckglas mit einem fokussierten Laserstrahl zum Schmelzen gebracht und verformt. Durch die kontrollierte Veränderung der Symmetrie lassen sich die lokalisierten Oberflächenplasmonen des Partikels gezielt beeinflußen. Neben der optischen Spektroskopie des Fluoreszenz- und des gestreuten Weißlichts werden die Veränderungen der Partikel mit einem Rasterkraftmikroskop und einem Rasterelektronenmikroskop sichtbar gemacht. Das Verfahren ist sowohl schrittweise durchführbar als auch umkehrbar und ermöglicht somit ein Feinabstimmen der Resonanzen eines plasmonischen Nanopartikels.

Contents

1. Introduction

Particles with diameters between some nano- and a few micrometers are of great interest in scientific research. Due to their small dimensions they can be used in applications with size limitations; for example, small sensors can be brought close to different targets with high spatial resolution [1] and nano-sized light sources can be integrated into complex photonic systems [2]. Another aspect is that most nanoparticles show size-dependent properties different from bulk material, like reduction of the melting point [3] and surface tension [4] with decreasing diameter. Even more spectacular is the optical behavior of some materials, when their particle dimensions are small enough. For example, colloidal and nanocrystal semiconductor quantum dots behave like artificial atoms [5], and the scattering and absorption cross sections of metal [6] as well as dielectric nanoparticles [7] strongly depend on the wavelength. Quantum effects caused by electronic carrier confinement influence the characteristic emission and absorption wavelengths of small particles depending on the particle size and shape [5, 8, 9]. However, particles too large to be directly affected by quantum effects also show remarkable size-dependent optical properties. Spherical microparticles, for example, can be used as optical cavities that confine light within a small mode volume, causing very high field intensities at the surface [10].

The applicability of nano- and microparticles, especially in optics [11–13], ranges from quantum optics [14–16] to technical applications [17–19] to biomedicine [20–23]. To name just a few examples: optically active particles can be used as bright light [24, 25] and single photon sources [26–28], while optical nanoantennas [29,30], optical cavities [31] and laser resonators [32] can be realized by particles with optical resonances. Furthermore, both particle types can be applied as markers and labels [21, 33], sensors [34–36] and in combination with each other for enhanced light emission or coupling effects [37, 38]. Even optomechanical interactions can be studied with single nanoparticles [39, 40].

These versatile uses are enabled by reliable fabrication techniques, like chemical synthesis [41, 42] of pure material or core-shell particles [43] from simple to complex geometries [44], melting [45], lithography [46, 47], milling [48, 49] and laser ablation [50, 51]. The surface of most particles can also be functionalized, depending on the envisaged application [52, 53].

Single nano- and microparticles can be investigated by optical microscopy, but conventional techniques give only little insight into structures smaller than half of the used wavelength due to the diffraction limit [54]. Particle characterization with higher resolution can be achieved by using smaller wavelengths, available in X-ray [55] and electron microscopes [56]. Additionally, scanning probe microscopes, like atomic force microscopes (AFM) and near-field scanning optical microscopes (NSOM), offer high resolution together with the possibility to manipulate the particles themselves [37]. In-situ manipulation of single particles is favorable in many experiments, not only in terms of translation [57], but also of specific particle properties, like controlled adjustment of the particle geometry or composition. This allows for individual particle adjustments independent from their

synthesis processes, for example to tune resonance properties [58–60].

Two different approaches to manipulating individual nano- and microparticles are pursued in this thesis. The major part of the work explores single particle levitation in a linear Paul trap for optical spectroscopy and demonstrates new experimental methods in the field of small particle handling, investigation and processing. In the second, minor part, a new method is developed to tune the optical resonance of plasmonic nanoparticles in-situ by a focused laser beam. Both topics are introduced in brief in the following paragraphs.

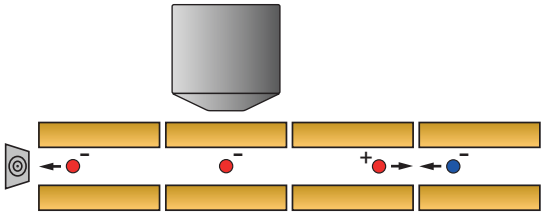

Levitation of single nano- and microparticles in free space can be realized by a variety of methods, which rely on different interactions. For neutral particles optical dipole traps are widely used, which can be realized by a strongly focused laser beam [61] or by standing waves in an optical cavity [62, 63]. Acoustic traps can also be used to levitate larger neutral particles [64].

If the particles are charged, electric and magnetic fields can be used for trapping, which generally enable stronger confinement. One approach is tracking of a single particle and counteracting its motion with quasi-static electric potentials in order to stabilize it in a so-called anti-Brownian electrophoretic (ABEL) trap [65]. More general methods avoid feedback signals from the particle's position in the first place and make use of static and dynamic fields. As a direct result of Maxwell's equations, Earnshaw's theorem [66] prohibits three-dimensional trapping of charged particles with a single static electric or magnetic field. The combination of both in a Penning trap is one solution to this problem, allowing for particle confinement on circular trajectories [67]. Using time-dependent potentials is another solution. In a Paul trap, charged particles can be confined in ac electric fields [68], as done in this thesis. The importance of trapping methods for charged particles can be seen from the vast number of different applications, and also from the Nobel prize in physics awarded to Wolfgang Paul and Hans Georg Dehmelt, who shared one half of the prize for the development of ion trapping methods in 1989 [69].

The regime of particle sizes that can be levitated in a Paul trap spans from single atomic [70] and molecular ions [71] to macroscopic particles with sizes of several micrometers [72, 73]. Such traps are widely used for mass spectrometry [74], high resolution optical spectroscopy [75–77], frequency standards [78–80] or as processor registers in experiments aiming at the realization of a quantum computer [81–83]. They can also be helpful to create idealized models for complex crystal behavior [84] or quantum simulators [85, 86].

Depending on the application, different Paul trap geometries are realized. Most common are classical [68] and linear [87] geometries and variations thereof [74, 88–90]. Simplified electrode arrangements are developed [91], as well as multi-pole traps, to generate potentials of higher order [92] than the typical quadrupole configuration. Also, specialized geometries like surface electrode [93,94] or stylus traps [95] provide improved optical access to the trapped particles.

In this thesis, linear Paul traps are used to isolate single nano- and microparticles in free space. With the trap integrated in an optical microscope, confined particles are characterized by fluorescence and scattering spectroscopy. Different optically active as well as resonant particles are trapped and investigated individually. The usability and applicabil-

ity of a Paul trap for nanooptical experiments is demonstrated by the presented work and even further improved by the development of new manipulation techniques for trapped particles.

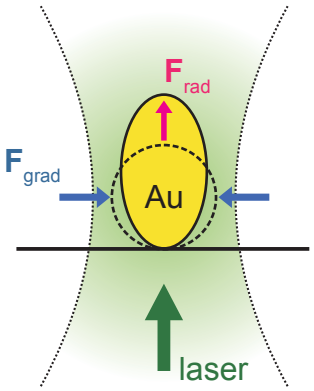

Localized surface plasmon polaritons in single metal nanoparticles are observed as strong resonances in absorption and scattering spectra. Surface plasmon resonances are collective oscillations of the conduction band electrons, confined to the dimensions of the specific nanoparticle, that are excited by the incident light. Plasmonic behavior is observable especially in the noble metals gold and silver [96], but also in other materials [97,98]. Plasmonic nanoparticles are used for manifold applications, like sensing [20], photovoltaics [17], catalysis [99], labeling [33], local heating [100] and various medical applications [101]. On a single particle level, strong field enhancement on the surface can be used for plasmon-enhanced single photon sources [29,102,103]. The ability of plasmonic nanoparticles to act as optical antennas enables the concentration of light into dimensions much smaller than the diffraction limit [104].

The resonances of localized surface plasmons are determined not solely by the electronic properties of the particle and the surrounding medium, but also by the particle size and shape [9]. Each of these parameters can be adjusted individually, in order to tune a plasmonic particle's resonance frequencies. Typically, the particle properties are set during synthesis and only the environment may be changed afterwards [105], but methods for subsequent particle modification are also known [59,60].

In this thesis, a new tuning method is developed aiming at in-situ modification of the particle shape. The all-optical method is demonstrated on a single gold nanoparticle by shifting its plasmon resonance in accordance with the geometry change in a controlled way.

The different aspects of individual particle characterization and manipulation investigated in this thesis are presented in the following chapters:

In **chapter 2** the interaction of light and matter with a focus on different nano- and microsized particles is theoretically described. Spherical microresonators and optical nanoantennas are introduced as well as optically active emitters, like nitrogen vacancy defect centers in diamond crystals and colloidal quantum dots.

Most of the particles are investigated and manipulated in a linear Paul trap. Its working principles are treated in **chapter 3**.

Two different linear Paul traps are constructed, which are described in **chapter 4**. The electrical supply of the traps is explained, including the developed high-voltage amplifiers, followed by a detailed characterization of the homemade optical microscope setup, used for particle observation and investigation. The particles are charged and injected into the trap by electrospray ionization, which is comprehensively introduced at the end of the chapter.

In **chapter 5** the experiments performed with the trap setup are presented. Various particles are investigated, like diamond particles with nitrogen vacancy defect centers, silver nanowires, silica microspheres, polystyrene beads containing organic emitters, and colloidal quantum dots. In addition, different manipulation techniques are developed, enabling individual assembly of complex particle systems and particle deposition on other photonic structures.

A completely different approach for the manipulation of individual plasmonic nanoparticles is demonstrated in **chapter 6**. The symmetry of a single gold nanosphere on a glass coverslip is changed by laser-induced melting and shaping, by which the particle's plasmon resonance is tuned in a controlled way.

The results of this thesis are summarized in **chapter 7**. Furthermore, a brief outlook is given for on-going and possible future developments and applications.

2. Interaction of Light and Matter

The diversity of nano- and microparticles investigated in this work requires a treatment of electrodynamics in matter in combination with an explanation of different material properties. This chapter presents the basic concepts. It starts with a classical approach to electrodynamics via the Maxwell equations. The solution of the wave equations leads to the formalism of Mie scattering, that allows for analysis of the scattering behavior of small spheres. The scattering resonances of dielectric microspheres are explained by their natural modes. For metal particles, solid state theory has to be involved to explain the optical characteristics using the material parameters. The chapter ends with a short introduction to the fluorescent emitters involved in this work, which cannot be covered by classical electrodynamics. The basic introductions in this chapter follow [106–108].

2.1. Analytical Description

Classical electrodynamics can be used to explain the propagation and interaction of electromagnetic fields. The Maxwell equations form the basis of this treatment. The material properties enter as input parameters.

2.1.1. Maxwell Equations in Matter

The Maxwell equations in matter are

$$\nabla \cdot \mathbf{D} = \rho, \tag{2.1}$$

$$\nabla \times \mathbf{E} = -\frac{\partial \mathbf{B}}{\partial t}, \tag{2.2}$$

$$\nabla \cdot \mathbf{B} = 0, \tag{2.3}$$

$$\nabla \times \mathbf{H} = \mathbf{J} + \frac{\partial \mathbf{D}}{\partial t}. \tag{2.4}$$

They describe the electric field $\mathbf{E}$, the magnetic induction $\mathbf{B}$ as well as the electric displacement $\mathbf{D}$ and the magnetic field $\mathbf{H}$. These auxiliary fields are defined by:

$$\mathbf{D} = \varepsilon_0 \mathbf{E} + \mathbf{P}, \tag{2.5}$$

$$\mathbf{H} = \frac{1}{\mu_0}\mathbf{B} - \mathbf{M}, \tag{2.6}$$

with the electric polarization $\mathbf{P}$ and the magnetization $\mathbf{M}$. The constants ε_0 and μ_0 are the permittivity and permeability of free space, respectively. The charge density ρ and the current density $\mathbf{J}$ are related to the free charges of the medium. The macroscopic Maxwell equations (2.1) to (2.4) need supplementary constitutive relations to specify the

fields. For a linear, homogeneous and isotropic material they can be written as

$$\mathbf{J} = \sigma\mathbf{E}, \tag{2.7}$$
$$\mathbf{B} = \mu\mathbf{H}, \tag{2.8}$$
$$\mathbf{P} = \varepsilon_0\chi\mathbf{E}. \tag{2.9}$$

The conductivity σ, the permeability μ and the electric susceptibility χ are frequency-dependent phenomenological coefficients that characterize the respective medium.

Typically, the fields are time-harmonic and given by

$$\mathbf{E}(\mathbf{r}, t) = \mathbf{E_0}(\mathbf{r})e^{-i\omega t}. \tag{2.10}$$

$\mathbf{E_0}$ is the complex amplitude, which may depend on position, and ω is the angular frequency. The Maxwell equations (2.1) to (2.4) together with the constitutive relations (equations (2.7) to (2.9)) change to

$$\nabla \cdot (\varepsilon\mathbf{E}) = 0, \tag{2.11}$$
$$\nabla \times \mathbf{E} = i\omega\mu\mathbf{H}, \tag{2.12}$$
$$\nabla \cdot \mathbf{H} = 0, \tag{2.13}$$
$$\nabla \times \mathbf{H} = -i\omega\varepsilon\mathbf{E}, \tag{2.14}$$

with the complex permittivity

$$\varepsilon = \varepsilon_0(1 + \chi) + i\frac{\sigma}{\omega}. \tag{2.15}$$

The electric field is divergence free unless $\varepsilon = 0$. In this case, the electric field in the medium is no longer transverse but rather longitudinal.

2.1.2. Wave Equations

The Maxwell equations (2.11) to (2.14) lead to the vector wave equations in Coulomb gauge, in the form of the Helmholtz equation, which have to be satisfied by each physical time-harmonic electro-magnetic field in a linear, homogeneous and isotropic medium:

$$\nabla^2\mathbf{E} + k^2\mathbf{E} = 0, \tag{2.16}$$
$$\nabla^2\mathbf{H} + k^2\mathbf{H} = 0, \tag{2.17}$$

with $k = \sqrt{\omega^2\varepsilon\mu}$. A set of linearly independent solutions to the Maxwell and the wave equations is

$$\mathbf{M} = \nabla \times (\mathbf{r}\psi), \tag{2.18}$$
$$\mathbf{N} = \frac{\nabla \times \mathbf{M}}{k}. \tag{2.19}$$

The constant vector $\mathbf{r}$ is arbitrary and can be chosen according to the individual problem. The scalar function ψ is the generating function for the vector harmonics $\mathbf{M}$ and $\mathbf{N}$. With this set, the problem of finding solutions to the vector wave equations (2.16) and (2.17) can be reduced to finding a solution to the scalar wave equation

$$\nabla^2\psi + k^2\psi = 0. \tag{2.20}$$

For the spherical-symmetric problem of scattering by a sphere the scalar wave equation can be transformed to spherical coordinates:

$$\frac{1}{r^2}\frac{\partial}{\partial r}\left(r^2\frac{\partial\psi}{\partial r}\right)+\frac{1}{r^2\sin\theta}\frac{\partial}{\partial\theta}\left(\sin\theta\frac{\partial\psi}{\partial\theta}\right)+\frac{1}{r^2\sin\theta}\frac{\partial^2\psi}{\partial\phi^2}+k^2\psi=0. \tag{2.21}$$

By separation of variables one finds solutions to the spherical scalar wave equation

$$\psi_{eml}=\cos(m\phi)P_l^m(\cos\theta)z_l(kr), \tag{2.22}$$
$$\psi_{oml}=\sin(m\phi)P_l^m(\cos\theta)z_l(kr), \tag{2.23}$$

that generate the vector harmonics by equations (2.18) and (2.19). The subscripts e and o label linearly-independent even and odd modes, respectively. The functions $P_l^m(\cos\theta)$ are the associated Legendre functions of the first kind with positive integer values for the degree l and order $m \geq l$. The function $z_l(\rho)$ with $\rho = kr$ stands for a spherical Bessel function of the first (j_l) or second (y_l) kind, related to the ordinary Bessel functions of the first (J_l) and the second (Y_l) kind by

$$j_l(\rho)=\sqrt{\frac{\pi}{2\rho}}J_{l+\frac{1}{2}}(\rho), \tag{2.24}$$
$$y_l(\rho)=\sqrt{\frac{\pi}{2\rho}}Y_{l+\frac{1}{2}}(\rho). \tag{2.25}$$

Any combination of these can also be used for $z_l(kr)$, like the spherical Bessel functions of the third kind, called spherical Hankel functions

$$h_l^{(1)}(\rho)=j_l(\rho)+iy_l(\rho), \tag{2.26}$$
$$h_l^{(2)}(\rho)=j_l(\rho)-iy_l(\rho). \tag{2.27}$$

The functions in equations (2.22) and (2.23) together form a complete set. Thus, any function satisfying equation (2.21) can be expanded as an infinite series in these functions.

The generated vector spherical harmonics are

$$\begin{aligned}\mathbf{M}_{eml} = &\frac{-m}{\sin\theta}\sin(m\phi)P_l^m(\cos\theta)z_l(\rho)\hat{\mathbf{e}}_\theta \\ &-\cos(m\phi)\frac{dP_l^m(\cos\theta)}{d\theta}z_l(\rho)\hat{\mathbf{e}}_\phi, \qquad (2.28)\\ \mathbf{M}_{oml} = &\frac{m}{\sin\theta}\cos(m\phi)P_l^m(\cos\theta)z_l(\rho)\hat{\mathbf{e}}_\theta \\ &-\sin(m\phi)\frac{dP_l^m(\cos\theta)}{d\theta}z_l(\rho)\hat{\mathbf{e}}_\phi, \qquad (2.29)\\ \mathbf{N}_{eml} = &\frac{z_l(\rho)}{\rho}\cos(m\phi)l(l+1)P_l^m(\cos\theta)\hat{\mathbf{e}}_r \\ &+\cos(m\phi)\frac{dP_l^m(\cos\theta)}{d\theta}\frac{1}{\rho}\frac{d}{d\rho}[\rho z_l(\rho)]\hat{\mathbf{e}}_\theta \\ &-m\sin(m\phi)\frac{P_l^m(\cos\theta)}{sin\theta}\frac{1}{\rho}\frac{d}{d\rho}[\rho z_l(\rho)]\hat{\mathbf{e}}_\phi, \qquad (2.30)\\ \mathbf{N}_{oml} = &\frac{z_l(\rho)}{\rho}\sin(m\phi)l(l+1)P_l^m(\cos\theta)\hat{\mathbf{e}}_r \\ &+\sin(m\phi)\frac{dP_l^m(\cos\theta)}{d\theta}\frac{1}{\rho}\frac{d}{d\rho}[\rho z_l(\rho)]\hat{\mathbf{e}}_\theta \\ &+m\cos(m\phi)\frac{P_l^m(\cos\theta)}{sin\theta}\frac{1}{\rho}\frac{d}{d\rho}[\rho z_l(\rho)]\hat{\mathbf{e}}_\phi. \qquad (2.31)\end{aligned}$$

Now, an electromagnetic field can be expanded in an infinite series of vector spherical harmonics. The electric field $\mathbf{E}$ is obtained from

$$\mathbf{E} = \sum_{m=0}^{\infty}\sum_{l=m}^{\infty}\left(B_{eml}\mathbf{M}_{eml} + B_{oml}\mathbf{M}_{oml} + A_{eml}\mathbf{N}_{eml} + A_{oml}\mathbf{N}_{oml}\right), \qquad (2.32)$$

with the associated magnetic field, using equation (2.32) in equation (2.12),

$$\mathbf{H} = \frac{k}{i\omega\mu}\sum_{m=0}^{\infty}\sum_{l=m}^{\infty}\left(B_{eml}\mathbf{N}_{eml} + B_{oml}\mathbf{N}_{oml} + A_{eml}\mathbf{M}_{eml} + A_{oml}\mathbf{M}_{oml}\right). \qquad (2.33)$$

The expansion coefficients A_{eml}, A_{oml}, B_{eml} and B_{oml} are calculated depending on the actual field. Two different types of modes exist for each l. If the coefficients A_{eml} and A_{oml} vanish, the generated $\mathbf{E}$ field has no radial field components, and its modes are called transverse electric (TE). In contrast, if all B_{eml} and B_{oml} are zero, no radial field components in the $\mathbf{H}$ field can be found, and its modes are called transverse magnetic (TM).

2.1.3. Mie Theory

The scattering of light by small particles was first described theoretically by Lorenz Mie in 1908 [109]. In Mie theory, the problem of scattering by a spherical particle is solved by expanding the incident and the scattered field as well as the internal field of the sphere in vector spherical harmonics, as shown before in equations (2.32) and (2.33). If the incident wave is a plane wave, almost all expansion coefficients vanish. Only A_{e1l} and B_{o1l} remain.

The expansions of the internal field of the sphere and the scattered field can be simplified in a similar way. The fields are related through the boundary conditions at the surface of the sphere, which require the tangential components of **E** and **H** to be continuous:

$$(\mathbf{E}_i + \mathbf{E}_s - \mathbf{E}_e) \times \hat{\mathbf{e}}_r = (\mathbf{H}_i + \mathbf{H}_s - \mathbf{H}_e) \times \hat{\mathbf{e}}_r = 0. \tag{2.34}$$

The subscripts i, s and e stand for the incident field, the field inside the sphere and the scattered field, respectively. The expansion coefficients of the scattered field are identified as the scattering coefficients a_l and b_l and can be written as

$$a_l = \frac{\mu_2 N^2 j_l(Nx)[x j_l(x)]' - \mu_1 j_l(x)[Nx j_l(Nx)]'}{\mu_2 N^2 j_l(Nx)[x h_l^{(1)}(x)]' - \mu_1 h_l^{(1)}(x)[Nx j_l(Nx)]'}, \tag{2.35}$$

$$b_l = \frac{\mu_1 j_l(Nx)[x j_l(x)]' - \mu_2 j_l(x)[Nx j_l(Nx)]'}{\mu_1 j_l(Nx)[x h_l^{(1)}(x)]' - \mu_2 h_l^{(1)}(x)[Nx j_l(Nx)]'}. \tag{2.36}$$

The differentiation indicated by the prime has to be done with respect to the argument of the respective spherical Bessel or Hankel function. If the denominator of a particular coefficient becomes zero, the corresponding mode is dominant in the scattering field. The frequencies of these scattering resonances are called natural frequencies of the sphere and can be identified by solving the following equations for the a_l modes

$$\frac{[x h_l^{(1)}(x)]'}{h_l^{(1)}(x)} = \frac{\mu_1 [Nx j_l(Nx)]'}{\mu_2 N^2 j_l(Nx)}, \tag{2.37}$$

and the b_l modes

$$\frac{[x h_l^{(1)}(x)]'}{h_l^{(1)}(x)} = \frac{\mu_2 [Nx j_l(Nx)]'}{\mu_1 j_l(Nx)}. \tag{2.38}$$

The relative refractive index $N = \frac{n_1}{n_2}$ is the ratio between the refractive indices of the particle n_1 and the medium n_2. The same subscripts are used for the permeability μ. The size parameter

$$x = kR = \frac{2\pi n_2 R}{\lambda} \tag{2.39}$$

is a dimensionless scattering parameter, combining the vacuum wavelength λ and the radius of the sphere R. Knowledge of the scattering coefficients allows for calculation of the scattering and extinction cross sections

$$C_{sca} = \frac{2\pi}{k^2} \sum_{l=1}^{\infty} (2l+1)(|a_l|^2 + |b_l|^2), \tag{2.40}$$

$$C_{ext} = \frac{2\pi}{k^2} \sum_{l=1}^{\infty} (2l+1)\,\mathrm{Re}\{a_l + b_l\}, \tag{2.41}$$

as well as the absorption cross section

$$C_{abs} = C_{ext} - C_{sca}. \tag{2.42}$$

The revealed degeneracy in m is only valid for perfect spherical particles. If the particle's symmetry is broken, as is the case for a spheroidal particle geometry, the degeneracy is lifted and different frequencies for the split modes can be observed.

2.2. Dielectric Microspheres

Small dielectric particles with spherical or spheroidal geometry are able to confine light by internal guiding of specific modes. They act as optical resonators which support so-called whispering-gallery modes (WGM). In the following subsection WGM are explained with the previously obtained results from Mie theory.

2.2.1. Whispering-Gallery Modes

The term whispering-gallery mode originates from the acoustic effect of sound waves traveling along round galleries of dome-like buildings. Whispers spoken into the gallery are audible all around the gallery wall, while they are hardly noticeable when they are directed straight to the listener. This effect was explained in detail by Lord Rayleigh for the case of St. Paul's Cathedral with reflection of sound waves at the concave walls [110] and a mode structure due to resonantly interfering waves. WGM are also known for other wave types, like matter waves [111] and electromagnetic waves [10]. Most prominent for the latter case are light waves, guided inside a round dielectric structure with refractive index n_1, the resonator, surrounded by a medium with a lower index of refraction $n_2 < n_1$. In the regime of geometrical optics this can be explained by a ray of light which is reflected at the interface between the two materials, as shown in figure 2.1. The ray is incident on the interface at an angle α, that fulfills the criterion for total internal reflection

$$\alpha \geq \arcsin\left(\frac{n_2}{n_1}\right), \tag{2.43}$$

and thus, is completely reflected and not refracted out of the resonator. For a circular structure, the light can be guided all around the interface in this way. After each round trip, the guided light interferes constructively with the primary beam only when their phases vary by an integer multiple of 2π. The result is a standing wave inside the resonator. The resonance condition depends on the resonator's circumference and the wavelength of the light, in addition to the dielectric properties on both sides of the interface. In analogy to the acoustic effect, these resonances are also called WGM.

The ray-optics picture is appropriate for structures much larger than the wavelength of the guided light. For smaller resonators, a wave-optics picture has to be used to determine

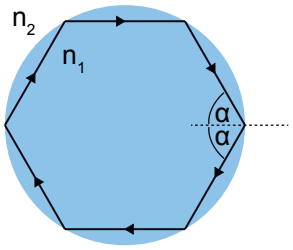

Figure 2.1.: Whispering-gallery modes (WGM) explained with ray optics. A light ray is completely reflected due to total internal reflection at the interface between the dielectric resonator with refractive index n_1 and the surrounding medium with $n_2 < n_1$ for sufficiently large incidence angles α. If the guided light is in phase with the primary beam after one round trip, standing resonant waves can be observed inside the resonator.

the modes. For the case of spherical resonators, this has already been done in the previous subsection by solving the scattering problem of a sphere. The normal or eigenmodes of the sphere are determined by the solutions of equations (2.37) and (2.38), which are labeled by l, m and the number of the root of the Bessel function n. Each normal mode of the sphere is generated by one of the vector spherical harmonics $\mathbf{M}$ or $\mathbf{N}$ (see section 2.1.2) and can be classified as TE or TM according to the radial components of the modes. In the normalized intensity distributions of the electric field shown in figure 2.2, the TE mode of a silica microsphere with a diameter of 5 µm in air with $n = 1$ and $m = l = 31$ is compared to the TM mode with the same mode numbers. The modes are calculated using the vector spherical harmonics in equations (2.28) to (2.31) with respect to the boundary conditions in equation (2.34). The material model for the refractive index including dispersion is given in appendix A.1. For the field inside the sphere the spherical Bessel function of the first kind $j_l(k_1 r)$ is used for $z_l(kr)$ to fulfill the condition of a finite field at the origin. Outside the sphere the spherical Hankel function $h_l^{(1)}(k_2 r)$ is used (compare to equations (2.24) and (2.26)). The corresponding magnetic field distributions are not shown, but can easily be obtained in the same way.

Two higher TE modes are shown in figure 2.3. The images illustrate the influence of the mode numbers n, l and m: the radial mode number n gives the number of maxima in the radial direction, while l and m are the angular mode numbers which predict $2m$ maxima along the equator (xy-plane) and $l - m + 1$ maxima along the meridians (e.g. xz-plane) of the sphere.

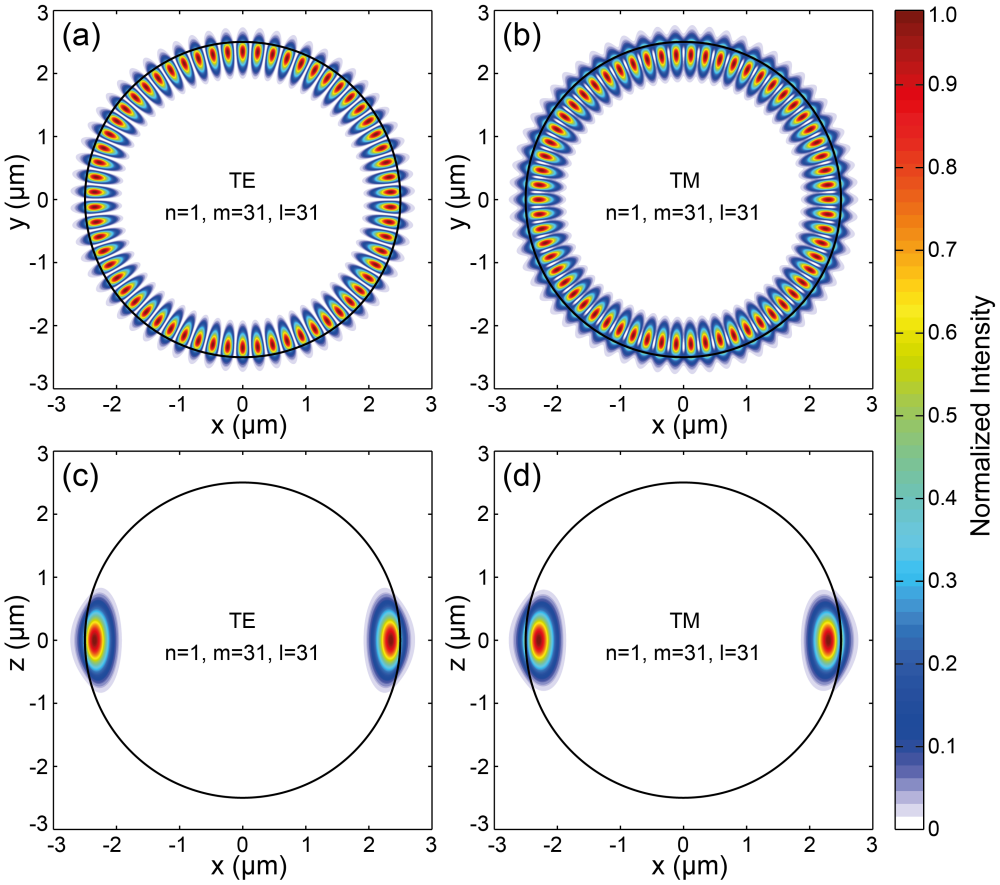

Figure 2.2.: Normalized electric field intensity distributions of TE and TM modes with $n = 1$, $m = l = 31$ inside a 5 µm spherical silica microresonator in air. The (a) TE and (b) TM mode is calculated in the xy-plane ($\theta = \frac{\pi}{2}$). (c) and (d) show the same modes in the xz-plane ($\phi = 0$), respectively. The intensity of the electric field is discontinuous at the interface (black circles) between sphere and surrounding medium for the TM mode due to the non-vanishing radial component of the electric field.

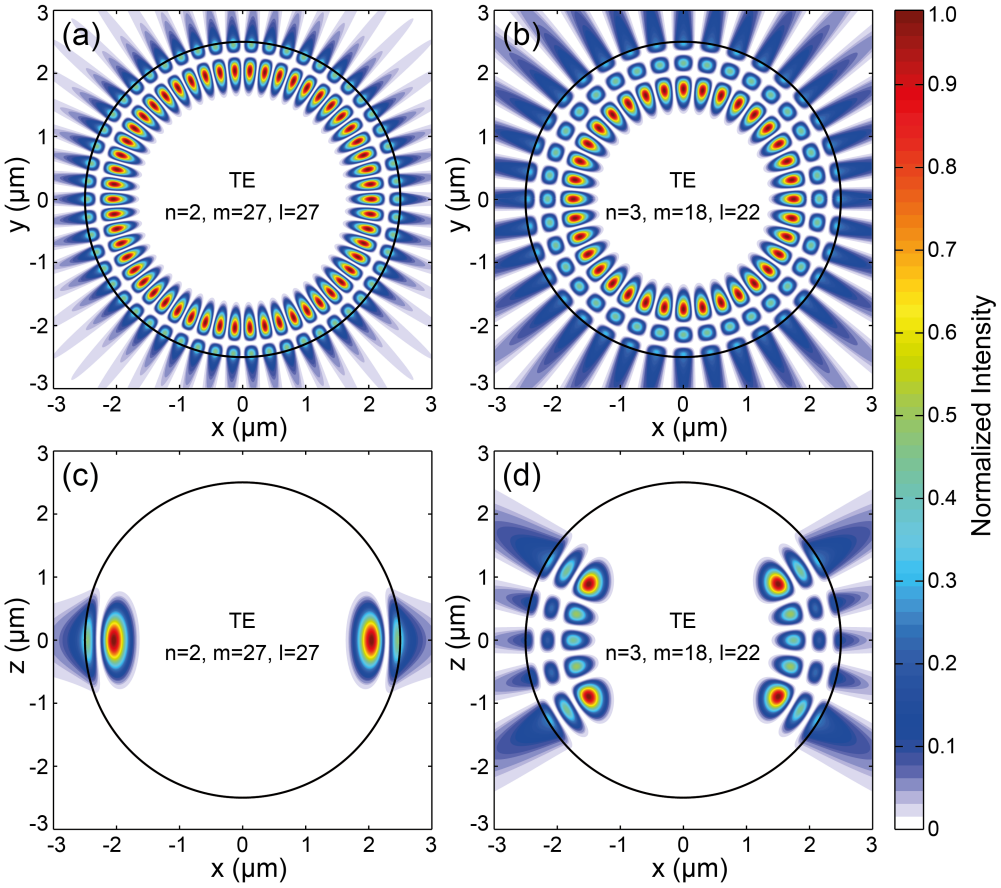

Figure 2.3.: Normalized electric field intensity distributions of TE modes with higher mode numbers inside a 5 µm spherical silica microresonator in air. Modes in the xy-plane with (a) $n = 2$, $m = l = 27$ and (b) $n = 3$, $m = 18$, $l = 22$. (c) and (d) show the same modes in the xz-plane ($\phi = 0$), respectively. In the radial direction n maxima can be observed. The number of maxima along the equator (xy-plane) is given by $2m$ and along a meridian (xz-plane) by $l - m + 1$.

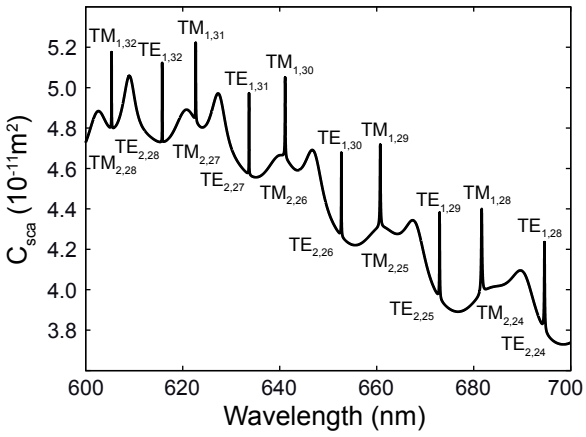

Figure 2.4.: Scattering cross section calculated from 600 nm to 700 nm of a 5 µm silica sphere in air showing resonances at the spectral positions of the sphere's natural modes.

The scattering cross section of a 5 µm silica sphere in air in the spectral range of 600 nm to 700 nm calculated with equation (2.40) can be seen in figure 2.4. One can clearly distinguish between different sharp resonances, representing different normal TE and TM modes of the sphere. Resonances with larger radial mode numbers n show peaks with larger widths due to the lower confinement strength of the optical modes. From figures 2.2 and 2.3, it can be seen that the electromagnetic field is guided in the sphere, but a small part protrudes into the medium as an evanescent field. With increasing radial mode number n, the radial distribution of the field expands in the two radial directions: towards the center of the sphere as well as into the medium. As a result, modes with higher n show lower field intensities and the losses also rise.

2.2.2. Spherical Microresonators

Due to their ability to confine light, dielectric microspheres are optical resonators, enabling confinement of light and intensity enhancement. The amount of energy that can be stored in a particular mode of a resonator is specified by the quality factor Q, defined as

$$Q = 2\pi \times \frac{\text{energy stored}}{\text{energy loss per cycle}}. \tag{2.44}$$

The quality factor is related to the photon storage time τ at the frequency ν_0 by

$$Q = 2\pi\nu_0\tau = \frac{\nu_0}{\Delta\nu} = \frac{\lambda_0}{\Delta\lambda}, \tag{2.45}$$

which allows Q to also be defined by the linewidth of the resonance $\Delta\nu$. The same can be done in terms of the wavelength λ. Thus, for narrow resonance linewidths, high quality factors are needed. The quality factor is limited by different types of losses which contribute individually:

$$\frac{1}{Q} = \frac{1}{Q_{mat}} + \frac{1}{Q_{sur}} + \frac{1}{Q_{rad}} + \frac{1}{Q_{cou}}. \tag{2.46}$$

Q_{mat} is related to absorption and scattering losses in the resonator material. Losses due the roughness and contamination of the surface contribute by Q_{sur}. Radiation losses Q_{rad}

are caused by the curvature of the spherical microresonator and Q_{cou} covers losses related to electromagnetic coupling to other structures. Provided that the resonator material itself has negligible loss, it is the surface quality that limits the quality factor of resonators that are sufficiently larger than the resonance wavelength. However, for smaller resonators, like the microspheres used in this work, radiation losses cannot be neglected either.

In addition to the quality factor, further parameters are used to characterize optical resonators. The free spectral range λ_{FSR} describes the spectral spacing of the resonator modes, which is related to the linewidth $\Delta\lambda$ by the finesse

$$\mathcal{F} = \frac{\lambda_{\mathrm{FSR}}}{\Delta\lambda} = Q\frac{\lambda_{\mathrm{FSR}}}{\lambda_0}. \tag{2.47}$$

The finesse is a measure of the number of photon round-trips during their lifetime in the resonator. Furthermore, the volume of the optical modes in the resonator is important, as a small mode volume enables high field intensities. The mode volume can be calculated from the mode's electric field $\mathbf{E}$ by [112]

$$V_{mode} = \frac{\int \varepsilon(\mathbf{r})|\mathbf{E}(\mathbf{r})|^2 d^3\mathbf{r}}{\varepsilon(\mathbf{r}_M)|\mathbf{E}(\mathbf{r}_M)|^2}, \tag{2.48}$$

with $\mathbf{r}_M$ being the point of maximum field intensity.

High quality factors and small mode volumes are important for cavity quantum electrodynamic (CQED) experiments [10], which however are not of interest in this thesis.

2.3. Plasmonic Nanoparticles

Metal nanoparticles and nanowires are able to confine electromagnetic fields to dimensions much smaller than the vacuum wavelength. Their outstanding optical behavior is explained by surface plasmon polaritons (SPPs) and localized surface plasmons (LSPs), respectively, which are described in this section, starting with a short introduction to the optical properties of metals.

2.3.1. Dielectric Function of Metals

The dielectric function of metals can be described using the Drude model. The basis of this microscopic model is the assumption of a free electron gas for the conduction band electrons, which can be excited by an electric field to perform collective oscillations.

The equation of motion for a single electron with electric charge e and effective mass m^* in an electric field $\mathbf{E}$ can be written as

$$m^*\ddot{\mathbf{x}} + m^*\gamma\dot{\mathbf{x}} = -e\mathbf{E}, \tag{2.49}$$

where the constant γ accounts for the damping of the electron oscillations. The solution of the differential equation for a harmonic time-dependent driving field $\mathbf{E}(t) = \mathbf{E}_0 e^{-i\omega t}$ is obtained from

$$\mathbf{x}(t) = \frac{e}{m^*(\omega^2 + i\gamma\omega)}\mathbf{E}(t). \tag{2.50}$$

When the whole electron gas with electron density n is displaced by $\mathbf{x}$ from its resting position, the polarization is given by

$$\mathbf{P}(t) = -ne\mathbf{x} \tag{2.51}$$

and the dielectric displacement can be written as

$$\mathbf{D}(t) = -\frac{\omega_p^2}{\omega^2 + i\gamma\omega}\varepsilon_0\mathbf{E}(t), \tag{2.52}$$

with the plasma frequency

$$\omega_p^2 = \frac{ne^2}{\varepsilon_0 m^*}. \tag{2.53}$$

Comparison to equation (2.5) results in the complex dielectric function of the Drude model

$$\varepsilon(\omega) = 1 - \frac{\omega_p^2}{\omega(\omega + i\gamma)}, \tag{2.54}$$

or, separated into real and imaginary components, $\varepsilon = \varepsilon_1 + i\varepsilon_2$ with

$$\varepsilon_1(\omega) = 1 - \frac{\omega_p^2}{\omega^2 + \gamma^2}, \tag{2.55}$$

$$\varepsilon_2(\omega) = \frac{\omega_p^2\gamma}{\omega(\omega^2 + \gamma^2)}. \tag{2.56}$$

For large frequencies, equation (2.54) becomes predominantly real with the simplified expression

$$\varepsilon(\omega) = 1 - \frac{\omega_p^2}{\omega^2}, \tag{2.57}$$

which results in the dispersion relation for transverse electromagnetic waves

$$\omega^2 = \omega_p^2 + k^2c^2 \tag{2.58}$$

$$\text{with } c^2 = \frac{1}{\varepsilon_0\mu_0}. \tag{2.59}$$

This condition can only be fulfilled when the frequency is larger than the plasma frequency ($\omega > \omega_p$). For smaller frequencies ($\omega < \omega_p$) light propagation in the metal is forbidden, since transverse electomagnetic waves are not allowed: the light is absorbed or reflected depending on the particular damping constant. In the case of $\omega \ll \gamma$, the metal is strongly absorbing with the absorption coefficient

$$\alpha = \sqrt{\frac{2\omega_p^2\omega}{\gamma c^2}}. \tag{2.60}$$

In this case electromagnetic fields fall off with $e^{-\frac{z}{\delta}}$ inside the metal (Beer-Lambert law), giving the penetration depth $\delta = \frac{2}{\alpha}$, also called skin depth in metals.

However, at the plasma frequency ω_p and with negligible damping the dielectric function becomes zero, and thus $\mathbf{D} = 0$, indicating a longitudinal oscillation mode of the free electron gas (compare to equation (2.11)). With equation (2.5), it turns out that the electric field is purely depolarizing in this case, because

$$\mathbf{E} = -\frac{\mathbf{P}}{\varepsilon_0}, \tag{2.61}$$

which can be understood as a collective displacement of the free electrons against the fixed, positively charged ion cores. The shifted charges cause an electric field that exerts a restoring force on them. The plasma frequency is the natural frequency of the undisturbed oscillation of the free electrons in the metal. The oscillations are called volume plasmons, if no surface effects are involved.

For noble metals, the Drude model needs an extension due to the highly polarized background of ion cores and bound electrons close to the Fermi surface, leading to the modified dielectric function

$$\varepsilon(\omega) = \varepsilon_\infty - \frac{\omega_p^2}{\omega(\omega + i\gamma)}. \tag{2.62}$$

The additional dielectric term ε_∞ can be assumed constant in the visible regime and is typically in the range of 1 to 10 [107].

Another adjustment is necessary for real metals, where the Drude model fails to describe the dielectric function at higher frequency accurately due to interband transitions. For gold, these excitations of electrons from filled bands below the Fermi surface to higher bands start at visible frequencies. They are responsible for the deviations from the theoretical Drude curve shown in figure 2.5. The interband transitions can be described as bound electrons, taken into account by the addition of resonance frequencies ω_0 in equation (2.49):

$$m^*\ddot{\mathbf{x}} + m^*\gamma\dot{\mathbf{x}} + m^*\omega_0^2\mathbf{x} = -e\mathbf{E}. \tag{2.63}$$

The solution extends the free electron term of the Drude model by using additional Lorentz oscillators to the dielectric function of the Drude-Lorentz model

$$\varepsilon(\omega) = \varepsilon_\infty - \frac{\omega_D^2}{\omega(\omega + i\gamma_D)} + \sum_j \frac{\Delta\varepsilon_j \Omega_j^2}{\Omega_j^2 - \omega(\omega + i\Gamma_j)}. \tag{2.64}$$

In addition to the plasma frequency ω_D and the damping rate γ_D of the Drude model, Lorentz terms with resonance frequencies Ω_j and damping rates Γ_j of the individual oscillators are included with weighting factors $\Delta\varepsilon_j$. With the extended model it is possible to get an appropriate analytical expression for the dielectric function, as shown for gold in figure 2.5 in the range of 1 eV to 2.5 eV corresponding to wavelengths between 500 nm and 1200 nm. While the Drude model alone gives adequate values only for the real part of the dielectric function, adding one Lorentz oscillator term is sufficient to also describe the imaginary part. For larger energies, more oscillator terms are needed (see appendix A.2 for more details).

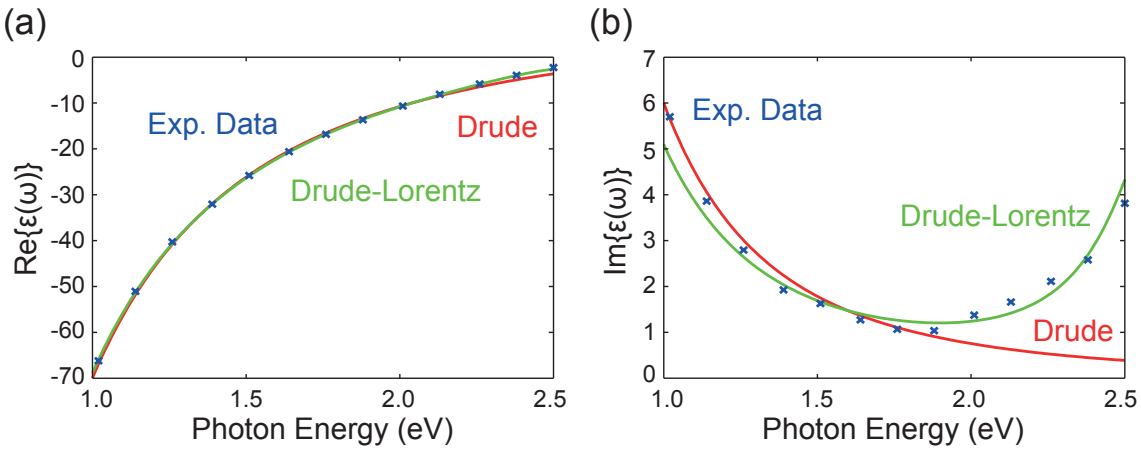

Figure 2.5.: Theoretical dielectric functions of gold compared to experimental data (blue crosses) from Johnson and Christy [113]. Their (a) real and (b) imaginary parts are calculated with Drude (red curves) and Drude-Lorentz theory with one Lorentz term (green curves). The used values are given in appendix A.2.

2.3.2. Surface Plasmon Polaritons

At the interface between a metal and a dielectric, electromagnetic surface waves can be excited by coupling electromagnetic fields to the free electron gas of the metal. Such surface plasmon polaritons (SPPs) propagate along the interface, as indicated in figure 2.6(a). Normal to the interface, the field is evanescent with a much shorter penetration depth in the metal than in the dielectric.

The propagating SPPs are assumed to be time-harmonic and thus have to fulfill the vector wave equations (2.16) and (2.17). Without loss of generality, the geometry is chosen as illustrated in figure 2.6(a), with a SPP propagating in x and ε only varying in the z direction. The ansatz for the electric field

$$\mathbf{E}(\mathbf{r}) = \mathbf{E}(z)e^{i\beta x}, \tag{2.65}$$

where $\beta = k_x$ is the propagation constant of the wave vector $\mathbf{k}$ with

$$\begin{aligned} k^2 &= k_x^2 + k_y^2 + k_z^2, && (2.66)\\ &= \beta^2 + k_z^2, && (2.67)\\ &= k_0^2\varepsilon, && (2.68) \end{aligned}$$

leads to a wave equation for guided electromagnetic modes

$$\frac{\partial^2 \mathbf{E}(z)}{\partial z^2} + (k_0^2\varepsilon - \beta^2)\mathbf{E} = 0. \tag{2.69}$$

A similar equation is found analogously for the magnetic field $\mathbf{H}$. By evaluating equations (2.12) and (2.14), two sets of equations can be derived, which differ by the polarization properties of the propagating waves. The field components of transverse magnetic

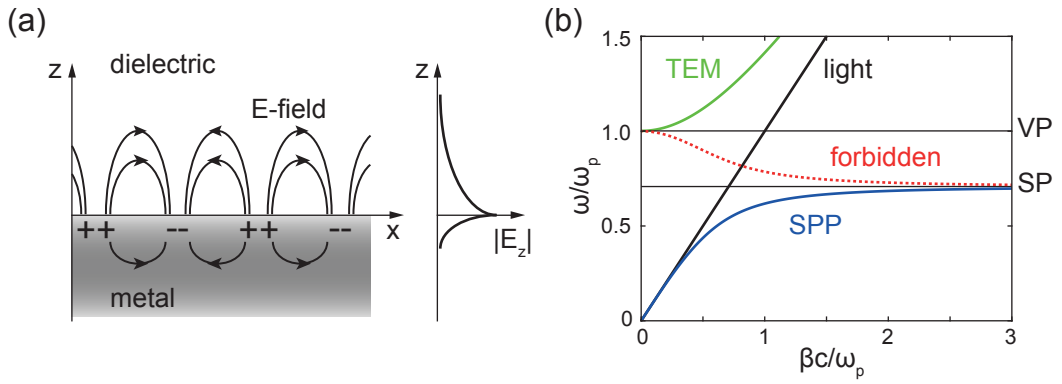

Figure 2.6.: Surface plasmon polariton (SPP) at a planar interface between a dielectric and a metal. (a) Charge oscillations in the metal propagate along the surface. The associated evanescent electromagnetic field decays much faster in the metal than in the dielectric. (b) Dispersion relations in the free electron gas of a Drude metal without damping at an interface to air. The frequency ω and the propagation constant β are normalized to the plasma frequency ω_p. For β the real (blue curve) and the imaginary part (red curve) are shown from the SPP dispersion relation in addition to that from the transverse electromagnetic waves (green curve). SP: surface plasmon, VP: volume plasmon.

(TM) modes are described by

$$E_x = -\frac{i}{\omega\mu\varepsilon_0\varepsilon}\frac{\partial H_y}{\partial z}, \tag{2.70}$$

$$E_z = -\frac{\beta}{\omega\mu\varepsilon_0\varepsilon}H_y, \tag{2.71}$$

$$\frac{\partial^2 H_y}{\partial z^2} + (k_0^2\varepsilon - \beta^2)H_y = 0, \tag{2.72}$$

while E_y, H_x and H_z vanish. For transverse electric (TE) modes the opposite is true and only the following components remain:

$$H_x = -\frac{i}{\omega\mu_0}\frac{\partial E_y}{\partial z}, \tag{2.73}$$

$$H_z = -\frac{\beta}{\omega\mu_0}E_y, \tag{2.74}$$

$$\frac{\partial^2 E_y}{\partial z^2} + (k_0^2\varepsilon - \beta^2)E_y = 0. \tag{2.75}$$

For the simple geometry of a planar interface at $z = 0$ between a non-absorbing dielectric with positive real dielectric constant ε_d and a metal with negative real dielectric function $\varepsilon_m(\omega)$, the solutions of the TM modes (equations (2.70) to (2.72)) for the dielectric half space ($z > 0$) are

$$H_y(z) = A_d e^{i(\beta x - k_{z,d}z)}, \tag{2.76}$$

$$E_x(z) = iA_d\frac{1}{\omega\varepsilon_0\varepsilon_d}k_{z,d}e^{i(\beta x - k_{z,d}z)}, \tag{2.77}$$

$$E_z(z) = -A_d\frac{\beta}{\omega\varepsilon_0\varepsilon_d}e^{i(\beta x - k_{z,d}z)}, \tag{2.78}$$

and for the metal half space ($z < 0$)

$$H_y(z) = A_m e^{i(\beta x + k_{z,m} z)}, \tag{2.79}$$

$$E_x(z) = -iA_m \frac{1}{\omega \varepsilon_0 \varepsilon_m} k_{z,m} e^{i(\beta x + k_{z,m} z)}, \tag{2.80}$$

$$E_z(z) = -A_m \frac{\beta}{\omega \varepsilon_0 \varepsilon_m} e^{i(\beta x + k_{z,m} z)}. \tag{2.81}$$

The continuity of H_y and εE_z at the interface yields

$$A_m = A_d, \tag{2.82}$$

$$\frac{k_{z,d}}{k_{z,m}} = -\frac{\varepsilon_d}{\varepsilon_m}. \tag{2.83}$$

The z components of the wave vector in the dielectric ($k_{z,d}$) and the metal ($k_{z.m}$) are obtained from equations (2.67) and (2.68), that combine together with equation (2.83) to obtain the expressions

$$\beta^2 = k_0^2 \frac{\varepsilon_m \varepsilon_d}{\varepsilon_m + \varepsilon_d}, \tag{2.84}$$

$$k_{z,d}^2 = k_0^2 \frac{\varepsilon_d^2}{\varepsilon_m + \varepsilon_d}, \tag{2.85}$$

$$k_{z,m}^2 = k_0^2 \frac{\varepsilon_m^2}{\varepsilon_m + \varepsilon_d}. \tag{2.86}$$

Equation (2.84) is the dispersion relation of a SPP propagating at the planar interface between the dielectric and the metal. For $\varepsilon_d > 0$ such a bound propagating mode requires $\mathrm{Re}\{\varepsilon_m\} < 0$ and $|\varepsilon_m| > \varepsilon_d$ due to equations (2.83) and (2.84) for a real propagation constant β. The reciprocal values of the pure imaginary z components $k_{z,d}$ and $k_{z,m}$ of the wave vector $\frac{1}{|k_{z.m}|}$ and $\frac{1}{|k_{z,d}|}$ define the evanescent decay length of the fields in the z direction in the metal and the dielectric, respectively.

In analogy, solutions for the TE modes (equations (2.73) to (2.75)) are found similarly to equations (2.76) to (2.81), but with the resulting condition

$$A_m(k_{z,m} + k_{z,d}) = 0, \tag{2.87}$$

that only has the trivial solution $A_d = A_m = 0$. Thus, TE-polarized surface modes do not exist, and SPPs are always TM polarized.

In figure 2.6(b) the dispersion relation of a SPP from equation (2.84) is plotted for a planar interface between air and a Drude metal without damping (compare to equation (2.57)) (blue curve). For small values of β it resembles the light line with dispersion relation $\omega = c\beta$, while for large values ω approaches the surface plasmon (SP) frequency $\omega_{SP} = \frac{\omega_p}{\sqrt{1+\varepsilon_d}}$. At this frequency $\varepsilon_m \to -\varepsilon_d$ and the surface plasmon mode becomes electrostatic with a vanishing group velocity, due to the infinite propagation factor $\beta \to \infty$. In contrast to the bound modes, radiative transverse electromagnetic (TEM) modes can be observed for $\omega > \omega_p$ (green curve) indicated by the dispersion relation in equation (2.58). Between the two regimes, any mode propagation is forbidden, as the propagation constant is completely imaginary (red curve).

The fact that the SPP dispersion curve does not cross the light line implies that SPPs cannot couple directly to photons, because this would violate the conservation of energy or momentum. The SPP has a shorter wavelength than the free wave propagating in the dielectric. Thus, different excitation schemes have to be involved, like the creation of evanescent fields at the surface of a prism by total internal reflection, in order to match the wave vectors in the metal and the dielectric [114, 115]. Another method makes use of light scattering into the SPP mode at discontinuities of the plasmonic waveguide. Rough surfaces or the ends of a nanofiber are sufficient for this [116].

Once excited a SPP propagates along the interface. For real metals the imaginary part of $\varepsilon_m(\omega)$ cannot be neglected, in general, and the propagating SPP is affected by damping due to Ohmic losses, interband transitions and free electron interactions. The imaginary part of β determines the attenuation through the surface plasmon propagation length

$$L = \frac{1}{2\,\mathrm{Im}\{\beta\}}, \tag{2.88}$$

as the length at which the SPP intensity decays by $\frac{1}{e}$.

2.3.3. Localized Surface Plasmons

Plasmonic nanoparticles also support surface plasmons, but instead of propagating they are localized to the small particle dimensions in all directions. The resonances of such localized surface plasmons (LSPs) are not only determined by the dielectric function of the particle material and the surrounding medium, but also by the size and the shape of the particle. In contrast to SPPs, matching of the wave vectors needs not be considered. As the nanoparticle is discontinuous in every direction, LSPs can be excited by direct illumination.

For particle sizes much smaller than the excitation wavelength and the skin depth, the quasi-static approximation can be used for a descriptive explanation. In this case, the exciting field is nearly constant over the whole particle as illustrated in figure 2.7. For a spherical particle with radius a in a static homogeneous electric field $\mathbf{E}_0$, the behavior of such a small particle can be described by an ideal dipole with induced dipole moment

$$\mathbf{p} = \varepsilon_0 \varepsilon_d \alpha \mathbf{E}_0, \tag{2.89}$$

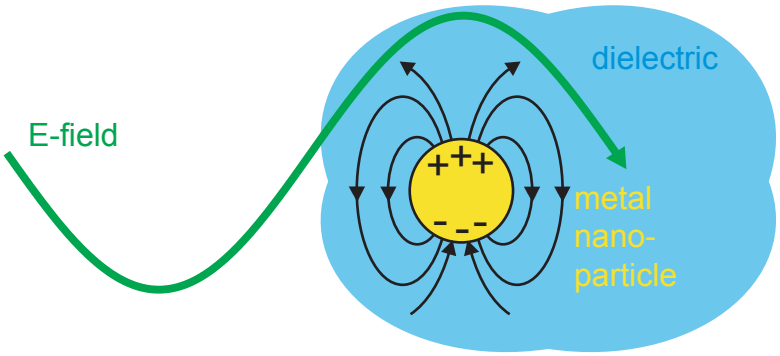

Figure 2.7.: Sketch of a localized surface plasmon (LSP).

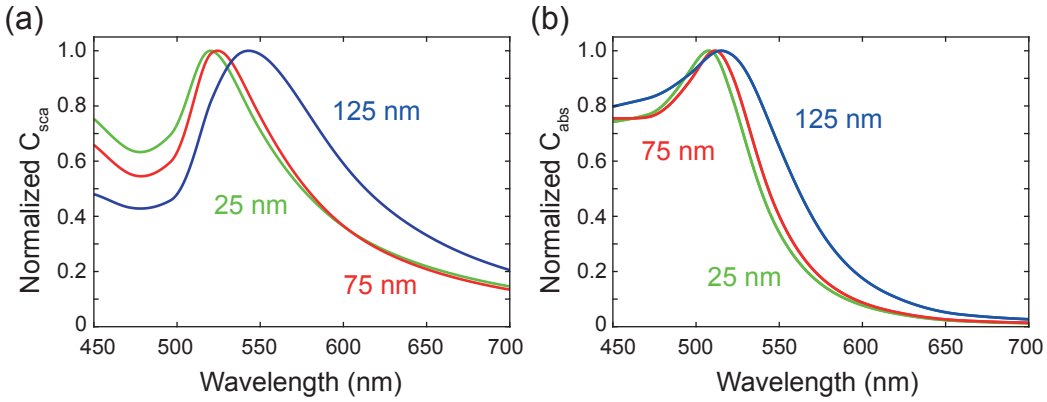

Figure 2.8.: Normalized (a) scattering and (b) absorption cross sections of spherical gold nanoparticles in air with different diameters calculated with Mie theory.

and polarizability

$$\alpha = 4\pi a^3 \frac{\varepsilon_m - \varepsilon_d}{\varepsilon_m + 2\varepsilon_d}, \tag{2.90}$$

with the permittivities ε_m and ε_d of the metal particle and the surrounding dielectric. Changing the incident static electric field to a time-varying plane wave, the dipole moment oscillates with the field frequency, and thus radiates an electric field itself, which explains the scattering. The cross sections for scattering and absorption in the quasi-static description can be derived as

$$C_{sca} = \frac{k^4}{6\pi}|\alpha|^2, \tag{2.91}$$

$$C_{abs} = k\,\mathrm{Im}\{\alpha\}. \tag{2.92}$$

For the minimum of $\varepsilon_m + 2\varepsilon_d$ the polarizability and also the scattering cross sections are maximum. But this is only valid for small particles. When the exciting field is not constant over the whole particle, the quasi-static approximation is no longer justified and a comprehensive electrodynamic description (introduced in section 2.1) is necessary. Taking the particle size into account, the spectral resonance position of a LSP of a spherical particle can be obtained using Mie theory (compare to section 2.1.3). In figure 2.8 normalized scattering and absorption cross sections for spherical gold particles in air calculated with equations (2.40) to (2.42) are shown. The size-dependence of the plasmon resonance can clearly be observed in the scattering cross section, which approaches the limit of the quasi-static approximation for small particles. In contrast, the spectral position of the maximum absorption cross section is less influenced by the particle size.

In analogy to the WGM of a dielectric sphere, as shown in figure 2.2, the LSP modes of a spherical plasmonic nanoparticle are the normal modes of the metal sphere. In figure 2.9 the TM mode of a gold sphere with a diameter of 80 nm in air is shown with $n = 1$ and $l = m = 1$. The field inside the sphere is non-zero and the electric field intensity is maximum at two opposing points on the surface of the sphere. Thus, this mode could be excited only by an electric field polarized in the x direction.

It is worth noting that for very small particles the permittivity is also known to be size-dependent, due to increased surface effects [117]. This dependence has to be taken into

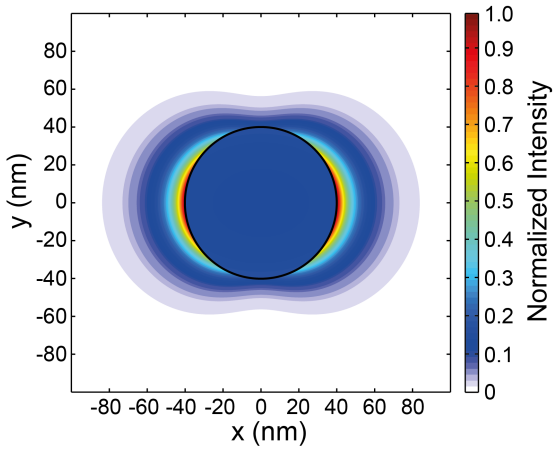

Figure 2.9.: Normalized electric field intensity distribution of the TM mode with $n = 1$ and $m = l = 1$ of a LSP in a gold nanoparticle with a diameter of 80 nm in air.

account for gold nanoparticles with radii up to a few nanometers. However, in this work only significantly larger gold nanoparticles are used, whose dielectric function is considered independent of particle size.

Elliptical particles

The description of non-spherical particles is more complex, because different angles of the incident electric field result in different scattering and absorption cross sections. A simple non-spherical particle geometry is an ellipsoid with semi-axes a, b and c, as shown in figure 2.10(a). For this geometry the polarizability in the quasi-static approximation changes to

$$\alpha_i = 4\pi abc \frac{\varepsilon_m - \varepsilon_d}{3\varepsilon_d + 3L_i\left(\varepsilon_m - \varepsilon_d\right)}, \tag{2.93}$$

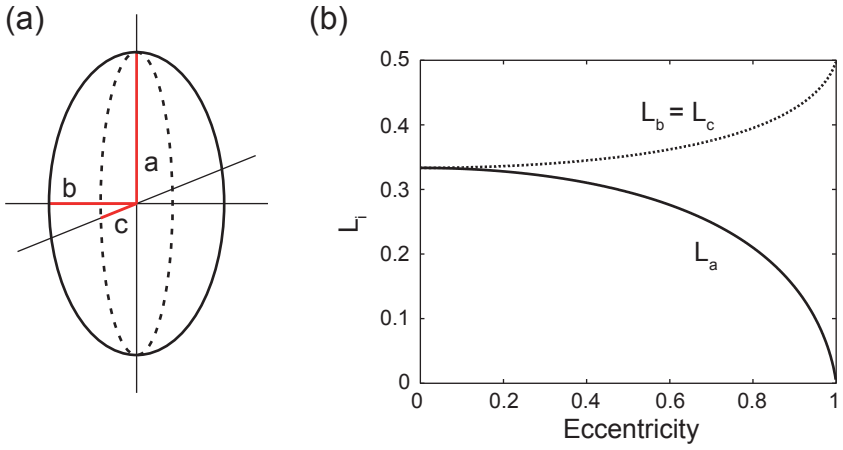

Figure 2.10.: Prolate spheroidal particle with semi-axes a and $b = c < a$. (a) Geometry of the particle. (b) Geometrical factors L_a and $L_b = L_c$ as a function of particle eccentricity.

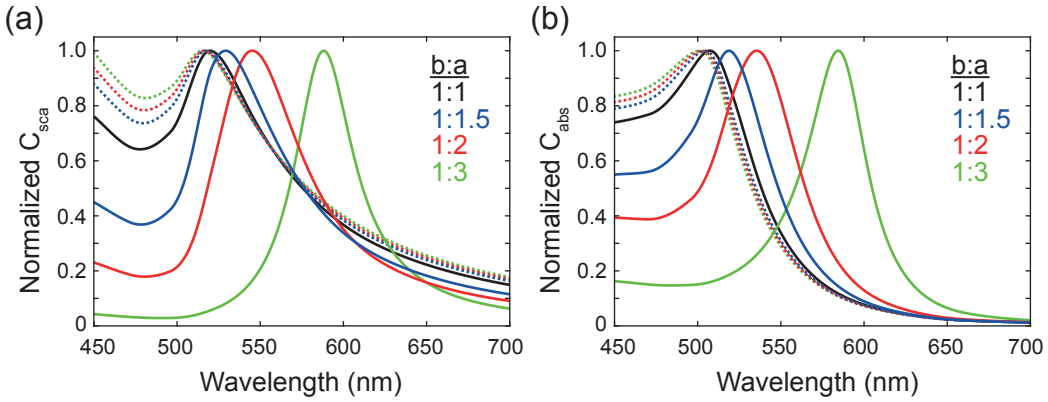

Figure 2.11.: Normalized (a) scattering and (b) absorption cross sections of prolate gold spheroids in air calculated within the quasi-static approximation. Calculations are done for particles with the same volume but different aspect ratios of the semi-axes $a \geq b = c$. The solid and the dashed lines show individually normalized cross sections for the long and the short particle axes, respectively.

if the polarization of the incident electric field is parallel to one of the three principal axes of the particle. The geometrical factors L_i $(i = a, b, c)$ have to fulfill $L_a + L_b + L_c = 1$, leaving only two of them independent.

For a prolate spheroid $(a > b = c)$ the geometry factors can be easily obtained from

$$L_a = \frac{1 - e^2}{e^2} \left(-1 + \frac{1}{2e} \ln \frac{1 + e}{1 - e} \right), \tag{2.94}$$

$$L_b = L_c = \frac{1}{2} \left(1 - L_a \right), \tag{2.95}$$

with the eccentricity

$$e = \sqrt{1 - \frac{b^2}{a^2}}. \tag{2.96}$$

In figure 2.10(b) the two independent geometrical factors for a prolate spheroid are shown as function of eccentricity. For $e = 0$, the geometrical factors are equal: $L_a = L_b = L_c = \frac{1}{3}$, and the polarizability (equation (2.93)) simplifies to that of a sphere (equation (2.90)).

Then, the scattering and absorption cross sections for a prolate spheroid can be calculated in the quasi-static approximation with equations (2.91) to (2.93). Figure 2.11 depicts the scattering cross sections for small prolate gold spheroids in air. Keeping the volume constant, the individually normalized cross sections show a red-shift for the elongated (solid lines) and a blue-shift for the compressed (dashed lines) particle axes with increasing aspect ratio.

As for spherical particles, the quasi-static approximation only holds true for small particles. However, a similar dependence of the scattering and absorption cross sections on the aspect ratio is known for larger particles [9].

Damping

From figures 2.8 and 2.11 it can be seen that not only the spectral positions of the maxima, but also the linewidths of the plasmonic resonances, differ for different particle sizes

and shapes. In general, the resonance peaks are broadened with the particle extension perpendicular to the plasmon oscillation direction. The resonance linewidths of spherical particles increase with diameter and are broader than those of prolate spheroidal particles with the same spectral resonance position. This behavior is explained by damping of the plasmon oscillations, which decay radiatively and non-radiatively. The radiative decay enables the possibility to optically detect the plasmon resonance and increases with particle size. The non-radiative decay is dominated by excitations of electron-hole pairs and scattering of electrons by other electrons, defects or phonons. For particles smaller than the mean free electron path, scattering at the particle surface also influences the plasmon oscillations. In the case of gold, this is significant only for particles smaller than 20 nm and thus does not affect the results in this work.

2.4. Fluorescent Emitters

In addition to particles with optical resonances, optically active nano- and microparticles are also used in this thesis, including polystyrene beads doped with organic molecules, defect centers in nanodiamonds and colloidal quantum dots, which are presented briefly in this section after a short introduction to fluorescence. The fluorescent properties of the emitters themselves are not a topic of this thesis. Sufficient literature for reference can be found in sections 2.4.1 to 2.4.4.

2.4.1. Fluorescence

Fluorescence is the immediate and spontaneous emission of light from a material that has been excited by electromagnetic radiation. For this process, which is known for many different gaseous, liquid and solid materials, an electron of an atom or a molecule is lifted to an excited energy level by absorption of a single photon. When the excited electron relaxes radiatively to the ground state a fluorescence photon is emitted. Usually, the emitted photons have a lower energy, and thus a higher wavelength, than the absorbed photons [118]. This behavior is known as the Stokes shift and can mainly be explained by non-radiative transitions between vibrational energy levels. However, the opposite effect can also occur, where the emitted photon has a higher energy than the absorbed photon, due to absorption of vibrational energy from the host or due to multi-photon absorption [119, 120]. The former is known as the anti-Stokes shift.

2.4.2. Dye-Doped Polystyrene Beads

Polystyrene beads are commercially available in a large range of sizes, from a few tens of nanometers to a few hundreds of micrometers (for example Invitrogen, FluoSpheres). In figure 2.12(a) polystyrene beads with an average diameter of 1 µm are shown. The beads can be doped with a manifold of different fluorophores [121, 122], making them small versatile light sources with adjustable emission spectra. A typical fluorescence emission spectrum of polystyrene beads doped with a red dye can be seen in figure 2.12(b). Unfortunately, fluorophore molecules suffer from photo-bleaching, reducing the usability of such particles for long-time experiments, especially when using higher excitation intensities.

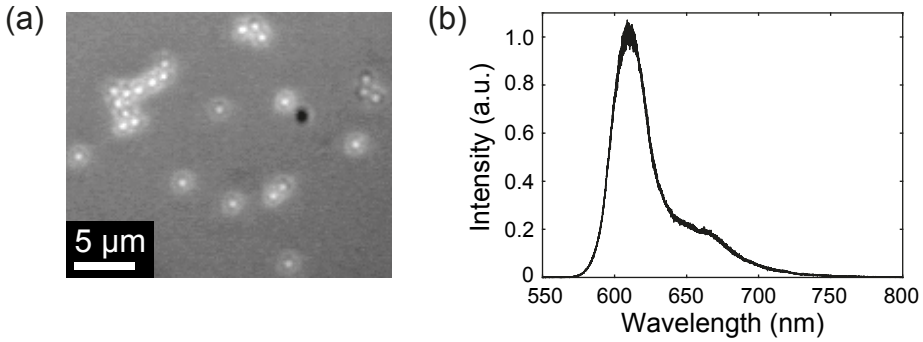

Figure 2.12.: Dye-doped polystyrene beads. (a) Bright-light microscope image of polystyrene beads on a coverslip with an average diameter of 1 µm. The black spot is an artifact of the microscope system. (b) Typical fluorescence emission spectrum of polystyrene beads doped with a red dye. The spectral absorption and emission maxima are at 580 nm and 605 nm, respectively.

2.4.3. Nitrogen Vacancy Defect Centers in Nanodiamonds

Nanodiamonds are diamond nanocrystals with sizes around 100 nm and smaller, as can be seen in figure 2.13(a). Different interstitial or substitutional defects can occur in diamond. The latter consist of impurities or vacancies replacing one or more carbon atoms in the diamond lattice [123]. More than a hundred such defect centers are known to be optically active [27]. Very prominent is the nitrogen vacancy (NV) defect center [124]. In figure 2.13(b) its fluorescence emission spectrum can be seen, which is characterized by visible zero-phonon lines (ZPLs) at 575 nm and 637 nm, respectively, and broad phonon sidebands. The remarkable optical and electronic properties of the NV defect center make them photostable single-photon emitters that can already be used at room temperature [27]. As diamond itself has a large band gap of 5.5 eV, absorption in the host matrix can be neglected down to ultra-violet wavelengths, and the high refractive index of 2.42 enables efficient guiding of light in diamond-based devices [126]. Furthermore, diamond

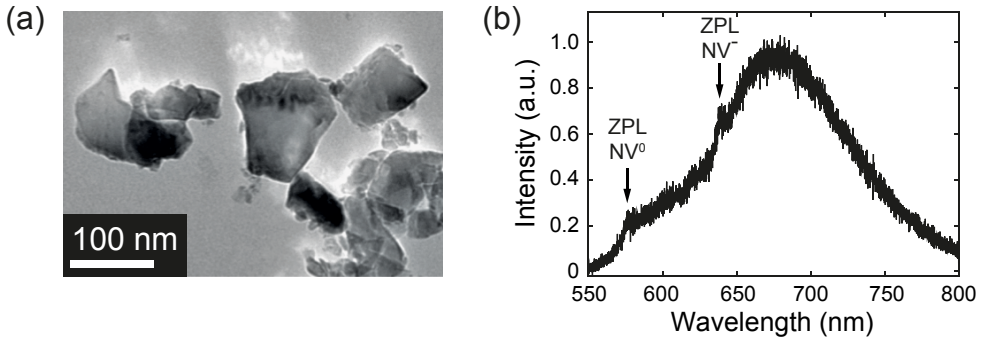

Figure 2.13.: Diamond nanocrystals with nitrogen vacancy (NV) defect centers. (a) Transmission electron microscope image of differently-sized diamond nanocrystals as measured by Gaponik [125]. (b) Fluorescence emission spectrum of many NV defect centers in a cluster of several nanodiamond particles. The visible zero-phonon lines (ZPLs) of the neutral (NV^0) and the negative (NV^-) defect center can be identified at 575 nm and 637 nm, respectively. (See section 5.1.2 for details of the measurement.)

has a high thermal conductivity, facilitating cooling of the crystal lattice.

As shown in figure 2.14(a), the NV center consists of a single nitrogen atom replacing a carbon atom with an adjacent vacancy in the diamond lattice. Thus, this defect center has a C_{3v} molecular symmetry. Occurrence of the NV center is common in natural as well as in synthetic diamond, and can be further increased by electron irradiation and annealing [127]. This requires substitutional nitrogen impurities, which have to be already present in the diamond lattice (type 1b diamond) or can be implanted individually into otherwise pure diamonds [128].

The NV center is found in two different charge states, the neutral NV^0 and the negative NV^- center [129], due to configurations of five or six electrons, respectively. In both cases the five unbound electrons (two from the nitrogen and three from the three carbon atoms) surrounding the vacancy contribute to the defect center, while for the NV^- center an additional electron is assumed to be captured from the lattice [130]. Under optical pumping, the NV center can alternate between the two charge states NV^0 and NV^- [27], which are distinguishable by their characteristic, visible ZPLs as pointed out in figure 2.13(b).

The simplified energy level scheme of the NV^- center is shown in figure 2.14(b). It consists of the spin triplet ground ($^3A_2$) and excited (^3E) states as well as two spin singlet states (^1E, $^1A_1$) [124]. The triplet states can be split by strain or external fields. Typically, optical excitation from $^3A_2$ to ^3E is done by off-resonant pumping with lasers at 514.5 nm or 532 nm. From this state the NV^- center can return to the ground state $^3A_2$ directly by emission of a photon into the visible ZPL at 637 nm or by non-radiative intersystem crossing over $^1A_1$ and ^1E. With weak probability, an additional infrared ZPL_{IR} at 1042 nm, induced by transition between the two singlet states, can also be detected [131]. However, only the visible transition ZPL is of importance in this thesis. Since the NV center is affected by the vibronic modes of the diamond lattice, the emission spectrum shows large phonon broadening of the zero-phonon lines, as can be seen in figure 2.13(b). Even at low temperatures only a small fraction of the overall emission is directly emitted into the ZPLs. Additionally, the meta-stable states further reduce the radiative quantum efficiency.

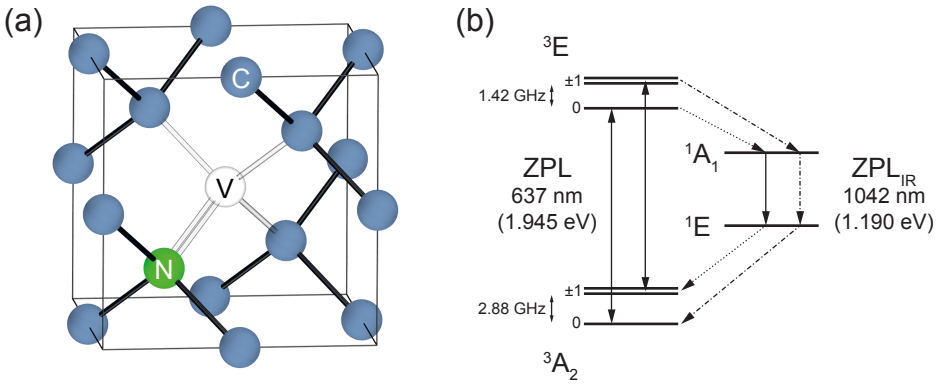

Figure 2.14.: The NV defect center in diamond. (a) Atomic structure of the NV center in the diamond lattice. (b) Energy level scheme of NV^- without the influence of strain or external fields, after [124]. Solid arrows indicate radiative transitions, and dotted and dash-dotted arrows indicate weak and strong non-radiative transitions, respectively.

2.4.4. Colloidal Quantum Dots

Quantum dots are semiconductor structures that tightly confine electric charge carriers. Typically, this confinement is achieved in small islands of a certain semiconductor embedded in a semiconductor matrix with a larger band gap [132], or in colloidal semiconductors with sizes of a few nanometers [16], as shown in figure 2.15(a). Colloidal quantum dots are often capped with an additional shell of a semiconductor material with a larger band gap to improve isolation of the charge carriers and to adjust the optical properties of the quantum dots [133–135]. An example of the fluorescence emission spectrum of colloidal quantum dots consisting of a CdSe core and a ZnS shell with an overall diameter of 4 nm can be seen in figure 2.15(b).

An exciton is a correlated electron-hole pair (see figure 2.16(a)), which can be created by electrical or optical excitation. It can recombine radiatively by emission of a single photon. When the size of the quantum dot is comparable or even smaller than the Bohr radius of the exciton, quantum confinement effects (see figure 2.16) start to influence the energy levels. Typically, there is a shift to larger separations between the energy levels with decreasing quantum dot size [136]. In the strongly confined regime, the emission wavelength of a quantum dot is determined by its size, in addition to the specific materials. Generally, single photons from quantum dots can be observed efficiently only at low temperatures, which requires a cryostat. At higher temperatures the charge carriers escape thermally, assisted by phonon absorption [137]. Also, bleaching and blinking reduce the radiative rate of quantum dots [13].

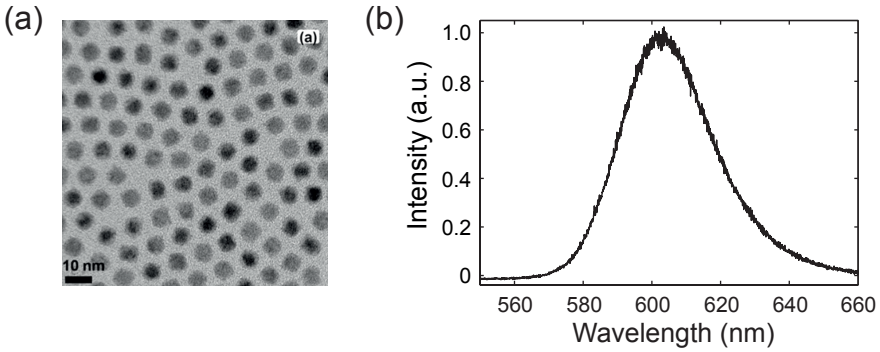

Figure 2.15.: Colloidal core-shell quantum dots. (a) Transmission electron microscope image of PbS/CdS quantum dots with a diameter of 6.5 nm as measured by Zhao et al. [138]. (b) Fluorescence emission spectrum of a cluster of CdSe/ZnS quantum dots with individual diameters of 4 nm. (Details of the measurement can be found in section 5.4.4.)

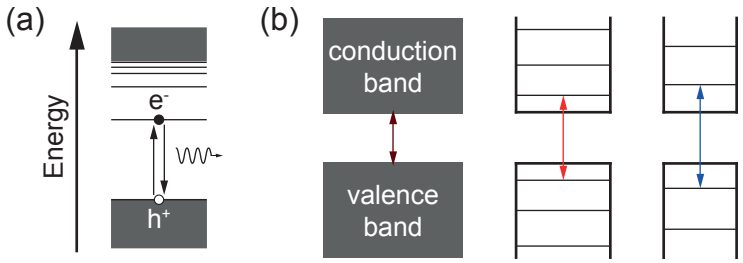

Figure 2.16.: Optically active semiconductor quantum dots. (a) The lowest excitation is an exciton, a correlated electron-hole pair that can recombine by emission of a single photon. (b) With decreasing crystal size the valence and the conduction band change to discrete energy levels with increasing distance. The schematic energy level structure of a quantum dot (middle) is compared to bulk semiconductor (left) and a smaller quantum dot (right). The arrows indicate the lowest optical transition between the energy bands or levels.

3. Linear Paul Trap

Single nano- and microparticles are levitated in linear Paul traps in this thesis. The basic concepts of this kind of particle trap are introduced in the following chapter. Starting from the ideal trap geometry, the theoretical conditions for stable particle confinement are derived from the equations of motion in the form of the normalized Mathieu's differential equation. External influences on the particle trajectories are discussed theoretically before additional aspects of real trap geometries are addressed.

3.1. Ideal Linear Paul Trap

The ideal linear Paul trap consists of four hyperbolically shaped electrodes arranged in quadrupolar configuration as shown in figure 3.1. The parallel electrodes are extended in axial direction similar to a quadrupole mass spectrometer [139]. Opposing electrodes are electrically connected and a direct-current (dc) voltage V_{dc} in series with an alternating-current (ac) voltage V_{ac} with angular frequency Ω is applied between the electrode pairs. The potential difference between the electrodes can be written as

$$\Phi_0(t) = V_{dc} + V_{ac}\cos(\Omega t). \tag{3.1}$$

Like in an electrical quadrupole mass analyzer the created electric field has components only in radial trap direction. For particle stabilization in all three dimensions electric field components in axial direction have to be introduced by additional end cap electrodes or segmentation of the quadrupole electrodes. In the following subsections the mechanisms of radial and axial particle confinement are explained in detail.

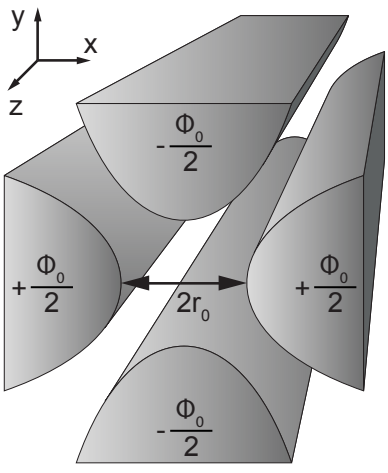

Figure 3.1.: Electrode configuration for radial confinement (xy-plane) in a linear Paul trap. Axial stabilization has to be ensured by additional electrodes.

3.1.1. Radial Stabilization

As already mentioned, a single static electric field is not sufficient to stabilize a charged particle in three dimensions. This problem can be solved by using a dynamic electric field. In the case of a linear Paul trap two-dimensional confinement in radial trap direction is accomplished by using an oscillating trap voltage. Most aspects of the following trap theory are taken from [68, 72, 73, 140] and [141, 142]

Equations of motion

For particle confinement a restoring force has to affect the particle which in the simplest case is proportional to the distance from the trap center:

$$\mathbf{F} \propto -\mathbf{r}. \tag{3.2}$$

The corresponding potential is parabolic

$$\Phi \propto (\alpha x^2 + \beta y^2 + \gamma z^2) \tag{3.3}$$

and has to fulfill the Laplace condition [143], as it is an electric potential

$$\Delta\Phi = 0 = \alpha + \beta + \gamma. \tag{3.4}$$

For the linear quadrupolar electrode configuration $\alpha = 1 = -\beta$ and $\gamma = 0$ satisfy this condition. With respect to equation (3.1) the resulting electric potential is

$$\Phi(x, y, t) = (V_{dc} + V_{ac}\cos(\Omega t))\frac{x^2 - y^2}{2r_0^2}. \tag{3.5}$$

The size parameter r_0 is the minimum distance between the electrodes and the center of the trap. In figure 3.2 the electric potential is depicted at the time $t = 0$ and after half of one periode $t = \frac{T}{2}$. The potential has the form of a saddle that oscillates in time. When the trap parameters are adjusted for the specific charge of a certain particle it can be stabilized between the electrodes.

With $\mathbf{E} = -\nabla\Phi$ and $M\frac{d^2\mathbf{r}}{dt^2} = Q \cdot \mathbf{E}$ the equations of motion for a particle with mass M and charge Q in the oscillating parabolic potential can be written as

$$\frac{d^2x(\tau)}{d\tau^2} + (a + 2q\cos(2\tau)) \cdot x(\tau) = 0, \tag{3.6}$$

$$\frac{d^2y(\tau)}{d\tau^2} - (a + 2q\cos(2\tau)) \cdot y(\tau) = 0, \tag{3.7}$$

$$\frac{d^2z(\tau)}{d\tau^2} = 0, \tag{3.8}$$

with the dimensionless trapping parameters

$$\tau = \frac{\Omega t}{2}, \tag{3.9}$$

$$a = 4\frac{Q}{M}\frac{V_{dc}}{\Omega^2 r_0^2}, \tag{3.10}$$

$$q = 2\frac{Q}{M}\frac{V_{ac}}{\Omega^2 r_0^2}. \tag{3.11}$$

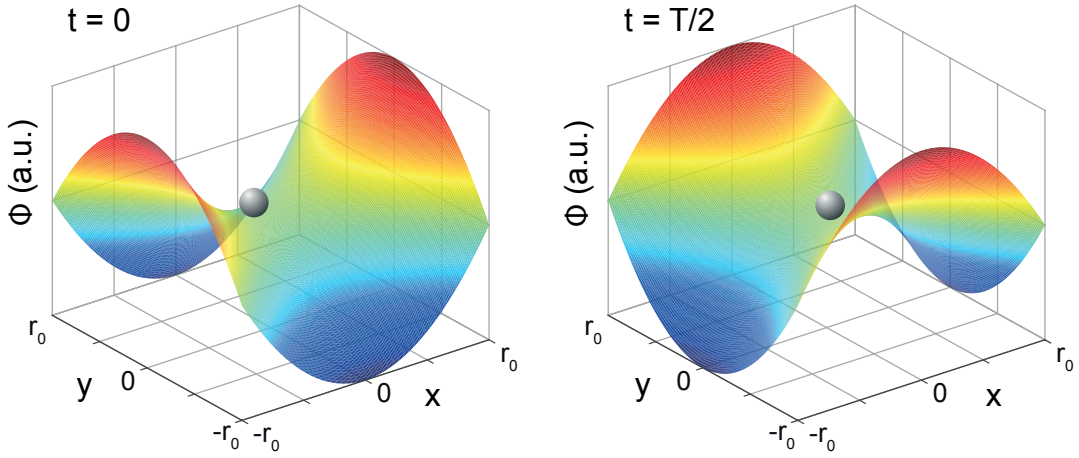

Figure 3.2.: Oscillating saddle potential in the radial plane of the linear Paul trap that is used to stabilize charged particles (indicated by the gray sphere). The left plot shows the potential at the time $t = 0$ and the right plot after half of the oscillation period $t = \frac{T}{2}$.

Equations (3.6) and (3.7) are in the normalized form of Mathieu's differential equation. They describe independent motions in the radial trap directions x and y while equation (3.8) indicates that the quadrupole potential has no effect in the axial trap direction z.

Solution of Mathieu's differential equation

Mathieu's differential equation belongs to the class of Hill's differential equations which are ordinary linear differential equations of second order with periodic coefficients. According to Floquet's theorem, the general solution for x (analogous for y) is given by the following series [140–142]

$$x(\tau) = A_x e^{\mu_x \tau} \sum_{n=-\infty}^{\infty} C_{2n,x} e^{i2n\tau} + B_x e^{-\mu_x \tau} \sum_{n=-\infty}^{\infty} C_{2n,x} e^{-i2n\tau}. \tag{3.12}$$

Equation (3.12) delivers two different kinds of trajectories describing stable or unstable particle motion in the trap. Whether the series converges or diverges with time depends on the characteristic exponent μ_x. For imaginary $\mu_x = i\beta_x$ with non-integer, real values of β_x the solution is periodic with limited amplitudes, which corresponds to stable particle trajectories. A and B are initial values of the particle position. The coefficients C_{2n} depend on the trapping parameters a and q and can be obtained by recursion. In the case of an imaginary characteristic exponent and the assumption $a, q \ll 1$, β_x can be approximated by

$$\beta_x \approx \sqrt{a + \frac{q^2}{2}}. \tag{3.13}$$

Thus, it is determined by a and q alone if stable particle confinement is possible or not. In combination with equations (3.10) and (3.11) this means for trapping of a given charged particle the properties of the voltages applied to the trap electrodes (V_{dc}, V_{ac} and Ω) have to be adjusted with respect to the specific charge of the particle $\frac{Q}{M}$.

For the case of stable trapping, the particle trajectory can be rewritten as

$$x(\tau) = A'_x \sum_{n=-\infty}^{\infty} C_{2n,x} \cos\left((2n+\beta_x)\tau\right) + B'_x \sum_{n=-\infty}^{\infty} C_{2n,x} \sin\left((2n+\beta_x)\tau\right) \tag{3.14}$$

with $A'_x = A_x + B_x$ and $B'_x = i(A_x - B_x)$. Consequently, the particle motion in the trap is a superposition of different harmonic oscillations with the frequency spectrum

$$\omega_{x,n} = \left(n + \frac{\beta_x}{2}\right)\Omega. \tag{3.15}$$

The trajectory can be described as an oscillation at the frequency $\omega_{x,0} = \frac{\beta_x}{2}\Omega$, the so-called secular motion, superposed by integer multiples of the driving trap frequency Ω, the so-called micromotion. For the y trajectory similar results are obtained as only the signs of a and q have to be changed.

Stability diagram

The classification of the solutions of Mathieu's differential equation can be illustrated very clearly in a stability chart as shown in figure 3.3. Depending on the combination of a and q stable and unstable solutions are depicted by gray and white areas, respectively. Because equations (3.6) and (3.7) are not coupled, the solutions are independent from each other for the x and y directions. Where stabilization in both radial trap directions is possible, the areas overlap (yellow areas). Only the first area of stability is shown here, which is in general sufficient for quadrupole ion traps. Stable areas for higher values of a and q can be found [71], but they are difficult to access and do not offer significant advantages for particle trapping. The boundary lines between stable and unstable areas are described by characteristic functions, obtained from a series expansion of the stability parameter a in q for stable trajectories (equation (3.14)) separated in even (a_m) and odd (b_m with $m \in \mathbf{N}$)

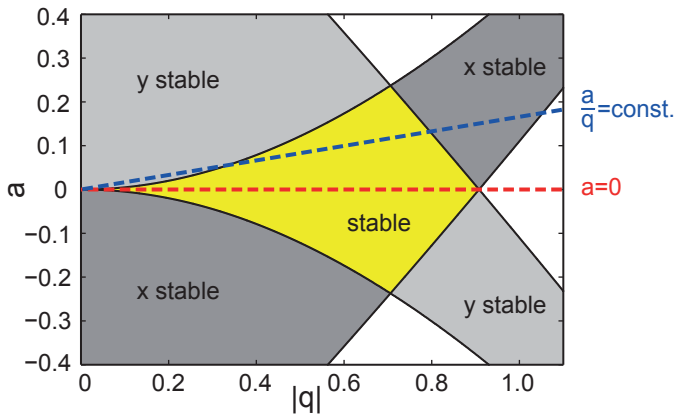

Figure 3.3.: Stability chart of a linear Paul trap. Gray and white areas depict stable and unstable trajectories, respectively. Stable areas for both directions x and y overlap in the yellow intersection area, where particle confinement in the radial trap plane is possible. For constant $\frac{a}{q}$ different specific particle charges are found on the same operating line (blue dashed line). If $a = 0$ stable confinement demands $0 < q < 0.908$ (red dashed line).

solutions [142]. The first area of stability is defined by the characteristic functions

$$a_0(q) = -\frac{1}{2}q^2 + \frac{7}{128}q^4 - \frac{29}{2304}q^6 + \mathcal{O}(q^8), \tag{3.16}$$

$$b_1(q) = 1 - q - \frac{1}{8}q^2 + \frac{1}{64}q^3 - \frac{1}{1536}q^4 - \frac{11}{36864}q^5 + \frac{49}{589824}q^6 + \mathcal{O}(q^7), \tag{3.17}$$

and the conditions $a_0(q) < a < -a_0(q)$ and $-b_1(q) < a < b_1(q)$.

When the trap parameters are kept constant, different specific particle charges are found in the stability diagram on the same operating line with slope $\frac{a}{q} = \frac{2V_{dc}}{V_{ac}} = const.$ For simple particle trapping often $V_{dc} = 0$, and thus $a = 0$, is chosen (red dashed line in figure 3.3), which requires $q < q_{max} = 0.908$. Then, the condition for stability can be given in the following form

$$\frac{Q}{M} < \frac{q_{max}}{2}\frac{\Omega^2 r_0^2}{V_{ac}}. \tag{3.18}$$

A non-zero dc voltage V_{dc} is useful for filtering of certain specific particle charges, for example in mass spectrometry [68]. As a result, narrower limits for q have to be considered for stability (blue dashed line).

Approximate solution of Mathieu's differential equation

In the following, an approximate solution of the equations of motion is presented for a more vivid description of the particle trajectory [144,145]. For small values of a and q only the three coefficients C_{2n} with $n = -1, 0, 1$ contribute dominantly in the series expansion of equation (3.14), which allows separation of the particle motion into two oscillation components, as shown here for the x direction (analogous for y)

$$x(\tau) = \delta_x(\tau) + \bar{x}(\tau), \tag{3.19}$$

with the micromotion $\delta_x(\tau)$, a fast oscillation driven with trap frequency Ω, and, averaged over the driving frequency, the slower varying secular motion $\bar{x}(\tau)$. After insertion in equation (3.6) and assuming $a \ll 1$ one obtains

$$\frac{d^2\delta_x}{d\tau^2} + 2q\cos(2\tau)\bar{x}(\tau) = 0, \tag{3.20}$$

which delivers directly the trajectory of the micromotion

$$\delta_x(\tau) = -\frac{q}{2}\cos(2\tau)\bar{x}(\tau). \tag{3.21}$$

One can see that the amplitude of the micromotion is proportional to the trap parameter q and the deviation from the center of the trapping field. Inserting equation (3.19) again in equation (3.6) together with equation (3.21) and subsequently averaging over one period of the micromotion, one arrives at the differential equation for the secular motion

$$\frac{d^2\bar{x}(\tau)}{d\tau^2} = -(a + \frac{q^2}{2})\bar{x}(\tau). \tag{3.22}$$

This is the equation of motion of an harmonic oscillator for which the solution is well known as

$$\bar{x}(\tau) = x_0 \cos(\bar{\omega}_x \tau). \tag{3.23}$$

The dimensionless secular frequency

$$\bar{\omega}_x = \sqrt{a + \frac{q^2}{2}} \tag{3.24}$$

matches the characteristic exponent of equation (3.13) in the adiabatic approximation $a, q \ll 1$. Now, the overall trajectory of the particle motion in the trap can be written for real time t as

$$x(t) = x_0 \cos(\omega_x t) \left(1 - \frac{q}{2} \cos(\Omega t)\right) \tag{3.25}$$

with the angular frequency of the secular motion

$$\omega_x = \sqrt{a + \frac{q^2}{2}} \frac{\Omega}{2}. \tag{3.26}$$

The same secular frequency is obtained from equation (3.15) with $n = 0$ in combination with equation (3.13). The results for the y direction differ only in the sign of the trapping parameters a and q

$$y(t) = y_0 \cos(\omega_y t) \left(1 + \frac{q}{2} \cos(\Omega t)\right), \tag{3.27}$$

$$\omega_y = \sqrt{-a + \frac{q^2}{2}} \frac{\Omega}{2}, \tag{3.28}$$

and for $a = 0$ the secular frequencies for both radial trap directions are the same:

$$\omega_x = \omega_y = \frac{Q}{M} \frac{V_{ac}}{\sqrt{2}\Omega r_0^2}. \tag{3.29}$$

For the purposes of illustration, in figure 3.4 example particle trajectories in the radial trap plane with generic starting points are shown calculated with equations (3.25) to (3.28). One can clearly identify the slow secular motion with large amplitude superposed by the faster micromotion with a much smaller amplitude. The secular trajectory in figure 3.4(a) resembles a 1:1 Lissajous curve for the case of a linear Paul trap with $a = 0$. In figure 3.4(b) the decoupled trajectories for the x and y directions are shown individually over time. An example trajectory for $a \neq 0$ is given in figure 3.4(c) and (d). Now, the secular trajectory resembles a more complex Lissajous curve because the secular frequencies ω_x and ω_y are no longer equal.

Pseudopotential

For the harmonic secular motion a pseudopotential [146] can be written using equation (3.29) in the form of

$$\bar{\Phi} = \frac{1}{2} \frac{M}{Q} (\omega_x^2 x^2 + \omega_y^2 y^2) = \frac{Q}{4M} \frac{V_{ac}^2}{\Omega^2 r_0^4} (x^2 + y^2). \tag{3.30}$$

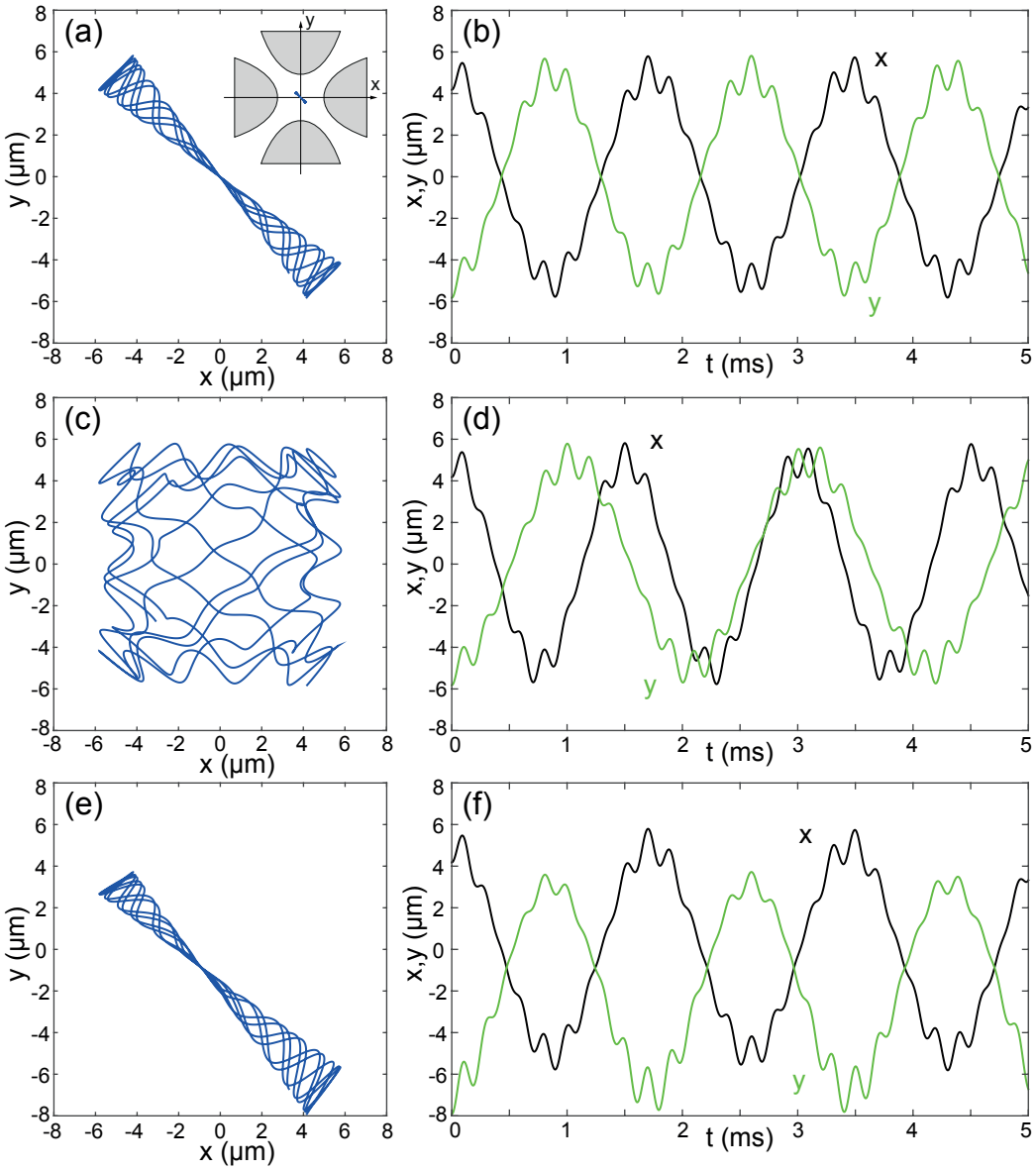

Figure 3.4.: Approximated particle trajectories in the radial plane of a linear Paul trap, as indicated in the inset in (a). The curves are calculated for $q = 0.3276$, $\Omega = 2\pi \times 5\,\mathrm{kHz}$ and $x_0 = 5\,\mu\mathrm{m}$, $y_0 = -5\,\mu\mathrm{m}$. (a) Trajectory for trapping parameter $a = 0$, which corresponds to $V_{dc} = 0$. (b) Decoupled x (black curve) and y (green curve) trajectories showing the slow secular motion superposed by the faster micromotion. (c) and (d) illustrate the situation for $a = 0.0164$. The secular oscillations in x and y direction have different frequencies. (e) and (f) exemplify the influence of an external static force in y direction. Here, $a = 0$ and $\Delta y = -0.18\,\mu\mathrm{m}$.

It depends on the specific charge of the trapped particle in addition to the trap parameters. The potential difference between the trap center $(x, y = 0)$ and the surface of the electrodes $(x^2 + y^2 = r_0^2)$ is

$$\bar{\Phi}_{max} = \frac{Q}{4M}\frac{V_{ac}^2}{\Omega^2 r_0^2}. \tag{3.31}$$

The pseudopotential indicates the minimum energy needed for a specific particle to leave the trap. Thus, for stable confinement, the trap parameters should be adjusted to increase $\bar{\Phi}$ but with respect to the stability condition in equation (3.18).

Influence of an external static force

An external force exerted on the particles in the radial trap plane will influence their trajectories. In the case of a static, homogeneous force F, like gravity or an additional electric field, the equation of motion in the form of Mathieu's differential equation is changed [72, 73] to

$$\frac{d^2y(\tau)}{d\tau^2} - (a + 2q\cos(2\tau)) \cdot y(\tau) = \frac{4F}{M\Omega^2}. \tag{3.32}$$

Without loss of generality the external force is set parallel to the y-direction. In analogy to the derivation of the approximate solution in the previous paragraph, one obtains for the overall particle trajectory

$$y(t) = (y_0\cos(\omega_y t) + \Delta y)\left(1 + \frac{q}{2}\cos(\Omega t)\right) \tag{3.33}$$

shifted from the trap center by

$$\Delta y = \frac{F}{M\omega_y^2}. \tag{3.34}$$

In figure 3.4(e) and (f) an example of a shifted particle trajectory due to an external static force calculated with equations (3.25) and (3.33) is shown. The frequency of the secular motion ω_y is not changed compared to the undisturbed trap but the central shift of the particle trajectory induces an enhancement of the micromotion. In most cases this effect is undesirable and the particle shift has to be compensated, for instance by an auxiliary static electric field that counterbalances gravity.

Influence of damping

Another influence that has to be considered is damping of the particle motion by atmospheric friction as most of the results presented in this work are obtained under atmospheric pressure. Buffer gas cooling is a known method to decrease the kinetic energy of trapped particles usually using dry, cold gases [147–149]. Air friction can be incorporated into the equations of motion by adding a frictional term. For the case of a laminar air flow the frictional force on a spherical particle with radius R and density ρ in a medium with viscosity η is given by Stokes' law [73]:

$$\mathbf{F}_d = -6\pi\eta R\frac{d\mathbf{x}}{dt}. \tag{3.35}$$

Then, Mathieu's differential equation (only shown for the x direction) is changed to

$$\frac{d^2x(\tau)}{d\tau^2} + 2k\frac{dx(\tau)}{d\tau} + (a + 2q\cos(2\tau)) \cdot x(\tau) = 0, \tag{3.36}$$

with the friction coefficient

$$k = \frac{9}{2}\frac{\eta}{\rho R^2 \Omega}. \tag{3.37}$$

The damped equation (3.36) can be solved with the ansatz [150]

$$x(\tau) = e^{-k\tau} \cdot v(\tau), \tag{3.38}$$

which leads to the following modified Mathieu's differential equation

$$\frac{d^2v(\tau)}{d\tau^2} + (a - k^2 + 2q\cos(2\tau)) \cdot v(\tau) = 0. \tag{3.39}$$

The familiar formulation of equation (3.6) can be obtained by the substitution $a' = a - k^2$. The solution is found in analogy to equation (3.12)

$$x(\tau) = A_x e^{(\mu'_x - k)\tau} \sum_{n=-\infty}^{\infty} C_{2n,x} e^{i2n\tau} + B_x e^{(-\mu'_x - k)\tau} \sum_{n=-\infty}^{\infty} C_{2n,x} e^{-i2n\tau}. \tag{3.40}$$

In contrast to the undamped case, here the additional term $e^{-k\tau}$ leads to a decrease of the oscillation amplitude of the particle over time. As a result, the solution is periodic with limited amplitudes not only for imaginary but also for real characteristic exponents μ'_x with

$$\left|\mathrm{Re}\{\mu'_x\}\right| < k. \tag{3.41}$$

Thus, particle stability is improved with increased damping. For small particles trapped under atmospheric pressure the stable areas in the stability chart are extended, compared to vacuum [151]. For equation (3.18) this means a much higher q_{max} in the case of $a = 0$. Furthermore, the frequency spectrum of the trapped particles is changed

$$\omega'_{x,n} = \left(n + \frac{\beta'_x}{2}\right)\Omega. \tag{3.42}$$

While the frequency of the micromotion remains the same, the secular frequency is reduced. In the case of $a', q \ll 1$, β'_x can be approximated in analogy to equation (3.13) and the modified secular frequency $\omega'_{x,0}$ can be calculated from the secular frequency without friction $\omega_{x,0}$ by

$$\omega'^2_{x,0} \approx \omega^2_{x,0} - k^2\frac{\Omega^2}{4}. \tag{3.43}$$

Again, similar results are obtained for the y trajectory as only the signs of a and q have to be changed.

In figure 3.5 the influence of damping on the generic trajectory of a trapped particle can be seen. The curves are obtained by solving the damped Mathieu's differential equation (3.36) (analogous for the y-direction) with a numerical Runge-Kutta method [152], in

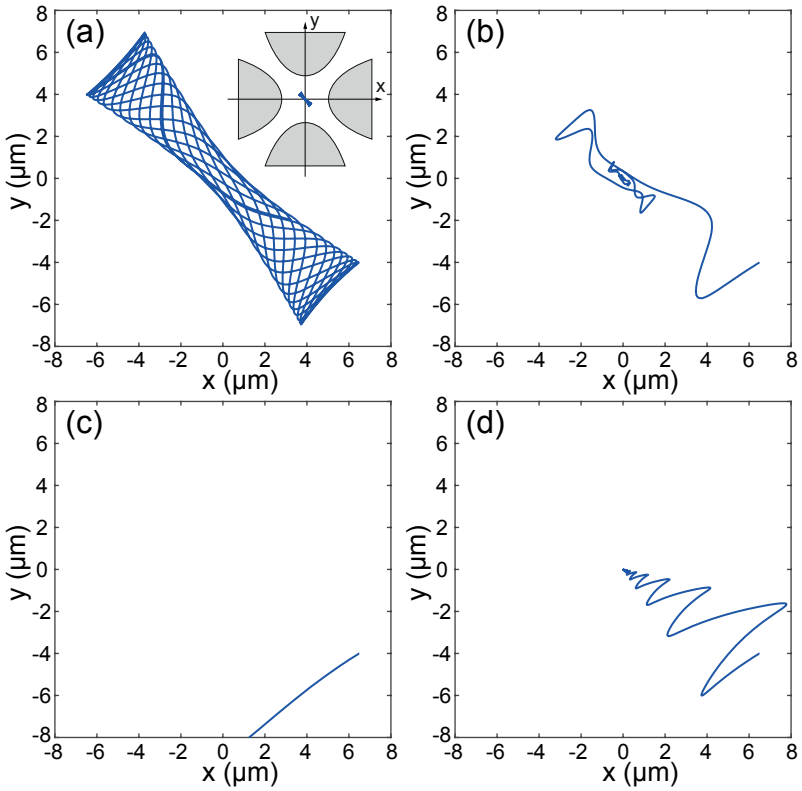

Figure 3.5.: Calculated particle motions in the radial plane of a linear Paul trap under the influence of friction. (a) Undamped (vacuum) trajectory calculated for stable trapping parameters ($a = 0$ and $q = 0.49$). The inset indicates the observed trap plane. (b) Trajectory under the same trapping conditions but now including weak damping by friction with $k = 0.082$ ($\bar{\omega}_x = \bar{\omega}_y = 0.35$). (c) Undamped (vacuum) trajectory calculated for unstable trapping parameters ($a = 0$ and $q = 1.47$). (d) same as (c) but strongly damped with $k = 1.310$ ($\bar{\omega}_x = \bar{\omega}_y = 1.04$).

contrast to the trajectories shown in figure 3.4, which are plotted from the approximated solutions of the undamped Mathieu's differential equation. In figure 3.5(a) conditions are set for stable trapping in vacuum with $a = 0$ and $q = 0.49$. In figure 3.5(b) weak damping ($k = 0.082$) is taken into account for otherwise the same stability parameters. It becomes clear that only the secular motion is damped. The micromotion is unaffected by the damping and its amplitude is mostly determined by the distance between the particle and the center of the trap. Over time the particle approaches the trap center. Because $k < \bar{\omega}_x, \bar{\omega}_y$ (see equation (3.24)) the shown secular oscillations are underdamped [150]. With equation (3.38) the relative amplitude change of an underdamped harmonic oscillator during one period $T_p' = \frac{2\pi}{\omega'}$ can be calculated by

$$\frac{x(t_0 + T_p')}{x(t_0)} = e^{-k\pi\frac{\Omega}{\omega'}}. \tag{3.44}$$

For the case shown in figure 3.5(b) this ratio is 0.22. Figure 3.5(c) shows an example of an unstable trajectory ($a = 0$, $q = 1.47$), where the particle is not confined to the trap dimensions. Nevertheless, stabilization of the particle can be achieved in this case when the amplitude of the particle motion is sufficiently damped as shown in figure 3.5(d) for $k = 1.310$. This gives also an example of strong damping (overdamping) with $k > \bar{\omega}_x, \bar{\omega}_y$. Here, the particle approaches the trap center without any secular oscillations. As a remark, strong damping is not necessary to stabilize the particle, as this can also be achieved for certain weak damping conditions. However, strong damping due to atmospheric friction affects most experiments described in this thesis performed under normal pressure. For example, with an assumed air viscosity of $\eta = 1.8 \times 10^{-5}\,\mathrm{kg\,m^{-1}\,s^{-1}}$ [151] the friction coefficient $k = 0.16$ for a silica microsphere 5 µm in diameter trapped at a frequency of $\Omega = 2\pi \times 5\,\mathrm{kHz}$, while $k = 29.3$ for a spherical 100 nm diamond particle and a trap frequency of $\Omega = 2\pi \times 50\,\mathrm{kHz}$.

One comment on the shown trajectories: In comparison to figure 3.5 one can see that the waist of the overall trajectory in figure 3.4(a) is much smaller. This is because of the approximations made in deriving equations (3.25) and (3.27), which do not account for the higher multiples of the driving frequency. In contrast, the full frequency spectrum (see equation (3.15)) is respected in the solutions obtained numerically for the case of damping, shown in figure 3.5.

Thermal motion

The damping reduces the secular motion until the limit of the Brownian motion. The statistical collisions with gas molecules cause a residual amplitude that can be derived from the gas temperature T [74]. Following the equipartition theorem for a three-dimensional harmonic oscillator

$$\langle E \rangle = \langle E_{kin} \rangle + \langle E_{pot} \rangle = 3k_B T \tag{3.45}$$

with the Boltzmann constant k_B, one arrives at the following condition (y-direction analogously)

$$\frac{1}{2} M \omega_x^2 \left\langle x_{max}^2 \right\rangle = \frac{k_B T}{2}. \tag{3.46}$$

For nano- and microparticles trapped at room temperature ($T = 300\,\mathrm{K}$) typical residual amplitudes of up to 100 µm may occur, depending on the specific particle and the trap parameters, which has to be avoided.

3.1.2. Axial Stabilization

To confine radially stabilized particles in axial trap direction additional potentials have to be involved. Generally, these are generated by applying static voltages to additional electrodes which can be of different types. A common method is to use end-cap electrodes like rods [87], rings [153] or other shapes [154] at both ends of the trap. Quadrupole electrodes curved to form a complete ion storage ring are also known [155]. Another solution is to divide two [156] or all four [157] quadrupole electrodes into smaller segments and apply individual voltages to them. This has the advantage that in addition to confinement in the axial trap direction, it also allows for separation and transport of particles within the trap. However, if a particle is axially stabilized by applying a static voltage U_z to end-caps or electrode segments with an axial distance z_0 to the center of the trap, the potential on the trap axis can be assumed to be nearly harmonic and can be written in the form [158, 159]

$$\Phi_{ax} = \frac{\kappa U_z}{z_0^2}(z^2 - \frac{1}{2}(x^2 + y^2)), \tag{3.47}$$

$$= \frac{M}{2Q}\omega_z^2(z^2 - \frac{1}{2}(x^2 + y^2)). \tag{3.48}$$

The factor κ is determined by the specific trap geometry and is a measure of the attenuation of the created potential at the center of the trap ($\kappa \leq 1$). To fulfill the Laplace condition (see equation (3.4)) the potential Φ_{ax} provides focusing in the z direction as well as defocusing components in the radial trap directions x and y. By comparison of equations (3.47) and (3.48) the angular frequency of the axial motion can be derived as

$$\omega_z = \sqrt{\frac{2\kappa Q U_z}{M z_0^2}}. \tag{3.49}$$

The addition of equations (3.5) and (3.47) gives the overall potential

$$\Phi_{tot} = (V_{dc} + V_{ac}\cos(\Omega t)) \cdot \frac{x^2 - y^2}{2r_0^2} + \frac{\kappa U_z}{z_0^2} \cdot (z^2 - \frac{1}{2}(x^2 + y^2)), \tag{3.50}$$

and new equations of motion accounting for the influence of the axial potential on the radial motion (compare with equations (3.6) to (3.8)) are obtained in the form [160]

$$\frac{d^2x(\tau)}{d\tau^2} + (\hat{a}_x + 2q\cos(2\tau)) \cdot x(\tau) = 0, \tag{3.51}$$

$$\frac{d^2y(\tau)}{d\tau^2} - (\hat{a}_y + 2q\cos(2\tau)) \cdot y(\tau) = 0, \tag{3.52}$$

$$\frac{d^2z(\tau)}{d\tau^2} + \hat{a}_z \cdot z(\tau) = 0, \tag{3.53}$$

with

$$\hat{a}_x = a - \frac{1}{2}\hat{a}_z, \tag{3.54}$$

$$\hat{a}_y = a + \frac{1}{2}\hat{a}_z, \tag{3.55}$$

$$\hat{a}_z = 8\frac{Q\kappa U_z}{M\Omega^2 z_0^2}. \tag{3.56}$$

For small $\hat{a}$ and q the characteristic exponent $\hat{\beta}_x$ (similar for $\hat{\beta}_y$) can be approximated in analogy to equation (3.13)

$$\hat{\beta}_x \approx \sqrt{\hat{a}_x + \frac{q^2}{2}}, \tag{3.57}$$

to obtain the modified secular frequency

$$\hat{\omega}_{x,0} = \frac{\hat{\beta}_x}{2}\Omega = \sqrt{\omega_{x,0}^2 - \frac{1}{2}\omega_z^2}. \tag{3.58}$$

The same result is obtained from the total pseudopotential that can now be written as the sum of equations (3.30) and (3.48)

$$\bar{\Phi}_{tot} = \frac{M}{2Q}(\hat{\omega}_x^2 x^2 + \hat{\omega}_y^2 y^2 + \hat{\omega}_z^2 z^2), \tag{3.59}$$

$$= \frac{M}{2Q}((\omega_x^2 - \frac{1}{2}\omega_z^2)x^2 + (\omega_y^2 - \frac{1}{2}\omega_z^2)y^2) + \omega_z^2 z^2). \tag{3.60}$$

The secular frequencies are reduced which corresponds to a reduced depth of the radial pseudopotential in comparison to equation (3.31). Generally, this influence has little effect on trapped particles, but has to be taken into account for weak pseudopotentials.

The defocusing effect of the axial potential also changes the stability conditions as the trapping parameter a is changed [161]. In figure 3.6, the stability chart for the ideal linear

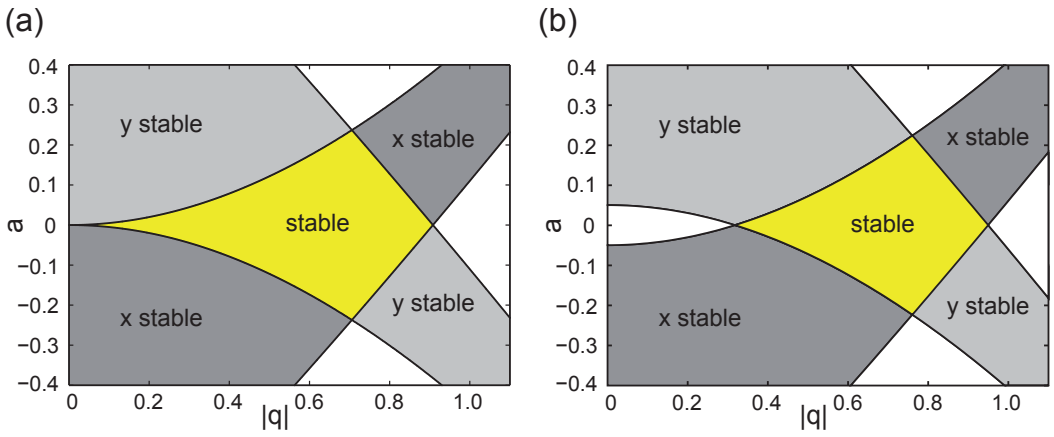

Figure 3.6.: Change of the stability chart due to an axial potential. (a) Undisturbed stability chart representing the ideal linear Paul trap without axial confinement. (b) An additional axial potential ($a_z = 0.1$) compresses the stable area and shifts it towards higher q values.

Paul trap is compared to a stability chart altered by $\hat{a}_z = 0.1$. While typical values in the experiments presented in chapter 5 are smaller, maximum values of $\hat{a}_z$ might be higher by up to one order of magnitude. Although this must be avoided for vacuum conditions, usually particle stability is ensured in this thesis because of the high damping of the particle motion by atmospheric friction (see figure 3.5). The shown first area of stability is compressed and shifted to higher values of q. As this affects the minimum value of q for stable radial trapping, for $a = 0$ a lower limit for the specific charge $\frac{Q}{M}$ has to be considered in contrast to equation (3.18). Thus, in the experiment the axial potential has to be chosen as low as possible to reduce the influence of the axial potential on the particle stability [160].

3.2. Real Linear Paul Traps

So far, only ideal conditions for the potentials and particles have been assumed. Some influences on particle stability have been discussed in the previous sections, but there are others which have to be considered:

- Most important are deviations from the ideal trap geometry. Like in this work, cylindrical instead of hyperbolic electrodes are used because of easier fabrication [162]. But other electrode geometries are also known [163, 164]. In such cases the created radial potential differs from the ideal quadrupole potential by additional terms in the multipole expansion. For cylindrical electrodes the contribution of higher multipoles can be reduced by choosing the ratio between the electrode radii R and their distance to the trap center r_0 to be

$$\frac{R}{r_0} = 1.14511, \tag{3.61}$$

  which ensures a maximum area around the trap center with almost constant field gradients [165]. Further disturbances arise from inaccuracies in the adjustment of the electrodes. Additional unwanted potentials like charged dielectric depositions on the trap electrodes or mounts also alter the potential. Moreover, the finiteness of the quadrupole electrodes in axial direction and radial components of axial end-cap potentials change the trapping potential as already discussed in section 3.1.2. Besides the trap geometry, the applied ac voltage can cause deviations from the ideal quadrupole potential when the generated signal is not perfectly sinusoidal.

- Another important deviation from the ideal case comes from the particles themselves. For a large trapped particle, like the nano- and microparticles used in this thesis, the assumption of a point mass and point charge is questionable. The particles rather have an extended geometry with a charge distribution on its surface. Additionally, it is possible that the center of gravity differs from the center of charge. For a sufficiently large trap and small particle trajectories this might be neglected.

- If more than one particle is trapped, the Coulomb force between charged particles creates an additional potential that acts like an external force on the other particles. This can easily be avoided by isolating a single particle in the trap.

- Furthermore, external effects like scattering forces exerted on the particle from the excitation light or local heating may be observed in addition to gravity and gas friction which have been discussed in section 3.1.1.

Almost all of these effects modify the ideal quadrupole potential by adding higher order multipole terms. As a result, the equations of motion describing the particle trajectory are no longer decoupled. This causes non-linear resonances [166] which lead to unstable particle motion, despite being within the stable areas in the stability chart (figure 3.3). The general condition for these resonances is [167]

$$n_x \frac{\beta_x}{2} + n_y \frac{\beta_y}{2} = \nu, \tag{3.62}$$

with integers n_x, n_y and ν and

$$|n_x| + |n_y| = N, \tag{3.63}$$

where N gives the order of the resonance. Regarding equation (3.15) this can be interpreted as a condition for the secular frequencies:

$$n_x \omega_x + n_y \omega_y = \nu \Omega. \tag{3.64}$$

So, resonances occur if the sum of integer multiples of the secular frequencies in both radial trap directions is equal to a multiple of the driving trap frequency. Such resonances can be observed either for only one of the radial directions or coupled for both directions, depending on the involved secular frequencies [168]. As most of the trapping experiments presented in this thesis are performed under atmospheric pressure, which overdamps the secular motion, resonant excitation of particle motion inside the first area of stability can be neglected.

4. Experimental Setup for Levitated Nano- and Microparticles

Investigation and manipulation of individual nano- and microparticles stabilized in free space places high demands on the experimental setup. In this thesis, different linear Paul traps are constructed that are used for particle isolation. The traps are driven by high sinusoidal voltages generated by home-made amplifier systems. The development of one of them (amplifier HV6) led to a publication in Review of Scientific Instruments [169]. Integration of the traps in an optical microscope allows for detection and observation of confined particles. The particles are charged and injected into the trap by electrospray ionization, which is performed at atmospheric pressure. Vacuum trapping conditions can be achieved after injection. In the following sections all parts of the experimental trap setup are explained in detail. The chapter ends with an introduction to the experimental techniques for trapping and characterization of particles used in this thesis.

4.1. The Traps

Starting from a linear trap design with end-cap electrodes implemented by simple rods [170], two different general trap designs are used for different experimental requirements. All traps used in this thesis are based on a quadrupolar electrode configuration, like the one depicted in figure 3.1. They provide radial confinement in the same way, but differ in size, and more importantly, in the way of axial confinement:

- For the **end-cap trap**, a combination of four additional electrodes at each end is used, as shown in figure 4.1(a). These end-cap electrodes are connected to individually adjustable voltages V_1-V_8 with respect to ground. By using these end-caps to generate repelling potentials, a charged particle can not only be stabilized between the electrodes in the axial trap direction, but its position can also be corrected relative to the trapping potential. For instance, by changing the voltages of the lower electrodes V_3, V_4, V_7 and V_8 with respect to the voltages of the upper electrodes V_1, V_2, V_5 and V_6, the particle can be moved in the vertical direction. The same can be achieved for the two horizontal directions (radial and axial) by changing the voltages of the left and right or front and back electrode groups.

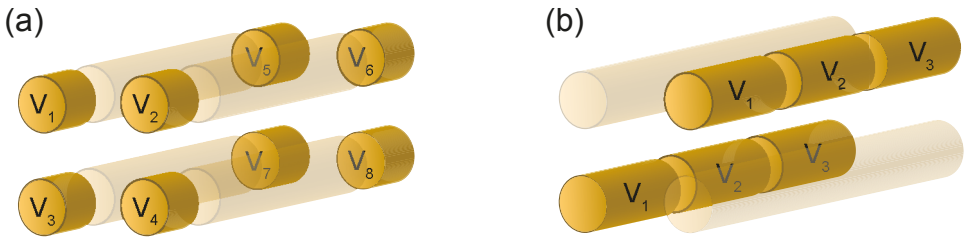

Figure 4.1.: Electrode configurations used for axial confinement in the linear traps. (a) End-cap trap with eight additional electrodes connected to individually adjustable voltages. (b) Segmented trap with subdivided quadrupole electrodes.

- For the **segmented trap**, two of the main quadrupole electrodes are divided into smaller sections, as shown in figure 4.1(b). Opposing sections are electrically combined to form segments and connected to individual voltages V_1-V_3, in addition to the oscillating high voltage applied between the unsegmented and the segmented quadrupole electrode pairs. Similar to the end-cap trap, the outer segments can be used as end-cap electrodes, in order to confine particles in the axial trap direction. If several segments are aligned adjacent to each other, as indicated in figure 4.2, various local potential minima can be defined in the axial trap direction. Such minima can be shifted by changing the individual segment voltages, so that the particles can be separated from each other and moved along the trap.

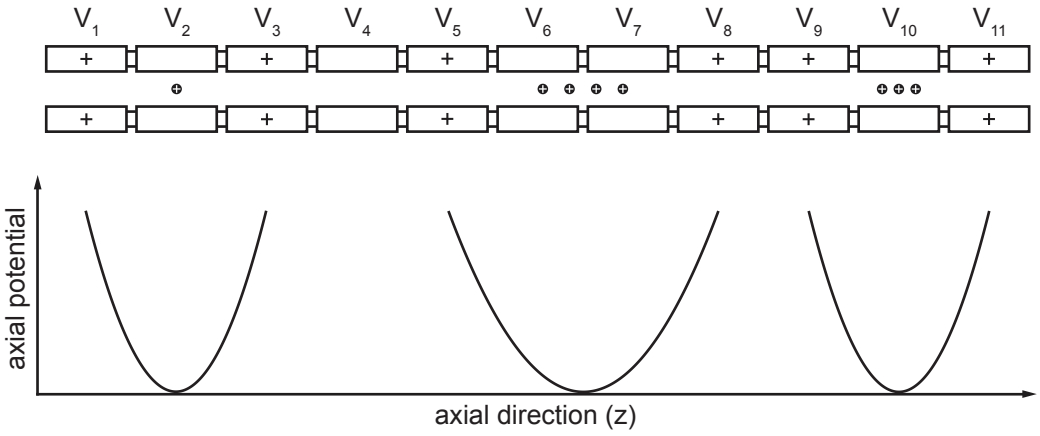

Figure 4.2.: Axial potentials in the segmented trap. Applying individual voltages to the single segments allows to define local potential minima used to separate and transport particles in axial direction. Unsegmented electrodes are omitted for clarity.

In addition to axial confinement and transport, particle removal is another aspect. In both traps, it is possible to eject a particle from the end in the axial direction, but only the segmented trap allows to remove a certain particle from anywhere on the trap axis. This can be done by applying a voltage across the two pieces of one segment, in order to remove a particle in the radial direction.

4.1.1. End-Cap Trap

The experimental realization of the trap configuration with end-caps (schematically shown in figure 4.1(a)), can be seen in the photograph in figure 4.3. The linear trap consists of cylindrical brass electrodes with a diameter of $2R = 4\,\text{mm}$ in the well-known quadrupolar arrangement. The oscillating high voltage is applied between the pairs of opposing main electrodes, which have a length of 7 mm and are held between two mounting plates milled out of 1 mm thick composite epoxy material. The minimum distance between the electrodes and the trap center r_0 is 1.75 mm, which fulfills the condition given in equation (3.61) for the optimum quadrupole potential. End-cap electrodes with a length of 2 mm are mounted on glass fiber rods with a gap of 1 mm between the main electrodes and the end-caps at each end, to which individual static voltages are applied. The whole trap is fixed to an aluminum holder used for mounting the trap in the optical setup.

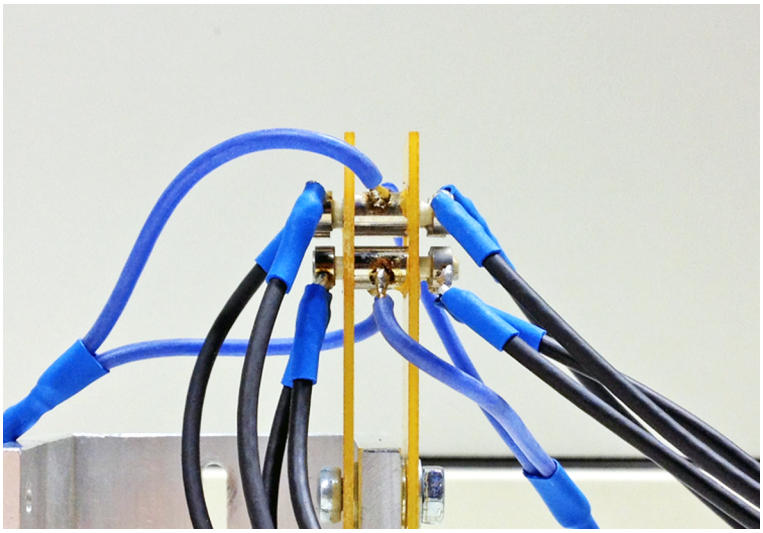

Figure 4.3.: End-cap trap. The four quadrupole electrodes are connected to the oscillating voltage (blue wires) to generate the alternating radial trapping field. For axial confinement eight end-cap electrodes are mounted at the ends of the trap which are connected to individual static voltages (black wires). The whole trap is attached to an aluminum mount for integration in the optical setup. The gap between two neighboring quadrupole electrodes is 1.3 mm.

4.1.2. Segmented Trap

The segmented electrode configuration shown in figure 4.1(b) is used for the other linear trap type. A photograph of the segmented trap can be seen in figure 4.4. One can identify one pair of opposing electrodes that is not segmented and one pair that is divided into 11 sections. The trap has a total length of approximately 110 mm and each segment is 10 mm long. All electrodes are made of brass, have a diameter of 4 mm and are held by 1 mm thick plates milled out of composite epoxy material. The segments are mounted on glass fiber rods. The minimum distance between the electrodes and the trap center r_0 is 2.95 mm. With respect to equation (3.61) this means that the quadrupole potential is no longer optimum, but allows for a better optical and physical access to the trap center due to a larger gap between neighboring electrodes. The alternating high voltage

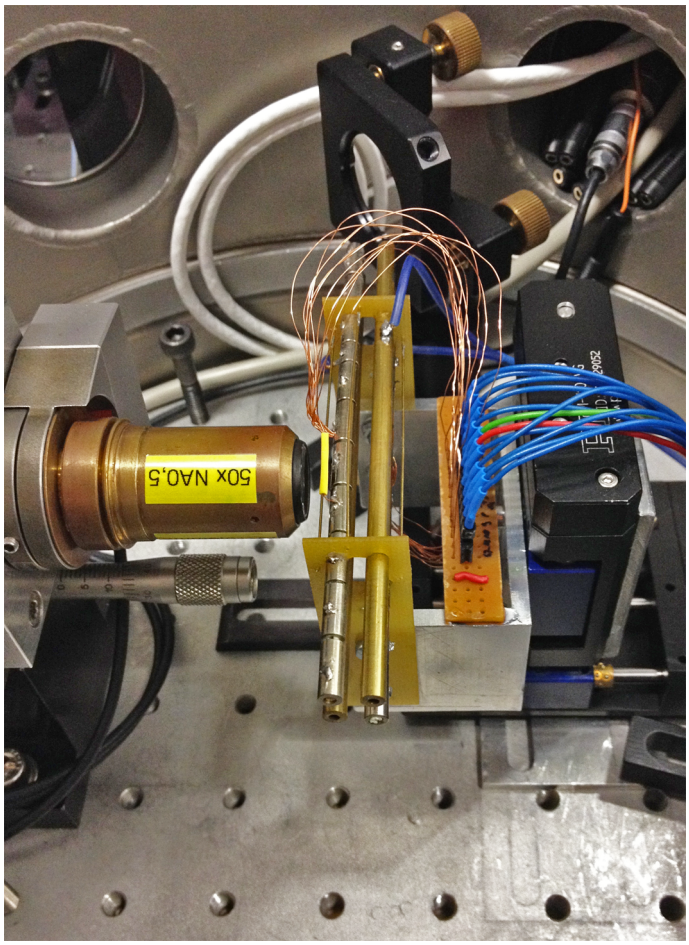

Figure 4.4.: Segmented trap. The alternating high voltage is applied between the plain and the segmented pair of quadrupole electrodes. Additional static voltages can be applied to the individual segments for axial confinement. The trap is shown integrated in the optical setup. It is mounted on an aluminum holder attached to two linear translation stages, in order to align the trap in front of the microscope objective. The gap between two neighboring quadrupole electrodes is 3 mm.

is applied between the plain and the unsegmented electrode pair, while the segments can be connected to static offset voltages individually (see section 4.2 for details).

Like the shorter end-cap trap, the segmented trap is fixed on an aluminum holder, to attach the trap to two linear translation stages (see figure 4.4). With these stages the trap position is adjusted with respect to the focus of the microscope objective in the vertical and horizontal directions, perpendicular to the trap axis. In the remaining horizontal direction, parallel to the trap axis, the particle position is controlled by adjusting the voltages of neighboring segments.

4.2. Electrical Supply

The traps are driven by a high-voltage sinusoidal signal. According to the targeted range of particle specific charges, trap frequencies from several hertz to gigahertz and voltage amplitudes up to a few kilovolts are used. For large particles with small specific charges ordinary audio amplifiers in combination with transformers can be used to produce voltages up to a few kilovolts within a typical frequency range of hertz to kilohertz [73]. Smaller particles with usually larger specific charges require higher frequencies. Typical for atom ion traps, amplification of the trap voltage in the megahertz regime can be achieved by different types of resonators, like helical [91, 171], coaxial [89] or RLC resonators [172]. Since stabilization of single nano- and microparticles is envisaged in this thesis, neither audio amplifiers nor resonator-based amplifiers satisfy sufficiently the need of high-voltage amplification with an output signal of up to $2\,\mathrm{kV_{pp}}$ tunable over a frequency range from 1 kHz to 100 kHz. Most of the commercially available as well as the reported high-voltage amplifiers [173, 174] do not reach the desired output voltage over the given frequency range. Thus, a home-made solution is the method of choice here. To be more precise, two different high-voltage amplifiers, named HV1 and HV6, were developed during this thesis, which operate with different amplification principles.

Basically, the generated sinusoidal trap voltage can be applied to the quadrupole electrodes in two different configurations, known as asymmetric (HV1) and symmetric (HV6), as illustrated in figure 4.5. Both amplifiers are driven by a frequency generator (GW Instek, SFG-2004) and the output signals are monitored via reduced monitor signals with an oscilloscope (Tektronix, TDS 2024B). In figure 4.5(a) the asymmetric voltage supply HV1 is depicted. The high voltage output with respect to ground is applied to one pair of diagonally opposing quadrupole electrodes while the other electrode pair is connected to ground. In contrast, for the symmetric voltage supply HV6, shown in figure 4.5(b), two paraphase output signals, which oscillate around ground with a phase shift of π, are applied to the two pairs of opposing quadrupole electrodes.

The symmetric voltage supply generates the potential Φ_{sym} described with equation (3.5). In the case of the asymmetric voltage supply the potential Φ_{asym} is shifted by half of the applied voltages $\Phi_0 = V_{dc} + V_{ac}\cos(\Omega t)$:

$$\Phi_{sym} = \Phi_0 \frac{x^2 - y^2}{2r_0^2}, \tag{4.1}$$

$$\Phi_{asym} = \Phi_{sym} + \frac{\Phi_0}{2} = \frac{\Phi_0}{2}\left(1 + \frac{x^2 - y^2}{r_0^2}\right). \tag{4.2}$$

Because $\mathbf{E} = -\nabla\Phi$, the electric field is the same for both potentials and both result in

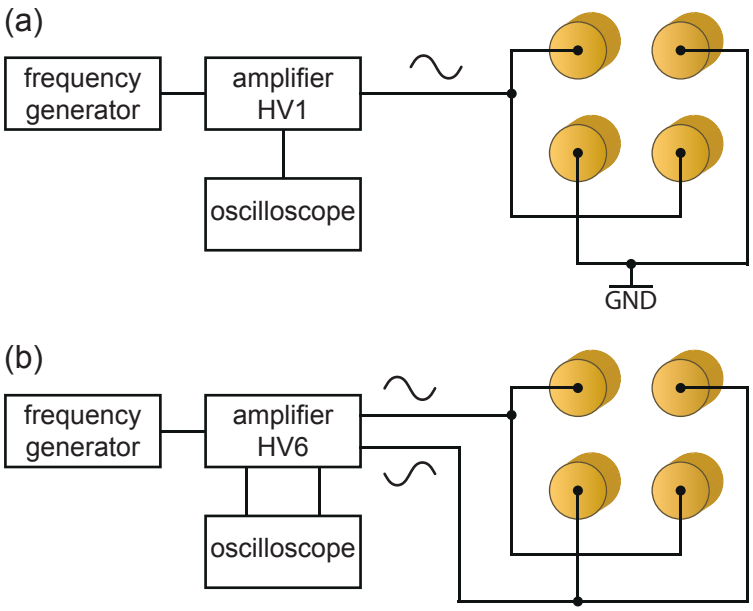

Figure 4.5.: Electrical wiring of the quadrupole electrodes. (a) Asymmetric voltage supply HV1. (b) Symmetric voltage supply HV6.

the same equations of motion given in equations (3.6) to (3.8). The two traps, presented in section 4.1, can be operated by both types of voltage supply, especially for the plain quadrupole electrodes of the end-cap trap. For the segmented trap, asymmetric driving is more straightforward, since the segmented electrodes can be ac-grounded and connected to static potentials in order to define the axial potentials without further effort. However, symmetric driving of the segmented trap is possible, if the oscillating potential applied to the segmented electrode pair is defined as virtual ground for the static voltages. A floating power supply has to be used, which can hold the high load of the input resistance, to apply offset voltages to the segments. Here, a simple, home-made power supply without regulation is used, similar to the module shown in figure 4.15.

HV1 and HV6 are both linear high-voltage amplifiers for sinusoidal signals. In addition to the different output configurations, they can be distinguished as class AB and class A amplifiers, respectively [175]. Class A devices amplify the full wave cycle of the input signal with the same active elements, while class AB devices split the input signal and amplify each half-wave with different active elements. Class A amplifiers are generally used for small signals. For power amplification class AB amplifiers are convenient due to their better efficiency, but complementary pairs of NPN and PNP transistors or dual voltage supplies have to be used. The used amplifiers are explained in detail in the following subsections.

All other static voltages are produced by commercial laboratory power supplies which provide up to 120 V (e.g. TTi, PLH120). Different home-made circuits are used to switch and adjust the dc potentials connected to the end-cap electrodes and segments individually.

4.2.1. High-Voltage Amplifier HV1

The linear amplifier HV1 consists of a high-voltage power supply and an output stage, as shown in figure 4.6. The input signal can be amplified up to $2000\,\mathrm{V_{pp}}$. Because the gain is fixed, the output has to be adjusted by the input voltage of up to $5\,\mathrm{V_{pp}}$. A single output signal with respect to ground is provided and can be used for asymmetric voltage supply of one of the Paul traps. To observe the output, a monitor signal can be used with a ratio between output and monitor of 1000 : 1. All circuits are set up from commercially available standard components and are housed in a small aluminum case, which can be seen in figure 4.7. The amplifier is cooled by a fan and perforations in the housing, in addition to heat sinks inside the box.

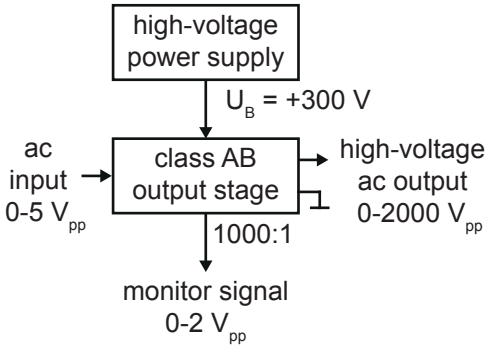

Figure 4.6.: Working principle of HV1.

HV1 circuits

The output stage of HV1 is a class AB amplifier. The schematic circuit is shown in figure 4.8. It consists of two bipolar junction transistors (Q2, Q3) combined in a push-pull configuration. The NPN transistor of type BF759 and the complementary PNP transistor of type BF761 conduct the two half-waves of the input signal alternately. They can withstand collector-emitter voltages of at least 300 V and can safely be used with the supply voltage of $U_B = +300\,\mathrm{V}$. The diodes D1 and D2 are responsible for a voltage drop of $2 \times 0.7\,\mathrm{V}$. These base-emitter bias voltages U_{BE} shift the operating points of the transistors towards a slightly conducting state to enable class AB instead of class B operation for a more linear amplification characteristic. The common emitter transistor Q1 is controlled by the ac coupled (capacitor C1) input signal and drives the base currents of Q2 and Q3. The push-pull configuration of Q2 and Q3 resembles a power amplifier, while Q1 is used for voltage amplification. The operating point of Q1 is stabilized by current (R2) and voltage (P1, R3) feedback loops. To stabilize the operating points of Q2 and Q3, current feedback loops are realized by the resistors R7 and R8, which also limit the emitter currents. The parallel diodes D3 and D4 define the upper limit of the voltage drops at R7 and R8. The amplified signal drives the capacitor C2 to eliminate the dc signal due to the usage of a single positive supply voltage. The pure ac voltage avoids premagnetization of the transformer TR1, which steps up the voltage with a winding turns ratio of 1 : 12.7. Subsequently, the voltage is applied to the output against ground. It can also be measured by a reduced monitor signal with the help of the measurement voltage

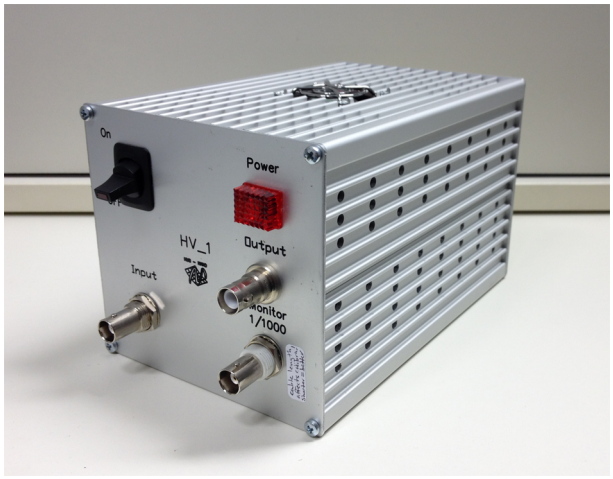

Figure 4.7.: Photograph of amplifier HV1.

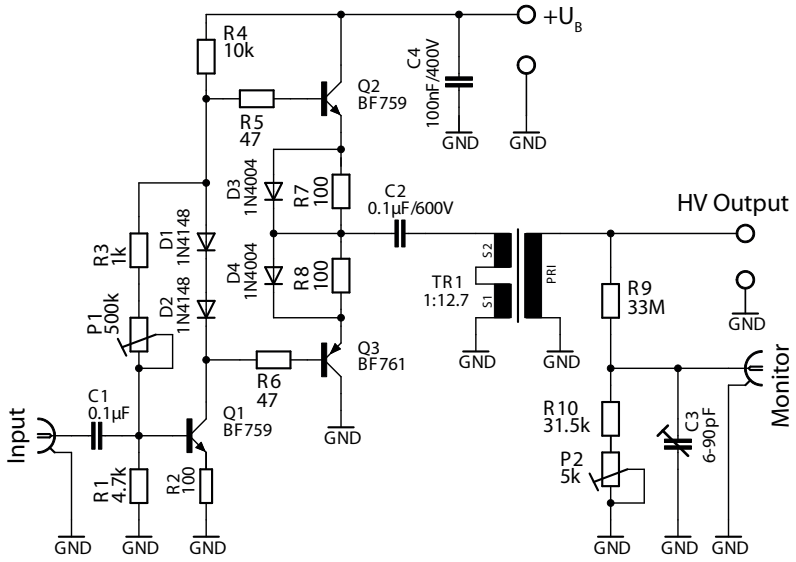

Figure 4.8.: Schematic circuit of the class AB output stage of HV1.

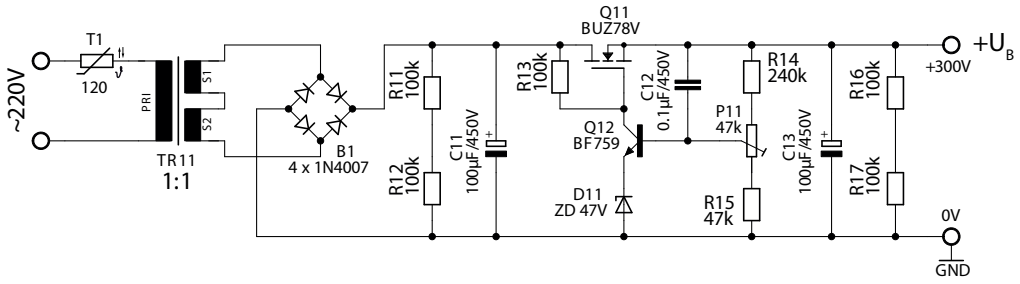

Figure 4.9.: Schematic circuit of the power supply of HV1.

divider R9/(R10+P2). The capacitor C3 compensates the frequency-dependent influence of the capacitance of the connected monitor cable.

The supply voltage U_B of +300 V is produced by the stabilized power supply shown in figure 4.9. A Graetz bridge rectifier (B1) and filter capacitors (C11, C12, C13) are used for smoothing the output supply voltage. The MOSFET Q11 is used as variable resistor in series to the load. This determines the output resistance and keeps the output voltage almost constant. The transistor Q12 together with the Zener diode D11 adjusts the operating point of Q11. The control voltage is set by R14/P11/R15. The power supply is connected to line voltage by the transformer TR11. The thermistor T1 is used as an inrush current limiter to inhibit current peaks in the transformer.

HV1 performance

The performance of HV1 was tested with a commercial high-voltage differential probe (Testec, TT-SI9010) in combination with an oscilloscope (Tektronix, MSO2014). The differential input impedance of the probe has a resistivity of 20 MΩ and a capacitance of 5 pF. The probe is necessary to measure the high-voltage output (V_{out}) while the input (V_{in}) and the monitor signal can be applied directly to the oscilloscope. The output and the monitor voltage are compared to the each other in order to validate the adjustment of the frequency compensation. The gain is calculated from

$$\text{Voltage Gain} = 20 \log \left(\frac{V_{out}}{V_{in}} \right) \text{dB}, \tag{4.3}$$

and plotted in figure 4.10.

Typically, the bandwidth of an amplifier is determined by the frequencies, where the output voltage dropped to $\frac{1}{\sqrt{2}}$ of the maximum value, called −3 dB point. However, this criterion is common for small-signal amplifiers. As HV1 (as well as HV6) is a large-signal amplifier, the voltage gain is largely frequency dependent and the −3 dB method is not applicable. Here, the input is adjusted as a function of the frequency during the measurement, in order to keep the output voltage constantly at 2 kV_{pp}. Identification of the cutoff frequencies is decided by observance of waveform deformations (see figure 4.19).

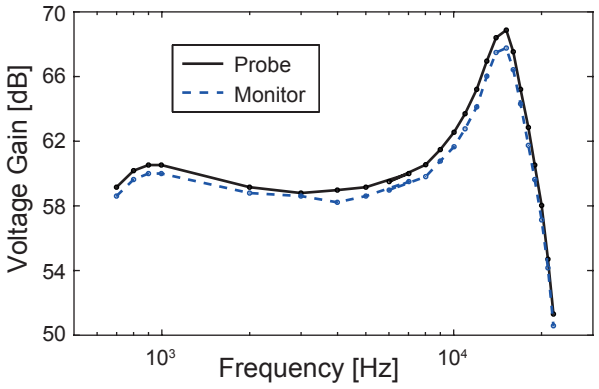

Figure 4.10.: Measured frequency response curve of HV1. The high-voltage gain measured with the differential probe is compared to the gain calculated from the monitor signal.

Amplifier HV1 is capable of delivering $2\,\mathrm{kV_{pp}}$ over a frequency range from 0.7 kHz to 20 kHz under the load of the differential probe. Around 15 kHz a resonance in the output stage occurs. This resonance can be explained by the arrangement of the capacitor C2 and the transformer TR1 (shown in figure 4.8). The capacitance of C2 in series with the ohmic resistance and the inductance of the windings S1+S2 form a serial RLC circuit with resonance frequency of approximately 15 kHz. This resonance can be used to achieve output voltages of more than 3 kV at 15 kHz but has to be accounted for with compensation of the input voltage, when the trap frequency is changed during operation. The lower part of the frequency range is determined by the input coupling capacitor C1 and the upper part by the operating frequency of transformer TR1. By swapping the transformer TR1 of the output stage, the frequency range of HV1 can be shifted by a few kHz. The amplifier HV1 means an improvement in terms of device size and reliability over the amplifier system used previously, consisting of an audio amplifier and several transformers [170], but neither a higher output voltage nor a broader frequency range can be achieved. That is the reason why the whole mechanism of amplification is changed for the amplifier HV6, as explained in the following subsection.

4.2.2. High-Voltage Amplifier HV6

The amplifier HV6 is also a linear amplifier but uses a completely different operating principle than HV1. As indicated in figure 4.11, the single input of up to $5\,\mathrm{V_{pp}}$ is split into two signals by an input amplifier, inverting one part to achieve a phase shift of π between the two signals. The output stage is a combination of two class A amplifiers which deliver voltages up to $850\,\mathrm{V_{pp}}$ against ground. Due to the usage of paraphase signals, the potential difference between both outputs is twice the voltage of one port. Thus, the differential output voltage is $1.7\,\mathrm{kV_{pp}}$. In contrast to HV1, the supply voltage needs to be much higher because class A amplification has a lower efficiency. The output can be observed via monitor signals with a ratio of 1000 : 1 between output and monitor voltages. Measurement amplifiers are used to compensate for frequency-dependent influences of the capacitances of connected coaxial cables. Like for HV1, all circuits are set up from commercially available standard components. The high-voltage power supply is housed in

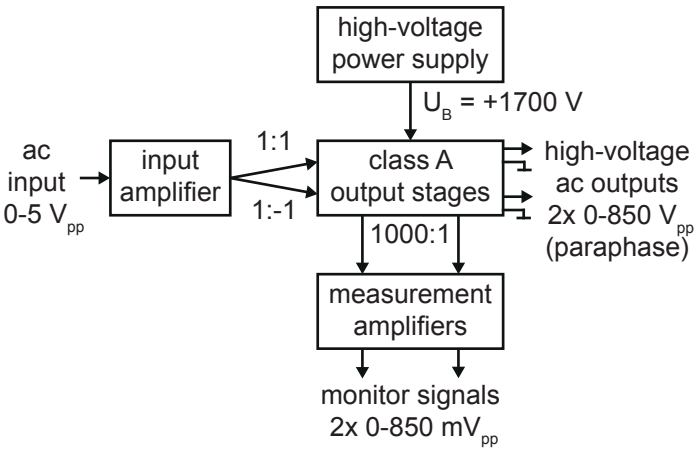

Figure 4.11.: Working principle of HV6.

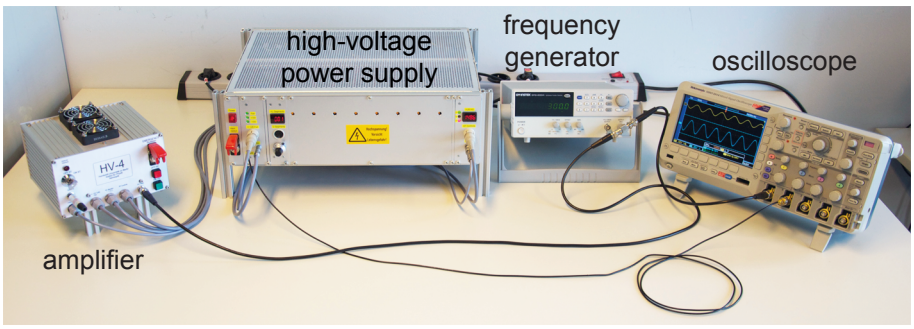

Figure 4.12.: Photograph of amplifier HV6 (Actually shown is version HV4 with identical housing.) together with the frequency generator (GW Instek, SFG-2004) and the oscilloscope (Tektronix, TDS 2024B).

a 19-inch rack while input-, output-, and measurement amplifiers are housed in a smaller aluminum case. Figure 4.12 shows a photograph of the complete system, including the housing with the amplifiers, the power supply, the frequency generator and the oscilloscope. Cooling is achieved by fan cooling, abundant case perforations, and heat sinks.

HV6 circuits

As shown in the schematic in figure 4.11, the amplifier HV6 consists of a high-voltage power supply, an input amplifier, two combined high-voltage output stages and two measurement amplifiers. The output stages are class A amplifiers used in paraphase combination to double the output voltage. The schematic circuit can be seen in figure 4.13. The heart of each output stage is an extended cascode stage [176] formed by three bipolar junction NPN transistors. This combination increases the bandwidth due to a reduction of the so-called Miller capacitances [175]. Each common emitter transistor (T31, T41) controls a series of two common base transistors (T32, T33 and T42, T43, respectively). The transistor cascades in combination with the power resistors (R312, R412) divide the supply voltage U_B into smaller parts. The specified maximum voltage for the transistors of type BF759 is 350 V, which is sufficient to withstand an overall supply voltage of up to 1.7 kV. Each of the power resistors R312 and R412 consists of a series of five resistors rated for 20 W. Compact thick film resistors are used here to reduce inductive loads. During operation, the ac coupled (C301, C401) input signals drive the common emitter transistors in order to sinusoidally vary the collector currents of the cascades. The voltage drops at the power resistors (R312, R412) due to the oscillating currents are connected to the output ports of each stage after dc filtering (C303, C403). The resistor R13 means an ohmic ballast parallel to the capacitive load of the trap and is used as reference between the two stages. The operating points of T31 and T41 are current- (R303, R403) and voltage-stabilized (R304, R404). The output voltages of each output stage can be measured with help of the voltage dividers R310/R311 and R410/R411, respectively.

In order to split the single input into two paraphase signals, an input amplifier is used. The scheme can be seen in figure 4.14. The voltage dividers R101/P1(1) and R201/P1(2), which are adjusted by the dual gang potentiometer P1, cause voltage drops as separate input signals for the operational amplifiers IC1 and IC2. Similar circuits are used for both channels to prevent unwanted phase shifts, which would reduce the differential voltage

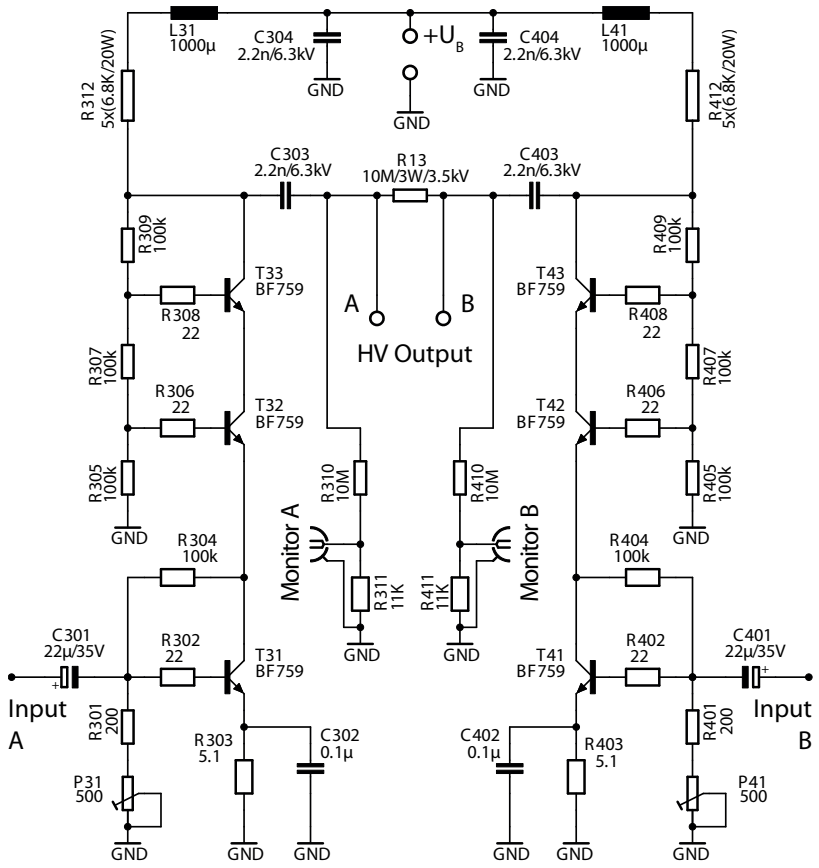

Figure 4.13.: Schematic circuit of the class A output stages of HV6 used in paraphase combination. Also shown in [169].

between the output ports, especially at higher frequencies. The phase shift of π between both supplied signals is achieved by using IC1 in inverting and IC2 in non-inverting configuration. Both channels are set to a resulting amplification of 1. The used operational amplifiers of type LT1224 have a gain-bandwidth product of 45 MHz. Even set up in the shown configuration, the whole input amplifier is capable of transmitting signals up to 5 MHz, which is not the limiting factor for the frequency range.

The supply voltage U_B is produced by a series of eight identical power supply modules. The schematic circuit in figure 4.15 shows one of them. In contrast to the power supply of HV1, stabilization of the output voltage is not needed. The load of the output stages is constant due to the asymmetric working principle. The Graetz bridge rectifier (B1) and the filter capacitors (C1-C4) smooth the output dc voltage. A resistor (R3) instead of a MOSFET (Q11 in figure 4.9) is used in series with the load, to determine the output resistance and to limit the output current. Similar to the power supply of HV1, a transformer (TR1) connects to line voltage and a thermistor (T1) is used as an inrush current limiter. In addition to that, the series of eight power supplies is switched on and off by a microcontroller via relays (K1), to change the supply voltage slowly. Special care is taken to prevent short circuits in the transformers, which are mounted on insulating composite epoxy boards. In particular, transformers at the end of the series are at high potentials

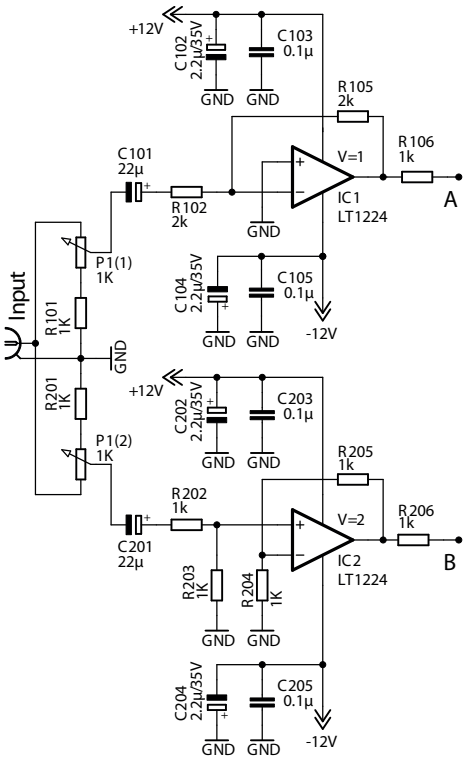

Figure 4.14.: Schematic circuit of the input amplifier of HV6. Also shown in [169].

compared to ground.

The reduced measurement signal at the monitor ports A and B in the output stages (compare with figure 4.13) can be connected directly to the oscilloscope. Unfortunately, different measurement values would be obtained for different lengths of the connecting coaxial cables due to the capacitances of the cables. This problem can be overcome by a frequency-dependent compensation, as was done in HV1 (achieved by C3 in figure 4.8). In this case, for a given length of the monitor cable, the frequency compensation can be set and has to be revised when the cable is changed. Here, a different approach is chosen that uses measurement amplifiers, as shown in figure 4.16. A non-inverting operational amplifier (IC5), acting as an impedance converter, changes the high resistive input from the monitor port to a low resistive output in order to reduce the influence of the cable capacitances. The resulting amplification of the shown circuit is 1. The measurement amplifiers are

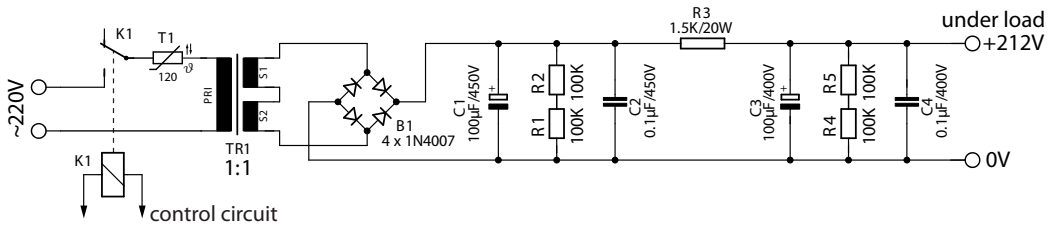

Figure 4.15.: Schematic circuit of one of the eight power supply modules of HV6. Also shown in [169].

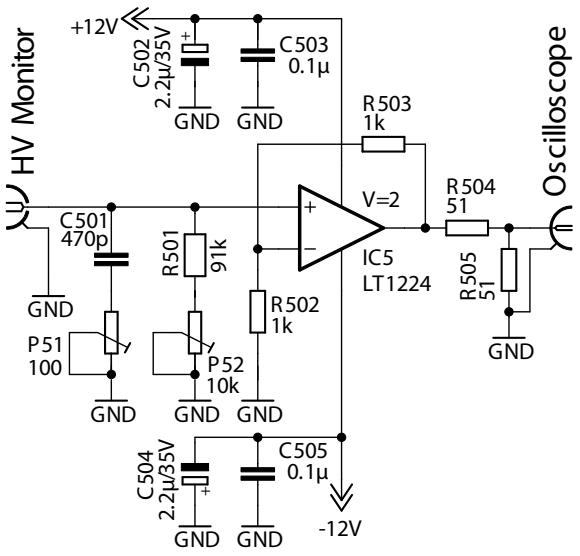

Figure 4.16.: Schematic circuit of one of the two measurement amplifiers of HV6. Also shown in [169].

calibrated by applying a low ac voltage with respect to ground to the high-voltage output ports of the output stages. With the measurement amplifiers connected to the monitor ports, the input test signals are compared to the monitor signals at the measurement amplifiers. In each measurement amplifier the resistor R501 and the potentiometer P52 are used in series for dc adjustment with respect to the measurement voltage dividers R310/R311 and R410/R411 in the output stages, respectively. The potentiometer P51 and the capacitor C501 are used for ac adjustment.

HV6 performance

The performance of amplifier HV6 was tested in two different test environments. The first is the same as used for HV1. The output voltage is measured with the commercial high-voltage differential probe (Testec, TT-SI9010), which is the only load in this measurement. The input voltage is measured directly and the monitor voltages through the measurement amplifiers connected to the monitor ports. All values are recorded with the same oscilloscope (Tektronix, MSO2014). Each output stage delivers a separate monitor signal against ground. The two signals are subtracted to obtain the monitor value of the differential voltage between both high-voltage output ports. Additionally, the sum of the monitor signals are a measure for the imbalance between both output signals. This value should be kept at zero by adjusting the dual gang potentiometer P1 in the input amplifier (see figure 4.14).

For each measurement the differential output voltage is set to 1.7 kV. The voltage gain measured with the differential high-voltage probe is compared to the voltage gain calculated with the summed up monitor signals in figure 4.17(a). The voltage gain of all shown frequency response curves is calculated from equation (4.3). The monitor signal is proven to be an adequate measure of the output voltage, as it is in good agreement with the high-voltage signal, measured with the commercial probe, up to a frequency of 50 kHz.

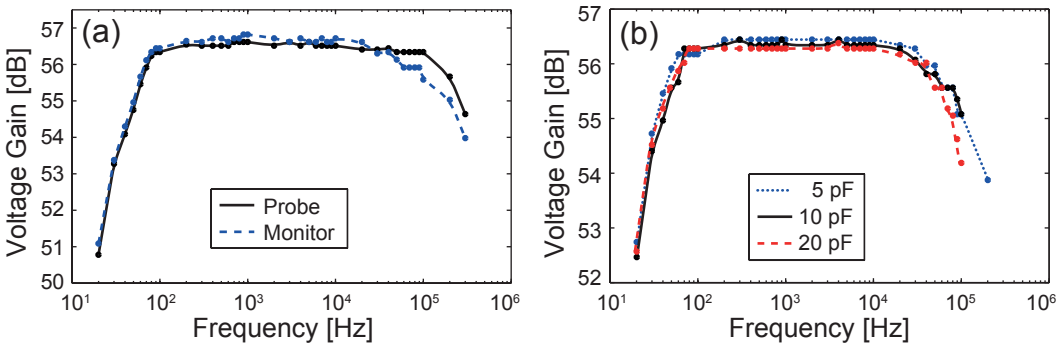

Figure 4.17.: Measured frequency response curves of HV6. The output voltage is set to 1.7 kV. (a) Voltage gain measured with the differential probe compared to the combined monitor values. (b) Voltage gain calculated from the monitor signal for three different capacitive loads and an output voltage of 1.7 kV. Also shown in [169].

For higher frequencies, the monitor values are too small by up to 10 %, what has to be taken into account during operation.

For the second test setting, the high-voltage probe is replaced by a home-made parallel-plate capacitor filled with air (see figure 4.18). The amplifier is intended to drive the linear Paul traps. The traps and the associated connections and feedthroughs mean a capacitive load on the order of 10 pF to the amplifier. Thus, the distance between the capacitor plates is adjusted to set the capacitance to 5 pF, 10 pF and 20 pF, respectively. In these measurements only the monitor ports in combination with the measurement amplifiers are used to observe the output voltage. Measurements are performed for the three different capacitive loads at three different output voltages (500 V_{pp}, 1000 V_{pp} and 1700 V_{pp}), respectively. The results are summarized in table 4.1. One can see that the usable frequency range of amplifier HV6 depends on the load and on the output amplitude. For the maximum output voltage of 1.7 kV the frequency response curves are shown in figure 4.17(b). The maximum output amplitude of 1.7 kV_{pp} is determined by the specifications of the transis-

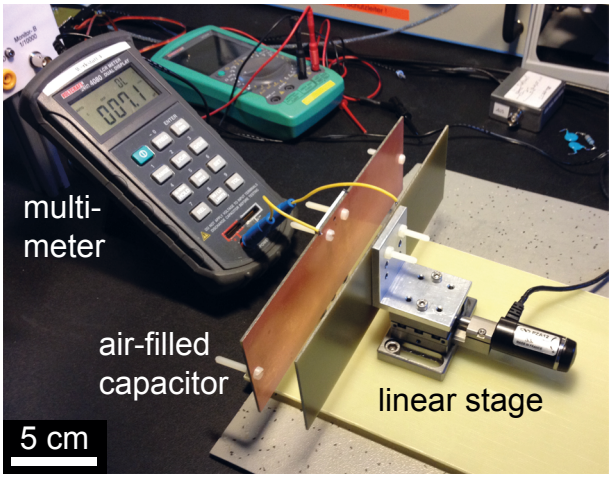

Figure 4.18.: Home-made parallel-plate capacitor with air as dielectric. The capacitance is adjusted by moving one plate on a linear stage.

Load	Output voltage	Frequency range
5 pF	500 V_{pp}	10 Hz-1.2 MHz
	1000 V_{pp}	10 Hz-500 kHz
	1700 V_{pp}	20 Hz-200 kHz
10 pF	500 V_{pp}	10 Hz-1 MHz
	1000 V_{pp}	10 Hz-300 kHz
	1700 V_{pp}	20 Hz-100 kHz
20 pF	500 V_{pp}	10 Hz-600 kHz
	1000 V_{pp}	10 Hz-200 kHz
	1700 V_{pp}	20 Hz-100 kHz
Testec,	500 V_{pp}	10 Hz-1.8 MHz
TT-SI9010	1000 V_{pp}	20 Hz-900 kHz
(20 MΩ || 5 pF)	1700 V_{pp}	20 Hz-300 kHz

Table 4.1.: HV6 amplifier performance

tors: more precisely, by their maximum collector-emitter voltage of 350 V. Higher output voltages can be reached but not without going outside the specifications. For instance, operation for several hours at 2 kV_{pp} was successfully tested but cannot be guaranteed for the long term. For the approved maximum output voltage of 1.7 kV_{pp} the amplifier HV6 can be used over a frequency range spanning four orders of magnitude from 20 Hz to 100 kHz under a load of 10 pF. With the mentioned 10 % discrepancy between monitor and high-voltage output, the real frequency response of HV6 seems to be even better than shown in figure 4.17(b). However, the lower part of the usable frequency range is affected by the input coupling capacitors C301 and C401 and the capacitors C302 and C402, and the upper part by the transistors. With more powerful transistors it should be possible to further improve the performance of HV6.

Similar to HV1, the input has to be adjusted as a function of the frequency in order to keep the output voltage constant. The cutoff frequencies are identified by the total harmonic distortion (THD) of the monitor signals. As shown through testing with the differential high-voltage probe, distortions observed in the monitor signals affect the high-voltage output to the same extent. The recorded signal was Fourier transformed and the THD was calculated from the effective voltage amplitudes V_n of the first $m \geq n$ harmonics contributing to the output signal using [174]

$$\mathrm{THD} = \frac{1}{V_1}\sqrt{\sum_{n=2}^{m} V_n^2}. \tag{4.4}$$

The index $n = 1$ represents the fundamental harmonic at the frequency of the input signal. For the measured frequency response curves a THD of up to 3 % is accepted. In figure 4.19 two example waveforms and their Fourier transforms can be seen, with THD lower and higher than 3 %, respectively. Figure 4.19(a) shows the monitor signal for an output voltage of 1.7 kV_{pp} under a load of 10 pF at a frequency of 100 kHz. The Fourier transform of this signal in figure 4.19(b) shows the fundamental harmonic and only a few higher harmonics with much smaller amplitudes. The THD is calculated to be 0.7 %. The signal in figure 4.19(c) is obtained under the same conditions but at a frequency of 200 kHz.

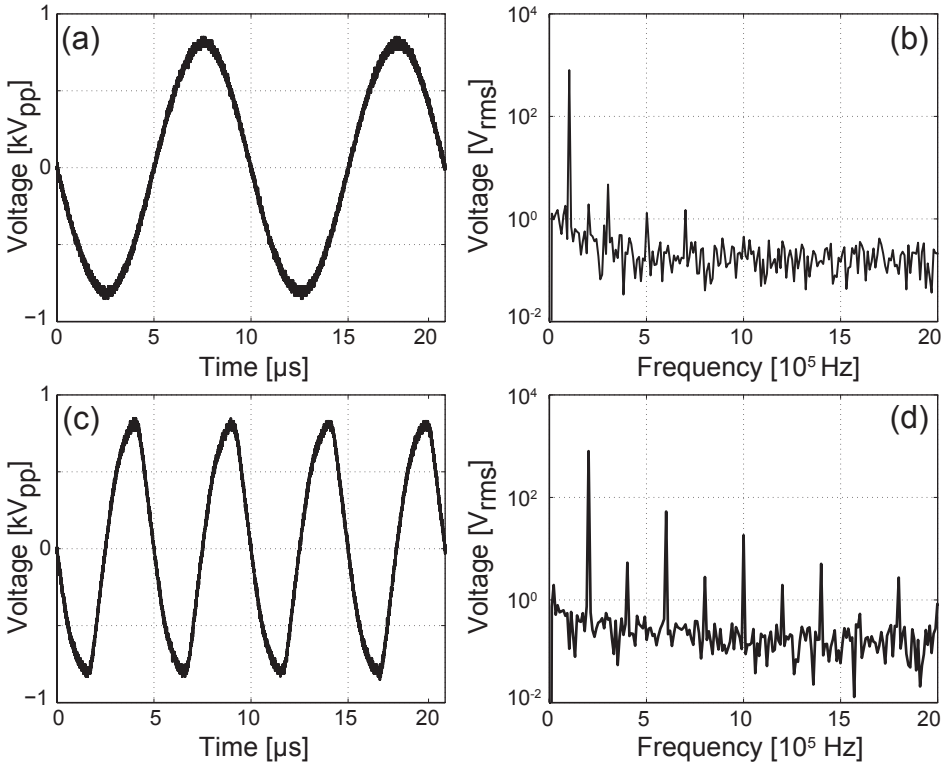

Figure 4.19.: Waveform distortion of output signals of HV6. Recorded differential monitor signal for an output voltage of 1.7 kV_{pp} under a load of 10 pF. (a) Waveform and (b) respective Fourier transform of a signal with 100 kHz and THD of 0.7 %. (c) and (d) show a signal with 200 kHz but otherwise the same conditions. The THD is already at 7 %. Also shown in [169].

Now, more higher harmonics with significantly higher amplitudes can be identified in the Fourier transform shown in figure 4.19(d). For this case the THD is calculated to be 7 %, and thus, 100 kHz is determined as the maximum frequency for HV6 for this load and this output voltage.

Both amplifiers are used to drive the linear Paul traps introduced in section 4.1. While HV1 is predestined for asymmetric and HV6 for symmetric trap driving, both amplifiers can be used with both traps. In contrast to HV1, HV6 is sustained short-circuit and earth-fault proof. Thus, the amplifier system HV6 will not be damaged by short circuits on the output side, which is successfully tested by a short-circuit test run for over an hour. The usable frequency range of HV1 spans over two orders of magnitude from 700 Hz to 20 kHz, while HV6 can be operated over a frequency range spanning four orders of magnitude from 20 Hz to 100 kHz at comparable values of the output voltage. Assuming constant particle charges and constant trap voltage amplitudes, the frequency ranges can be translated into ranges of particle masses, using equation (3.11), that can be stabilized within the available frequency range. A mass range spanning three orders of magnitude for HV1 and seven orders of magnitude for HV6 can be calculated. For spherical particles, the mass scales with the cube of the radius. Thus, the particle radius can vary within one order of magnitude for HV1 and more than two orders of magnitude for HV6. This range can be further expanded by changing the trap voltages and the particle charges as well.

4.3. Linear Paul Trap Integrated in Optical Microscope

A home-made optical microscope was set up for optical detection and analysis of trapped particles. Almost any kind of particle can be isolated, in either the end-cap or the segmented trap, and investigated by different microscopy and spectroscopy methods: detection of fluorescence emission under wide-field or confocal excitation is possible, as well as of scattered white light under dark-field illumination. A major advantage is the absence of coverslips or other substrates in the trap. Thus, background emission is significantly reduced, compared to supported particles. The optical setup used with the traps is presented subsequently to brief introductions to the different microscopy techniques in this section.

4.3.1. Optical Microscopy

Optical microscopy is the most frequently used method to obtain magnified images of small samples. It is a versatile and essential technique especially for scientific research [54]. In conventional wide-field microscopy the sample is illuminated homogeneously with light. With an objective lens, often called microscope objective, light from the sample is collected and a real image is formed inside the microscope. This image is magnified by an ocular lens, also called eyepiece, which results in an inverted virtual magnified image of the sample. As is the case in this thesis, CCD cameras or other detectors are often used without any eyepiece. The light is focused in the image plane which coincides with the location of the detector. In addition, modern infinity-corrected microscope objectives can be used which send out a collimated beam, which is focused by a tube lens in front of the detector. The space between objective and tube lens can be used to insert auxiliary components to filter and shape the beam without introducing image errors. In the following, some important properties of such an optical system are explained.

Magnification

The magnification of a microscope is usually given by the magnification of the objective times the magnification of the eyepiece. For infinity-corrected systems the magnification given by the microscope objective is only valid in combination with the appropriate tube lens. Using a CCD camera in the image plane, the overall magnification depends on the microscope objective and the pixel sizes of the detector and screen instead of the magnification of an eyepiece.

Numerical aperture

The numerical aperture (NA) is a measure of the acceptance angle of a microscope objective. The dimensionless NA can be calculated using

$$\mathrm{NA} = n \sin \alpha, \tag{4.5}$$

with the refractive index of the surrounding medium n and the maximum angle to the optical axis α under which light can enter the objective. For microscope objectives used in air ($n = 1.0$), NA values of up to 0.95 can be reached. This value can be increased even further by using oil immersion objectives, where the volume between the front lens of the

microscope objective and the sample is filled with immersion oil with $n > 1$. Different synthetic oils can be used to increase the index of refraction n in order to achieve NA values of up to 1.4 and even higher [177].

Resolution

The resolution of an optical microscope is defined by the minimum distance between two points that can still be distinguished. The capability to resolve the two points is limited by the wave nature of light and can be expressed by the point spread function (PSF). The PSF describes an imaging system by giving the three-dimensional image obtained from a single point emitter. For diffraction-limited systems, whose resolution is limited only by diffraction and not by imperfections of the optical system, only the numerical aperture and the wavelength determine its shape. The image of an arbitrary sample is the actual object appearance convolved with the PSF of the microscope system. Knowledge of the PSF can be obtained by imaging a very small point-like emitter [178] and allows improvement of images by deconvolution [179]. Typically, the lateral resolution limit Δx is given by the Rayleigh criterion, which states that two equally bright points can be distinguished when the intensity maximum in the Airy pattern of one point coincides with the first minimum in the Airy pattern of the other point [180]. It can be calculated as follows

$$\Delta x = 0.61 \frac{\lambda}{\mathrm{NA}}. \tag{4.6}$$

To reach high resolution, a high numerical aperture and shorter wavelengths should be used. With X-ray or electron wavelengths the resolution can be further increased [181–183]. In the optical regime the resolution limit can be improved through confocal techniques [184] or even surpassed by using optical near-field techniques [185, 186].

4.3.2. Confocal Microscopy

In confocal microscopy only one point is illuminated at a time. This can be done by imaging a point-like light source into the sample. More often a laser is used instead, brought into the optical path by a beam splitter and focused by the objective lens, as shown in figure 4.20(a). For detection the objective lens images the focal point on a pinhole (solid red lines in figure 4.20(a)). Light not stemming from the focal point (dashed red lines) is suppressed by a spatial filter, consisting of a pinhole at the focus point between two lenses forming a telescope. The confocal point spread function is obtained from the product of the point spread functions of the illumination and the detection. This increases the optical resolution of the microscope, which is in the lateral direction improved to

$$\Delta x = 0.44 \frac{\lambda}{\mathrm{NA}}. \tag{4.7}$$

Even more important than the higher resolution is the reduced signal from regions outside the focal point with the result of a heavily increased signal to noise ratio. To obtain a full image, the sample has to be scanned, as only one point per time can be imaged. In this thesis, confocal microscopy is used to reduce the background signal during the investigation of single nano- and microparticles without scanning. The pinhole sizes are chosen according to the specific particles and applications.

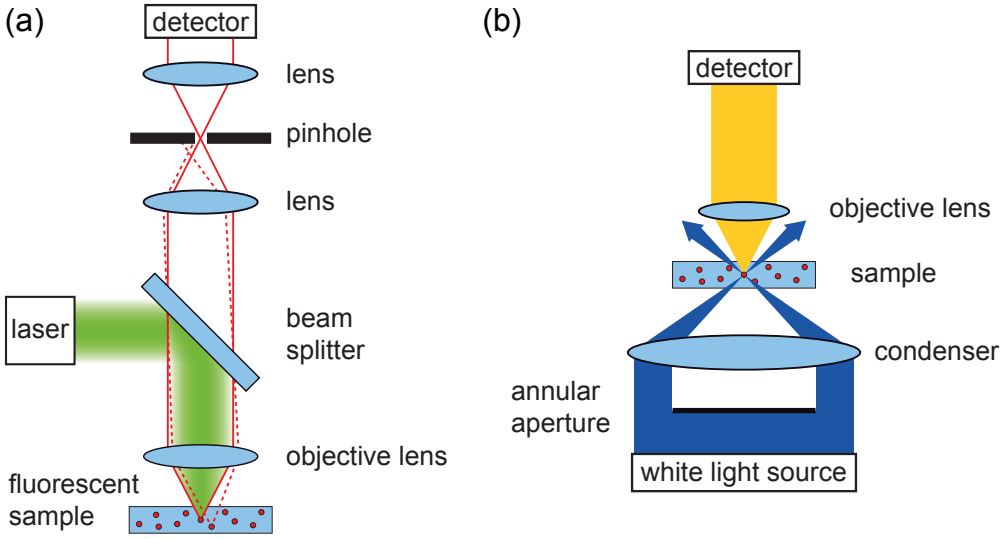

Figure 4.20.: Schemes of (a) confocal and (b) dark-field microscopy. The tube lens as part of the detector system is not shown.

4.3.3. Dark-Field Microscopy

In dark-field microscopy the illuminating light is not detected directly. This can be done by blocking it or by aligning the beams in such a way that it is not collected. A possible scheme is shown in figure 4.20(b). White light passes an annular aperture which blocks out the central light rays. The resulting hollow beam is focused, so that only oblique rays reach the sample. When the NA of the objective lens is smaller than the NA of the condenser lens, the annular aperture can be adjusted to block all light that would enter the microscope objective. The result is that light only scattered from the sample is collected. The observed structures appear as bright objects on a dark background. The resolution is the same as for conventional bright-field microscopy, but different features are enhanced which might change the optical character of the images [54]. In addition to the shown configuration, different illuminating techniques are known. For example, often illumination and detection occurs from the same side by oblique beams focused onto the sample from around the microscope objective. In this thesis, dark-field microscopy is used to image levitated particles in the trap and gold nanoparticles on a glass coverslip. Furthermore, white-light scattering spectra are obtained under dark-field illumination.

4.3.4. Optical Setup

The scheme of the microscope setup with integrated Paul trap is shown in figure 4.21. The trap is mounted in front of an optical microscope (Olympus, LMPLFLN 50x) with a numerical aperture of 0.5. The long working distance of 10.6 mm is necessary to maintain a safe distance from the high-voltage electrodes of the trap. The trap is attached to a two-axis translation stage (Physik Instrumente, M-112.1VG in combination with M-110.1VG), which is used to align the trap in the two radial directions. Alignment of the particle position in the axial trap direction is done by individually adjusting the electrostatic potentials in the trap segments. The position of the microscope objective can be

controlled roughly by a mechanical translation stage and finely by a linear piezoelectric actuator (piezosystem jena, MIPOS 100). For excitation, green light from a water-cooled argon-ion laser (Spectra Physics, BeamLok 2080) with a wavelength of 514.5 nm and an optical output power of continuous wave emission up to 1 W is used. The laser light is spatially filtered by a single-mode optical fiber, and spectrally by a laser line filter. The resulting collimated beam has a Gaussian profile and is nearly monochromatic. Adjustment of the laser intensity is performed linearly using a neutral density (ND) filter wheel. For particle detection and fluorescence excitation, the laser light can be focused into the trap from two different directions, switchable by a flip mirror. A beam sampler with a reflectivity of about 5 % (Thorlabs, BSF10-A) is used to send the laser light to the microscope objective for focused excitation or, in combination with a wide-field lens (focal length 50 mm), for near homogeneous illumination. The light can also be slightly focused by a lens (focal length 50 mm) and sent into the trap from the side. A part of the fluorescence emission from the particle stabilized in the focus is collected with the microscope objective and sent to detection through the beam sampler with a transmittance of about 95 %. Long-pass filters (Omega Optical, 538ALP or Schott, OG550) block the reflected excitation light and a confocal pinhole (different diameters up to 1 mm, confocal telescope

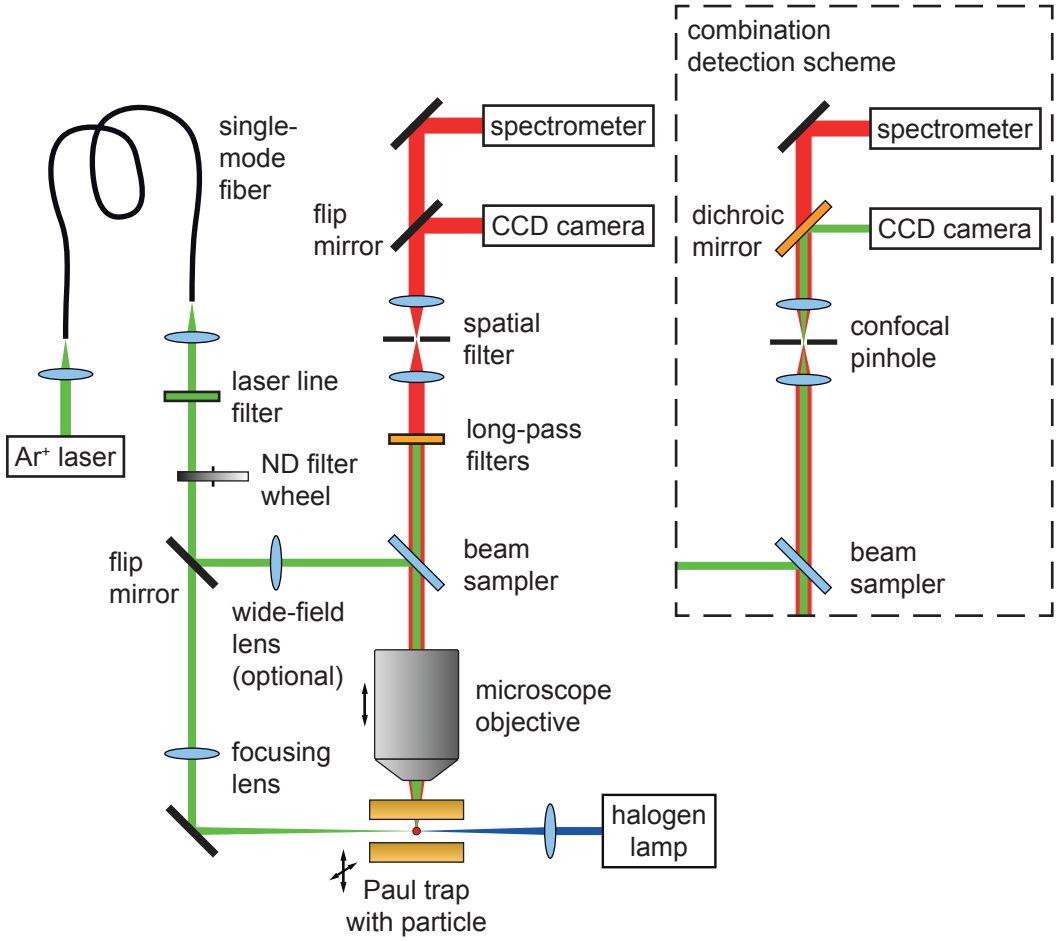

Figure 4.21.: Schematic of the optical microscope setup with integrated linear Paul trap.

length $2 \times 20\,\mathrm{mm}$) can be used for spatial filtering. Using another flip mirror, the light is eventually detected by a CCD camera (PCO, pco.1300) or spectrally analyzed by a spectrograph (Acton Research Corporation, Spectra Pro 2500i) in combination with a liquid nitrogen-cooled camera (Princeton Instruments, LN/CCD-1K-EB). For fluorescent particle samples it has proven useful to use a dichroic mirror instead of a flip mirror in front of the CCD camera. In this way, the particle can be observed with the CCD camera by the green scattered laser light, while simultaneously detecting the dispersed fluorescence emission with the spectrometer, which enables adjusting the particle position with respect to the microscope focus during long-time measurements. When the confocal pinhole is used with this combination detection scheme, the camera image quality is reduced due to chromatic aberration of the telescope lenses, but the particle position can still be sufficiently determined. Optionally, white light from a halogen lamp can be directed into the trap for dark-field imaging and scattering spectroscopy. Detection of the scattered white light is similar to the detection of fluorescence light, but without the long-pass filters and the dichroic mirror.

In figure 4.22 a photograph of the whole microscope setup on an optical table can be seen. The trap and the microscope objective are located in a vacuum chamber (see figure 4.4). The beam paths are bordered by metal shields and covered by cardboard lids to reduce background light during the measurements.

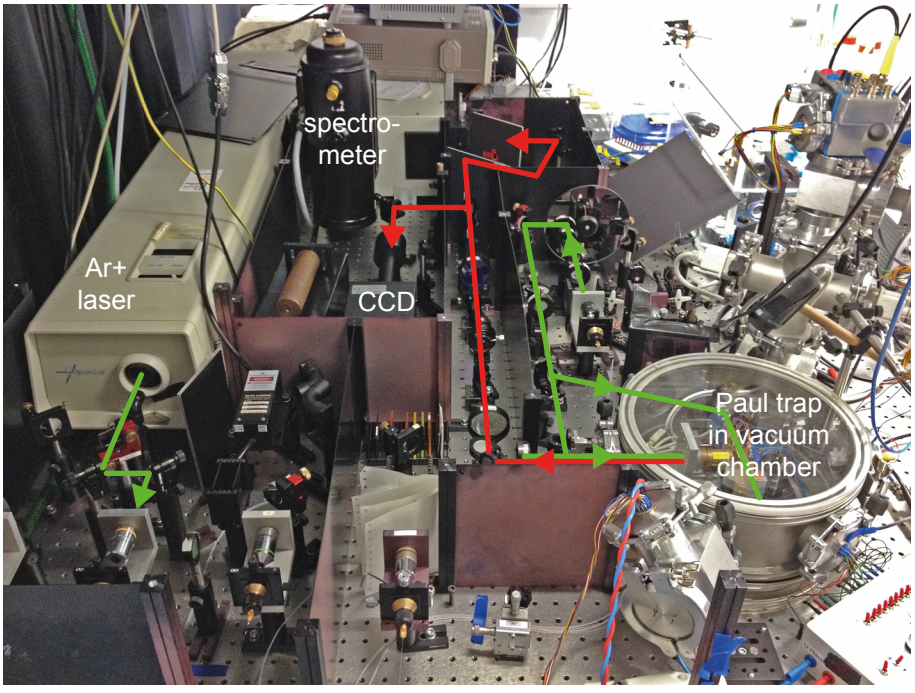

Figure 4.22.: Photograph of optical microscope setup with linear Paul trap in vacuum chamber. The excitation and detection beam paths are indicated by green and red lines, respectively.

4.4. Vacuum Chamber

To further isolate trapped particles, the trap is integrated in a vacuum chamber, which also houses the linear stages and the microscope objective. The vacuum chamber, which has an inner diameter of 26 cm, can be seen in the photograph of figure 4.22. Several electrical feedthroughs are used to apply the trap voltages and to connect the stages. Optical access is ensured by two glass windows and an acrylic glass cover. The pressure inside the chamber can be measured by a Pirani gauge (VEB Hochvakuum Dresden, VM221) or a gauge that combines Bayard-Alpert and Pirani measurement systems (Leybold Inficon, IR090). A pump stand (Pfeiffer, TSH 064D) consisting of a diaphragm pump and a turbo drag pump is used to decrease the pressure down to 10^{-4} mbar.

Instead of reducing the pressure, the air inside the chamber can also be exchanged with an industrial gas like nitrogen or helium. This could be used to reduce humidity, change the refractive index, prevent chemical reactions or as buffer gases. The gases are brought into the chamber by a gas inlet which can be sealed by a valve.

Ambient Conditions

Most of the measurements for this thesis are done under atmospheric pressure and the vacuum chamber is only used as a shield against air currents. Under ambient conditions particle trajectories are damped due to air-friction as indicated in figure 3.5. This damping facilitates stabilization, especially trapping of particles with different specific charges at the same time, as it is done for the electrostatic assembly of custom particle compounds in the trap presented in section 5.4.

Evacuation

For thermal isolation of trapped particles from the environment, the vacuum chamber has to be evacuated. Restricted by the ionization method (see section 4.5), which works at ambient conditions, the particles are injected into the trap under atmospheric pressure. Thus, the particles must be transferred from ambient to vacuum conditions after ionization. This can either be done with differential pumping stages [187,188], or by trapping the particles at ambient conditions and reducing the pressure afterwards. The latter is used in this thesis. Subsequent evacuation requires special attention to avoid gas discharges and electrical sparkover between the trap electrodes. Both effects can cause loss of the trapped particles and can even damage the trap and the electronics. Gas discharges can be explained by free charges which are accelerated in the field between the electrodes [189]. The two dominating effects are electron impact excitation or ionization of neutral molecules and electron emission from the electrodes by ion bombardment [190]. For a homogeneous static electric field Paschen's law [191] gives the breakdown voltage V_{break} as a function of the pressure p and the electrode distance d as

$$V_{break} = \frac{Bpd}{\ln(Apd) - \ln[\ln(1 + \frac{1}{\gamma})]}, \tag{4.8}$$

with A and B being roughly constant for a given gas. The coefficient γ accounts for the secondary electron emission from the electrodes. A Paschen curve for air is plotted in figure 4.23. A minimum breakdown voltage can be identified. Starting from this

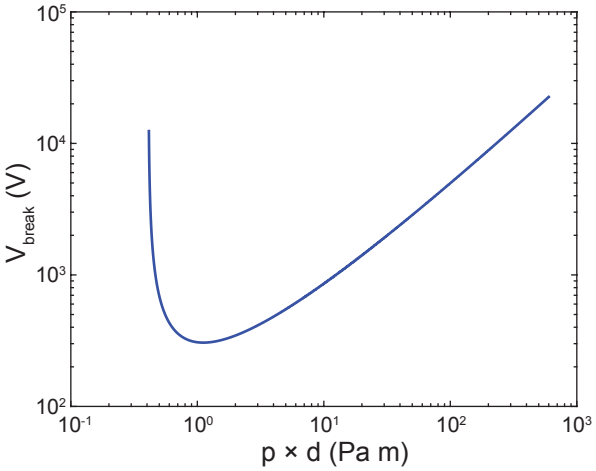

Figure 4.23.: Paschen curve for air with $A = 11.25\,\mathrm{Pa}^{-1}\,\mathrm{m}^{-1}$, $B = 274\,\mathrm{Pa}^{-1}\,\mathrm{m}^{-1}$ and $\gamma = 0.01$ [192]. For example, a minimum electrode distance of $d = 3\,\mathrm{mm}$ results in a pressure around 370 Pa for the minimum breakdown voltage.

minimum, V_{break} increases with the product $p \times d$ because of a decreasing kinetic energy of the free charges, either by a reduction of the electric field due to an increasing electrode distance or by a reduction of their mean free path due to a higher pressure with a higher collision probability. For decreasing values of $p \times d$ smaller than the minimum value, the breakdown voltage rises again, as the distance between the electrodes becomes too short or the amount of remaining molecules is too low for impact ionization. The shown Paschen curve is valid for static voltages. For oscillating voltages the values of the breakdown voltage increase slightly with frequency up to 20 kHz [193], but decrease for even higher frequencies ($> 500\,\mathrm{kHz}$) below the static breakdown voltages [194]. From this data, it becomes clear that the trap voltage needs to be reduced as a function of the pressure during evacuation in order to avoid particle loss due to discharges.

4.5. Electrospray Injection

Electrospray ionization is used for charging and injection of particles into the trap. Compared to other ionization techniques [195], like electron impact ionization, chemical or laser ionization methods, electrospray ionization offers several advantages. It is a so-called soft ionization technique used for molecules, but also for heavier objects like nano- and microparticles. Electrospray ionization avoids fragmentation or modification of the sample and offers high flexibility, as the charge sign of the final charged particles can be changed by switching the applied voltage. The invention of electrospray ionization enabled charging and vaporization of larger molecules and became a widely-used tool in mass spectrometry [196–198], which was honored by the Nobel prize in chemistry awarded to John B. Fenn in 2002 [199, 200].

4.5.1. Electrospray Ionization

The general mechanism of electrospray ionization is depicted in figure 4.24. The sample material is dissolved or dispersed in a polar liquid. This mixture is pumped through a metal capillary, which is connected to a high static potential with respect to ground. In the electric field between the tip of the capillary and a grounded counter electrode, the so-called Taylor cone is formed [201]. With a positive capillary potential, as shown in the schematic, the metal capillary is the anode and the counter electrode is the cathode. The liquid cone forms because of positive ions which are drawn out along the electric field. Inside the capillary negative ions are attracted from the anode and move in the opposite direction [202]. When this charge separation does not stop due to a balanced field inside the liquid, the cone will become destabilized. Eventually, the Coulomb repulsion exceeds the surface tension of the liquid cone and charged droplets are ejected from its tip. Depending on the strength of the field, this occurs in one or more jets of droplets [203]. The created droplets are accelerated in the electric field and pass through the central hole of the cathode. Evaporation of the solvent reduces the droplet size down to a critical minimum, which is called the Rayleigh limit. Beyond this limit the surface tension of the droplet can no longer counterbalance the Coulomb repulsion and the droplet ejects fine jets of smaller charged droplets [204]. According to the Rayleigh limit, the maximum amount of charge q_{max} that can be carried by a liquid droplet with radius R and surface tension γ can be written as [202]

$$q_{max} = 8\pi\sqrt{\varepsilon_0 \gamma R^3}. \tag{4.9}$$

To explain the final charge of the particles after evaporation, two different models can be used depending on the possible final size of the droplet [205]. The Charge Residue Model claims that evaporation and droplet fission continue until the solvent is gone. Eventually, only the particles or analytes from the droplets will remain, with the surface charges of the former droplet. If the droplets reach sizes smaller than 20 nm in diameter, the Ion Evaporation Model can be considered, which suggests that ion emission occurs directly from the droplet due to the strong electric field at the droplet surface. However, as all particles used in this thesis are significantly larger than 20 nm, the charge residue model is sufficient for these experiments.

The charge sign of the injected particles can be selected by the polarity of the voltage applied to the metal capillary. Generally, electrospray ionization has to be performed under ambient pressure. At reduced pressures, evaporation of the solvent is dramatically

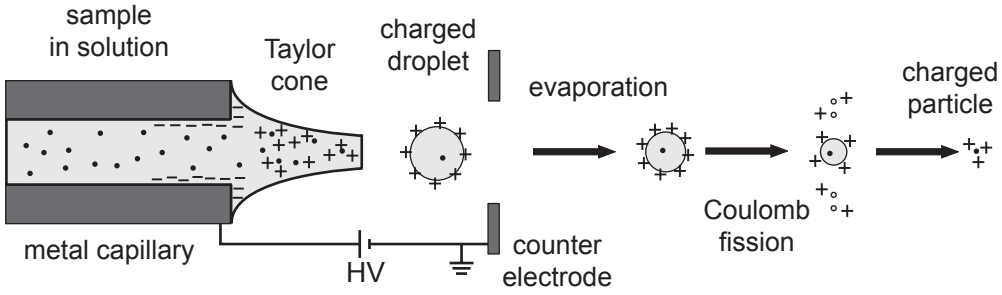

Figure 4.24.: Scheme of electrospray ionization.

increased and freezing of the capillary may occur [206]. This could be circumvented by heating the capillary [207]. Furthermore, special solvents like glycerol could be used with reduced pressures [208] but with the disadvantage of a very high viscosity.

4.5.2. Electrospray Injector

The electrospray injector, used in most experiments of this thesis, can be seen in the photographs of figure 4.25. It consists of a glass syringe (Fortuna Optima, 2 mL Glass Luer) with a metal cannula (Hamilton, 91039) mounted in a holder made of standard optical posts. Individual syringes and cannulas are used for different sample mixtures to avoid cross-contamination. The cannula has an inner diameter of 130 µm, an outer diameter of 470 µm and a flat point. Depending on the chosen solvent, the polarity, and the distance between the cannula tip and the counter electrode, a static voltage of 1.7 to 3.5 kV from a high-voltage power supply (Stanford Research Systems, PS 300) is applied between the cannula and the grounded counter electrode via an SHV (safe high voltage) connector. During operation the injector is placed outside the vacuum chamber in such a way that the injector is directed to the front end of the used linear trap with a distance of 20 to 30 mm between the counter electrode and the trap. The injector stands on a magnetic base that allows for easy positioning and removal. By applying weak pressure on the plunger of the syringe, it is ensured that enough solution is available at the tip of the cannula for the electrospray process.

A motorized injector was also developed during this thesis, but could only be used in larger housings due to the limited space inside the vacuum chamber. For future experiments it might be worthwhile to use an automated injector with smaller dimensions. However, the manual injector offers some advantages concerning flexibility and loading speed.

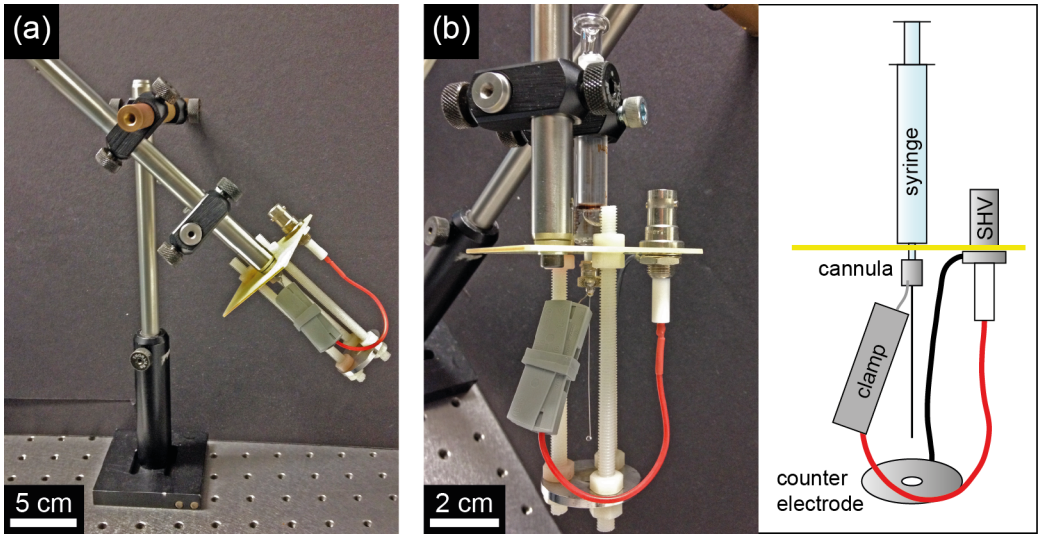

Figure 4.25.: Electrospray injector. (a) Injector mounted on magnetic stand. (b) Close-up of the injector. The schematic explains the important parts of the photograph in b.

4.6. Trapping and Characterization of Particles

After presentation of the main constituents of the trap setup, the most important experimental techniques used in this thesis are explained in detail in the following section. This includes the preparation of the sample material and the subsequent injection into the trap by electrospray ionization, the stabilization of particle trajectories in the trap, the characterization and handling of confined particles as well as different kinds of particle characterization.

4.6.1. Sample Preparation

For investigation of particles in a Paul trap, the specific sample solution has to be prepared first. All particles used in this thesis are obtained in aqueous solution from commercial suppliers. To reduce the high initial concentration, the samples are diluted in ethanol. In the beginning water was used as dilutant, but was later replaced by ethanol. The higher volatility of ethanol reduces the risk of liquid conducting paths developing between the trap electrodes during electrospray injection (see section 4.5). Depending on the particles and their initial concentration, different dilution steps are necessary to obtain a satisfying concentration. Typical values of the solid contents of the final solutions are in the range of 10^{-5} to 10^{-9} wt% (percentage by mass), to obtain a mean particle number per electrospray droplet of less than one. The preparation is completed by filling the solution into a glass syringe which is mounted into the electrospray injector.

4.6.2. Particle Injection and Axial Isolation

As described in section 4.5, electrospray ionization is used to charge and inject particles into the trap. Due to the nature of the electrospray process all charged solvent droplets carry approximately the same amount of charge. Thus, almost independent from the actual particle sample, the droplets reaching the trap have similar specific charges $\frac{Q}{M}$ for a particular solvent, and initial stabilization is done under the same conditions. Typical trap parameters for particle injection are $V_{ac} = 1\,\mathrm{kV}$ for the ac amplitude, $\Omega = 2\pi \times 2\,\mathrm{kHz}$ for the angular frequency and $U_z = 10\,\mathrm{V}$ for the axial trapping voltage. When the solvent evaporates, the specific particle charges increase and further adjustment of the trap parameters may be required. For this, the trap parameters can be changed individually up to $V_{ac} = 1.5\,\mathrm{kV}$, $\Omega = 2\pi \times 100\,\mathrm{kHz}$ and $U_z = 120\,\mathrm{V}$. This cannot be done before particle injection, because the oscillating electric field outside the trap shields the trap center very efficiently. In particular, when the frequency is too high, injected particles are deflected from the trap. To allow particles to reach the trap center, the trap parameters are slightly detuned.

Usually, more than one particle is trapped during injection. Due to the Coulomb repulsion from their charges, the trapped particles line up in a linear Coulomb crystal, as shown in figure 4.26(a). The one-dimensional particle structure changes to a two- and even a three-dimensional configuration [209], when the particle number is further increased, or the ratio between radial and axial confinement is reduced in order to compress the crystal in axial direction, as shown in figure 4.26(b). Most of the particles are not stabilized on the trap axis anymore, giving rise to an increased micromotion, that scales with the distance to the center of the trap (compare to equation (3.33) and figure 3.4(e) and (f)) [210]. Similar

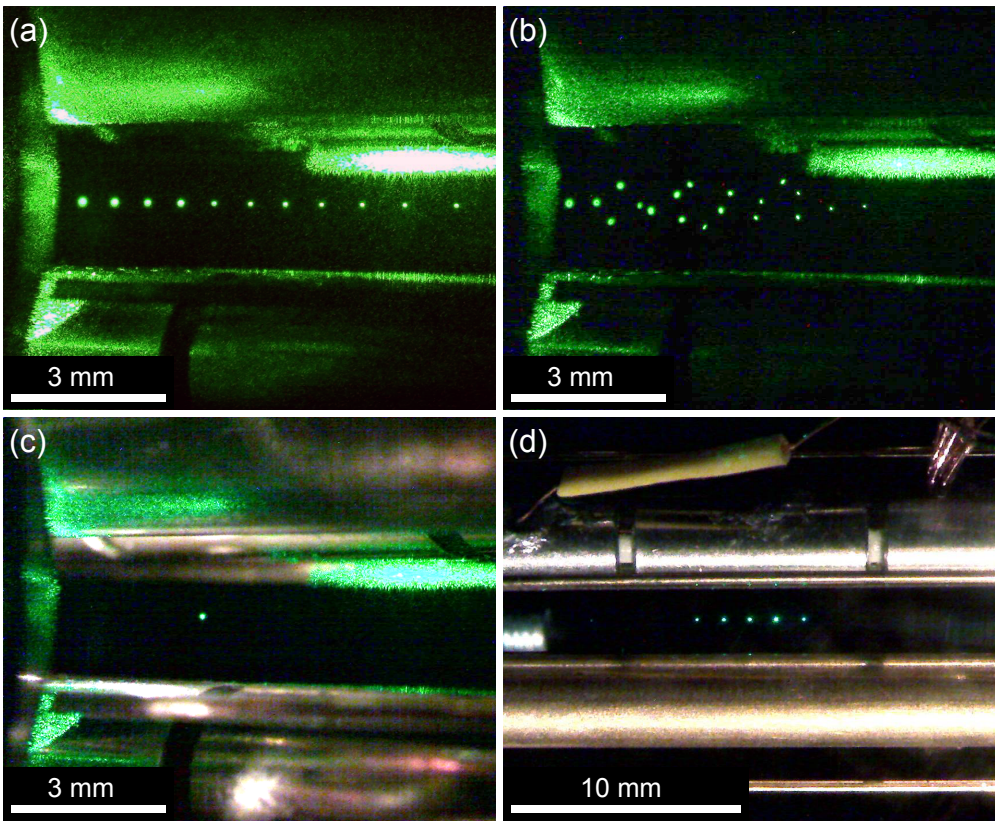

Figure 4.26.: Polystyrene beads with diameters of 100 nm in the segmented Paul trap. (a) Linear Coulomb crystal, typically observed after particle injection. (b) Three-dimensional crystal as a result of a reduced ratio between radial and axial confinement. (c) Single, isolated particle in front of the microscope objective. (d) Five particles in one segment form a linear Coulomb crystal. The trap is observed from the side in (a)-(c) and from above in (d).

crystals, made of atomic ions, can be used as simple model systems to investigate crystal topologies and defect formation [84, 211]. However, isolation of a single trapped particle is desired for optical spectroscopy in this thesis. In the segmented trap, particle isolation is done by switching the axial potentials, in order to separate an individual particle from the others. The single particle is transferred to the segment observed by the microscope objective, while the remaining Coulomb crystal is usually stored in a distant trap segment for subsequent measurements. When the investigated particle does not meet the requirements in terms of size or optical properties, but also when several particles of the same sample should be tested successively, particles are released from the trap by pushing them out at the unblocked end. Then, another particle is separated from the crystal and transferred to the microscope objective segment. The photographs in figure 4.26(c) and (d) show a single particle in front of the microscope objective and a linear Coulomb crystal formed by five particles confined in one segment, respectively.

Once trapped, the particles can be stabilized for several hours and even days. When brought into the microscope focus, particle stability can be further improved, as exemplified with a submicron diamond particle in figure 4.27. The initially large macromotion shown in figure 4.27(a) causes the large micromotion shown in figure 4.27(b), observed for

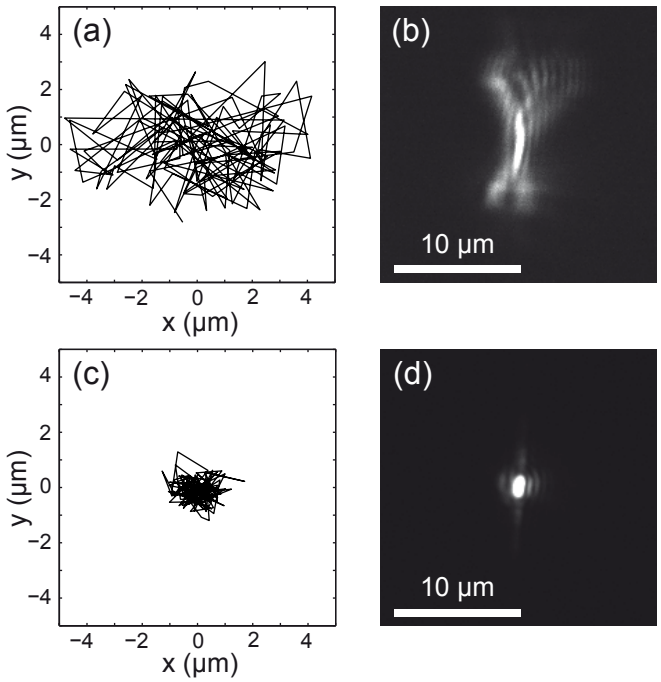

Figure 4.27.: Stabilization of a diamond cluster (estimated overall diameter: 2.5 µm) in the radial (vertical image axis) and axial (horizontal image axis) trap directions. (a) Large macromotion causing a (b) large micromotion trajectory observed for trap parameters used for particle injection. (c) Improving the confinement by increased trap parameters reduces the macromotion, which causes also a (d) reduction of the micromotion. The particle positions for the macromotion measurements in (a) and (c) are determined by tracking the center of the time-averaged micromotion trajectory. (b) and (d) are microscope images. The exposure time for (b), (d) and each data point in (a) and (c) is 1 ms. From [212].

trap parameters used for particle injection with the aforementioned values. As known from equation (3.21), the micromotion is proportional to the deviation of the particle position from the center of the trapping field. Thus, by reducing the macromotion the micromotion can be reduced as well. This is done by improving the confinement, in this case by increasing the trap parameters to $V_{ac} = 1.25\,\mathrm{kV}$, $\Omega = 2\pi \times 10\,\mathrm{kHz}$ and $U_z = 100\,\mathrm{V}$. The higher frequency leads to a decrease of the macromotion amplitude, as shown in figure 4.27(c), which causes a reduction of the micromotion, as shown in figure 4.27(d). In the end, the particle is confined to 1 µm in the radial as well as in the axial direction around the trapping center. A further improvement could be achieved by a stronger confinement. Actual limitations are the residual thermal motions as well as imperfections of the trapping field due to unwanted interference fields and deviations from the ideal electrode geometry (see section 3.2).

The explained injection and stabilization schemes also apply for the end-cap trap. The only difference is that particle separation in the axial direction is not possible. Trapping of more than one particle has be avoided during injection. Therefore, a trapped particle has to be released after characterization and a new one has to be injected for subsequent particle investigation.

4.6.3. Estimation of Particle Charges

The charges of the trapped particles are estimated by measuring the axial distance of two particles isolated in one segment. According to equation (3.47), the static potential in the axial direction can be written as

$$\Phi_z = \frac{\kappa U_z}{z_0^2} z^2. \tag{4.10}$$

Here, the defocussing radial components are neglected. This is justified for segments which are long compared to the radial trap dimension ($z_0 > r_0$), and when the radial potential is much larger than the axial one [160]. Due to Coulomb repulsion between two particles with the same charge polarity, the equilibrium position of each particle is found, where the Coulomb force F_C is compensated by the restoring force F_z of the axial trap potential exerted on each particle. Assuming equal charge values Q, the following relation holds true for particle i ($i = 1, 2$)

$$F_C = F_z, \tag{4.11}$$

$$\frac{1}{4\pi\varepsilon_0}\frac{Q^2}{d^2} = \frac{2Q\kappa U_z}{z_0^2}\frac{d}{2}. \tag{4.12}$$

With the axial distance d between both particles, Q is obtained from

$$Q = \frac{4\pi\varepsilon_0}{z_0^2} U_z \kappa d^3. \tag{4.13}$$

The geometric factor of the segmented trap is estimated to be $\kappa = 0.1$ with a similar linear trap [213]. This is in good agreement with other reported values [214,215]. Typically, for a segment voltage of $U_z = 20\,\mathrm{V}$, particle distances of 1 mm to 2 mm are measured, corresponding to particle charges of $10^{-15}\,\mathrm{C}$ to $10^{-14}\,\mathrm{C}$. This is equal to an absolute number of elementary charges on the surface of each particle on the order of $10^4 - 10^5$.

4.6.4. Optical Characterization

A particle stabilized in the microscope focus is observed with the CCD camera. Different images are obtained with different illumination methods (see section 4.3.1 for details).

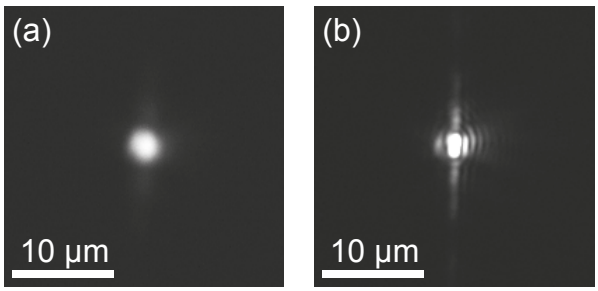

Figure 4.28.: Images of a trapped 100 nm dye-doped polystyrene bead. (a) Particle fluorescence obtained under laser excitation. (b) Dark-field images obtained from laser or white-light scattering. The diffraction pattern is explained by the trap electrodes and holders that form a rectangular aperture. From [216].

Fluorescence from optically active particles, as shown in the photograph in figure 4.28(a), is excited with the laser. When the collected light is sent to the spectrometer instead of the CCD camera, the particle signal can be spectrally analyzed. The scattered laser light itself is split from the fluorescence signal with a dichroic mirror (see section 4.3.4 for details). In this way, the particle position can be observed with the CCD camera from scattered laser light (and corrected if necessary), while the fluorescence light is spectrally dispersed and imaged by the spectrometer. A scattering image of the particle can be seen in figure 4.28(b). The particle can also be illuminated with white light from a halogen lamp for dark-field scattering images.

4.6.5. Deposition of Particles

For accurate size measurements and further manipulation, trapped particles are deposited on cleaved fiber end faces, where they are found without much effort in the clean and relatively small area of the facet. Large particles are visible in an optical microscope. For smaller particles, but also for exact size determination, an atomic force microscope (AFM) is used.

Deposition on Fiber Facets

Deposition of levitated particles for further analysis is best done on a planar surface. For instance, the cleaved end face of an optical fiber offers a clean and delimited area, on which deposited particles can be easily retrieved. Another advantage is the small fiber diameter, which allows for insertion of the fiber between the electrodes into the center of the trap. In figure 4.29 a simplified schematic of the deposition setup is shown.

Levitated particles are characterized by optical spectroscopy with the microscope setup shown in figure 4.21. Once a suitable particle is identified, the fiber is moved into one end of the trap, while the particle is transferred to this end by changing the segment voltages. The deposition is facilitated by always-present charges on the surface of the fiber due to friction from cleaving. Usually, the fibers are positively charged and thus attract negatively charged particles. But positively charged particles can also be deposited by using a negatively charged droplet of ethanol from the electrospray injector to change the charge polarity of the fiber tip. When the levitated particle is close enough, it is drawn to the fiber surface and hits the cleaved facet, if the fiber position is properly

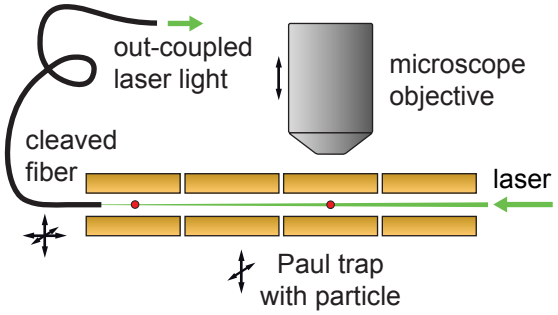

Figure 4.29.: Schematic setup with cleaved optical fiber in segmented trap. The full microscope setup is shown in figure 4.21. This method also applies for the end-cap trap.

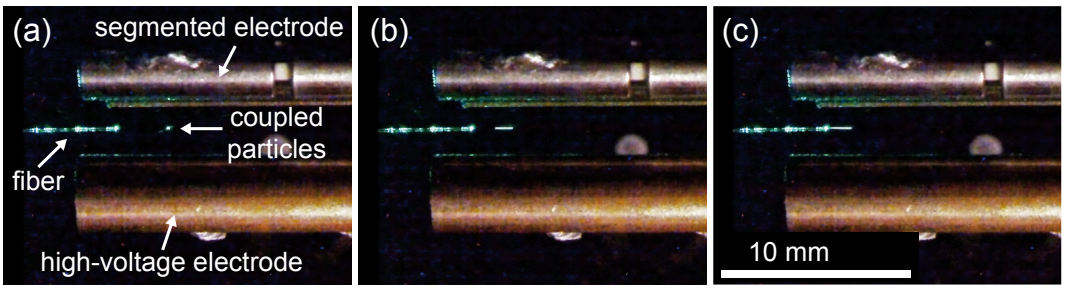

Figure 4.30.: Particle deposition on the cleaved facet of an optical fiber. (a) Particle and fiber seen by scattering of laser light. The free laser beam is directed along the trap axis and partially coupled into the fiber. (b) When the particle is close enough, it is attracted by the fiber due to the opposite charges, and (c) lands on the fiber facet. Note: the photographs show the deposition of a compound particle (see section 5.4). No difference is seen when only a single particle is deposited. From [216].

adjusted to the trap center. This is ensured by observing the laser light which is directed along the trap axis and coupled into the fiber during the alignment. When the light, coupled out at the distant end, is maximized, the fiber end inside the trap is centered. During characterization, transfer and deposition, the levitated particles are observed by scattering of the free laser beam. The photographs in figure 4.30 depict the deposition process. Although only the segmented trap is shown here, particles from the end-cap trap can be deposited on a fiber facet as well. Mounted on a motorized linear stage, the fiber can be moved into each trap along the axis. In this thesis, the fibers are inserted on-axis into the traps, but due to the small fiber diameter, this technique is also applicable with the fiber entering the trap perpendicular to the trap axis, between the electrodes.

Atomic Force Microscope

An AFM is a scanning probe microscope with the capability to resolve atomic structures [217]. Structures of a few nanometers and smaller, which are well below the diffraction limit of light, can be imaged [218]. The operating principle is shown in figure 4.31. A thin cantilever with a sharp tip, usually made of metal-coated silicon, is moved over the sample surface. The cantilever can be described as a leaf spring in the potential defined by different forces between the tip and the sample, for example van der Walls, capillary, electrostatic, or magnetic forces. Depending on the distance to the sample surface, the deflection of the cantilever is changed during the measurement. This is detected by a laser reflected from the upper side of the cantilever into a quadrant photodiode. A feedback loop can be implemented to keep the deflection at a constant value by adjusting the height of the tip with a linear piezoelectric actuator. The resulting AFM scan is an image depicting the topography of the investigated area.

According to the actual application, different operating modes can be used, which can be divided into contact and non-contact modes [219]. The contact mode is a static mode, used to move the tip with full contact to the sample over the surface and record the deflection of the cantilever or the control value of the height feedback loop. In contact mode, the cantilever tip can also be used for sample manipulation, especially for moving [220] and transferring single nanoparticles [221]. For the dynamic non-contact mode the tip is held

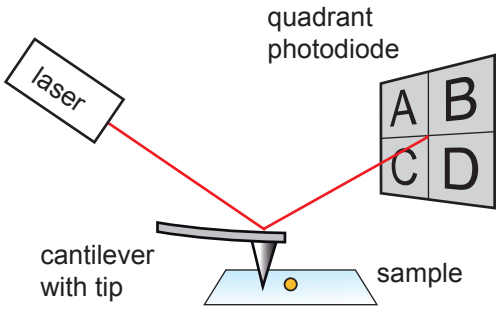

Figure 4.31.: Schematic of an atomic force microscope (AFM).

above the surface and is driven to oscillate close or on its resonance frequency by the piezoelectric actuator (typically with 50 kHz to 300 kHz). Due to the surface potential, the amplitude and the resonance frequency change with the distance between the tip and the sample. Using the feedback loop, the oscillation frequency or the amplitude is kept constant by adjusting the tip height. Information about the sample topography can be acquired from frequency, amplitude or phase measurements. Most AFMs also offer an intermittent contact or tapping mode, which is similar to the non-contact mode but with larger oscillation amplitudes of the cantilever (typically >100 nm instead of a few tens of nm) [219]. Periodically occurring approaches to the sample surface reduce the oscillation amplitude of the cantilever, which are monitored by the feedback loop, giving a measure for the surface roughness. The non-contact modes preserve the sample more in its original state during measurements than the contact mode, making it the method of choice for imaging of sensitive samples. Wear on the cantilever tip is also reduced in this mode, which is important for high image resolution, where artifacts due to broad or irregular tips have to be avoided.

AFM Fiber Setup

For AFM analysis of a particle deposited on a fiber facet, the fiber is clamped in a brass ferrule (Newport, FPH-S) and placed under the AFM (JPK Instruments, NanoWizard BioAFM), as shown in the schematic of figure 4.32(a). By coupling light into the distal end of the fiber, the position of the AFM cantilever is adjusted by observing its shadow in order to facilitate the critical alignment to the fiber facet. After the cantilever is approached to the fiber surface, the facet can be raster-scanned. An optical microscope image can help to navigate on the fiber facet to find the placed particle by revealing characteristic surface features, for example imperfections created during the cleaving process, in relation to the deposited particle's position. The photograph in figure 4.32(b) shows the fiber in the ferrule below the AFM cantilever chip. Once found, the particle height and expanse is measured. In contact mode one can also move the particle on the surface or try to separate it into smaller pieces, to test whether the particle is a single one, or a cluster consisting of several particles.

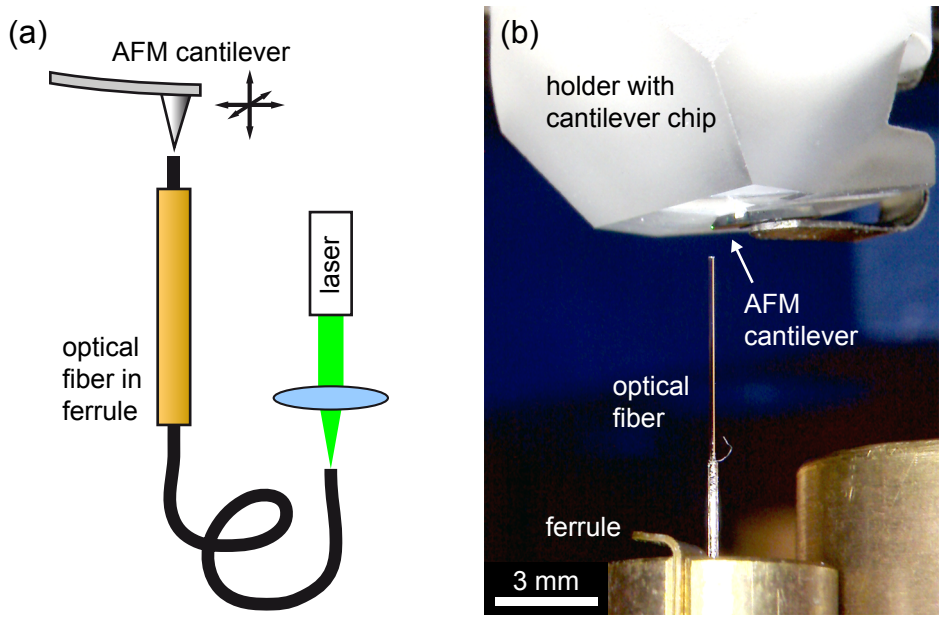

Figure 4.32.: AFM fiber setup used for height analysis of deposited particles. (a) Schematic of the AFM fiber setup. (b) Photograph of clamped fiber below AFM cantilever. At the left edge of the cantilever chip a small green laser spot can be recognized, indicating the position of the cantilever tip.

4.6.6. Transfer to Vacuum

The trap is mounted inside a vacuum chamber to isolate the particles from the environment. In this thesis all experiments are performed under atmospheric pressure, but transfer of levitated particles to vacuum conditions has been tested. After particle injection by electrospray ionization, the chamber is closed and the evacuation can be started. As explained in section 4.4, gas discharges and electrical sparkover have to be avoided during evacuation, to keep the particles within the trap. Basically, reducing the trap voltage impairs particle stability. At the beginning of evacuation, for pressures close to atmospheric values, a strong airflow is observable based on the motion of the particles, actually requiring a stronger confinement. In particular, smaller particles, like diamond nanocrystals, are easily lost under a variety of conditions. In contrast, transfer of trapped micron-sized particles to vacuum is possible with fewer problems. For instance, WGM spectra, obtained from a silica microsphere with an approximate diameter of 4.8 µm under dark-field excitation with white light from the halogen lamp, are observed at lowered pressures, as shown in figure 4.33(a). The peak structure shifts with the pressure, but not linearly, which can be seen in figure 4.33(b). This behavior is attributed to evaporation and condensation of humidity on the surface of the silica sphere [222, 223], as such a strong pressure dependence of the peak position is not expected for solid spheres [224]. Furthermore, similar peak shifts are observed, when the vacuum chamber is flooded with dry industrial gases (data not shown here). The pressure inside the vacuum chamber can be reduced down to approximately 10^{-3} mbar. For lower pressures, the vacuum chamber has to be improved with regard to seal tightness and outgassing. However, it is possible to transfer trapped particles to vacuum conditions with the presented method, although

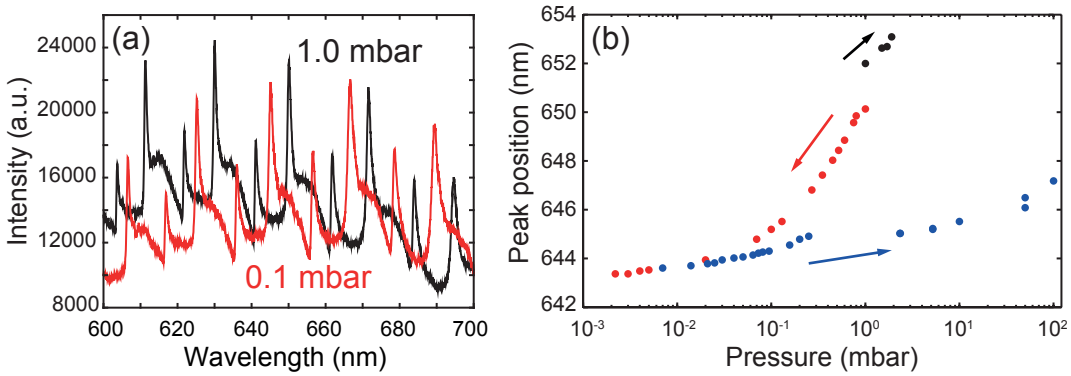

Figure 4.33.: Shifting WGM of a trapped microsphere with an approximate diameter of 4.8 µm. (a) By lowering the pressure, the characteristic peak spectrum is shifted to a lower wavelength. (b) Recorded spectral position of one peak for different pressures. The first spectrum is obtained at a pressure of 1 mbar. After a small increase (black data points), the pressure is reduced down to 2×10^{-3} mbar (red data points) and finally increased again (blue data points). The spectral changes are attributed to evaporation and condensation of humidity on the surface of the silica sphere.

for small nanoparticles it is necessary to refine the transfer method or use a different ionization technique that can be applied in vacuum.

5. Investigation and Manipulation of Individual Trapped Particles

In the following chapter the experimental results obtained with the Paul traps are presented. The trap setup enables optical spectroscopy of various individual levitated nano- and microparticles. In section 5.1 nitrogen vacancy defect centers in diamond crystals are investigated. The results, which are published in Applied Physics Letters [212], show how fluorescence from submicron diamond clusters stabilized in an electrodynamic trap can be detected. With silver nanowires it is shown in section 5.2 that also plasmonic particles can be analyzed in the trap. Fabry-Pérot-like resonances are observed in the scattering emission upon white-light excitation. The results are published in ACS Photonics [225]. A variety of manipulation techniques are also developed during this thesis. Deposition of optical active dye-doped polystyrene beads and quantum dots as well as optical resonant silica microspheres on tapered optical fibers is demonstrated in section 5.3. The investigation of these manipulation technique for functionalization of fragile photonic structures is described in Optics Express [226]. Additionally, assembly of individual particles in the trap is used for electromagnetic coupling of similar emitter and resonator particles. The creation and analysis of different particle compounds is published in Nano Letters [216].

5.1. NV Defects in Submicron Diamond Clusters

The most important aspect of using a particle trap is the opportunity to isolate particles from the environment. This not only enables single ion stabilization, but facilitates manipulation of larger particles as well. In the following section, isolation and characterization of submicron diamond clusters in a linear Paul trap is presented. The fluorescence of included nitrogen vacancy (NV) defect centers is detected, and the particles are deposited on fiber end-faces for exact size determination. The results presented in this section are published in Applied Physics Letters [212].

5.1.1. Introduction

Nitrogen vacancy defect centers in diamonds show remarkable characteristics, as explained in section 2.4.3. In addition to their application in quantum optics and quantum information experiments [126], optomechanical interactions [227] in a single diamond nanocrystal can also be studied, where the defect center is used as an interface between photons of the excitation light and phonons of the crystal lattice. Optical refrigeration [228] is envisioned, like already shown for rare-earth-doped glasses [229] and semiconductors [230]. The cooling cycle depends on the excitation of anti-Stokes fluorescence, in which the emitted photons are of higher energy than the absorbed photons. An emitter with discrete energy levels and a high quantum efficiency is needed for this. Both are fulfilled by a NV defect center in a nano-sized diamond crystal. In particular, the problem of re-absorption

is negligible, as radiation trapping due to total internal reflection cannot occur in such small systems.

The experimental needs for such an experiment are comparatively high. Most importantly, the particle has to be decoupled from any environment, to maintain the high mechanical quality factor of the diamond crystal. For this task, particle isolation in a Paul trap is promising, as contact to substrates and other particles is prevented. Trapping of single diamond crystals in optical dipole traps is already demonstrated in solution [231,232] and air [233, 234], but quenching of NV fluorescence has been observed due to the high intensity of the trapping laser [233]. This behavior would not be expected from a particle in an electric-field trap.

In the experiment described in this section, NV fluorescence is observed from submicron diamond particles levitated in the end-cap trap. So far, no influence on the investigated particles can be seen from the trapping method or the high amount of surface charges. The results presented in the following are an important first step towards optomechanical experiments with individually trapped nanocrystals.

5.1.2. NV Fluorescence from Levitated Diamond Particles

Commercial available diamond particles (Microdiamant, DiaScene 125) with an average diameter of 125 nm are used in this experiment. The diamonds are irradiated with electrons in order to increase the density of NV defect centers [235]. Unfortunately, no values about the NV density are provided with the diamonds. The end-cap trap introduced in section 4.1.1 is used in this experiment. For the same applied voltages, this trap enables a higher pseudopotential compared to the segmented trap, and thus, ensures better confinement of stabilized particles (see equation (3.31)). After electrospray injection (see section 4.6.2), differently sized particles are observed in the trap by scattering of laser light. The intensity of the scattering signal gives a first indication of the particle size. More precise values are obtained from AFM measurements after particle deposition. Approximately, particles and clusters between 0.1 µm to 5 µm are confined. Figure 5.1 shows a photograph of a single submicron diamond cluster levitated in the trap. The green light

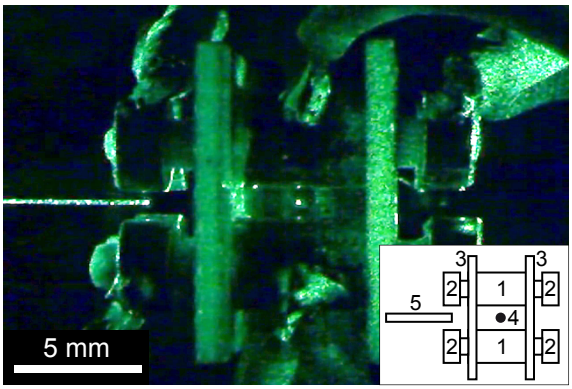

Figure 5.1.: Submicron diamond cluster in the end-cap trap. To deposit the particle, the optical fiber is moved towards the trap center. The inset shows a sketch of the trap with (1) quadrupole electrodes, (2) end-cap electrodes, (3) mounting plates, (4) trapped diamond particle, and (5) optical fiber with cleaved facet. From [212].

of the argon-ion laser is slightly focused from the side onto the single particle in the center of the trap.

The fluorescence of the NV defect centers in the diamond crystal is excited with the laser from the side or focused through the microscope objective, as described in section 4.3.4. The emitted fluorescence light is collected by the same microscope objective and eventually detected with the CCD camera and the spectrometer. The spectra in figure 5.2(a) show fluorescence emission obtained from levitated diamond clusters with an approximate diameter of 2.5 µm. At 575 nm and 637 nm the typical zero phonon lines (ZPLs) and their large phonon sidebands of the neutral (NV^0) and the negative (NV^-) charge state of the defect centers can be recognized, respectively. Because of the large number of NV defect centers contributing to the spectrum, inhomogeneous broadening is observed for the ZPLs [236]. The influence of the high amount of surface charges on the defect centers is estimated by comparing the fluorescence spectra of two equally sized diamond clusters with opposite charge polarities. The two curves in figure 5.2(a) show the measured fluorescence spectra obtained for a positively (black curve) and a negatively (blue curve) charged diamond cluster of similar size. It is assumed that the surface charges do not influence

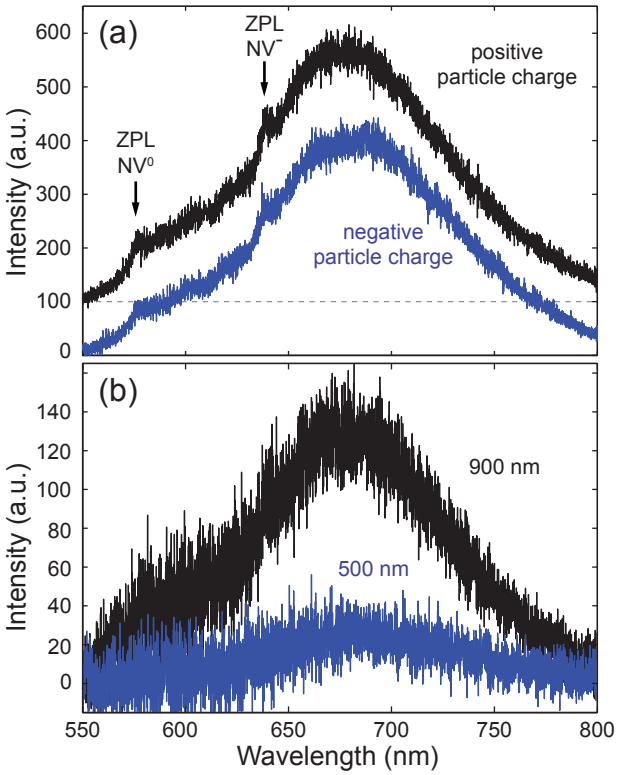

Figure 5.2.: Fluorescence emission spectra of NV defect centers in single diamond clusters levitated individually in the trap. (a) No difference in the spectral properties is found for positively (black curve) and negatively (blue curve) charged particles. At 575 nm and at 637 nm the ZPLs of the neutral (NV^0) and the negative (NV^-) charge states of the defect centers can be identified, respectively. Both diamond clusters have diameters around 2.5 µm. The black curve is offset by 100 counts to separate the two curves. (b) Fluorescence emission detected from levitated diamond clusters with sizes of 900 nm (black curve) and 500 nm (blue curve). The shown spectra are corrected for background light obtained from the empty trap. From [212].

the NV defect centers in the large clusters, as no difference in the spectral properties is found. With smaller particle sizes the detected fluorescence signal gets weaker, due to a decreasing number of NV defect centers contributing to the signal. In figure 5.2(b) two spectra are shown for individually trapped diamond clusters with diameters of 900 nm (black curve) and 500 nm (blue curve). Identification of the spectral features of the NV centers is challenging. In particular for the smaller cluster, only the phonon sideband of the NV^- charge state can be identified as the signal to noise ratio is very small. For particles smaller than 500 nm no fluorescence emission has been detected, so far. They can only be observed in the trap by scattered laser light. This does not mean that diamond clusters smaller than 500 nm do not contain any NV defect centers. No values are available from the supplier, but at least one NV defect center per 125 nm diamond crystal seems to be a realistic expectation [235].

The reason for the poor signal is the low detection efficiency of the microscope used in combination with the trap. Although the microscope objective has a numerical aperture of 0.5, the effective numerical aperture of the system is around 0.2, because of a reduction of the accessible opening angle by the electrodes and the mounting plates of the trap, as indicated in the schematic in figure 5.3. With such a low numerical aperture, only 1 % of the light emission from an isotropically radiating point source is collected. According to the specifications of the spectrometer, the quantum efficiency of the CCD chip is 0.4. This multiplies to 0.003 for the overall detection efficiency of the whole microscope system, after including the losses at all optical elements which are estimated to be 25 %.

The emission rate of the NV defect center can be estimated from its lifetime. For the transition from the excited (^{3}E) to the ground state ($^3A_2$), described in section 2.4.3, a lifetime of 25 ns is assumed for nanodiamonds at room temperature [124]. Thus, for the given optical setup a rate of 10^5 counts per second should be expected for an assumed quantum efficiency of 1 [237]. But this does not include the long lived metastable state (^{1}E) with a lifetime longer than 300 ns [124]. A reduction of the expected count rate by one order of magnitude due to this process seems to be realistic, which is consistent with other observations [237]. The resulting 10^4 counts per second are too low to be detected with the system efficiently. For ten or more contributing defect centers, the overall count rate should be large enough for measuring the spectrum, which is in accordance to the observation, that fluorescence can be detected only for cluster particles consisting of nanodiamonds in

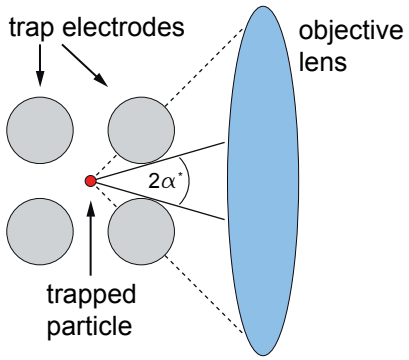

Figure 5.3.: The accessible opening angle of the microscope objective α^* is limited by the trap electrodes and the mounting plates (not shown). The dashed lines indicate the full opening angle of the microscope objective without the trap.

the order of ten or more particles. Longer exposure times would improve the signal, but drifts of the particle out of the microscope focus disrupt the measurement signal, making an active stabilization of the particle position necessary. The shown spectra are measured with an exposure time of 60 s, which multiplies to a measurement duration of almost ten minutes, as each spectrum is acquired with a so-called step-and-glue procedure. For this, individual high-resolution spectra are captured for smaller spectral ranges, determined by the line spacing of the grating and the focal length of the spectrograph as well as the size of the CCD chip. After the measurement the single spectra are combined to cover the full desired spectral range. The measurement duration could be shortened, for instance by using a grating with a smaller line density, to increase the spectral width of each individual spectrum step, but this cannot be a sufficient compensation for the low detection efficiency.

For exact size determination, a trapped particle is deposited on the cleaved facet of an optical fiber. The fiber is aligned to the trap axis, as shown in figure 5.1, and moved towards the particle with a motorized linear translation stage. The deposition is facilitated by attracting surface charges on the particle and on the fiber. More details of the deposition technique are given in section 4.6.5. During the deposition the landing position cannot be chosen exactly, but if the fiber is properly adjusted to the trap center, the particle can

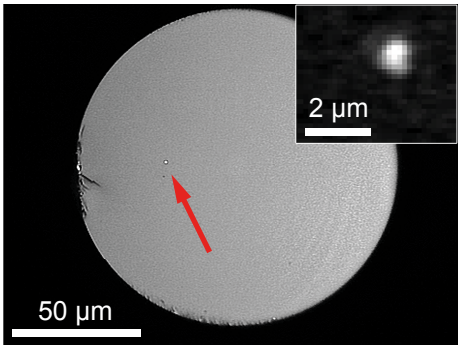

Figure 5.4.: Optical microscope image showing a submicron diamond cluster on the cleaved facet of an optical fiber (diameter 125 µm). The arrow points to the particle, that is shown in the inset with higher magnification. The breaking edge of the fiber can be identified on the left. From [212].

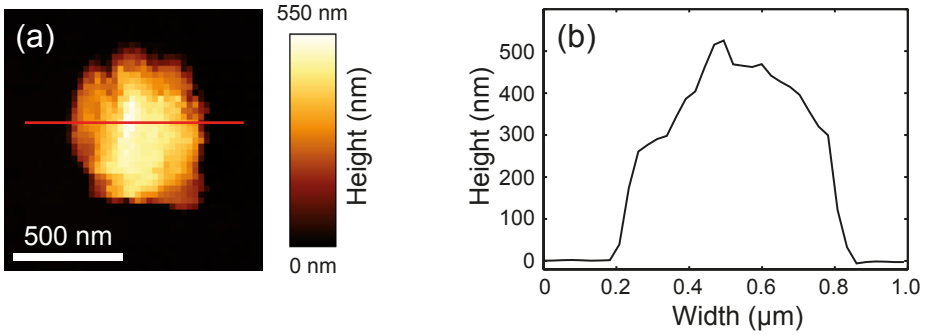

Figure 5.5.: AFM measurement of the diamond particle deposited on the fiber facet. (a) Height image of the particle. The colored bar indicates the measured height. (b) Cross section of particle height measured along the red line in panel (a). From [212].

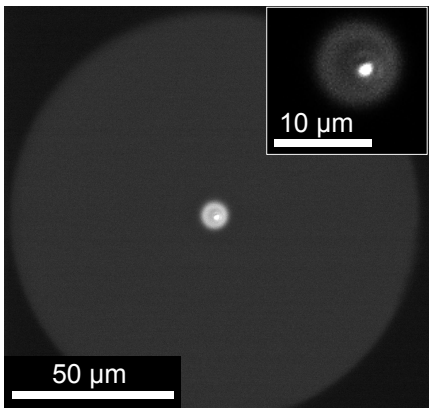

Figure 5.6.: Fluorescence image of a diamond cluster on the fiber core. After deposition from the trap the particle is transferred to the fiber core by pushing it with the AFM tip. Excitation occurs by green laser light coupled into the other end of the fiber. The laser is blocked by long-pass filters in the detection path. The core can be seen because of the fluorescence of the fiber. Additional white light is used to illuminate the whole fiber facet. The inset shows the diamond on the fiber core with a higher magnification and a different contrast.

be found within the relatively small area of the fiber facet, afterwards. In figure 5.4 the facet of an optical fiber with a diameter of 125 µm can be seen with a submicron diamond cluster particle deposited approximately 30 µm off the center. The fiber is placed under an AFM for precise size determination, as described in section 4.6.5. The breaking edge of the fiber in the microscope image is used to navigate the AFM tip to the diamond cluster. In figure 5.5 the measured height image of the same particle reveals a diameter of approximately 500 nm.

With the AFM tip in contact mode, the particle can be separated into smaller fragments, proving that it is indeed a cluster of several diamond nanocrystals. Furthermore, the AFM tip can also be used to manipulate the particle position on the fiber facet after the deposition. For example, a deposited diamond particle can be moved to the fiber core by pushing it with the AFM tip. This improved position allows for excitation of the fluorescence through the fiber by coupling laser light into the other end, as can be seen in figure 5.6. The facet is observed with the microscope setup shown in section 4.3.4, with the trap being replaced by the mounted fiber with the facet facing the microscope objective. Green laser light guided by the fiber excites the fluorescence of the NV defect centers in the diamond cluster, which is collected by the microscope objective and detected by the CCD camera. Due to the long-pass filters, the image shows only fluorescence and white light with wavelengths above 550 nm. One can see that the argon-ion laser also excites the fiber itself to emit fluorescence light. The inset proves that the particle is transferred to the fiber core, but detection of the NV fluorescence through the fiber is difficult due to the high amount of background light.

Optical characterization of the deposited diamond particles has to be done by confocal fluorescence microscopy. The spectrum in figure 5.7 shows the fluorescence emission spectrum of a deposited micron-sized diamond cluster excited and measured through the microscope objective. Compared to the levitated particles, the same spectral features are visible in the spectrum, but a bigger signal is achieved for nevertheless shorter integration times, due to the better optical access.

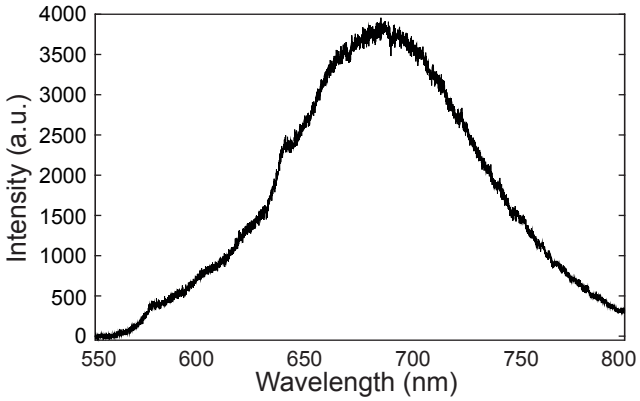

Figure 5.7.: Fluorescence emission spectrum of a micron-sized diamond cluster deposited on a cleaved fiber facet. Excitation and detection are done via the microscope objective. The spectrum is corrected for background light from the fiber.

5.1.3. Conclusion

Observation of NV defect center fluorescence from individual submicron diamond particles levitated in the trap is an important first step towards studying optomechanical interactions of crystals with high mechanical quality. A prerequisite is the stabilization of a single levitated diamond nanocrystal containing only one NV defect center. This seems to be feasible, when certain aspects of the actual trap setup are considered. First, the optical access to the trapped particle has to be improved. The problem of low detection efficiency is well known for such ion traps and can be overcome by a reduction of the trap geometry [74, 91, 238] or by special trap designs, like surface [94] or stylus electrode [95] traps. Very simple trap geometries in combination with special optics are also promising for this task [239]. Second, the stability of particles with diameters less than 100 nm has to be ensured. Due to the nature of the electrospray method, different ionized particles will carry similar amounts of surface charges (see section 4.5.1 and section 4.6.2). Thus, smaller diamond particles with a much smaller mass will have an increased specific charge compared to micron-sized diamond clusters. Regarding equation (3.18), this means that the trap parameters have to be changed to use higher frequencies Ω or lower voltage amplitudes V_{ac} without decreasing the pseudopotential too much (compare to equation (3.31)). Another solution might be to reduce the particle charge to the same extent by using a different ionization method. For instance, particle [240] or electron [195] bombardment could be involved to keep the change of the charge to mass ratio ($\frac{Q}{M}$) as low as possible when using different particles. Third, transfer of trapped particles to vacuum conditions is necessary, as optomechanical experiments require the crystals to be isolated from the environment and residual thermal amplitudes impair the particle stability (compare to equation (3.46)). So far, transfer of micron-sized particles to vacuum conditions is possible as described in section 4.6.6, but stabilization of smaller particles is difficult during evacuation, as the trap voltage has to be significantly decreased to avoid electrical sparkover between the electrodes (see section 4.4).

Besides reducing the particle size and the number of included NV defect centers, the shown method can be used to assemble diamond-based fiber-optical probes and light sources. Time-consuming searches for appropriate particles and complicated pick-and-

place methods for particle transfer [221] are not needed in this method. In contrast, growing of diamonds on the fiber facet [241] does not allow for functionalization with a preselected particle. With the shown technique, particles levitated in the trap can be easily characterized and deposited on the fiber facet. The problem of high fiber fluorescence could be overcome by using a photonic crystal fiber [242].

5.2. Plasmonic Nanowires

Similar to the investigation of levitated diamond clusters in the previous section, other particles can also be trapped and characterized. Confinement in the trap is not restricted to a specific particle material or geometry. For instance, silver nanowires with a high aspect ratio are isolated in the trap, characterized and deposited for further analysis as well. In the following section, experiments with such a plasmonic system are presented, demonstrating the high potential and versatility of the trap setup constructed in this thesis. The results of the experiment described in this section are published in ACS Photonics [225].

5.2.1. Introduction

Silver nanowires support surface plasmons at the interface between the metal and the surrounding dielectric [243], as explained in section 2.3. For investigation of their plasmonic behavior without any symmetry-breaking effects due to supporting substrates, trapping of single nanowires seems to be worthwhile. So far, various studies with trapped nanowires aim at improved particle handling or particle alignment: silver and gold nanowires in aqueous solutions can be manipulated with optical forces [244, 245], while full control of trapped nanowires is achieved by specially shaped laser beams [246]. Furthermore, even one or more semiconductor nanowires can be oriented and translated, which might facilitate pick-and-place assembly of nanophotonic structures [247]. However, none of these methods include optical characterization of the nanowires. This would allow for fundamental studies of their optical properties and seems to be of some importance for a suitable outcome of eventually assembled nanostructures. In addition, trapping of plasmonic nanowires in air would improve the applicability of such manipulation techniques.

Here, individual silver nanowires are used, which are ionized and brought into the trap under atmospheric pressure. Surface plasmons are excited by scattering of light at the ends of the wires. The nanowires support plasmonic cavity modes, which are observed as interference fringes in the scattering spectra. Levitated nanowires are optically characterized and deposited subsequently for exact analysis of their geometry.

5.2.2. Optical Setup with Crossed Polarizers

For efficient observation of metal nanowires levitated in the trap, the microscope setup shown in figure 4.21 has to be expanded. Additionally, a supercontinuum fiber laser (PicoQuant, Solea) is used as a white light source to excite propagating surface plasmon polaritons (SPPs) in the nanowires, as indicated in figure 5.8. A flip mirror enables switching between the supercontinuum laser and the argon-ion laser, which is not shown in this schematic. Optionally, the output laser spectrum can be limited by an integrated band-pass filter to a certain wavelength within the spectral range of 525 nm to 700 nm

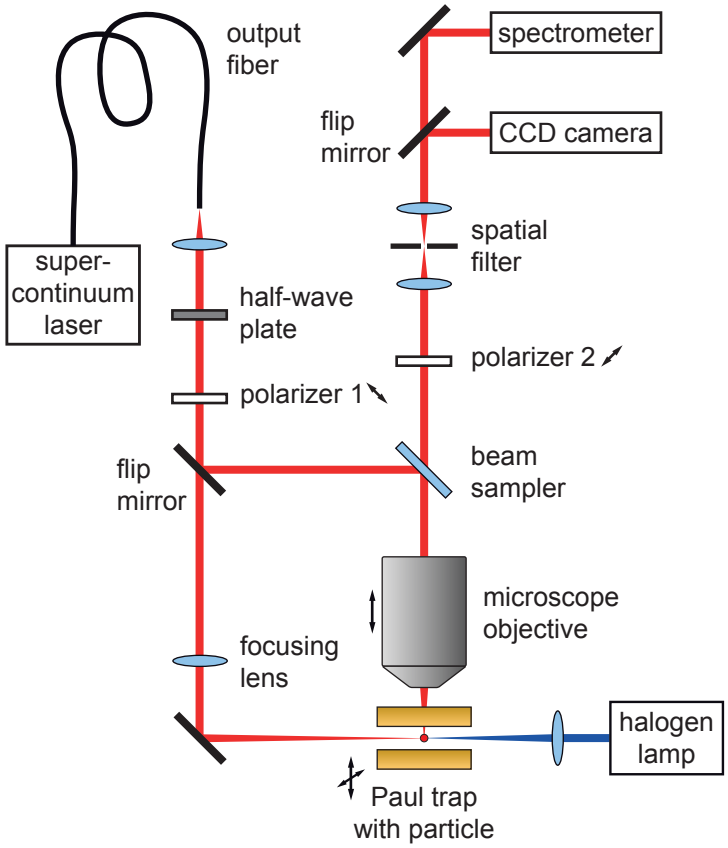

Figure 5.8.: Linear Paul trap integrated in optical microscope with supercontinuum laser and crossed polarizers. The argon-ion laser and the rest of the setup from figure 4.21 is not shown in this schematic. Flip mirrors and flip mounts allow for fast switching between the two lasers and detection schemes.

with a width of 5 nm. The laser emission is linearly polarized, where the axis can be rotated by a half-wave plate. Polarizer 1 sets the orientation of the linear polarization of the excitation light, that is focused on the particle. For filtering, polarizer 2, with polarization axis orthogonal to polarizer 1 is used. This crossed-polarizer configuration blocks the excitation light in the detection path. By turning the half-wave plate in front of the fixed polarizer, the amount of laser power used for excitation is adjusted. The rest of the setup remains the same as in the original setup (see figure 4.21). In particular, the white laser light can also be focused into the trap from the side in addition to white light from a halogen lamp, in order to excite the nanowires almost homogeneously.

5.2.3. Levitated Plasmonic Nanowires

Like every other particle sample in this thesis, the chemically grown silver nanowires (PlasmaChem, Silver Nanowires) are charged and injected into the trap by electrospray ionization (see section 4.6.2). According to the specifications, the wires have an average diameter of 100 nm ± 20 nm and a length of up to 50 µm. The sample also contains very short wire fragments and even spherical particles, which are all injected into the trap together with the longer nanowires. The end-cap trap is used primarily to trap

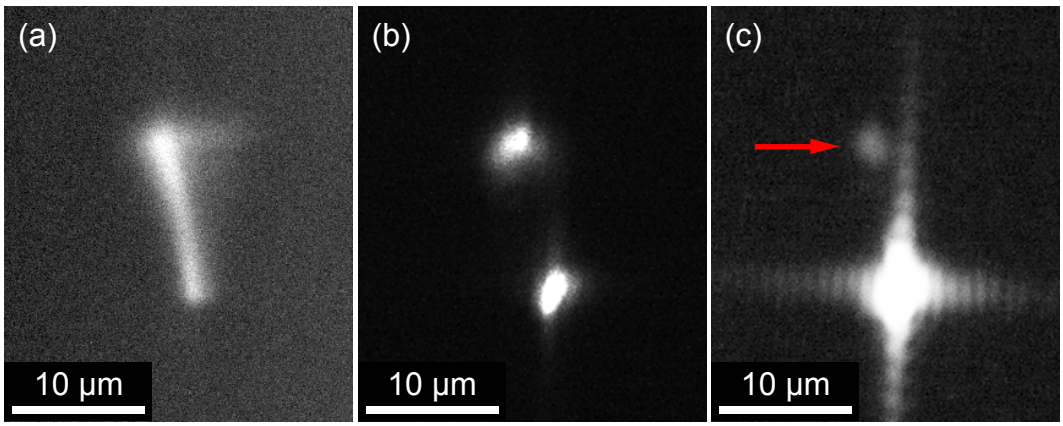

Figure 5.9.: CCD camera images of silver nanowires individually levitated in the Paul trap. Approximately, the wires have a length of 12 µm and a diameter of 120 nm. (a) Scattered white light from the halogen lamp shows the whole wire. (b) White light from the supercontinuum laser, polarized parallel to the long wire axis, is efficiently scattered from the ends. (c) White laser light focused onto the lower end excites propagating surface plasmon polaritons (SPPs), scattering out at the upper end of the nanowire (indicated by the arrow). From [225].

the nanowires. In the trap, nanowires can be distinguished from other particles very easily by their scattering behavior. Due to the elongated geometry, they scatter light anisotropically in the directions of the long and the short wire axes. Thus, trapped wires, slightly oscillating in the laser beam, show a blinking behavior, unlike rather spherical particles. This blinking indicates promising particles, which are then observed with the CCD camera. In figure 5.9(a) a 12 µm-long silver nanowire can be seen via scattered white light from the halogen lamp. The stabilized nanowires tend to align in the vertical direction due to gravity and the axial trap potentials, but horizontally oriented nanowires are also observed in the trap. When white light from the supercontinuum laser, polarized parallel to the long wire axis, is directed from the side onto a levitated nanowire, the two ends are visible via a strong scattering intensity, as shown in figure 5.9(b). The laser light is coupled to SPP modes by scattering at the wire ends [248]. Such surface plasmons propagate along the wire and are partially scattered into light again at the opposite ends. Between the ends no light is emitted from the wire, as the propagating surface plasmon modes only couple to the far-field at discontinuities in the wire. The ability of the plasmonic nanowire to guide light is directly proven in figure 5.9(c). Laser light from the supercontinuum laser is focused only onto the lower end through the microscope objective. The excited surface plasmons propagate to the upper end of the nanowire, where they are scattered out. This can be seen from the light originating from this point. When the laser is focused onto the wire at a position between the two ends, no light emission is observed, in contrast.

For a more detailed analysis, the spectral properties of the guided light are investigated. In figure 5.10(a) the spectrum of the light scattered from the upper end of a 12 µm long levitated wire is shown. Only the lower end is excited by white laser light, polarized parallel to the wire and focused by the microscope objective in this transmission experiment. The situation is similar to figure 5.9(c), but with the detection pinhole adjusted to the upper end of the wire. The spectrum clearly shows a pronounced peak structure, that can be explained by surface plasmon cavity modes in the wire, similar to standing waves in a

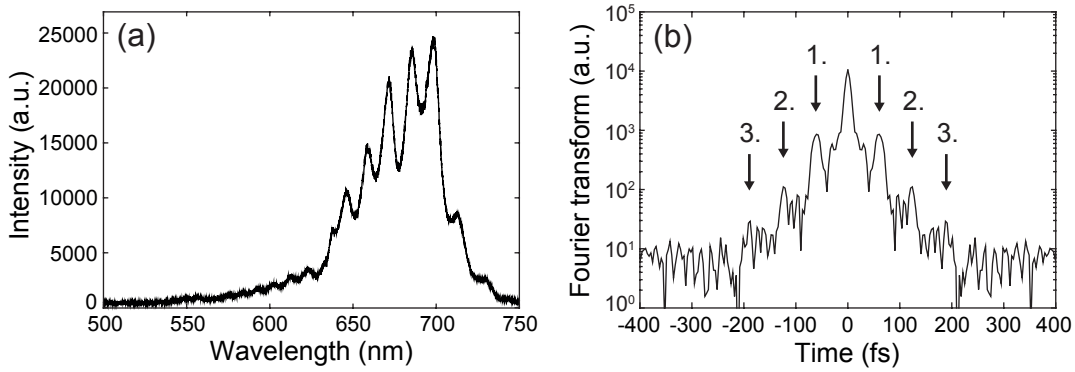

Figure 5.10.: Analysis of a trapped silver nanowire with a length of 12 µm. (a) Scattering spectrum obtained with the detection pinhole adjusted to the upper end, while white excitation light is focused only onto the lower end. (b) Discrete Fourier transform of the spectrum shown in (a) converted to time differences. Three round trips can be recognized.

Fabry-Pérot resonator [116]. The excited surface plasmons are not completely scattered into light at the opposing end. Some of them are reflected and propagate back to the input end of the wire, where they are again partially reflected. More than one roundtrip is possible, limited by the propagation loss A and the reflectivity of the wire end faces R. The large linewidths of the peaks indicate a low quality factor of the plasmon Fabry-Pérot resonator due to high losses. If the propagation length is long enough, standing surface plasmon waves are produced along the wire, when the wire length is an integer multiple of half the surface plasmon wavelength. To characterize the overall loss in this cavity, a discrete Fourier transformation of the scattering spectrum is applied in figure 5.10(b), in analogy to the analysis of Fabry-Pérot resonators [249]. This analysis draws information from the overall shape of the peaks and not only from their width and separation. The first three sidebands can be identified in the Fourier transform, which correspond to one, two and three roundtrips of the surface plasmon in the resonator, respectively. The amplitude ratio of the adjacent harmonics r_h is related to the resonator losses by [249]

$$r_h = RA = Re^{-\frac{l}{L}}, \tag{5.1}$$

where l is the length of the nanowire and L is the surface plasmon propagation length. For the shown spectrum r_h is 0.13. This value is compared to the roundtrip loss $r_m = RA$ deduced from the relative modulation depth of the spectrum [116]

$$\frac{\Delta I}{I_{min}} = \frac{I_{max} - I_{min}}{I_{min}} = \frac{4r_m}{(1 - r_m)^2}. \tag{5.2}$$

It is obtained at a certain spectral position from the interpolated values of the local intensity minimum I_{min} and maximum I_{max}. For a wavelength of 685 nm, a relative modulation depth of $\frac{\Delta I}{I_{min}} = 0.53$ is estimated, which results in a value of $r_m = 0.11$ for the product of the losses derived from the relative modulation depth. Both values r_h and r_m are in good agreement, in particular, when taking the strong variation of the modulation depth in figure 5.10(a) into account. Similar results are reported for experiments with silver nanowires on substrates [250, 251].

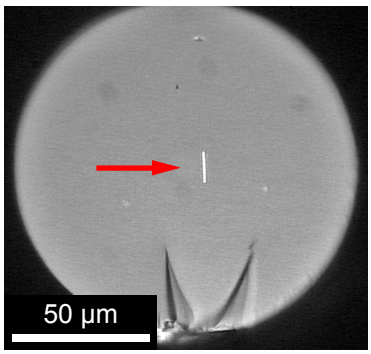

Figure 5.11.: Optical microscope image of the silver nanowire from figure 5.10 deposited on a cleaved fiber facet. The arrow points to the nanowire. From [225].

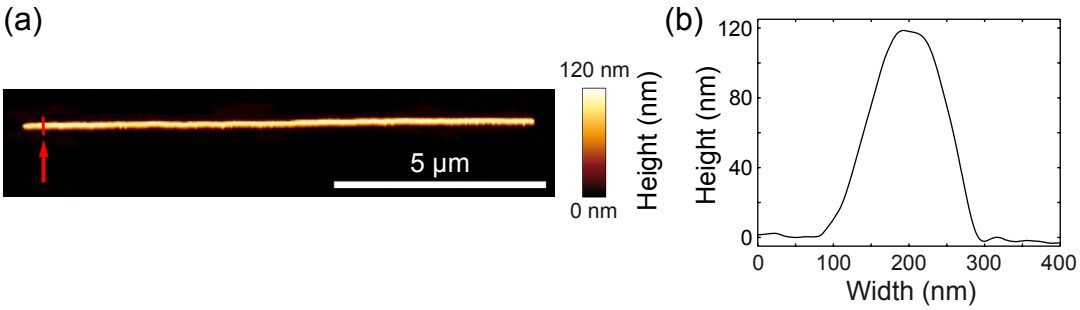

Figure 5.12.: AFM image of the deposited silver nanowire with a length of 12 µm. (a) Measured height image. (b) Height cross section measured with a higher resolution along the red line in (a). The diameter of the nanowire is approximately 120 nm. From [225].

To measure its exact size, the nanowire is deposited on the cleaved facet of an optical fiber, as explained in section 4.6.5. The optical microscope image in figure 5.11 shows a fiber facet with the deposited silver nanowire. The length of the nanowire is measured to be 12 µm. More detailed values, especially for the wire diameter, are obtained from AFM measurements, when the fiber is mounted under the cantilever. In figure 5.12(a) the measured height image of the deposited nanowire can be seen, which confirms the nanowire length of 12 µm. For the wire diameter a value of 120 nm is obtained from the height difference. The cross section measured along the red line with a higher resolution is plotted in figure 5.12(b). Exact knowledge of the diameter allows for further characterization of the cavity losses. As the propagating SPP is not damped by radiation, the propagation length L is assumed to be comparable to 10.1 µm, reported for one experiment with a silver nanowire with a diameter of 110 nm at a wavelength of 785 nm [116]. Using this propagation length and $r_h = 0.11$ in equation (5.1), a reflectivity of the fiber end faces of $R = 0.36$ is obtained, which is higher than the reported value of 0.25 in [116]. However, these results have to be treated with caution. It is difficult to make a direct comparison, as the plasmon propagation length used is obtained from a measurement at a higher wavelength, as well as being based on silver nanowires with a smaller diameter and supported by a substrate.

The spectral distance between the peaks observed in figure 5.10(a) is determined by the phase difference ϕ between the input light and the light scattered from the surface plasmon

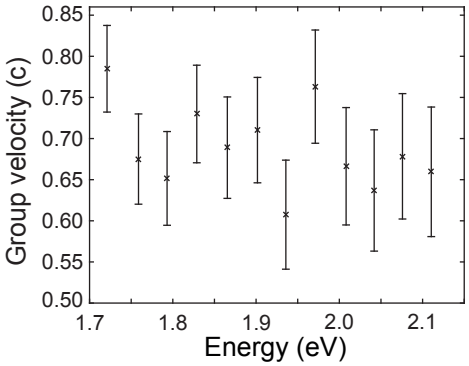

Figure 5.13.: Group velocity of the surface plasmon calculated for selected energies from the spectrum shown in figure 5.10(a).

after one roundtrip in the wire with the wave number k_p. For a scattering maximum the condition

$$\phi = 2lk_p = 2\pi m \tag{5.3}$$

with integer m has to be fulfilled. Then, the group velocity v_g of the surface plasmons can be estimated by

$$v_g = \frac{\partial\omega}{\partial k} \approx \frac{\Delta\omega}{\Delta k} \approx \frac{2lc}{\lambda_0^2}\frac{\Delta\lambda}{\Delta m}. \tag{5.4}$$

For two adjacent maxima ($\Delta m = 1$) at spectral positions λ_1 and λ_2 the group velocity at the center wavelength $\lambda_0 = \frac{1}{2}(\lambda_1 + \lambda_2)$ is given by

$$v_g = 2lc\frac{\Delta\lambda}{\lambda_0^2}. \tag{5.5}$$

For the 12 µm silver nanowire the group velocities are calculated and shown in figure 5.13. A group velocity of $0.69 \times c$ in terms of the vacuum speed of light c averaged over the spectral region in figure 5.13 is in good agreement with other reported experimental and theoretical values [250].

The trap setup allows characterization of several different particles within a short time. Silver nanowires with lengths from 9 µm to 25 µm are observed in the trap. In figure 5.14(a) the scattering spectra obtained from a silver nanowire with a length of 16 µm are shown. In this case, excitation occurs with white laser light from the side weakly focused onto the whole wire with linear polarization parallel to the long wire axis. The configuration is similar to the situation in figure 5.9(b). Determined by the pinhole position, either light scattered from the upper (black curve) or the lower end (red curve) can be detected. At both ends, the familiar interference fringes are visible in the spectrum, but, compared to figure 5.10(a), the separation of the maxima is smaller due to the longer wire length. A phase shift between the two spectra obtained from the opposing ends is observable, which is more obvious in the zoom into the region from 650 nm to 700 nm in figure 5.14(b). Since both wire ends are excited, several effects may contribute to the measured signals, in contrast to figure 5.10(a). The light stemming from surface plasmon cavity modes may

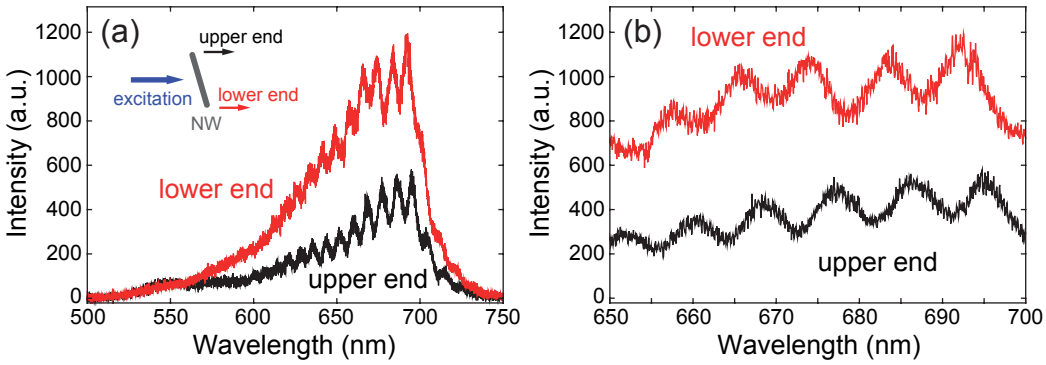

Figure 5.14.: Scattering spectra from the upper (black curve) and the lower end (red curve) of a trapped silver nanowire with a length of 16 µm. White laser light excitation occurs onto the whole wire from the side. (a) The intensity maxima and minima, observed at both ends, are phase-shifted. The schematic shows the labeling of the ends. (b) Zoom into the region from 650 nm to 700 nm of the same spectrum as in (a). From [225].

interfere with directly scattered excitation light and light, coupled into the opposite end and guided along the wire. For a plasmon Fabry-Pérot resonator excited only at one side, intensity maxima measured at one end would be expected to correspond to minima measured at the other end and vice versa [116].

Finally, scattering spectra collected from the lower end are shown in figure 5.15, taken under the same conditions as in figure 5.14, but for two different linear polarization directions of the excitation light. The red curve is obtained for excitation light with vertical polarization, parallel to the wire. The spectrum shows the characteristic peaks as before. This situation changes completely when the incident light is polarized in horizontal orientation, perpendicular to the nanowire. Only a weak signal can be recognized, resembling the general shape of the lamp spectrum but without significant modulations. This is a further verification of the plasmonic nature of the scattering signal [116, 250]. Light with a polarization axis that is perpendicular to the long nanowire axis cannot excite the propagating SPPs efficiently, due to the perpendicular wave vectors.

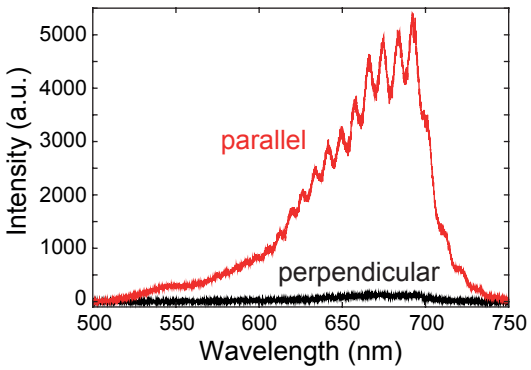

Figure 5.15.: Scattering spectra from the lower end of the trapped silver nanowire shown in figure 5.14 for different polarization excitations. The white laser light is focused onto the whole wire from the side with linear polarization oriented parallel (red curve) and perpendicular (black curve) to the long wire axis. From [225].

5.2.4. Conclusion

Stabilization of individual silver nanowires in the Paul trap indicates the potential of the microscopy setup built in this thesis. The high amount of surface charge applied by the electrospray ionization seems to have no drastic influence on the plasmonic properties, as the observed scattering characteristics are in good agreement with similar experiments on supported nanowires [116, 251]. The pronounced peak structures in the scattering spectra are interpreted as Fabry-Pérot resonances in the metal cavities in accordance with other works [116, 250].

In future experiments, scattering properties of levitated and subsequently deposited nanowires can be compared to theoretical simulations in order to investigate the influence of the substrate. For exact analysis of the surface plasmon propagation length and the reflectivity of the wire ends, several wires with the same length and diameter should be analyzed. The setup can also be used to place preselected nanowires on other photonic structures. Furthermore, an additional dipole trap can be included for polarization-dependent manipulation of the levitated nanowires [245], to improve the accuracy of the measurements and the deposition technique. Optomechanical experiments with rotational and torsional motions can be envisioned [252–254], as well as thermodynamic experiments [40, 255, 256], and even plasmomechanical experiments [257].

Waveguiding of surface plasmon propagation is not restricted to nanowires made of silver. For instance, it is also demonstrated for gold [258, 259]. In contrast to silver, gold does not suffer from oxidation under ambient conditions. However, silver nanowires show lower absorption losses, causing higher propagation length than gold nanowires, which is crucial for efficient transport of signals [260]. At longer wavelengths the losses decrease, but silver always shows lower damping [113]. To protect levitated silver nanowires against oxidation during longterm investigation, the vacuum chamber can be evacuated or filled with an inert gas to prevent oxidation.

5.3. Functionalization of Tapered Optical Fibers

Trapped particles can be deposited onto other structures for further particle analysis but also for functionalization of photonic components. It is a very flexible non-contact method to bring together arbitrary particles, characterized and pre-selected in the trap, and (fragile) photonic structures. Two different targets made of optical fibers are used in this thesis: tapered optical fibers and cleaved fiber facets. This section describes the experiments performed with tapered fibers in detail. Particle deposition on fiber facets is explained in section 4.6.5 and demonstrated in sections 5.1, 5.2 and 5.4. Some of the results presented in this section are published in Optics Express [226].

5.3.1. Introduction

Tapered optical fibers are fibers containing a region with submicron diameter, which show a strong confinement of the supported modes. In the tapered region, a significant fraction of the transmitted light is guided outside the fiber in the evanescent field [261]. The interaction between the evanescent field of the taper and the surrounding medium is used in many different applications, like sensing [262, 263], spectroscopy [264], interferometry [265], mode-filtering [266] and even trapping and moving of particles [267]. For sensing

applications, variations in the refractive index of the surrounding material can be detected by changes in the guided modes through the fiber [268]. This is done by application of sensitive material layers on the taper surface [262], or by bringing sample particles into the evanescent field [269]. The same method is used for spectroscopy of emitter ensembles [264] and even single photon emitters [270]. Tapered optical fibers are also used to couple light to optical microcavities [10]. Such resonators can be realized with different geometries, like spheres, discs or toroids. They show interesting optical properties, like a high optical quality and a strong confinement of the optical modes, which make them very useful for sensing applications [36] as well as for studying nonlinear effects [271] or cavity quantum electrodynamic (CQED) experiments [272].

In most of the mentioned methods the taper has to be aligned very carefully with respect to the sample or the cavity. Also, mechanical stress is often applied to the fragile fiber when sample particles are brought in contact with the taper [270, 273]. In the following, a novel method for functionalization of tapered optical fibers is described. Levitated particles are optically characterized and pre-selected in the Paul trap. Afterwards, deposition of individual particles on the tapered region of an optical fiber is achieved by making use of electrostatic attraction between the surface charges of the particle and the fiber. This technique is demonstrated by placing micron-sized active emitter particles as well as spherical microresonators onto tapered optical fibers.

5.3.2. Taper Production

To achieve guiding of light in the evanescent field outside of an optical fiber, the fiber has to be thinned down to waist diameters below 1 µm. Such tapered fibers are produced from standard optical fibers by heating up a section and pulling the ends apart [274]. During the elongation of the fiber the heated section is thinned down to the desired diameter, as illustrated in figure 5.16(a). Different methods are used to heat the fiber. Most common are laser- and flame heating [274, 275], but also ceramic heaters can be involved [276], as used to produce the tapers for the experiments presented in this section. With such methods, low loss tapers can be obtained [277]. It is even possible to thin down microstructured optical fibers, in order to produce nanofibers that are insensitive to the environment for very small photonic circuits [278].

A schematic of the fiber-drawing setup is shown in figure 5.16(b). The optical fiber is clamped onto two linearly aligned translation stages. Between the stages is an electric ceramic heater, which encloses the fiber (except for a small slit) over a length of 19 mm, but can be retracted to remove the fiber. The heater increases the temperature of the fiber homogeneously up to 1500 °C to soften the silica. With the linear stages the soft fiber is pulled apart in consecutive steps, while the transmission through the whole fiber is monitored with a laser and a photodiode, to observe the fiber drawing progress. An additional microscope is used to characterize the final result. Typically, tapered optical fibers with waist diameters of 0.7 to 1.2 µm over a length of 4 to 10 mm are produced. More details of the tapered fiber production can be found in [279]. After the fiber drawing procedure, the fragile fiber is glued onto a U-shaped holder to reduce the risk of breaking. The photograph in figure 5.17 shows the taper holder attached to two linear stages, which are used to align the tapered region of the fiber to the center of the trap.

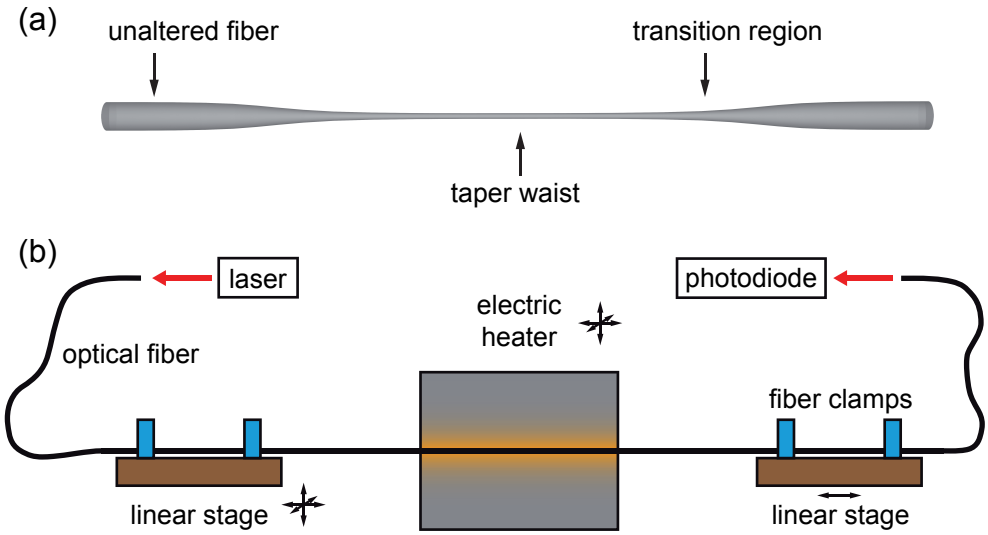

Figure 5.16.: Fabrication of tapered optical fibers. (a) Illustration of a tapered optical fiber. (b) Schematic of the fiber drawing setup.

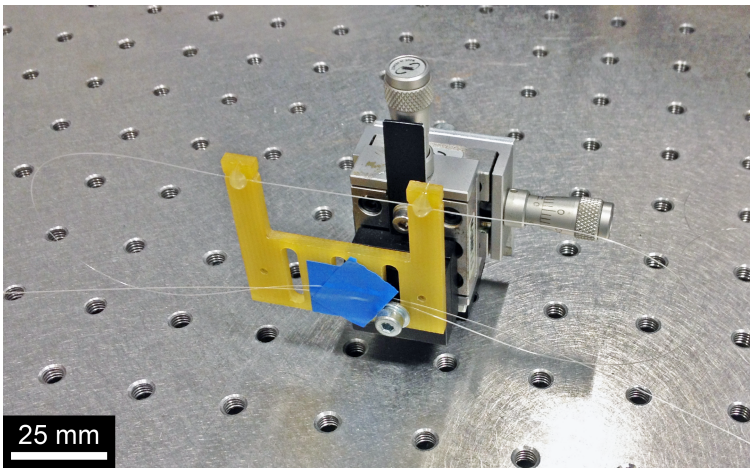

Figure 5.17.: Photograph of the fiber holder attached to two linear stages. The shown fiber is not tapered to clarify its position. The tapered region would be between the two arms of the U-shaped holder.

5.3.3. Deposition Procedure

In addition to the deposition of pre-characterized particles on fiber facets described in section 4.6.5, particles can also be landed on other structures. For instance, tapered optical fibers are used in a similar way, as depicted in figure 5.18. Due to the better physical access, the segmented trap is used here. The fiber can be moved in and out of the trap between the electrodes with a motorized linear stage. To avoid unwanted contamination, the fiber is removed from the trap and the tapered region is covered up during particle injection. Characterization of levitated particles is done with the microscope setup shown in figure 4.21. When a particle is selected for deposition, the uncovered tapered fiber is moved into one end of the trap and the particle is approached to it. In the same way as for the fiber facets, deposition is facilitated by the fact that the fiber is always slightly charged. After the landing, the deposited particle scatters out laser light guided by the fiber, and can also be detected through the fiber by a reduced transmission or, if possible, by a fluorescence signal excited and collected through the fiber. The photographs in figure 5.19 show a silica microsphere with a diameter of 4.8 µm in the trap before and after the deposition onto a tapered optical fiber. The particle is visible by scattering of laser light.

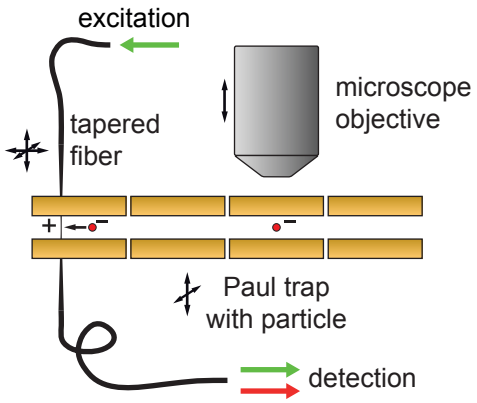

Figure 5.18.: Schematic setup with tapered optical fiber in segmented trap. The full microscope setup is shown in figure 4.21.

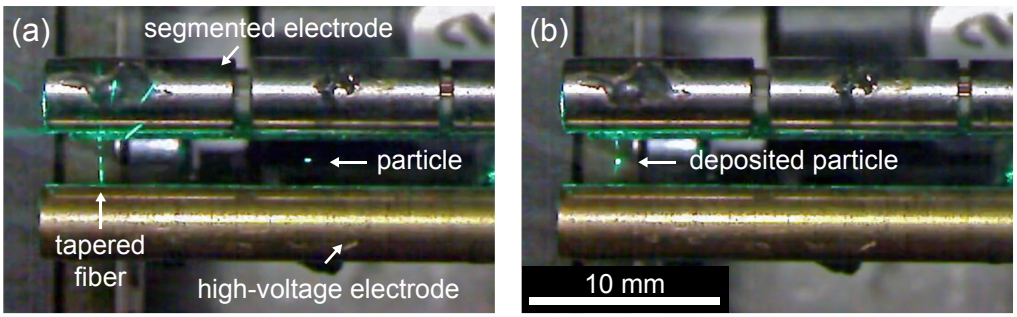

Figure 5.19.: Particle deposition onto a tapered optical fiber demonstrated with a silica microsphere with a diameter of 4.8 µm. (a) The particle and the tapered fiber can be seen by scattering of laser light. The free laser beam is directed along the trap axis. (b) After deposition the particle scatters out laser light guided by the fiber.

5.3.4. Deposition of Dye-Doped Polystyrene Beads

In a first experiment, clusters of polystyrene particles are characterized in the trap and subsequently landed onto the tapered region of an optical fiber. The individual particles have a mean diameter of 100 nm and are doped with a red fluorescent dye (Invitrogen, FluoSpheres carboxylate-modified). The trapped particles are identified by their fluorescence signal, which is excited with the argon-ion laser tuned to 514.5 nm and focused on the particle. The spectrum in figure 5.20(a) shows the detected fluorescence emission of a levitated particle collected by the microscope objective. After deposition the particle can be addressed optically by the fiber. When the laser light is coupled in, the evanescent field in the tapered region excites the particle on the surface. The emitted fluorescence couples partially to the taper modes and is detected through the fiber. The result is shown in figure 5.20(b). The taper has a waist diameter of 700 nm, that allows for a large evanescent field and a good coupling efficiency between the emitter and the optical modes. Clearly, the spectra show the same spectral characteristics and differ only in intensity. Since the excitation laser power is set to 30 µW in both cases, the fluorescence yield for the measurement via the fiber is higher by a factor of 11 compared to the measurement via the microscope objective.

In addition to fluorescence spectroscopy, a landed particle can also be detected by fiber transmission. This is done in a further experiment by coupling laser light into the fiber containing the taper and measuring the output signal with a photodiode. A frequency-doubled ND:YVO_4 laser (Coherent, Verdi V10) with a wavelength of 532 nm is used here. The measured waist diameter of the used taper is 850 nm. As shown in figure 5.21(a), the transmission signal decreases abruptly when the particle is deposited. This corresponds to an increased scattering of the taper modes, that can also be observed from the outside (see figure 5.19(b)). A second drop in transmission can be recognized, indicating the laser switch-off. The deposited particle affects the transmission, which changes to 46 % of the initial value. This indicates that the particle is a cluster of several 100 nm polystyrene beads. A much smaller transmission change of only a few percent would be expected

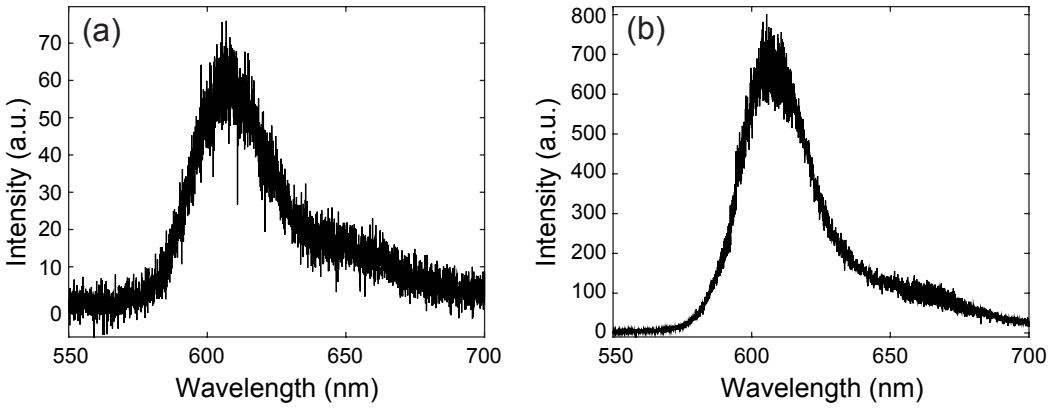

Figure 5.20.: Cluster of dye-doped polystyrene beads (overall diameter 1.5 µm) deposited on a tapered optical fiber. (a) Fluorescence emission spectrum of the particle levitated in the trap, excited and collected through the microscope objective. (b) Fluorescence spectrum of the same particle deposited on the tapered region of the fiber with a diameter of 700 nm, excited and collected through the tapered fiber. The excitation power for (a) and (b) is the same (30 µW). From [226].

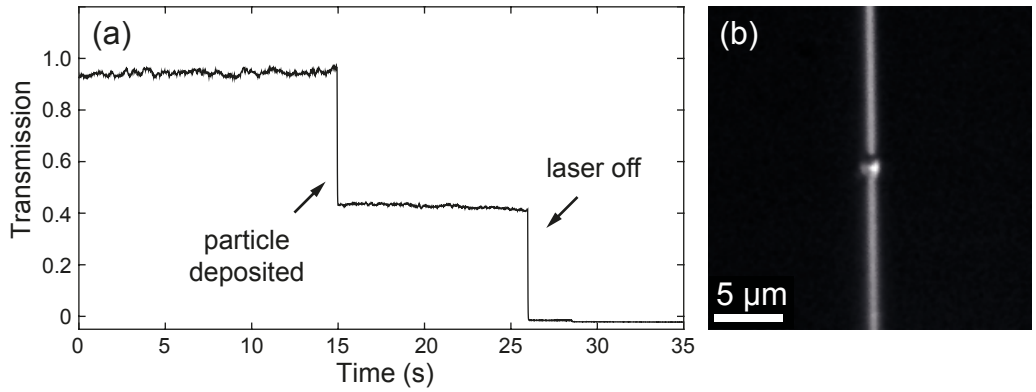

Figure 5.21.: (a) Measured taper transmission at 532 nm, normalized to the transmission before the particle is deposited. (b) Microscope image of the soft-landed cluster of dye-doped polystyrene beads with an estimated overall diameter of 1.5 µm. From [226].

for a single bead [280]. This presumption is confirmed by the optical microscope image in figure 5.21(b) of the cluster particle on the tapered fiber, taken subsequently to the deposition. The particle cluster size is measured to be 1.5 µm.

The measured reduction of the transmission due to the particle deposition is confirmed by FDTD simulations performed by Markus Gregor (AG Nanooptik, Institut für Physik, Humboldt-Universität zu Berlin) [226, 279]. Corresponding to the experimental observations, the problem is modeled with a silica cylinder with a diameter of 850 nm and a length of 100 µm piercing a large polystyrene sphere. The transmission of the fundamental mode (HE_{11} at 532 nm) through the simplified fiber is calculated for different sphere diameters and plotted in figure 5.22. For a sphere diameter of up to 1 µm, corresponding to a thin polystyrene layer of up to 150 nm around the taper, the predicted change in transmission is only a few percent, corresponding to the fraction of the power guided in the evanescent

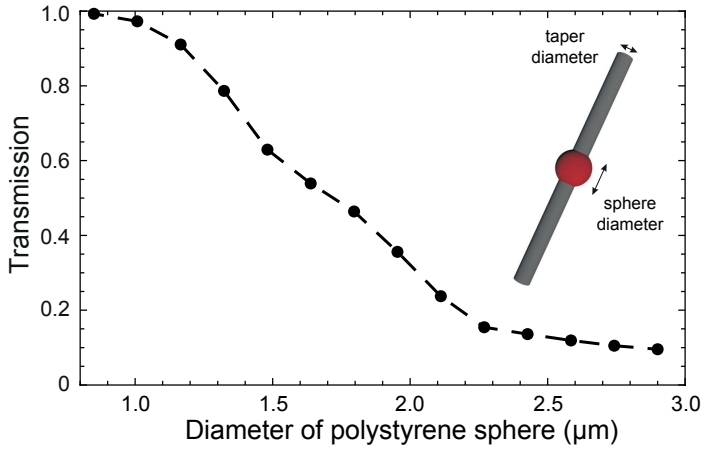

Figure 5.22.: FDTD simulation results of the transmission of the fundamental mode (HE_{11}) at 532 nm through a silica cylinder (diameter 850 nm, length 100 µm) enclosed by a polystyrene sphere with variable diameter. The output is normalized to the input signal. The model geometry is shown in the inset. From [226].

field. For larger sphere diameters the scattering increases and disturbs the waveguide more and more. For a polystyrene sphere with a diameter of 1.5 µm the predicted transmission changes to 61 %. This is in good agreement with the observed value, especially considering the fact that higher modes, which can cause higher losses, and geometrical deviations of the model from reality are not taken into account.

The FDTD simulations are also used to understand the stronger fluorescence signal of the taper compared to the microscope objective (shown in figure 5.20). For the levitated particle, excitation and collection of fluorescence occurs through a microscope objective (Olympus, AchC 4x) with a numerical aperture of 0.1 instead of the one shown in figure 4.21. With this low power microscope objective a focal spot size of 17 µm is estimated, which results in a very low excitation efficiency. A spherical particle with a diameter of 1.5 µm has an overlap of only 0.8 % with this area. In addition, the numerical aperture is also predicting that only 0.25 % of the emission of an arbitrary oriented dipole can be collected [143]. For the taper with a diameter of 700 nm, excitation is even less efficient compared to the microscope objective. About 4 % of the laser power at a wavelength of 514.5 nm is guided outside the taper [281], but the overall transmission through the tapered fiber is measured to be only 6.3 % because of coupling and fiber losses. This gives a resulting excitation power of 0.25 % of the input power, which is roughly three times smaller than the free beam excitation. Despite its lower excitation efficiency, the taper is able to collect the fluorescence emission much more efficiently than the microscope objective. The taper collects approximately 5 % of the total fluorescence of a 1.5 µm dye-doped particle enclosing the fiber [226, 279]. This value is calculated using a FDTD simulation with a model geometry similar to that shown in the inset of figure 5.22. In sum, these numbers already account for a factor of 7 difference between the measurements with the tapered fiber and the microscope objective, which can easily explain the observed factor of 11 with the same order of magnitude.

The deposition procedure can be repeated for several particles on the same taper. In figure 5.23 a fiber is shown with four polystyrene particles placed onto the tapered region. After each deposition, the taper is moved along the direction of the fiber. Otherwise, the subsequent particle could not be approached to the fiber due to the Coulomb repulsion between the similarly charged particles. This repulsion can be used to evenly adjust the

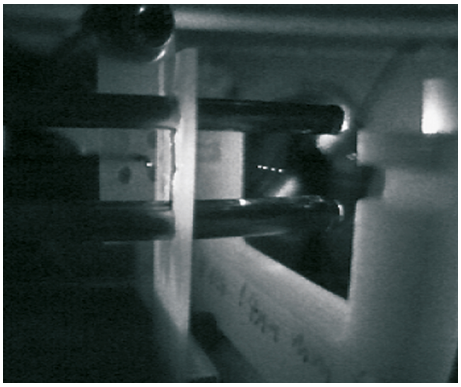

Figure 5.23.: Four particles evenly-spaced on a tapered fiber with an approximated distance of 2 mm. The particles are deposited one after another with an older version of the segmented linear trap. The particles can be seen via scattering of light guided inside the fiber. From [226].

spaces between the deposited particles. The repeated deposition of pre-selected particles on the surface of a tapered optical fiber can be used for the assembly of different particle compositions as demonstrated in the following subsection.

5.3.5. Deposition of Spherical Microresonators

In a second soft-landing experiment silica microspheres are pre-selected and deposited onto a tapered optical fiber. Such dielectric microspheres are optical resonators showing sharp resonances according to the supported whispering-gallery modes (WGM), as explained in section 2.2. Silica microspheres with diameters from 2 to 15 µm (microParticles, various samples) are tested in the trap and identified by white-light scattering. For this, microspheres stabilized in front of the microscope objective are illuminated from the side by unpolarized white light from the halogen lamp (see figure 4.21 for details). The scattered light is collected by the objective and sent to the CCD camera or the spectrometer for detection.

A typical result can be seen in figure 5.24(a) obtained from a single levitated silica microsphere. The overall shape is given by the spectrum of the lamp, but the characteristic peaks of the WGM can be easily recognized, corresponding to TE and TM modes in an alternating sequence with decreasing mode numbers (see section 2.2.1). To determine the actual size of the investigated microsphere, the experimental data is compared to scattering cross sections C_{sca} obtained from Mie theory with equation (2.40) for different sphere sizes. The spectrum in figure 5.24(b) is calculated for a silica microsphere with a diameter of 4.35 µm in air. Regarding the spectral position of the sharp peaks, it corresponds convincingly to the observed spectrum in figure 5.24(a). The overall shape of the theoretical spectrum is given by interference between the incident and the forward scattered light under spectrally uniform illumination [106], and thus, independent from the lamp used in figure 5.24(a).

Before the deposition, the transmission of the used tapered fiber is measured by coupling white light into one end of the fiber, while taking the spectrum of the light coupled out at the other end. In figure 5.24(c) the result can be seen. The white-light transmission signal shows the spectrum of the lamp. The small, sharp recurring dips can be explained by interference of the guided modes inside the taper [275]. Due to the gradual change of the fiber diameter at the transition region (compare figure 5.16(a)), light can couple from the fundamental to higher modes with subsequent interference at the second transition region, in analogy to a Mach-Zehnder interferometer. For reduced mode interference, and thus low energy loss in the taper, the change of the fiber diameter at the transition region should be as small as possible (adiabaticity criterion) [282]. However, the observed dips are small compared to the oscillation of the transmittance introduced by the deposited sphere. The spectrum in figure 5.24(d) shows the white-light transmission through the fiber after the microsphere is placed on the tapered region. The spectral position of the dips correspond to the WGM of the levitated sphere in figure 5.24(a). A microscope image shows the silica microsphere attached to the submicron fiber in figure 5.25.

To explain the observed transmission spectrum, the fiber-microsphere system is described by a simple two-dimensional model [283]. As illustrated in figure 5.26(a), the model consists of a circular cavity coupled to a fiber waveguide. Light guided by the fiber can couple to the resonator and, after one or more round-trips, back to the fiber. When the light in the cavity acquires a phase shift of $2\pi m$, with integer m, it interferes destructively

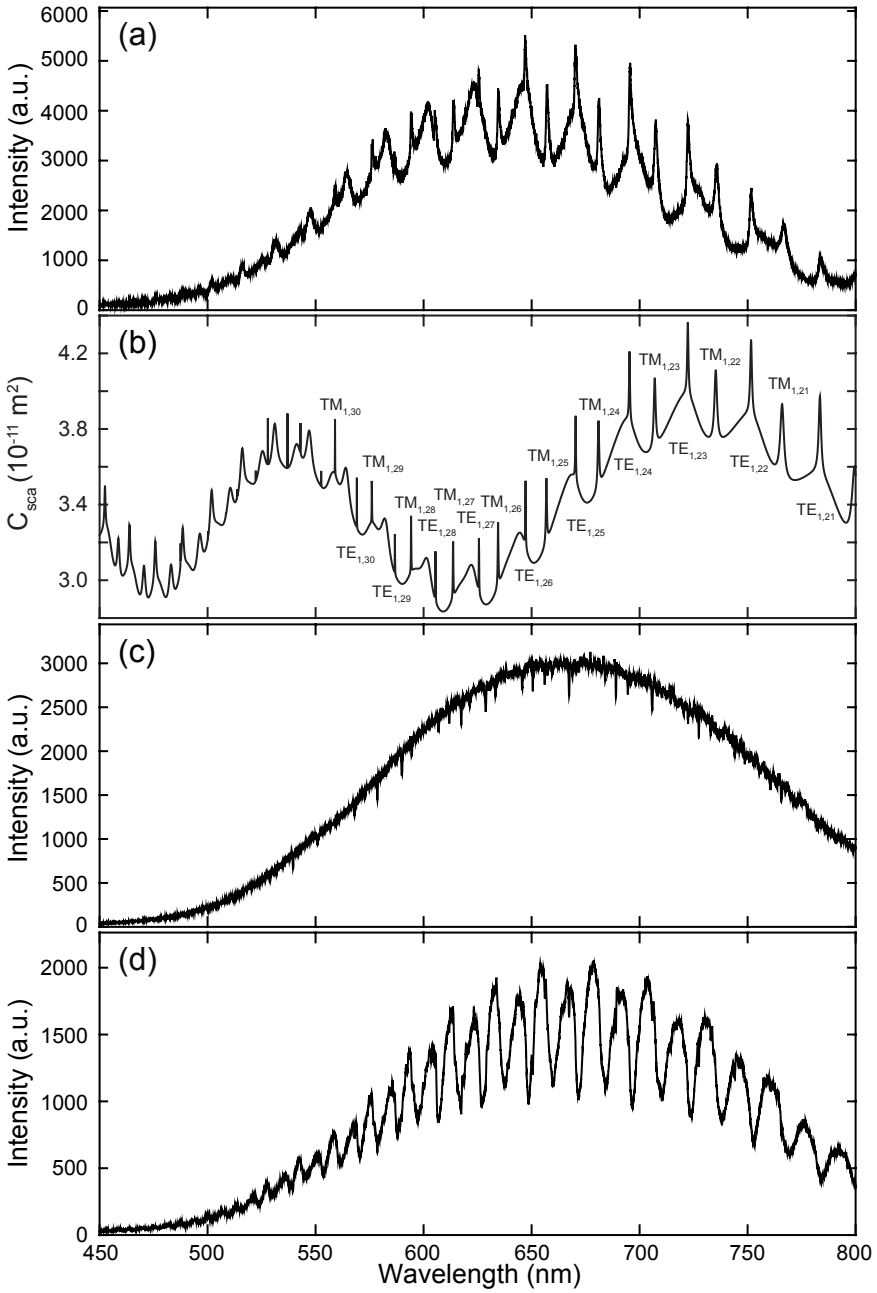

Figure 5.24.: Single silica microsphere deposited on a tapered optical fiber. (a) White-light scattering spectrum of the microsphere levitated in the trap. (b) Mie scattering cross section calculated for a silica sphere in air with a diameter of 4.35 µm. (c) Fiber white-light transmission spectrum before and (d) after deposition of the microsphere on the tapered region.

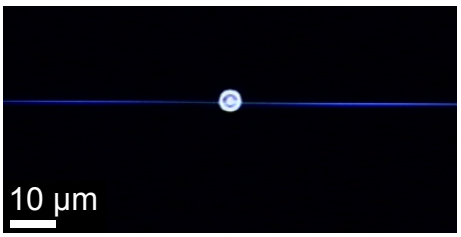

Figure 5.25.: Microscope image of a silica microsphere with a diameter of around 4.35 µm deposited on a tapered optical fiber.

with the light in the waveguide, due to a remaining phase shift of π [284], and extinction can be observed. Just two parameters describe this linear system: the amplitude transmission a, indicating the cavity loss after one round-trip, and the transmission coefficient t through the coupling region. The phase shift $\phi = kL$, denotes the field detuning from the incident field after one round-trip, which is determined by the length $L = 2\pi R$ of the circular cavity with radius R and the wave number $k = \frac{2\pi N}{\lambda}$. The formula for the refractive index N of silica can be found in appendix A.1. Details of the model are given in appendix B. Finally, the intensity transmission through the waveguide is calculated by

$$I_T = \left| \frac{E_{output}}{E_{input}} \right|^2 = \frac{a^2 + t^2 - 2at\cos(\phi)}{1 + a^2t^2 - 2at\cos(\phi)}. \tag{5.6}$$

As the model does not include polarization, it only accounts either for TE or TM modes in the sphere. To reproduce the transmission spectrum of unpolarized white light, the transmission is calculated for TM modes with $\phi = kL$ and TE modes with $\phi = kL + \pi$, individually. Afterwards, the sum of both curves is multiplied by a Gaussian function representing the halogen lamp spectrum (see appendix B.2). The theoretical result is compared to the measured transmission spectrum in figure 5.26(b). One can see that the calculated curve represents the experimental observations very well, especially when taking into account that the coupling of the TE and the TM modes in the sphere to the fundamental mode in the fiber might not be equal. The fit parameters $a = 0.8$ and $t = 0.7$ are used to determine the coupling strength. Critical coupling would be achieved for $a = t$, which means the field coupled back to the waveguide would have the same amplitude but a relative phase shift of π, compared to the incident transmitted field, and the transmission signal would vanish completely. However, here the system is over-coupled, since $a > t$, which is typical for touching resonator-fiber systems [283]. In this case, the light is scattered in and out as opposed to only coupling evanescently. As the losses in the cavity are lower than the coupling losses in the waveguide, the electric field coupled back into the fiber is higher than the transmitted field. Thus, the transmitted intensity is not extinguished completely at the spectral positions of the resonances. For completeness, under-coupling should also be mentioned, where the coupling losses are smaller than the cavity losses ($a < t$). This opposite of over-coupling is typically achieved by a gap between fiber and resonator larger than that needed for critical coupling.

The finesse of the system is given by [180, 283]

$$\mathcal{F} = \frac{\pi}{2}\sqrt{\frac{4at}{(1-at)^2}}, \tag{5.7}$$

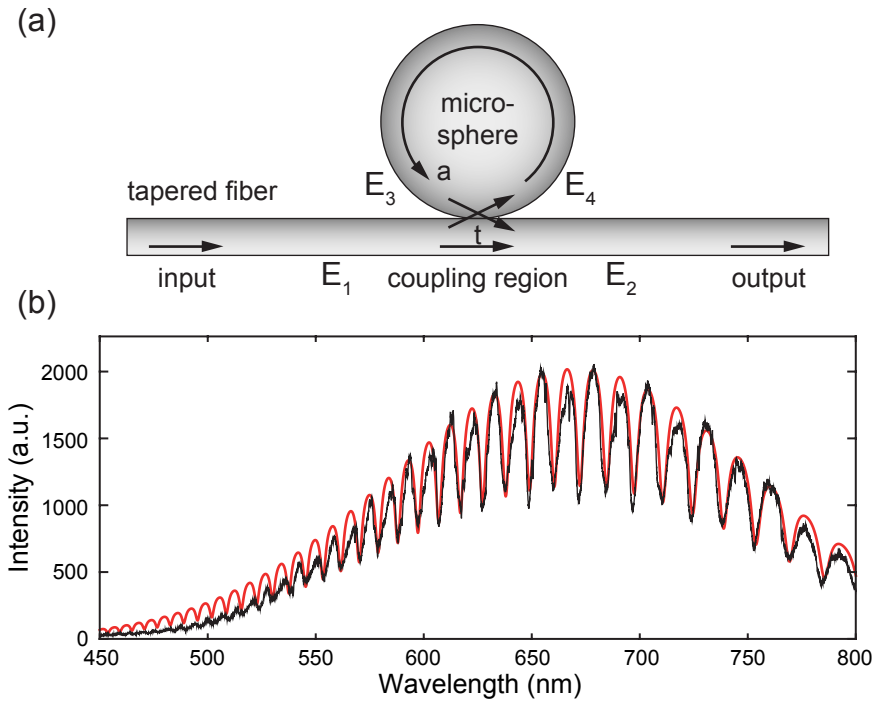

Figure 5.26.: Modeling the fiber-microsphere system. (a) The model geometry consists of a circular cavity coupled to a fiber waveguide. (b) Comparison of the calculated transmission spectrum (red curve) to the experimental observations (black curve). The parameters used are $a = 0.8$, $t = 0.7$ and $R = 2.02\,\mu\text{m}$.

which is determined by the parameters a and t. A finesse of 5.35 is calculated for the coupled fiber-microsphere system. Compared to other systems, this value is very low [10], but comprehensible, when taking over-coupling and the small sphere diameter into account.

One detail that is not considered so far is the size of the sphere. The diameter of the levitated sphere is estimated by Mie theory to be 4.35 µm (see figure 5.24). For the idealized model of the microsphere deposited on the tapered fiber a diameter of 4.04 µm fits best to the observed transmission spectrum. According to the manufacturer (microparticles GmbH) the mean diameter of the spheres in the sample used is 4.6 µm with a standard deviation of approximately 0.2 µm. This includes the Mie diameter of the levitated sphere within two, and the diameter estimated by the coupled cavity model within three, standard deviations. It might be that the size of the levitated sphere is slightly overestimated. Shifts of the WGM resonances are observed, which are attributed to water vapor condensing on the sphere (see section 4.6.6). After the deposition the assumed water film around the sphere would be deformed, changing the effective circumference. Another explanation might be that the sphere is not perfectly spherical and has a prolate or oblate spheroidal geometry [285]. Differently oriented WGM might be excited for the measurements in the trap and through the taper, which would lead to deviations in the calculated sizes. Furthermore, the coupled-cavity model itself might be considered to be too simplistic for an exact quantitative comparison.

As already shown in the previous subsection, more than one particle can be deposited

onto the tapered region of a single fiber. Subsequent to the first one, two more silica microspheres of comparable size are deposited on the the same optical fiber. After each deposition, the tapered fiber is moved by approximately 2 mm along the direction of the fiber, perpendicular to the trap axis. In the white-light transmission spectrum of the fiber shown in figure 5.27(a), a great number of dips can be identified, corresponding to several different WGM in the spheres.

In a third step of the experiment, an active particle consisting of a small cluster of colloidal core-shell quantum dots (Evident Technologies, CdSe/ZnS Core-Shell EviDots) is deposited onto the tapered fiber in line with the three microspheres. The fluorescence emission spectrum of the cluster particle levitated in the trap is shown in figure 5.27(b). According to the product specifications, the single quantum dots have a mean diameter of 4 nm. However, the trapped cluster has an estimated overall diameter of 1 µm. Similarly to the fluorescence detection described in section 5.3.4, the levitated quantum dot cluster is excited with the focused argon-ion laser. The emitted fluorescence light is collected by the microscope objective, long-pass filtered and detected by the CCD camera or the spectrometer. After the deposition of the quantum dot cluster, the active particle is addressed optically through the fiber. The position of the quantum dot particle within the line of positioned particles with respect to the detection direction is important. The quantum dot cluster is at the end of the line of particles and the collected and guided fluorescence can be detected at both fiber ends, independent of the laser input direction. When detection is performed at the end nearest to the quantum dot cluster, where the guided fluorescence light does not pass the microspheres, the fluorescence emission spectrum measured through the fiber looks like the signal of the undisturbed levitated particle. The result is more interesting when the detection direction is reversed. Then, the guided quantum dot fluorescence couples into the WGMs of the microsphere resonators one after another. As expected, the fluorescence signal is modulated by the mode spectrum of the spheres, as shown in figure 5.27(c).

5.3.6. Conclusion

Functionalization of tapered optical fibers by individual pre-selected particles is most promising for several different applications. For spectroscopy, the taper offers a high collection efficiency [286], which can even be doubled by detecting the guided fluorescence light at both ends of the fiber. Further improvement to the efficiency can be achieved, when Bragg mirrors are integrated in the fiber [287]. Tapered fibers used as probes to collect fluorescence from single quantum emitters [270] can be used in quantum information experiments [14,273] or as building blocks in quantum networks [288,289]. The deposition of a pre-selected active particle demonstrates the capability of this method for producing customized fiber-based light sources. Different fluorescent particles can be chosen in order to access different wavelengths and bandwidths.

For sensing, individual optical resonators can be placed onto the tapered optical fiber. Due to over-coupling, the observed quality factors are not as high as reported for critically coupled microresonators [290], but usage of the soft-landing method for the assembly of fiber-based sensors can be envisaged. Larger spheres with higher quality factors can be deposited [36] and critical coupling might be achieved by increasing the cavity losses with an additional probe positioned near the microsphere [283]. Furthermore, by doping the microsphere with fluorescent emitters, fiber-based laser systems can also be built [291].

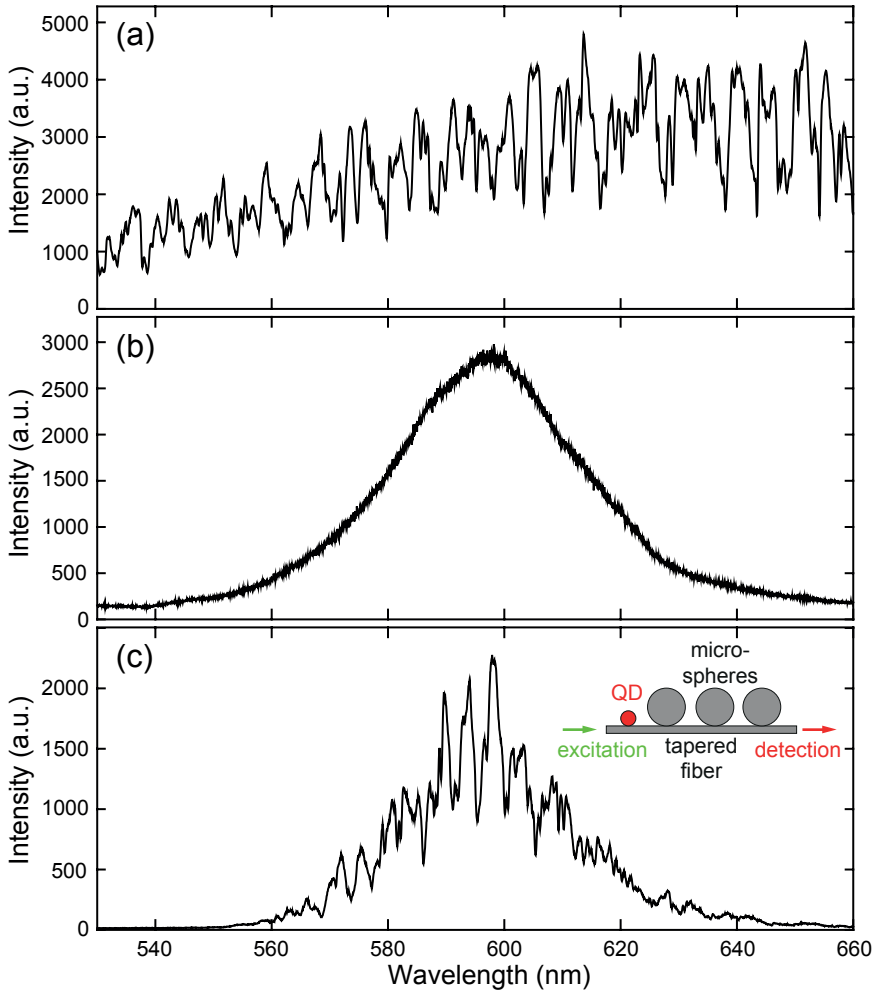

Figure 5.27.: Three microspheres and a quantum dot cluster deposited on a tapered fiber. (a) White-light transmission spectrum of the optical fiber with three silica microspheres deposited on the tapered region. (b) Fluorescence emission spectrum of the quantum dot (QD) cluster levitated in the trap. (c) Fluorescence emission spectrum measured through the fiber after deposition of the emitter particle. The fluorescence from the quantum dot cluster guided through the tapered fiber is modulated by the microspheres. The inset in (c) illustrates the configuration. Detection at the input end of the fiber results in the same spectrum as shown in (b).

When more than one particle is deposited, the Coulomb potentials of the already landed particles guide the subsequent ones. In the future, pre-characterized particles from the trap might be guided by specially designed potentials towards distinguished landing sites, including onto targets other than tapered optical fibers.

The presented technique offers a method for non-contact and alignment-free particle deposition, with reduced risk of taper damage. When the technique is performed in vacuum, contamination of the fiber is prevented, as only pre-selected particles from the trap are able to reach the fiber surface. A success probability of nearly 100 % makes this technique very reliable.

5.4. Particle Coupling in a Segmented Linear Paul Trap

Isolation of individual particles in a Paul trap enables almost interaction-free investigation of their optical properties. Besides deposition on photonic structures, assembly of two or more particles to electromagnetically coupled particle systems also offers a high potential for different applications. In this section, a novel method for one-by-one coupling of single nano- and microparticles is presented. The results presented here are published in Nano Letters [216].

5.4.1. Introduction

Single nano- and microparticles can be assembled into electromagnetically coupled structures enabling a manifold of different applications. Idealized model systems for complex photonic structures can be precisely set up [292], as well as self-similar optical antennas for improved light enhancement and collection [293]. Optically active particles, like single molecules [102], quantum dots [103] and defect centers in nanodiamonds [29] show increased quantum efficiencies when coupled to optical resonator particles, like dielectric microspheres [294] or plasmonic nanoantennas [295].

For precise manipulation, simple fiber probes [296] but more often probes of scanning probe microscopes, like atomic force microscopes (AFM) or near-field scanning optical microscopes (NSOM), are used to push single particles over surfaces or for pick-and-place methods [37]. Such techniques can also be employed to attach individual particles to each other. For suitable outcomes, characterization of the constituent particles and monitoring of the assembly can be done by optical [221] or scanning electron microscopy [292]. For this purpose, the particles are distributed on a substrate, which have to be identified by time-consuming raster scans in order to find appropriate candidates. Additionally, the transfer of particles is complicated, as particles often stick to the probe or to the substrate. In a more simple approach, particles are randomly distributed on a surface, which creates compound particles by chance [297, 298] or by self-organization [38, 299]. A certain degree of control is obtained when optical forces [300] or chemical linking [301, 302] is applied. Such methods lack the possibility to characterize and select individual particles within an ensemble with an inhomogeneous size distribution, which makes them more promising for fabrication on larger scales. Finally, customized particle combinations may be created by lithography [303]. But, these top-down approaches can only be applied to specific materials and the control of coupling is limited by the precision of fabrication.

In this section, a new coupling technique is described. Using the segmented trap, individual levitated particles are optically characterized and subsequently coupled in a fast

and reliable way. The assembly technique relies on electrostatic attraction between the single particles and does not require any further alignment of the particle positions. After assembly, the particles stay in the trap and can be deposited onto other structures for further analysis.

5.4.2. Electrostatic Assembly of Individual Particles

The coupling scheme is carried out in the segmented trap (see section 4.1.2 for details). The segmentation is needed for transport and storage of particles during the assembly, as shown in figure 5.28. In figure 5.28(a) several positively charged particles are injected into the trap by electrospray ionization (see section 4.6.2). They are stored in the far end (right side) of the trap in figure 5.28(b) between repulsive potentials created by neighboring segments. From this stock of particles, a single one is separated and transferred to the segment in the middle of the trap, which is observed by the microscope objective. Optical spectroscopy is used to characterize the particle. After identification of a proper particle, it is stored in a distant segment between the microscope objective and the remaining particles, as shown in figure 5.28(c). Subsequently, negatively charged particles are injected into the trap, which is easily achieved by changing the voltage polarity of the electrospray injector (compare to section 4.5). Particles with opposite polarity are needed, as the coupling scheme relies on electrostatic attraction. More than a single particle should be trapped and stored, but now in the incoming end of the trap. To transfer and align individual particles from the second injection to the microscope focus, the axial voltage has to be switched to negative as well, which is possible during operation without problems. For the previously loaded, positively charged particles, this leads to axial stabilization by attraction to the segments. Identification of the second particle occurs in the same way as the first one. Individual particles are characterized by optical spectroscopy until a fitting candidate is observed (figure 5.28(d)). Preparation of the particle assembly is completed after two particles are selected and transferred to neighboring segments, as illustrated in figure 5.28(e). By switching the segment voltages as shown in figure 5.28(f), the particles are pushed towards each other. When they are close enough, Coulomb attraction due to their opposite charges causes a collision. Usually, the assembled particle compound stays in the trap and can be characterized by optical spectroscopy (see figure 5.28(g)). The resulting charge of such coupled particles is not vanishing in most cases. This allows for adding even more particles, by repeating the steps (a) to (g) with respect to the resulting charge of the prior particle assembly. However, for precise analysis of the final particle compound, it is deposited on other structures (figure 5.28(h)), as presented for single particles in section 4.6.5. All segment potentials and particle charge signs used in the procedure can be inverted if necessary. During the assembly single particles have to be released from the trap when they show unwanted properties concerning material, size or optical characteristics. Before injection of the second particle load this is done by pushing the particle out at the ingoing end, as shown in figure 5.29(a). After the second injection both trap ends are blocked by stored particles and unwanted particles have to be removed in the radial trap direction. For this, the two electrodes of one segment in the middle of the trap can be electrically separated, as illustrated in figure 5.29(b), and an additional static voltage, applied between the two opposing electrodes, creates an electric field perpendicular to the trap axis. When the voltage is high enough to overcome the trap potential, the particle in this segment is released from the trap in the radial direction.

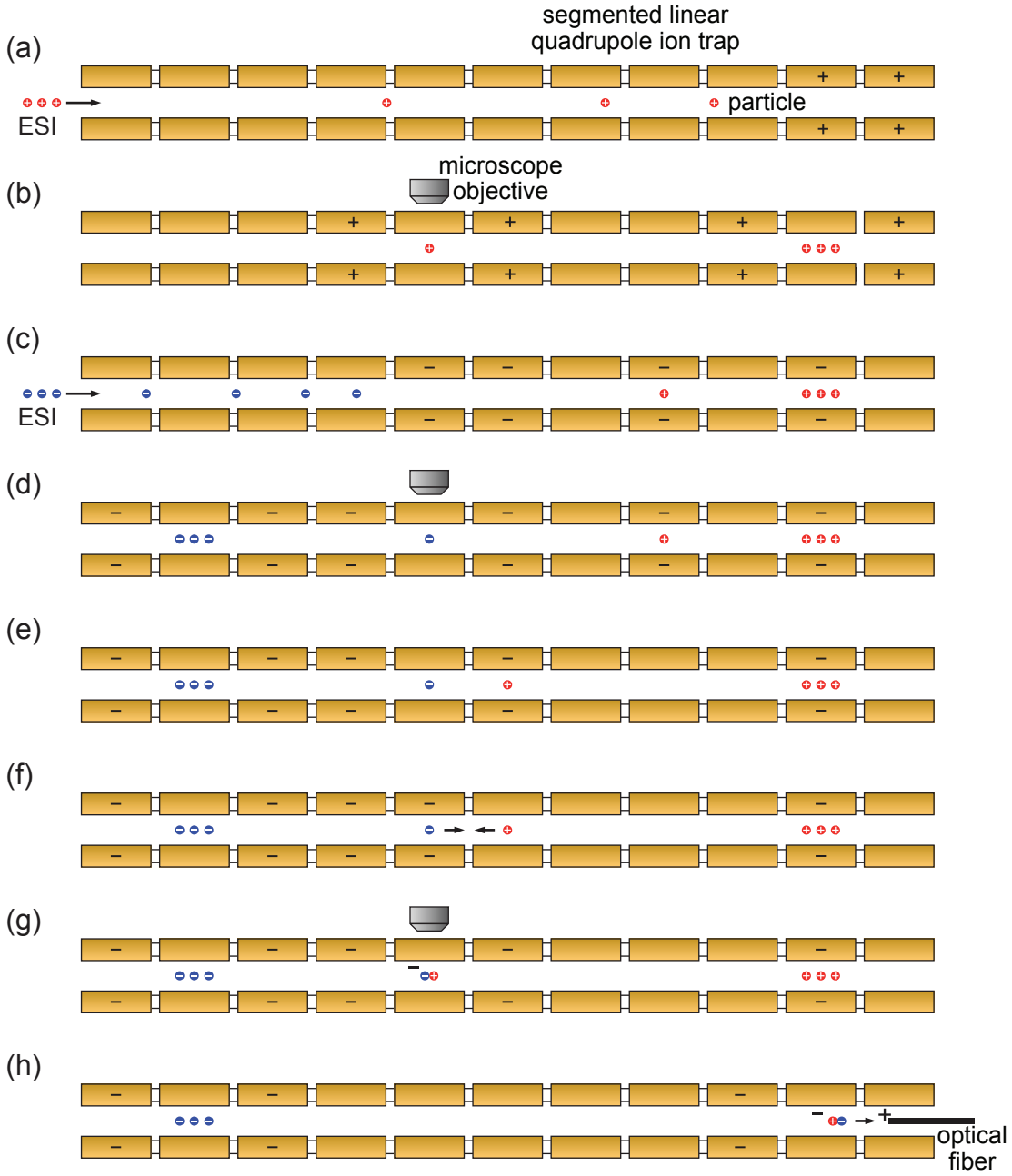

Figure 5.28.: Scheme of the electrostatic particle assembly in a segmented linear Paul trap. (a) Positively charged particles are injected into the trap by electrospray ionization (ESI) and (b) stored in the far end, while a single particle is separated for optical characterization. (c) Switching the polarity of the segment voltages from positive to negative allows for similar injection, storage and (d) characterization of negatively charged particles without losing the positive ones. (e) One particle of each load is selected and axially transferred to the middle of the trap, where (f) they collide due to their opposite charges. (g) The assembled particle compound stays in the trap and can be characterized by optical spectroscopy or (h) deposited on a surface for further analysis. The shown polarities of the particles and the segment potentials can be inverted if necessary.

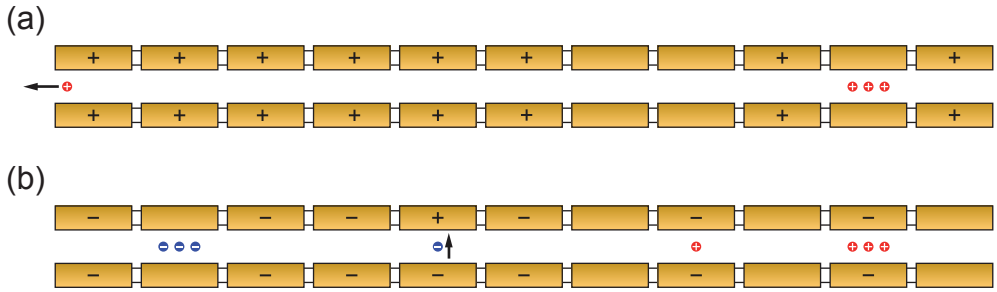

Figure 5.29.: Particle removal from trap. (a) A particle can be pushed out at one end. (b) If both ends are blocked, a particle can be removed in radial direction with an additional static electric field perpendicular to the trap axis.

5.4.3. Stability of Assembled Particle Compounds

The stability of the assembled particle compound can be explained by a simple model. The individual particles before as well as the compound particle after the assembly have to meet the stability requirements for the trap, explained in section 3.1.1. In figure 5.30 the first area of stability is shown (compare to figure 3.3) with exemplified trapping parameters for individual particles. For a random particle P_1 (red dots) with mass M_1 and charge Q_1, operating parameters can always be found to stabilize the particle in the trap. When the particle is confined in a segment without static voltage ($U_z = V_{dc} = 0$), the dimensionless trapping parameter a vanishes, which demands $|q| < q_{max}$ (compare equation (3.18)) for stability. This is the case for P_1 in figure 5.30, corresponding to the positively charged particle held in front of the microscope objective in figure 5.28(b). The particle is confined in axial trap direction through electrostatic repulsion from neighboring segments. When the polarity of the segment voltage is switched, particle P_1 is held by electrostatic attraction, as shown in figure 5.28(c). Now, $V_{dc} \neq 0$ in the segment where the particle is trapped and the particle position P_1^a in the stability chart is shifted to a non-zero value of

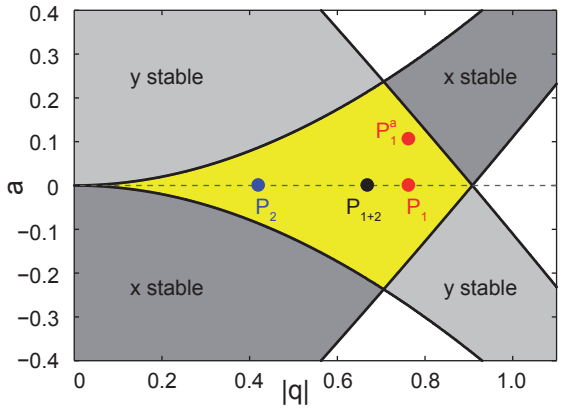

Figure 5.30.: First area of stability for the ideal linear Paul trap. P_1 and P_2 represent two individual particles with opposite charge polarity held in the axial trap direction by static repulsion from neighboring segments ($a = 0$). When a particle is attracted to a segment, the stability conditions change to $a \neq 0$ (P_1^a). After assembly the particle compound is always stable for $a = 0$, if the individual particles were stable before assembly. From [216].

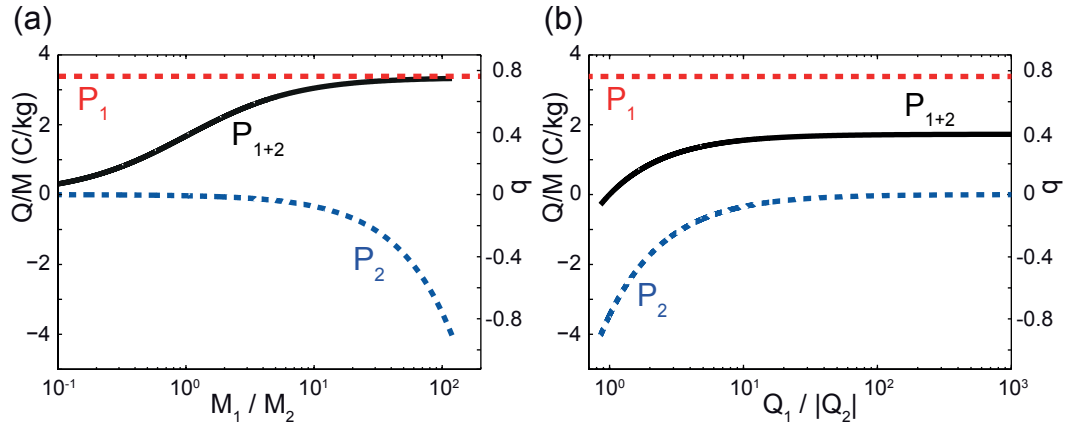

Figure 5.31.: Calculated specific charges for different particle assemblies. The properties of particle P_1 are set to $M_1 = 1.35 \times 10^{-13}\,\mathrm{kg}$ and $Q_1 = 5 \times 10^{-13}\,\mathrm{C}$. Particle P_2 has (a) a fixed charge of $Q_2 = -0.01Q_1$ and a variable mass of $M_2^{min} < M_2 < 10M_1$. In (b) particle P_2 has a fixed mass of $M_2 = M_1$ and a variable charge $Q_2^{min} < Q_2 < 0$. The values of the stability parameter $|q|$ are calculated for typical trap values ($r_0 = 3\,\mathrm{mm}$, $V_{ac} = 1\,\mathrm{kV}$ and $\Omega = 2\pi \times 5\,\mathrm{kHz}$). From [216].

a. The changed interval for stable values of the stability parameter q shows that the static voltage V_{dc} has to be chosen carefully, in order to keep the particle within the stable area. With the same trapping parameters, a second particle with opposite charge polarity can be stabilized, when its specific charge $\frac{Q_2}{M_2}$, with mass M_2 and charge Q_2, meets the stability conditions, indicated by P_2 in figure 5.30 (blue dot). This corresponds to the situation for the negatively charged particle in figure 5.28(d). After assembly, the two particles form a compound particle with mass $M_{1+2} = M_1 + M_2$ and overall charge $Q_{1+2} = Q_1 + Q_2$. It is convenient to set the maximum values $M_{1+2} > M_1, M_2$ and $|Q_{1+2}| < |Q_i|$, with $i = 1, 2$ being the index of the particle with the higher absolute charge value. This means the specific charge of the compound particle $\frac{Q_{1+2}}{M_{1+2}}$, and as a result also the stability parameter $|q|$, always show smaller absolute values than those of particle i, indicated by P_{1+2} (black dot) in figure 5.30. Thus for the case of $a = 0$, the compound particle can always be stabilized with the same operating trap parameters as the individual particles.

In figure 5.31 the resulting calculated specific charges for different initial single particles are shown. The corresponding values for the stability parameter q are obtained for the trap operating parameters $r_0 = 3\,\mathrm{mm}$, $V_{dc} = 0$, $V_{ac} = 1\,\mathrm{kV}$ and $\Omega = 2\pi \times 5\,\mathrm{kHz}$ (see section 3.1 for details). Particle P_1 resembles a positively charged silica microsphere with a diameter of $4.8\,\mu\mathrm{m}$, a mass of $M_1 = 1.45 \times 10^{-13}\,\mathrm{kg}$ and a charge of $Q_1 = 5 \times 10^{-13}\,\mathrm{C}$. Particle P_2 has a negative charge polarity. In figure 5.31(a) particle P_2 has a fixed charge of $Q_2 = -0.01Q_1$ and a variable mass $M_2^{min} < M_2 < 10M_1$. The minimum mass M_2^{min} is determined by the stability condition in equation (3.18). The maximum mass is limited for practical reasons, as in theory, neglecting gravity and spatial particle extension, there is no upper limit for a mass that can be stabilized in an ideal trap (see section 3.1). In figure 5.31(b) the mass of particle P_2 is set to the same mass as particle P_1 ($M_2 = M_1$) and its charge is varied between a minimum charge and zero as $Q_2^{min} < Q_2 < 0$. The minimum charge Q_2^{min} is the negative of the maximum absolute charge value for stable confinement given by equation (3.18). It is obvious that the absolute specific charge of the attached particles is always smaller than that of the particle with the higher absolute

charge. The same is true for the stability parameter $|q|$. Thus, the assembled particle compound is always stable in the trap, when the single particles are stable individually and the combined charges do not vanish completely ($Q_1 + Q_2 \neq 0$).

One should keep in mind, that the static voltage used for axial particle stabilization influences the area of stability and should be kept as low as possible as explained in section 3.1.2. In particular, for small values of q, care has to be taken not to lose the particles.

So far, vacuum conditions are assumed. Buffer gases at higher pressure increase the stable areas and improve stability (see figure 3.5). In this thesis, the traps are operated under atmospheric conditions, which allows for a broad range of specific particle charges to be stabilized at the same time and the same trap parameters.

5.4.4. Coupling of Optically Active Particles to Microresonators

The assembly technique is carried out with silica microspheres and different active particles. During the procedure, the particles are observed from above the trap by scattered laser light, as can be seen in figure 5.32. In the shown case particle 1 is a positively charged silica microsphere with a diameter of 4.8 µm. Particle 2 is a negatively charged cluster of 100 nm polystyrene beads with an overall diameter of around 3 µm. The size of the cluster is chosen to observe both particles with similar scattering intensities. Figure 5.32(a) shows the situation illustrated in figure 5.28(e). The polarity of the segment voltage is negative. In the axial trap direction particle 1 is stabilized by electrostatic attraction to an electrode segment, while particle 2 is held between two segments by electrostatic repulsion. Both particles are identified by fluorescence or scattering spectroscopy. The images in figure 5.32(b) and (c) correspond to figure 5.28(f). Both particles are brought closer together by switching on and off the segments, respectively, that hold both particles in place. Once close enough, the Coulomb attraction leads to an acceleration of both particles towards each other, as can be seen in figure 5.32(c). Eventually, the particles collide and form a compound particle, that stays in the trap. Its resulting charge depends on the initial single particles. In the axial trap direction the compound particle is stabilized by repulsion of neighboring segments, as depicted in figure 5.28(g). This ensures that the stability parameter a is almost zero to avoid particle loss (compare to figure 5.30). For optical analysis, the particle assembly is brought into the microscope focus, as shown in figure 5.32(d). The moment of particle collision can also be seen for two silica microspheres with diameters around 4.8 µm in figure 5.33. The image frame is captured with an exposure time of approximately 30 ms and shows the trajectories of the single particles as well as the assembled compound particle.

The coupling technique is carried out to assemble different particle systems in the trap. Optically active particles attached to spherical microresonators demonstrate the applicability of the method for electromagnetic coupling of small particles. In a first experiment, clusters of commercially available colloidal core-shell quantum dots (Evident Technologies, CdSe/ZnS Core-Shell EviDots) are coupled to silica microspheres (microParticles, silica particles). While the size of a single quantum dot crystal is 4 nm according to the product specifications, clusters of several quantum dots with overall diameters between 100 nm and 2 µm are typically trapped, which is mainly due to agglomeration of quantum dots prior to and during injection. The steps of the particle coupling are shown in figure 5.34. In figure 5.34(a) the measured fluorescence emission spectrum of a quantum dot cluster sta-

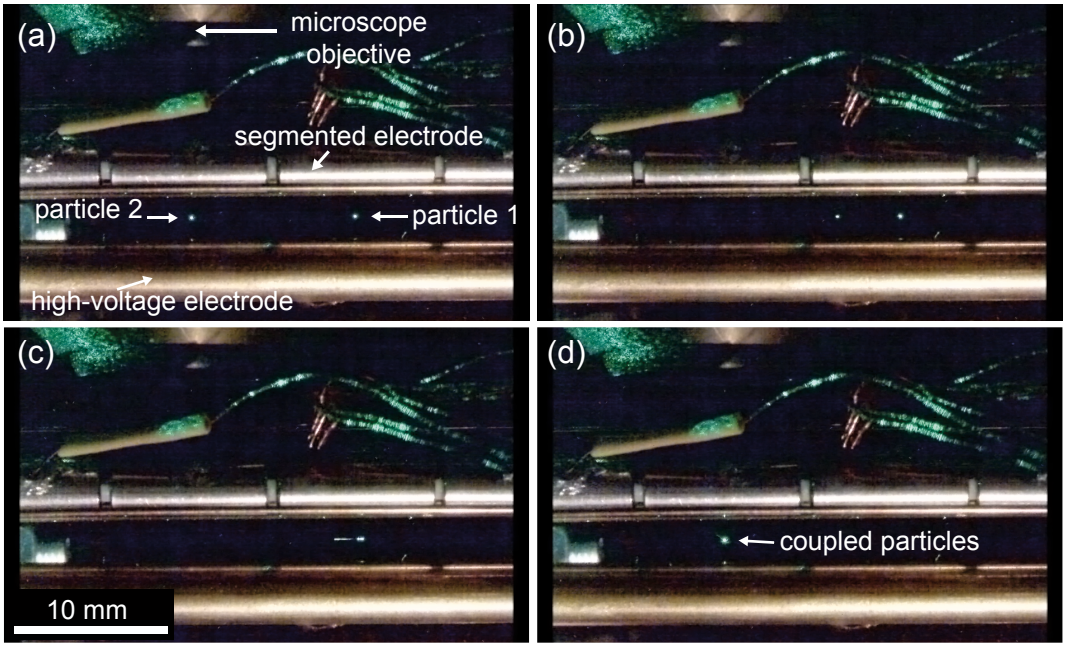

Figure 5.32.: Image sequence of particle assembly in the segmented trap. Both particles can be recognized by scattering of laser light guided along the trap. The microscope objective is used for particle characterization by scattering and fluorescence spectroscopy. (a) Two charged particles with opposite polarity are confined in two adjacent segments. (b) By changing the segment voltages the particles are pushed closer together until (c) they collide due to their Coulomb attraction. (d) The coupled particles stay in the trap and can be further analyzed by optical spectroscopy. The scale bar in (c) refers to all four images. From [216].

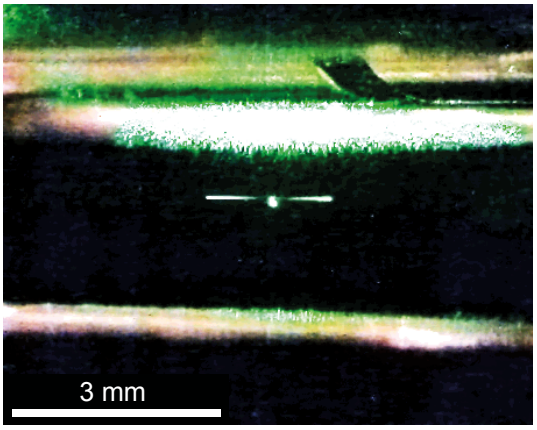

Figure 5.33.: Assembly of two silica microspheres with diameters around 4.8 µm in the trap. The particles are attracted towards each other due to their opposite charges. The exposure time of approximately 30 ms is long enough to show the trajectories of the two particles together with the finally assembled compound particle in one image.

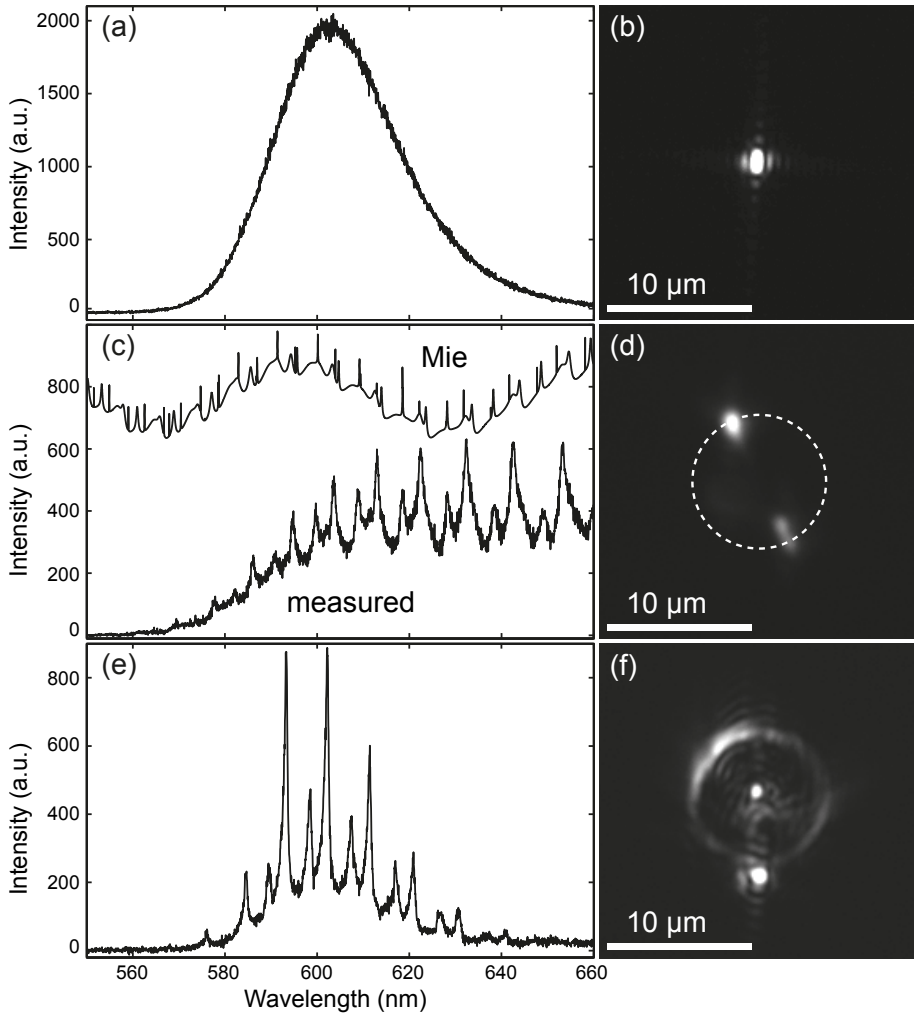

Figure 5.34.: One-by-one characterization and subsequent coupling of a single quantum dots cluster and a silica microsphere in the segmented trap. (a) Fluorescence emission spectrum of the submicron quantum dot cluster. (b) Image of laser light scattered by the cluster. (c) Measured and calculated white-light scattering spectra of the microsphere with an estimated diameter of 8.81 µm. (d) Image of the microsphere under dark-field illumination. Incident white light from the upper left is coupled to counterpropagating WGM. The white dashed ring indicates the position of the sphere. (e) Fluorescence emission spectrum of the assembled compound particle. Modulation of quantum dot fluorescence occurs through WGM of the microsphere. (f) Fluorescence image of the compound particle. The quantum dot cluster sits below the microsphere. Measured spectra are corrected for background light obtained from the empty trap. From [216].

bilized in the trap can be seen. The emission is centered around 600 nm with a full width at half-maximum (FWHM) of 30 nm. Excitation occurs from the side with the argon-ion laser at a wavelength of 514.5 nm (see figure 4.21 for details of the optical setup). The diameter of the cluster particle is estimated to be below 1 µm from the image of scattered laser light in figure 5.34(b). After characterization of the quantum dot cluster, a single silica microsphere is trapped and positioned in the focus of the microscope objective. The scattering spectrum measured under dark-field illumination with white light from the halogen lamp is shown in figure 5.34(c). By comparison of the spectral positions of the WGM resonances in the measured spectrum to calculated Mie spectra (see section 2.1.3), the size of the sphere is estimated, as already done in section 5.3.5. The best agreement is achieved for a theoretical diameter of the silica sphere of 8.81 µm. In figure 5.34(d) an image of the scattering light of the same sphere can be seen. Coming from the upper left, the light excites counterpropagating modes in the sphere, which can be observed at the two bright spots. At these points the light guided inside the sphere is partly scattered out towards the detection path. After assembly, both particles stick together and remain in the trap. The resulting charge polarity is equal to that of the initial single sphere. The electromagnetic coupling of the two particles is proven by the fluorescence emission spectrum obtained under excitation with the argon-ion laser in figure 5.34(e). The fluorescence emitted by the quantum dots is coupled into the WGM of the microsphere and eventually scatters into the microscope objective. Similarly to the single sphere illuminated by white light, the coupled system shows sharp peaks with the same spectral distances, but with the important difference that the overall shape of the spectrum is given by the spectral emission of the quantum dot cluster. The quantum dot cluster attached to the microsphere can clearly be identified in the image in figure 5.34(f), showing the fluorescence emission of the compound particle system under laser excitation.

To detect the fluorescence emission modulated by the sphere, spatial filtering of the collected light is needed, as the quantum dot cluster emits in all directions. The sketch in figure 5.35 illustrates the detection scheme. While the laser beam illuminates both particles, only fluorescence guided by the microsphere and scattered from that part of the sphere opposite to the emitter is detected. Light emitted to free space is blocked by a pinhole.

In another experiment, an active nanoparticle containing organic emitters (Invitrogen, FluoSpheres carboxylate-modified) is coupled to a smaller spherical microresonator (microParticles, silica particles). In figure 5.36(a) the fluorescence emission spectrum of a

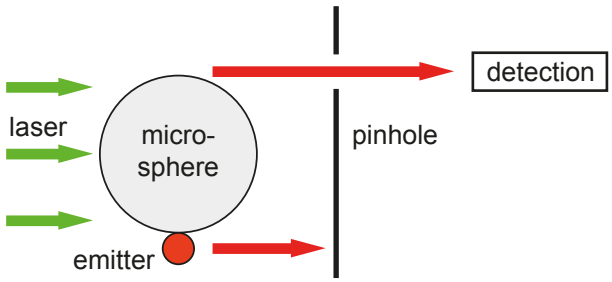

Figure 5.35.: Resonance detection scheme. Only emitter fluorescence guided by the microsphere is detected. The brighter emission to free space is spatially filtered out by the pinhole. Adapted from [216].

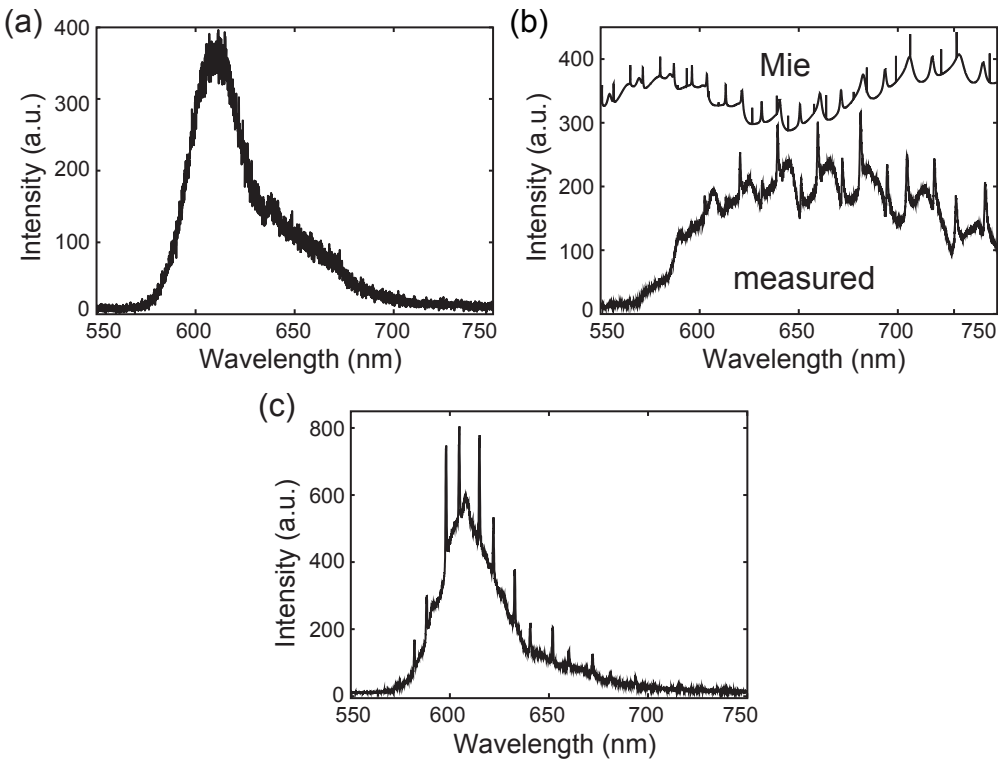

Figure 5.36.: One-by-one characterization and subsequent coupling of a single dye-doped polystyrene bead and a single microsphere in the linear trap. (a) Fluorescence emission spectrum measured on the 100 nm polystyrene bead containing red fluorescent molecules. (b) Measured white-light scattering spectrum of the silica microsphere with a diameter of 4.64 µm. The size is estimated by comparison to the theoretical scattering spectrum calculated by Mie theory. (c) Fluorescence emission spectrum of the levitated compound particle measured under laser excitation after assembly. Measured spectra are corrected for background light obtained from the empty trap. From [216].

levitated, dye-doped polystyrene bead with a diameter of 100 nm is shown. Similarly to the previous experiment, the silica microsphere is characterized by dark-field spectroscopy, after characterizing the fluorescent bead. The scattering spectrum measured under white-light excitation can be seen in figure 5.36(b). Comparison to calculated Mie scattering spectra results in an estimated diameter for the silica sphere of 4.64 µm. After assembly, electromagnetic coupling can be seen from the fluorescence emission spectrum in figure 5.36(c), by applying the detection scheme explained in figure 5.35. Again, the emitter fluorescence is modulated by the WGM of the spherical microresonator.

Almost all of the assembled particle compounds stay in the trap. They fulfill the same stability conditions as the initial single particles, as explained in section 5.4.3. In all coupling experiments done for this thesis, only a small fraction ($< 1\,\%$) failed due to particle loss. In such rare cases the resulting absolute charge value is believed to have been too small for stable confinement under the used trap parameters. With a fraction of cases ($< 5\,\%$) it happens more often that the particles collide but do not remain attached. After the contact they are again separated in the trap but repulsion between them is

observed. This can only be explained by a charge transfer during the contact, resulting in the same charge polarity on both particles.

Apart from being reliable, particle assembly in the segmented trap it is also very fast. Several particle compounds per hour can be produced, including characterization prior to and after the assembly, as well as deposition. Other selective assembly methods [37] do not reach such a high throughput. With the particles lined up in the trap, there is no need for time-consuming scans of a substrate. Additionally, the assembly is self-organizing and requires no further alignment. In contrast, random assembly methods can be even faster, but lack the flexibility to characterize and select individual particles. For instance, within an ensemble with inhomogeneous size distribution this capability is indispensable.

The assembly technique is not limited to a specific kind of particle ensemble. It can be applied to all particles that can be stabilized at the same time in the segmented trap. This is most convincing for particles with similar masses. In figure 5.37(a) two silica microspheres with diameters around 4.8 µm can be seen. After characterization they are combined and stay in the trap. A similar result for two differently-sized silica microspheres is shown in figure 5.37(b). It is even possible to attach further particles to the particle compound. In figure 5.37(c) three silica microspheres with diameters of around 4.8 µm are shown. The microspheres are trapped and characterized individually. After the assembly of the first two spheres, the third one is added by choosing the control voltages with respect to the overall charge of the two-sphere compound. The self-aligned linear structure of the three attached spheres demonstrates that the initial charges partially remain on the surface of each particle. While the third particle is attracted to the sphere with opposite charge, it is repelled from the other sphere with the same charge polarity. Thus, it contacts the particle compound while maintaining the largest distance possible from the repulsing charges. This assembly can only succeed when the overall attraction outweighs the repulsion.

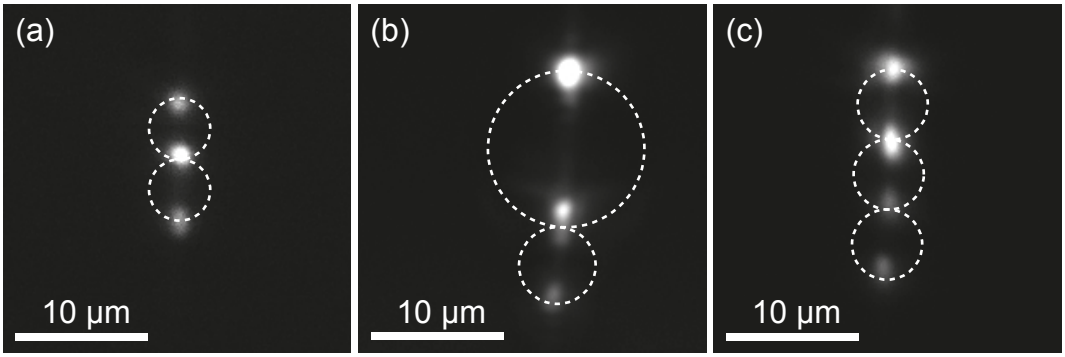

Figure 5.37.: Different levitated silica microsphere compounds assembled individually in the segmented trap. The spheres are visible by scattering of white light directed from the top. The white dashed rings indicate the positions of the spheres. (a) Two spheres with diameters around 4.8 µm. (b) Two spheres of different sizes (approximate diameters: small sphere 4.8 µm, large sphere 10 µm). (c) Three spheres with diameters around 4.8 µm. The self-aligned linear structure indicates remaining initial charges on the surfaces. From [216].

5.4.5. Deposition of Particle Compounds

For further analysis, assembled particle systems can be deposited onto other structures, as already shown for single particles in section 4.6.5. Again, attracting electric forces between the particle compound and the fiber facilitate landing. Thus, the fiber charge polarity has to be opposite to the overall charge polarity of the compound particle. For demonstration purposes, individual silica microspheres with approximate diameters of 4.8 µm are attached to each other and landed on cleaved facets of optical fibers with a diameter of 125 µm. Figure 5.38(a) shows a fiber facet from above, with two coupled microspheres deposited 23 µm off the center. Because of the small depth of field, only the lower sphere is visible. In figure 5.38(b) the same fiber is shown from the side, now revealing both particles. The particle assembly lands upright on the fiber surface. This can be explained by the dipole-like charge distribution on the particles, which aligns with the static electric field of the fiber. In figure 5.38(b) the fiber is positively charged and attracts the lower, negatively charged sphere. At the same time, the upper, positively charged sphere is repelled from the fiber, causing the upright orientation of the placed particle assembly. Deposition of more than two assembled particles is also possible, but the complex charge distribution leads to instabilities of the particle stacks. In figure 5.38(c) a deposited assembly of three spheres is shown. Again, the stack of spheres is oriented upright, but tends to bend towards the fiber surface. This might be due to attraction between the upper sphere and the fiber,

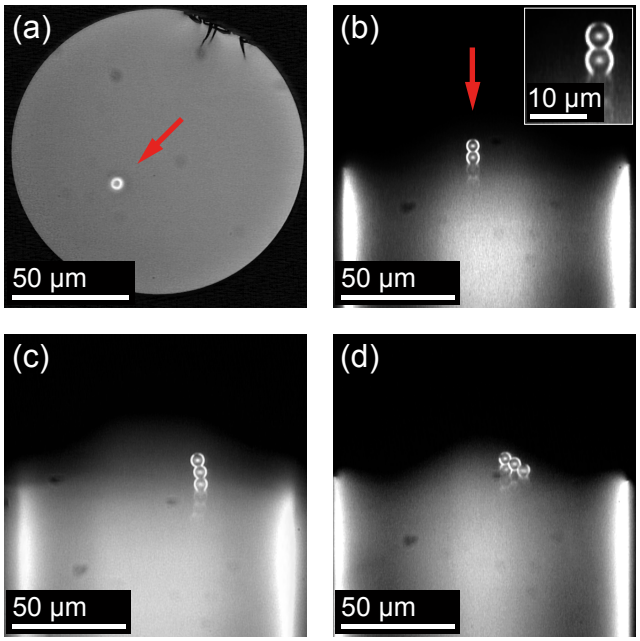

Figure 5.38.: Different assemblies of microspheres with diameters of around 4.8 µm deposited on cleaved facets of optical fibers with a diameter of 125 µm. (a) Two spheres deposited 23 µm from the fiber core. Only the lower sphere can be seen in this image, due to the small depth of field. (b) The view from the side reveals both spheres. Induced by the dipole-like charge distribution, the compound particle aligns with the static electric field of the fiber and lands upright on the facet. The inset shows the particles with a higher magnification. (c) Assemblies of three particles tend to bend towards the glass surface. (d) Stable stacks of four or more particles are not achieved due to the complex charge distribution. (a) and (b) from [216].

but it is also possible that the spheres did not perfectly align in the trap. In the case of four spheres no stable stacks are obtained at all. Due to the complex charge distribution, the particle assemblies collapse or fall apart, as shown in figure 5.38(d).

5.4.6. Conclusion

A new method for the assembly of individual nano- and microparticles in a segmented linear Paul trap is demonstrated. The presented technique enables attaching pre-selected levitated particles to each other in a versatile, reliable and fast way. Formation of compound particles is facilitated by electrostatic attraction. The assembled particles stay in the trap and are further analyzed and deposited on other structures.

Assembly of pre-selected spherical microresonators is a promising approach to study mode-splitting effects in large photonic molecules [296] without interaction with supporting surfaces. Resonant coupling of levitated individual microspheres goes beyond the scope of this thesis, but it might also be a useful method for building custom coupled resonant optical waveguides (CROW) [304, 305]. For filtering and selection of single modes it is even possible to combine differently sized microspheres.

Additionally, particles with differing sizes and masses are stabilized in the trap at the same time and assembled with the presented technique. This is promising for electromagnetic coupling of preselected emitters to resonator particles, for instance a NV defect center in a single diamond nanocrystal coupled to a microsphere or a plasmonic resonator [37]. There is no general limit of the method, as long as all involved particles fulfill the same stability condition (equation (3.18)).

Trapping of different particles at the same trap parameters requires similar specific particle charges $\frac{Q}{M}$. When the mass difference between the particles is large, it might be necessary to control the amount of their charges to maintain stability. This becomes even more important when the assembly is carried out in vacuum, where particle stability is no longer improved automatically by atmospheric friction (see figure 3.5). Different ionization methods might be used to generate different amounts of particle charges, but also a modification of the particle charge after injection seems to be feasible. A reduction of particle charges after electrospray ionization has been demonstrated by using alpha particles from a polonium source [240], but charge elimination with electrons from a nearby filament seems to be more applicable.

When further particles are attached to a priorly-assembled particle compound, self-alignment due to the particles' surface charges is observed, resulting in linear particle systems. For instance, this method could be used to compose self-similar antennas [293] very easily.

Deposition of compound particles onto other structures extends the usability of the assembly technique. Particle systems can be placed onto substrates for further analysis or to functionalize other photonic structures. This might be useful for integration of custom hybrid particles into nanophotonic devices. For instance, to overcome the problem of over-coupling between a spherical microresonator attached to a tapered optical fiber (compare to section 5.3.5), the distance between the two could be controlled by a small spacer particle attached to the microsphere. With the self-oriented deposition the particles could be landed on the taper, so that the microsphere is not directly touching the taper.

6. Laser-Induced Manipulation of Individual Gold Nanoparticles

Apart from experiments with particles in linear Paul traps, during this thesis, some additional work is done on the modification of plasmonic nanoparticles on a glass substrate. A new approach to tuning the plasmon resonances of individual metal nanoparticles solely with focused laser light is developed. The technique is demonstrated by controlled laser-induced melting and shaping of single gold nanoparticles. The results presented in the following chapter are also published in Nano Letters [306].

6.1. Introduction

The spectral response of metal nanoparticles is attributed to plasmon resonances, as explained in section 2.3. Their properties are determined by the size and the shape of the particle, in addition to the electronic properties of the particle material and the surrounding medium [9]. Thus, plasmon resonances can be adjusted by control of at least one of these parameters. Customization of plasmonic nanoparticles is advantageously used in various applications, like sensing [20], photovoltaics [17], catalysis [99] and plasmon-assisted light sources [307, 308].

The most obvious approach to such customization is to set the geometrical parameters at the time of particle synthesis by manipulation of the nucleation [44] or the particle growth [309]. Size and shape can also be altered after particle production by material ablation [310] or melting [311] with femtosecond laser pulses. Even shape transformation by laser-induced photoionization is observed for silver and gold nanoparticles embedded in glass [312–314]. More sophisticated methods involve particle deformation by pressure [59] or synthesis of porous nanoparticles, which offer efficient tuning by the particle size [315] or its percolated structure [316]. They can also be tuned by morphology changes induced by surface modifications [60]. A completely opposite approach is to modify the environment, without changing the particle itself, to adjust the plasmon resonance [105].

Most reported methods aim at the preparation of large particle ensembles in films or colloidal solutions with subsequent analysis by optical and scanning probe microscopy. None have been applied to in-situ tuning, where the plasmon resonance of a specific single nanoparticle is adjusted with respect to a specific configuration, with a priori unknown spectral properties. Such needs arise, when the plasmon resonance of an individual nanoparticle, acting as a nanoantenna, is matched to a nearby emitter, like a quantum dot [103] or a defect center in a nanodiamond [29], or to plasmon resonances of other metal particles in a multi-particle antenna assembly [317].

In this chapter, a new method is described that enables in situ plasmon resonance tuning of an individual metal nanoparticle for the first time. By laser-induced melting and shaping, the symmetry of a single gold nanoparticle is changed, which enables modification of its plasmon resonance in a controlled way, including the opportunity to reverse any

changes. The tuning process is monitored by observation of the optical and geometrical properties of the particle. The result is a splitting of the particle plasmon resonances by spectral shifts due to a symmetry break of the particle geometry. This new technique is versatile and reliable and can be applied without requiring an extensive experimental effort, as will be shown in the following.

6.2. Experimental Setup

A schematic of the experimental setup used to characterize and manipulate single gold nanoparticles is shown in figure 6.1. It is a home-made inverted optical microscope with an atomic force microscope (AFM, see figure 4.31 for details) above (JPK Instruments, NanoWizard BioAFM). This combination allows for almost simultaneous measurement of optical and geometrical properties of the particles. Dark-field microscopy (compare to section 4.3.3) is used to identify particles on the glass substrate and to measure their optical scattering spectra. Therefore, white light from a fiber-coupled xenon arc lamp (LOT-QuantumDesign, LSB511) is focused at a shallow angle onto the sample below the AFM. The light can be linearly polarized in order to excite separate plasmon modes in the different particle axes. Scattered light is collected with an oil-immersion microscope objective (Olympus, PlanApo 60x) with a numerical aperture of 1.4. The incident white light is blocked by a dark-field aperture in the detection path, to ensure measuring light only scattered by the particles. For investigation of a single particle the signal is spatially filtered with an additional confocal pinhole with a diameter of 50 µm. Eventually, detection occurs by an EMCCD (electron multiplying CCD) camera (Andor, iXon) or by a spectrograph (Princeton Instruments, Acton 2500i) in combination with a CCD camera (Andor, iDus). A flip mirror is used to switch between the two detectors. Both cameras are thermo-electrically cooled to reduce sensor noise.

For photoluminescence spectroscopy, particles are excited with blue light from a water-

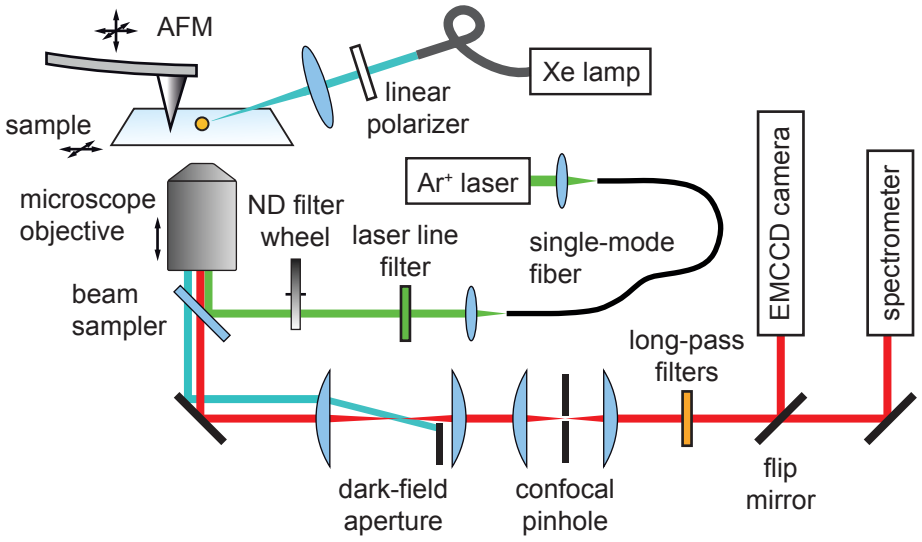

Figure 6.1.: Schematic of the optical microscope setup used for characterization and modification of single gold nanoparticles. Adapted from [306].

cooled argon-ion laser (Spectra Physics, BeamLok 2080) with a wavelength of 457.9 nm. The light is spatially and spectrally filtered by a single-mode fiber and a laser line filter, respectively, before it is brought into the optical path with a beam sampler with a reflectivity of about 5 % (Thorlabs, BSF10-A) and focused onto the sample with the oil-immersion microscope objective. Light from the sample is collected with the same objective and passes the beam sampler with a transmittance of about 95 % towards the detection system. Long-pass filters (Schott, GG495 and OG515) block the remaining excitation light while the confocal pinhole filters the signal spatially. Melting and shaping of single particles is done with the same laser but tuned to the green argon line with a wavelength of 514.5 nm. The wavelength of the laser emission in single-line operation mode is set by adjusting the prism assembly, consisting of a prism and a high reflector, at the rear end of the laser cavity. To be able to monitor the tuning progress by the particle photoluminescence, the laser line filter and the long-pass filter (Schott, OG550) are changed with the emission line of the laser.

Full control of the focus position on the sample is achieved by combinations of piezoelectric actuators attached to mechanical stages. Such combinations allow for fine and rough adjustment, respectively. In the two horizontal directions the sample position is adjusted (piezosystem jena, PXY 80 D12 in combination with Newport, M-406), while in the vertical direction the position of the microscope objective is set (piezosystem jena, MIPOS 3 in combination with Newport, M-UMR 5.16). The position of the AFM on top of the sample stage is controlled separately by individual, integrated stages and piezoelectrical actuators.

6.3. Plasmon Resonance Tuning

In this experiment, commercially available gold nanoparticles with a mean diameter of 80 nm are used (BB International, Gold Colloid 80 nm). The initial aqueous solution is spin-coated without further dilution onto a standard glass coverslip with a rotational speed of approximately 1800 rpm. The coverslip is cleaned in a previous procedure with water and an alkaline cleaning agent (Hellma, Hellmanex).

6.3.1. Optical Characterization of a Single Gold Nanoparticle

Orientation of the microscope to the sample is done by dark-field microscopy. Illuminated with unpolarized white light, the equally sized gold nanoparticles show similar scattering intensities, as shown in figure 6.2. A donut pattern can be recognized for each particle, similar to an oscillating dipole normal to the glass surface [102, 318]. The preferred emission direction indicates that the orientations of the localized surface plasmon modes are influenced by the glass substrate [319].

Prior to the modification procedure, a single nanoparticle is characterized by its scattering signal under white-light illumination. A typical dark-field scattering spectrum can be seen in figure 6.3(a) (black curve). When switching to laser excitation at 457.9 nm, a similar spectrum is obtained for the photoluminescence signal (red curve). Both signals arise from particle plasmon resonances [320] and show similar spectral properties. It is noticeable that the maximum peak in the scattering spectrum is always found at a higher wavelength than in the photoluminescence spectrum. This behavior fits reports of the photoluminescence coinciding with the extinction spectrum obtained from optical density

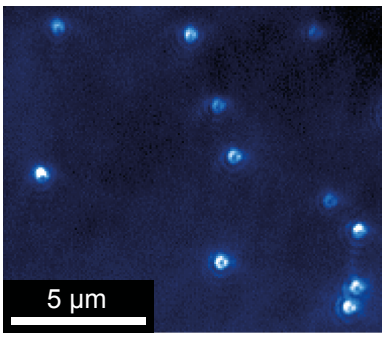

Figure 6.2.: Dark-field image of gold nanoparticles with an average diameter of 80 nm spin-coated on a glass substrate.

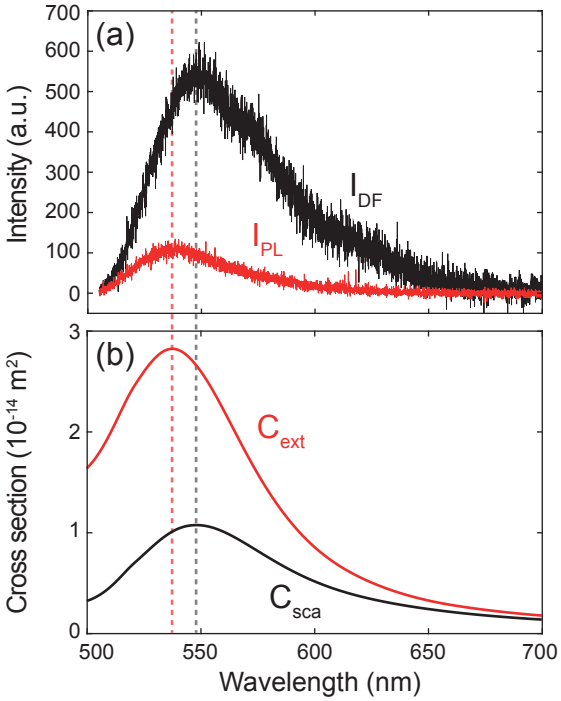

Figure 6.3.: Experimental and theoretical emission spectra of a single 80 nm gold nanoparticle. (a) Measured dark-field scattering (black curve) and photoluminescence (red curve) spectra. (b) Scattering (black curve) and extinction (red curve) Mie cross sections. The relative intensities of the measured spectra are insignificant due to the use of different excitation schemes.

measurements on gold nanoparticles in aqueous solution [320]. This shift is reproduced by theoretical scattering and extinction cross sections of an 80 nm gold sphere calculated with Mie theory (see section 2.1.3), as shown in figure 6.3(b). The effective index of refraction of the particle environment (averaged value considering the air and glass half-spaces) is estimated to be 1.25, by fitting the spectral peak position of the calculated scattering cross section to the measured scattering maximum. The spectral distance between the maxima of the calculated scattering (black line) and extinction (red line) cross sections resembles the distance between the measured spectra in figure 6.3(a) very well.

6.3.2. Laser-Induced Melting and Shaping

The plasmon resonance of a single gold nanoparticle is modified by laser-induced melting and shaping. After optical characterization the argon-ion laser is tuned to the emission wavelength of 514.5 nm and focused onto the particle. The tuning progress is observed in the photoluminescence image. In contrast to the scattering image, it shows no donut pattern prior to melting due to the different excitation direction, as shown in figure 6.4(a). When the laser intensity is increased, a change of the photoluminescence emission is observed. Starting at around $8 \times 10^5\,\mathrm{W\,cm^{-2}}$ the spot-like image begins to widen (see figure 6.4(b)) and transforms into a donut profile at approximately $1.2 \times 10^6\,\mathrm{W\,cm^{-2}}$ (figure 6.4(c)). The donut pattern becomes more distinct with higher laser intensities up to $1.8 \times 10^6\,\mathrm{W\,cm^{-2}}$ (figure 6.4(d)). At any time, the procedure can be stopped by reducing the laser intensity or switching it off, leaving the emission pattern in the current state.

After the modification, the increase in the dipole-like emission is also observable in the white-light scattering pattern of the elongated particle. The dark-field image in figure 6.5(a) shows three spherical gold nanoparticles. In figure 6.5(b) the same particles can be seen, after laser-induced melting and shaping has been applied individually. Particle 2 is modified with a maximum laser intensity of $1.1 \times 10^6\,\mathrm{W\,cm^{-2}}$ and particle 3 with $1.8 \times 10^6\,\mathrm{W\,cm^{-2}}$. Compared to particle 1, which is left in its original state for reference, particle 2 and even more particle 3 show enhanced scattering intensities towards the microscope objective and a stronger visibility of the donut pattern.

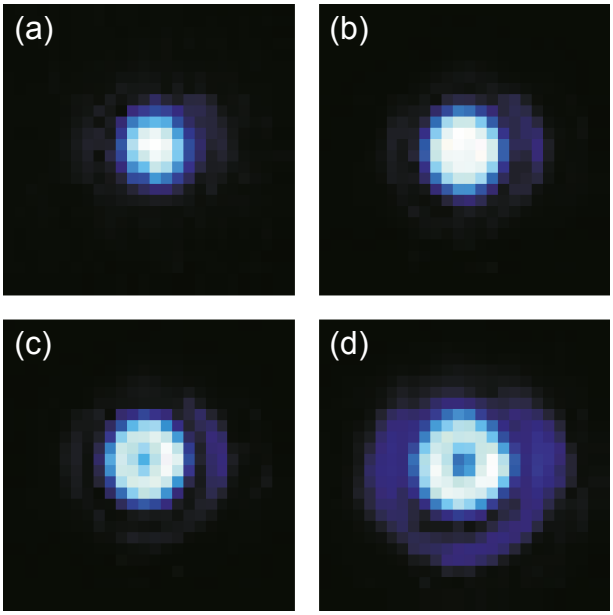

Figure 6.4.: Photoluminescence emission pattern of a single 80 nm gold nanoparticle during laser-induced tuning of its plasmon resonance. (a) In contrast to dark-field the photoluminescence image of the spherical particle shows no donut pattern prior to melting. (b) At a laser intensity of $I \approx 8 \times 10^5\,\mathrm{W\,cm^{-2}}$ the emission image starts to widen and (c) forms a donut pattern at $I \approx 1.2 \times 10^6\,\mathrm{W\,cm^{-2}}$. (d) The donut pattern becomes more pronounced with higher intensities up to $I \approx 1.8 \times 10^6\,\mathrm{W\,cm^{-2}}$. No scale bar is provided as each image is individually normalized. From [306].

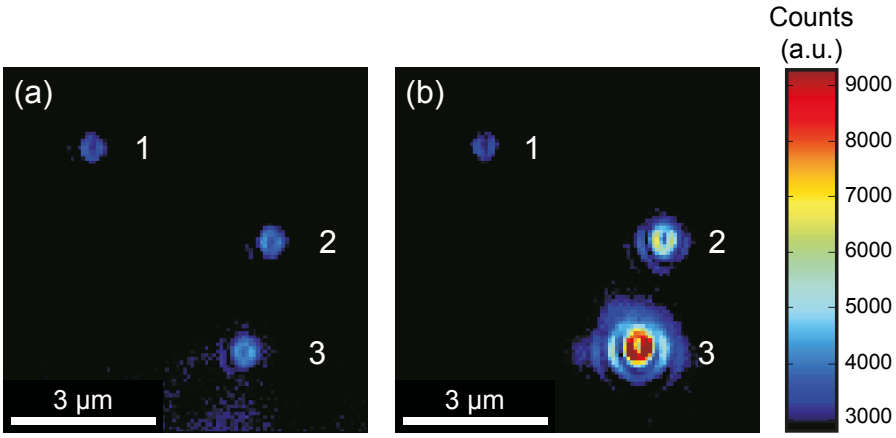

Figure 6.5.: Three 80 nm gold nanoparticles on a glass coverslip prior to and after tuning. (a) Dark-field images before and (b) after individual laser-induced elongation of particle 2 (laser intensity $1.1 \times 10^6\,\mathrm{W\,cm^{-2}}$) and particle 3 (laser intensity $1.8 \times 10^6\,\mathrm{W\,cm^{-2}}$). Particle 1 is not tuned for reference. The color bar refers to both (a) and (b). From [306].

The change of the emission pattern is caused by a controlled elongation of the initially spherical particle in the direction parallel to the laser beam due to laser-induced melting and shaping. The particles shown in figure 6.5 are characterized by the AFM on top of the microscope setup. As the particle distribution around the modified particles is known from the dark-field image, orientation onto the sample is straightforward with the AFM and the modified particles are easily retrieved. In figure 6.6 the height of the un-modified particle 1 (green curve) is measured to be approximately 80 nm, as expected. Similar heights are confirmed for the other particles before tuning. Afterwards, particles 2 and 3 are found elongated, standing upright on the glass coverslip. The height of particle 2 (black curve) is raised to 105 nm, and that of particle 3 (red curve) as high as 123 nm.

Spectral measurements of the scattered white light obtained under dark-field illumina-

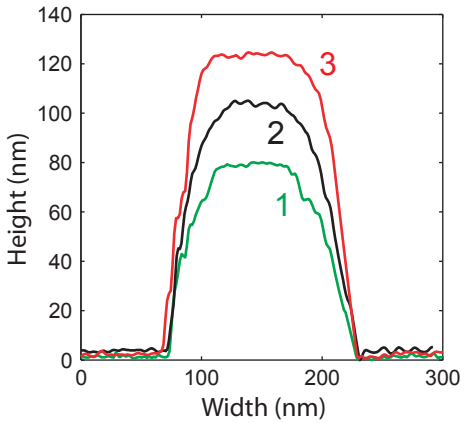

Figure 6.6.: Height of the particles from figure 6.5(b) measured with the AFM. Particle 1 (green curve) is not modified to be used as a reference. Particles 2 (black curve) and 3 (red curve) are tuned with laser intensities of $1.1 \times 10^6\,\mathrm{W\,cm^{-2}}$ and $1.8 \times 10^6\,\mathrm{W\,cm^{-2}}$, respectively, and stand upright on the glass coverslip. From [306].

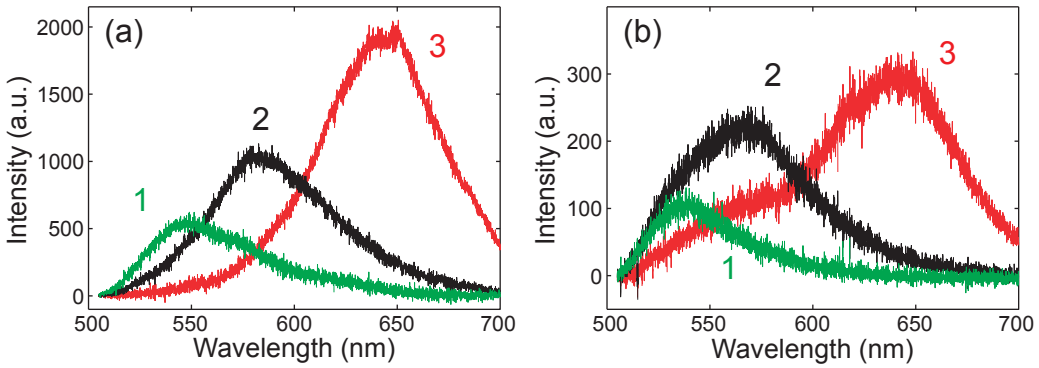

Figure 6.7.: Emission spectra of the particles from figure 6.5(b). After elongation of the initially spherical particles red-shifts of the plasmon resonance peaks can be observed in the (a) white-light scattering spectra and the (b) photoluminescence spectra. All spectra are corrected for a background signal from an empty site on the substrate. From [306].

tion reveals a red-shift of the plasmon resonance peak for each elongated particle, in addition to the increased scattering towards the microscope objective, as shown in figure 6.7(a). Similar behavior is observed for the photoluminescence emission spectrum measured under laser excitation at 457.9 nm (compare to section 6.3.1), shown in figure 6.7(b). For particles 2 and 3, red-shifts of the plasmon resonances of 35 nm and 90 nm are measured in the scattering as well as in the photoluminescence spectra, respectively. The strength of the spectral shift depends on the particle elongation reached which can be controlled by the laser intensity. For a set moderate value ($I < 2 \times 10^6\,\mathrm{W\,cm^{-2}}$) the particle elongation together with the change of the emission pattern and spectrum is permanently, and can be changed only when the used laser intensity is further increased.

The changed geometry of the tuned particles is confirmed with a scanning electron microscope (SEM). This method requires electrically conductive and grounded samples to avoid the accumulation of electrostatic surface charges which would disturb the image acquisition. For this purpose, an elongated gold nanoparticle is transferred from the glass coverslip to a glass substrate coated with an electrically conducting layer of indium tin oxide (ITO). The transfer is done with an elaborate pick-and-place method [29, 242], as depicted in figure 6.8. In the dark-field image shown in figure 6.8(a) an elongated particle with a strong scattering intensity towards the microscope objective can be identified. This particle is picked-up with the AFM tip in contact mode by pressing it on the particle. Typically, a few attempts are necessary for this task. Figure 6.8(b) shows that the particle is lifted from the sample. For deposition the uncoated coverslip is replaced by the ITO-coated substrate. Dark-field imaging is used for orientation on the new substrate as well. In figure 6.8(c) the shadow of the AFM tip almost approached to the surface can be seen. The tip of the shadow roughly indicates the position of the AFM tip on the sample. Generally, the new substrate offers no prominent characteristics in the dark-field image, as it is cleaned in a previous procedure (see section 6.3). To retrieve the particle in the SEM, a marking is applied on the surface with an ordinary permanent marker, that is visible as black lines in the dark-field image of the new substrate in figure 6.8(d). When the AFM tip is in the vicinity of the marking, the particle is deposited by dragging the AFM tip over the sample. The success of the deposition is verified by the appearance of a bright

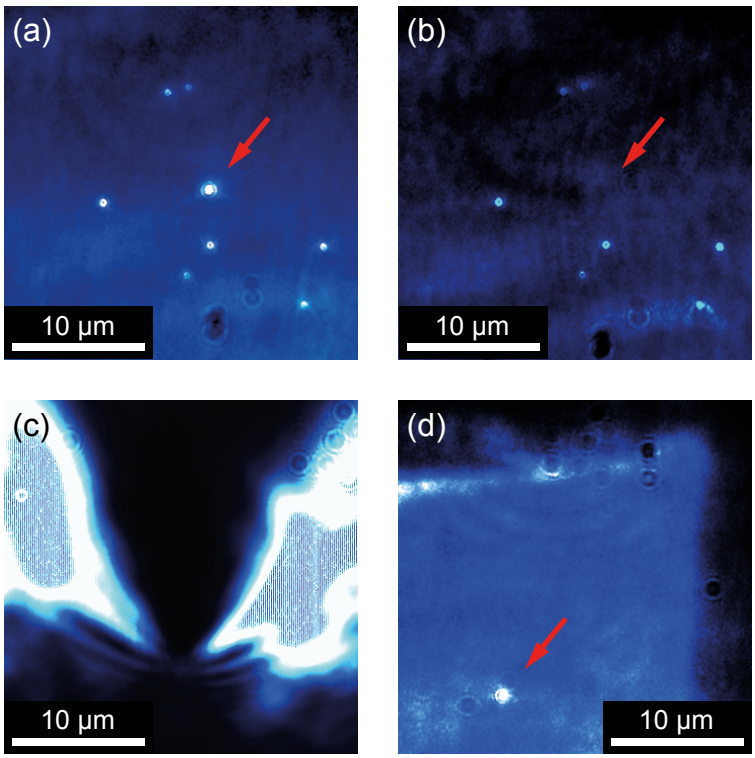

Figure 6.8.: Dark-field images depicting the transfer of an individual gold nanoparticle from the uncoated glass coverslip to an ITO-covered substrate. (a) The elongated particle is picked up with the AFM tip and (b) lifted from the surface. (c) The shadow of the AFM tip is used to navigate roughly on the sample. (d) The particle is deposited close to markings (black borders) on the otherwise empty ITO substrate to facilitate retrieval with the SEM.

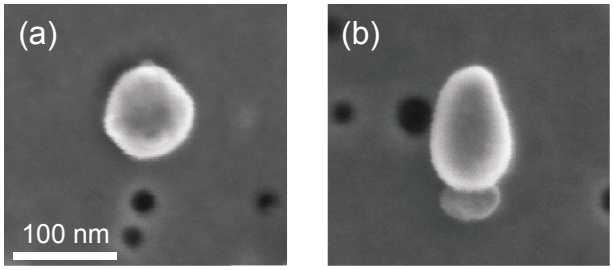

Figure 6.9.: SEM images of gold nanoparticles on ITO-covered glass substrates. (a) Unmodified spherical gold nanoparticle. (b) Prolate gold nanoparticle elongated by the melting laser. The elliptical object at the base of the particle is an artifact as it is not visible in the AFM image. From [306].

scatterer in the dark-field image of the new substrate. After deposition, the ITO-covered substrate is transferred into the evacuated sample chamber of the SEM and adjusted to focus the surface. The particles are found with the SEM by following the marking. In figure 6.9(a) the SEM image of a spherical gold nanoparticle with a diameter of 80 nm can be seen. The unmodified particles are put on the substrate by ordinary spin-coating. In

contrast, figure 6.9(b) shows an elongated gold nanoparticle, after tuning with the laser on the uncoated coverslip and subsequent transfer to the ITO substrate. The particle is lying on its side, revealing the changed symmetry very clearly.

The asymmetric shape of a tuned gold nanoparticle is also verified by optical means. Under dark-field excitation, linear polarization of the incident white light allows for selective excitation of particle plasmon modes along different particle axes independently of each other. In figure 6.10 measured white-light scattering spectra are compared to computed scattering cross sections for an initially spherical gold nanoparticle with a diameter of 80 nm elongated to a prolate spheroid with a long axis diameter of 110 nm. The linear polarization of the incident white light is chosen to be either normal (black curves) or parallel (red curves) to the glass surface, to excite the elongated or a shortened particle

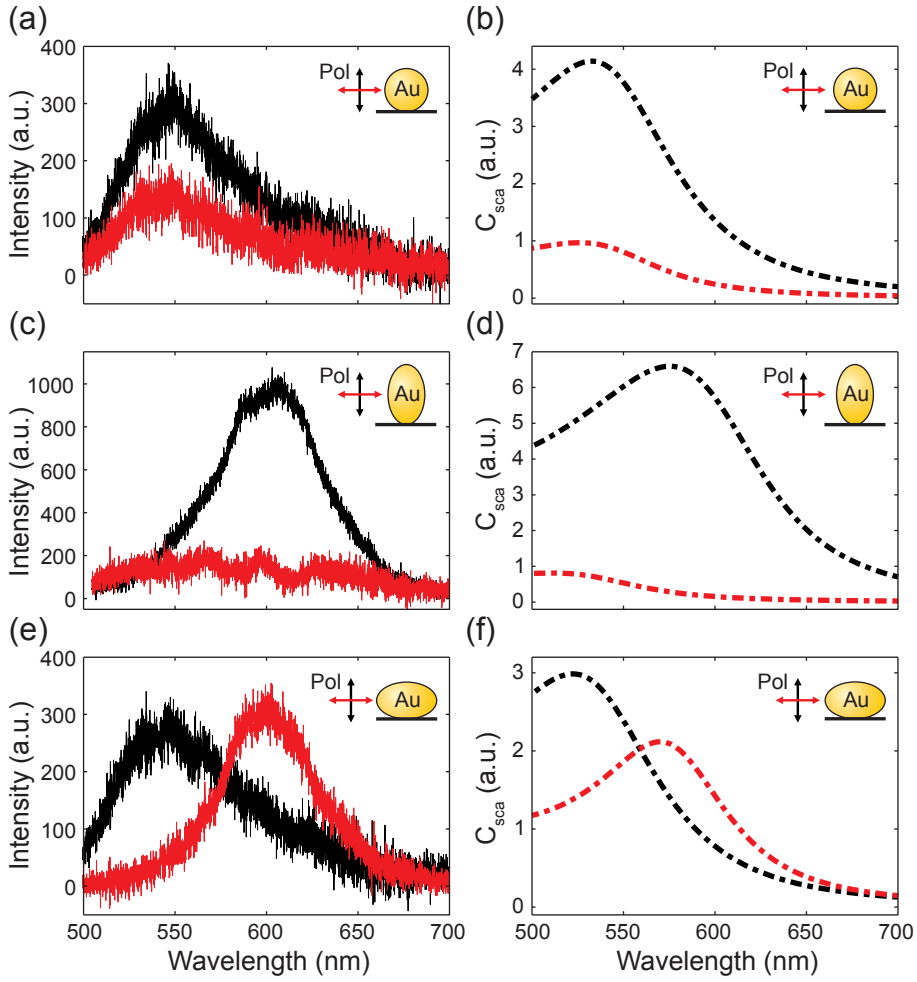

Figure 6.10.: Optical measurement of changed particle symmetry by scattering spectroscopy under linearly polarized dark-field excitation. Measured spectra (a, c, e) are compared to computed scattering cross sections (b, d, f) for a gold nanoparticle with an initial diameter of 80 nm elongated to a prolate spheroid with a height of 110 nm. The white excitation light is linearly polarized normal (black curves) or parallel (red curves) to the supporting glass surface. (a+b) Unmodified, spherical gold nanoparticle. (c+d) Elongated particle after laser tuning, standing upright on the coverslip. (e+f) Same particle as before, but lying on its side. From [306].

axis, individually. Figure 6.10(a) shows no spectral difference in the scattering spectra of an unmodified, spherical gold nanoparticle with a diameter of 80 nm for the two linear polarization directions. The only observable difference is the significant drop of the detected scattering intensity when switching the linear polarization direction of the excitation light from normal to parallel to the glass surface. This observation is legitimized in figure 6.10(b) by the computed scattering cross sections of the same configuration. After elongation, different particle plasmon resonances are excited, depending on the relative linear polarization of the incident light. As shown in figure 6.10(c) a red-shifted plasmon resonance is observed when the elongated axis of the upright particle is excited, similar to the theoretical result in figure 6.10(d). No signal is obtained from the upright particle if only a short axis is excited, although a blue shift is expected due to the shortened diameter. The collected signal is too small to reveal any spectral characteristics. However, a sufficient signal from the short axis is measured, when the particle is toppled over with the AFM. In figure 6.10(e) the measured plasmon resonances of the long and a short axes of the particle lying on its side can be seen. The blue shift is barely visible due to the less pronounced change of diameter compared to the long axis. This is verified by the theoretical findings for this configuration in figure 6.10(f).

The reduction of the particle width can be measured more efficiently with the AFM. In figure 6.11(a) the AFM image of another gold nanoparticle elongated to 110 nm is shown. With the particle standing upright, the width cannot be determined sufficiently due to convolution of the sample and the a priori unknown shape of the AFM tip [321]. This issue is overcome by toppling the elongated particle over with the AFM tip in contact mode (compare to section 4.6.5). The result is shown in figure 6.11(b). A particle width of 70 nm is measured with an uncertainty of ± 2 nm due to external vibrations of the setup. However, the measured particle width corresponds very well to the expected reduced width of 68 nm, calculated by assuming a constant particle volume and a prolate spheroidal particle geometry after the tuning. In figures 6.9 and 6.11 it is noticeable that the elongated geometry resembles more an ovoid than a prolate spheroid. This could explain the small deviation of the particle width measured with the AFM compared to the expected value.

The scattering cross sections shown in figure 6.10 are computed by Christian Matyssek (AG Theoretische Optik & Photonik, Institut für Physik, Humboldt-Universität zu Berlin)

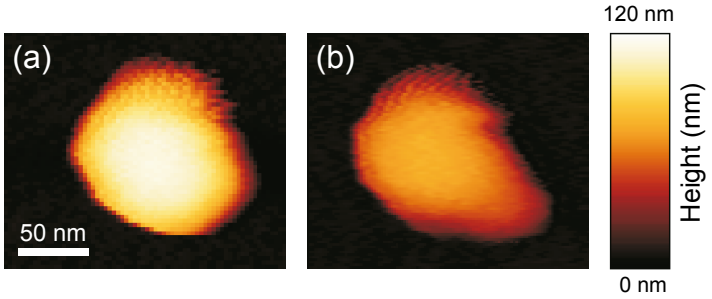

Figure 6.11.: AFM images of a gold nanoparticle after tuning. (a) The elongated particle stands upright on the glass coverslip with an elongated height measured to be 110 nm. (b) The diameter of the short particle axes is measured to be 70 nm on the particle toppled to the side with the AFM. Compared to the 80 nm diameter of the initially spherical particle, the short axis is decreased by 10 nm. The scale bar refers to (a) and (b). From [306].

using the discontinuous Galerkin time-domain method [322, 323] and the material model given in appendix A.2. The results are in good agreement with the experimental findings. All observed changes of the particle's plasmon resonances are confirmed very well, although a systematic shift to the blue is exhibited in the theoretical curves, as well as different relative heights between the two polarization directions compared to the measured signals. These deviations are attributed to differences in the indices of refraction of the particle surroundings and the collection angle of the detection between the experimental setting and the theoretical model. In contrast to the computation, which includes all scattering angles, the microscope objective has a limited acceptance given by its numerical aperture. In addition, deviations of the real particle geometry from the assumed ideal prolate spheroidal shape and a non-perfect alignment of the linear polarization direction relative to the designated particle axes might explain smaller spectral deviations.

6.4. A Simple Model for Melting and Shaping with a Focused Laser Beam

The laser-induced elongation of a metal nanosphere to a prolate spheroid on a glass coverslip involves an intricate interplay of heating and shaping effects, like frequency-dependent absorption of laser light and heat conduction, as well as a force balance between light pressure, surface tension and wetting. In this section a simple model is given that predicts the complete melting of the particle material and explains the forces responsible for the formation of the asymmetric nanoparticle.

6.4.1. Temperature Distribution

The temperature of a single gold nanoparticle in the focused laser beam is estimated by calculating the heat transfer to and from the particle in a one-dimensional heat conduction problem. The nanoparticle absorbs heat according to its absorption cross section C_{abs} and the laser intensity I_0. The resulting increase of the particle temperature is counteracted by heat conduction. After a short warming-up phase, a steady-state regime is assumed, where the temperature distribution in and outside the particle is constant over time. The air-glass environment of the particle with radius R is simplified to an isotropic medium with an effective thermal conductivity κ_f [324]. As a result from the model, the particle's surface temperature T_s is calculated from the room temperature T_0 with

$$T_s = T_0 + \frac{C_{abs} I_0}{4\pi\kappa_f R}. \tag{6.1}$$

More details about the one-dimensional temperature model are given in appendix C.

In figure 6.12 the results from the temperature model are shown, calculated for values from the experiment (see table C.1). In figure 6.12(a) the steady-state surface temperature of a gold nanoparticle with a diameter of 80 nm is shown as a function of the excitation laser wavelength. The laser power is set to 0.315 mW, corresponding to an intensity of $8 \times 10^5\,\mathrm{W\,cm^{-2}}$ in the diffraction limited spot of the focused laser at a wavelength of 514.5 nm (see equations (C.19) and (C.20)). The first changes in the emission pattern are observed in the experiment at this laser intensity (compare to figure 6.4). The graph indicates a particle temperature heated up above the melting temperature T_{melt} of bulk

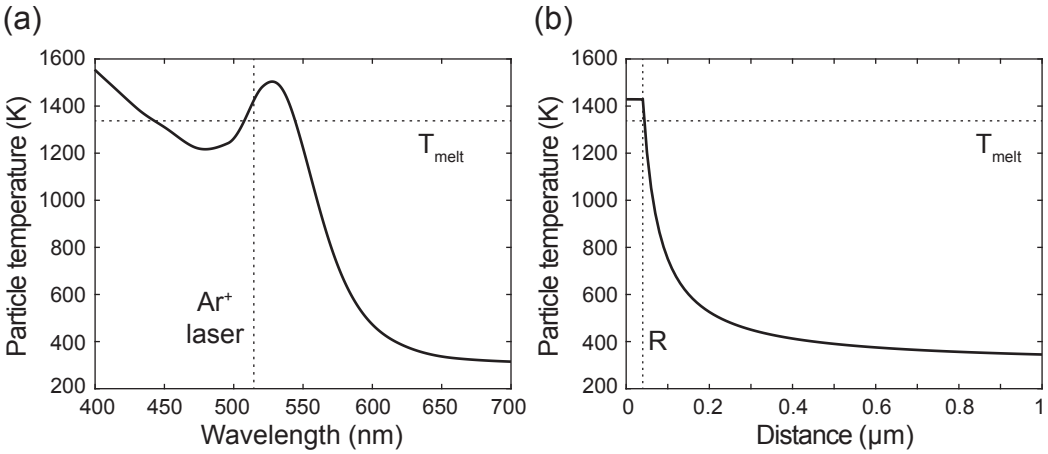

Figure 6.12.: Steady-state temperature calculations for a spherical 80 nm gold nanoparticle, heated up in the diffraction-limited spot of the focused laser. An isotropic surrounding medium is assumed with an effective thermal conductivity accounting for the presence of air and glass. (a) Particle surface temperature varying with the excitation wavelength. The laser power of 0.315 mW means an intensity of $8 \times 10^5\,\mathrm{W\,cm^{-2}}$ at a wavelength of 514.5 nm. (b) Temperature distribution around the particle for 514.5 nm excitation wavelength. The particle with radius R is centered at 0 µm. T_{melt} is the melting temperature of bulk gold.

gold at 1337 K [325]. A size-dependent reduction of the melting point, as known for very small nanoparticles, is not expected for a particle with a diameter of 80 nm [326, 327]. In figure 6.12(b) the radial temperature distribution is plotted for the same laser power, but with a fixed excitation wavelength of 514.5 nm. At a distance of 1 µm the particle with a steady-state temperature of 1428 K heats the surrounding medium by 45 K above the room temperature of 300 K.

The calculated temperatures fit the experimental findings very well. The minimum laser intensity needed to modify a spherical gold nanoparticle in the experiment is shown to be sufficient to heat the particle temperature slightly above the melting point.

6.4.2. Optical Forces

The geometry of the melted and thus liquid droplet of gold is shaped by the forces of the focused laser beam. Starting from spherical geometry, an elongated particle standing upright on the substrate is observed after the tuning procedure. A simple model for the mechanism of particle elongation is shown in figure 6.13. The focused laser beam exerts a force on the particle that can be separated into two components, as known from the optical tweezer [61]. The first one acts parallel to the beam direction and results from radiation pressure due to momentum transfer by absorbed or scattered photons. The second force component is called the gradient force, as it arises from the intensity gradient in the focused Gaussian beam, that draws small particles towards the focus. It has been shown that not only dielectric [328] but also metallic particles can be stabilized in all three dimensions [329, 330], when they are much smaller than the used laser wavelength (Rayleigh regime). Here, it is assumed that the main driving force for elongating the particle is the gradient force, squeezing the liquid particle in the radial beam direction. When the experiment is carried out with a lower intensity gradient, by using a microscope

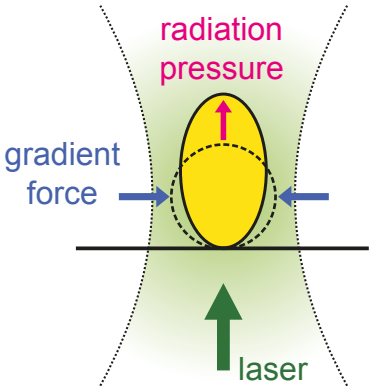

Figure 6.13.: Optical forces exerted on the gold nanoparticle in the Gaussian laser beam. The radiation pressure acts parallel to the beam direction and the gradient force towards the focus. From [306].

objective with a smaller numerical aperture of 0.7, tuning is not achieved. Even with higher intensities, elongation of the particle cannot be induced by the focused laser in this case, although the particle is heated above the melting temperature. This is proven by the fact that the particle can be pulled apart when it is moved through the laser focus by changing the position of the sample stage in the horizontal direction.

The forces that have to be overcome for particle elongation are gravitation and surface tension. Also surface effects like wetting between the particle and the glass substrate may effect the change in geometry. Though, the gradient force is assumed to be the dominant effect, as particle elongation is not observed with a smaller intensity gradient. However, a detailed numerical simulation of all contributing forces is required for a quantitative comparison, which goes beyond the scope of this thesis.

6.5. Self-Termination and Reversibility

As presented in section 6.3.2, the strength of the tuning is determined by the laser intensity. For a moderate value of up to approximately $2 \times 10^6\,\mathrm{W\,cm^{-2}}$, the shift of the plasmon resonance stops at a certain spectral position, corresponding to a certain amount of particle elongation. This self-termination is attributed to the modification of the particle geometry during the tuning. As shown in figure 2.11, not only the cross section for scattering, but also that for absorption, shifts with the particle elongation. Thus, when the absorption cross section shifts to the red, heating is reduced and the elongated particle solidifies. From this point the particle can be further elongated simply by using a higher laser intensity up to a value of approximately $2 \times 10^6\,\mathrm{W\,cm^{-2}}$.

When the laser intensity exceeds $2 \times 10^6\,\mathrm{W\,cm^{-2}}$, the elongated particle collapses or is damaged. In the case of particle collapse, it is assumed that the increased heating reduces the elasticity or viscosity of the fully melted, and thus liquid, droplet of gold too much. When the forces exerted on the particle cannot keep up the elongated shape anymore, the particle converges to a sphere again, due to the poor wetting of gold to glass. In the case of particle damage, it may be speculated that evaporation [331] or ablation [310] of some of the material leads to a loss of material.

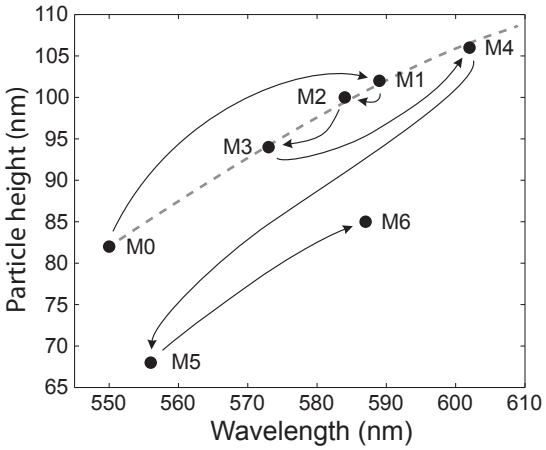

Figure 6.14.: Controlled plasmon resonance tuning of a single gold nanoparticle by laser-induced melting and shaping in consecutive steps. For each step, M0-M6, the measured particle height and peak wavelength of the white-light scattering spectrum is shown (see text for details). The gray dashed curve is meant as a guide to the eye to symbolize the achievable resonance positions depending on the particle height. From [306].

All mentioned effects, including self-termination, reversibility and particle damage, are demonstrated on a single gold nanoparticle in figure 6.14. The particle is repeatedly modified by laser-induced melting and shaping in consecutive steps, in order to tune the particle plasmon resonance either to longer or to shorter wavelengths. After each step, the laser is switched off and the cooled-down particle is characterized by its height and its white-light scattering spectrum. M0 indicates the spherical gold nanoparticle prior to modification. It shows the expected particle height of 80 nm and the maximum of the scattering signal at 550 nm. After the first tuning step (M1) the particle height is lifted and the plasmon resonance peak is shifted to a higher wavelength. This red shift is partly reversed in two tuning steps with higher laser intensities (M2 and M3), that reduce the particle height and the wavelength of the plasmon resonance peak successively. The following tuning step (M4) shifts the plasmon resonance peak and the particle height again to higher values, exceeding those of tuning step M1. However, shifting the plasmon resonance peak back to the initial wavelength often produces a particle height even smaller than the starting value of the spherical particle (M5). The higher laser intensity seems to cause material loss, as the measured combination of particle height and spectral position of the particle plasmon resonance peak can be explained by a smaller, slightly elongated particle. From this point, tuning of the plasmon resonance is continued as usual, but with a reduced particle volume (M6).

6.6. Conclusion

A new approach for tuning the plasmon resonance of a single gold nanoparticle by laser-induced melting and shaping is demonstrated. In contrast to most common methods, which control particle synthesis or the particle environment, the presented technique allows for selection of an individual, pre-characterized nanoparticle and subsequent in-situ tuning. Self-termination enables good control of the outcome and reversibility facilitates

fine adjustment. All experimental and theoretical findings confirm the interpretation that the particle geometry is modified by the laser and that the changes in the geometry are correlated to the observed plasmon resonance shifts.

Resonance tuning by radiation pressure is already shown for soft dielectric microspheres [58]. With this new method, the range of nanophotonic elements tunable by optical forces is extended to plasmonic systems, but with one major difference. The geometry change of the plasmonic particle is permanent, while the dielectric particle returns to its initial state, when the laser is switched off.

The tuning technique may be beneficial for different applications. The production and fine-tuning of tailored plasmonic systems with matched resonances can be envisioned, like self-similar antennas [293] in the substrate plane [332] or other plasmonic oligomers [333]. If the elongated particle can be tilted in a controlled way, either directly during the tuning by using an oblique beam or afterwards with the AFM, effects from crossed plasmonic resonators could be investigated and exploited for further applications [334, 335].

Furthermore, in-situ tuning of an individual plasmonic particle can be used to precisely match its plasmon resonance to a nearby emitter, for example to improve plasmon-enhanced single photon emission from custom assembled hybrid nano structures [29]. First results are published from laser-induced tuning of two 60 nm gold nanoparticles close to a diamond nanocrystal containing a single NV defect center [29]. The hybrid structure was assembled from individual pre-characterized particles with an earlier version of the experimental setup presented in section 6.2 but with the same laser and the same microscope objective. Tuning of the gold nanospheres was induced accidentally by increasing the laser intensity aiming at a higher fluorescence yield. Figure 6.15(a) illustrates schematically the hybrid system prior to and after tuning. The measured fluorescence time traces in figure 6.15(b) prove a boost of the excited-state decay rates in the NV defect center. Compared to the bare diamond (black curve), the decay rate is increased when one (blue curve) and even more when two spherical gold nanoparticles (red curve) are electromagnetically coupled to the diamond. After excitation of the system with a high laser intensity,

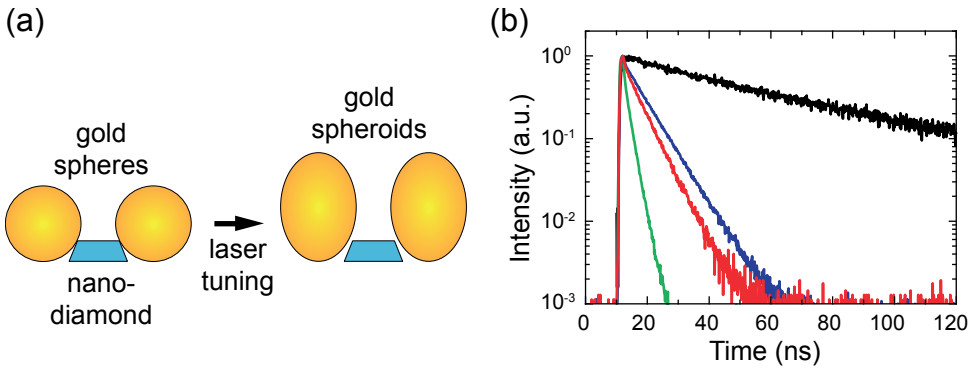

Figure 6.15.: Performance enhancement of a hybrid single photon source by laser-induced plasmon resonance tuning after nanoassembly. (a) Sketch of the gold-diamond system prior to and after tuning. (b) The decay rate of the excited state of the bare diamond (black curve) is increased when the first (blue curve) and the second (red curve) gold nanosphere are electromagnetically coupled to the diamond. After laser-induced plasmon resonance tuning, the decay rate can be increased even more (green curve). From [29].

the decay rate of the excited state was increased even further (green curve). This can be explained by plasmon resonance tuning through laser-induced elongation of one or both gold nanoparticles, although the AFM was not used to confirm the particle elongation. Unfortunately, the performance of the hybrid single photon source could not be enhanced due to a reduced quantum efficiency by increased coupling to dark plasmon modes.

In all conceivable applications, self-termination allows for a reproducible tuning process, comparable to the fabrication of toroidal microresonators by laser-induced melting of glass discs [290]. Further development of the tuning method may enable the production of larger arrays of elongated metal particles with similar plasmon resonances [336]. A related approach is demonstrated for gold nanoparticles embedded in glass matrices, where the accessible range of laser-induced geometrical changes is extended by changing the laser wavelength during the tuning [337].

7. Summary and Outlook

In this thesis different methods for the investigation and the manipulation of individual nano- and microparticles were investigated. The most interesting experiments were presented in the previous chapters. The results will enable many fascinating applications in the future. Evidently, new questions have also been raised, that should be considered in continuing experiments. Before providing an outlook, the main experimental results are reviewed in the following.

7.1. Summary

Two different microscopy setups were built for the particle manipulation, which can be distinguished mainly by their methods of particle handling: levitation in a Paul trap or support by a glass coverslip.

In **chapter 5** the results from experiments with levitated nano- and microparticles were presented. Single particles confined in linear Paul traps were studied without interaction with supporting surfaces. Characterization of the particles was done by optical scattering and photoluminescence spectroscopy. Different manipulation techniques were developed to process the particles afterwards for further analysis or fabrication of more complex photonic structures. Almost any kind of particle can be confined in the oscillating quadrupole electric field of such a trap. Here, several optically active as well as optical resonator particles were used in different experiments, demonstrating the capabilities of the trap setup and the developed manipulation techniques:

- For the first time, fluorescence from nitrogen vacancy defect centers in submicron diamond clusters levitated in an electric particle trap was observed [212]. After characterization, the diamond particles were deposited on cleaved facets of optical fibers to measure the overall cluster size with an atomic force microscope. The size of the levitated clusters could be decreased so far to a minimum of 500 nm, still allowing detection of the NV fluorescence. The results indicate a new opportunity to isolate single diamond nanocrystals for optomechanical experiments in the future.

- Single silver nanowires with lengths from 9 µm to 25 µm were levitated in the trap, which showed propagation of surface plasmon polaritons [225]. The observation of Fabry-Pérot-like resonances in the scattering spectra indicated the nanowires behave as a cavity for surface plasmon modes, in agreement with experiments with silver nanowires on substrates. The resonator losses as well as the group velocity of the propagating surface plasmons were estimated from measured scattering spectra. The exact geometry of the nanowires was determined with the atomic force microscope after deposition on a cleaved fiber facet. The experiments verify that levitated plasmonic particles can also be investigated in the trap setup. The influence of

supporting substrates on plasmonic particles could be analyzed by measurements on the same particle, both in the trap and after deposition.

- A new method for depositing single pre-characterized particles from the trap onto fragile photonic structures was developed [226]. This technique was demonstrated by functionalization of tapered optical fibers with dye-doped fluorescent polystyrene spheres and spherical silica microresonators. The particles were detected through the fiber by their fluorescence signal or by changes in the transmission. The deposition method was also successfully used in the other trap experiments to deposit different particles and particle assemblies on cleaved fiber facets for further analysis.

- For the assembly of single particles, a new alignment-free method was developed, that relies on electrostatic attraction between two neighboring particles in the trap with opposite electric charges [216]. Individual particles were characterized and stored in the trap before attaching them to each other. Through theoretical estimations it was shown that the resulting compound particles are always stable in the trap whenever the constituent particles are stable individually. The applicability of the method was demonstrated by electromagnetic coupling of optically active quantum dot clusters and dye-doped polystyrene beads to spherical silica microresonators with different sizes. Subsequent to the assembly, compound particles were deposited onto cleaved fiber facets, showing a self-organized orientation in the electric field of the charged fiber surface.

All presented experiments demonstrate the high applicability of the setup and the developed techniques for future applications in the fields of single particle spectroscopy and manipulation as well as functionalization and controlled assembly of photonic structures.

In **chapter 6** the results from manipulation experiments on single gold nanoparticles supported by a glass coverslip were presented. A new method to tune the plasmon resonance of individual metal nanoparticles in-situ in a controlled way was developed [306]. By melting and shaping with a focused laser, the symmetry of a gold nanoparticles with a diameter of 80 nm was changed from spherical to an elongated, spheroidal-like geometry. Experimental evidence is given for this modification and the correlation between the changed geometry and the observed spectral shifts of the plasmon resonance. An atomic force microscope was used to measure the particle shape prior to and after tuning, as well as to transfer single particles to an electrically conducting substrate, needed for imaging the particles with a scanning electron microscope. Additionally, it was shown that the measured spectra are in good agreement with theoretical scattering cross sections computed for different particle geometries. The geometry change and thus the plasmon resonance shift were applied stepwise, and even reversed, to demonstrate the full capability of this technique. Finally, simple models were given for the temperature distribution and the optical forces during the laser-induced particle modification.

Controlled adjustment of the plasmon resonance of individual particles could be beneficial for several applications. The in-situ method could especially facilitate the assembly of complex nano-systems, to adjust plasmonic nanoantennas, such as Yagi-Uda antennas [30], to each other or to nearby emitters. An automated version of the method could also be conceived, which would allow fast and remote tuning. The plasmon resonances of many single nanoparticles could be tuned individually by observing the photoluminescence

emission pattern or spectrum online during the modifications, while moving particle after particle into the microscope focus with a motorized translation stage.

7.2. Outlook

The results presented in this thesis enable a variety of new opportunities to investigate and manipulate individual nano- and microparticles. Here, some conceivable future developments are considered, from improvements of the current setups and theoretical clarifications to possible research approaches and applications.

7.2.1. Levitated Nano- and Microparticles

Before thinking about subsequent experiments with trapped particles, a further improvement of the experimental setup should be considered. First of all, the optical access to the trap center has to be increased, to be able to efficiently detect and characterize a levitated nanoparticle with little fluorescent output like a single diamond nanocrystal containing a single NV defect center. Various detection strategies have already been tested with mixed results. Different collection optics, like small aspherical lenses or high numerical aperture fibers, were approached to the trap center for a better detection signal. Unfortunately, such dielectric elements disturbed the particles in the trap due to the always-present surface charges on the glass surfaces. Metallizing and grounding removed the charges, but the changed electric trapping potential due to the electrode nature of the additional conducting objects did not improve the situation. Moreover, the risk of electrical sparkover was increased. Particle stability was also impaired when the detection was carried out along the trap axis. At each end of the trap the electrodes block much less light but the particle trajectory is disturbed by the electric fringe field. More promising seems to be the use of a curved mirror behind the trap, in order to reflect back light emitted from the particle towards the microscope objective. This has been tested successfully with bright dye-doped polystyrene beads, but is insufficient for a particle emitting single photons.

Instead of trying to compensate this disadvantage of the current devices, it is advisable to design a new trap, that enables a larger opening angle corresponding to a larger effective numerical aperture. A first attempt can be seen in figure 7.1(a). The shown trap consists of four tungsten needles, creating the quadrupole potential in the needle plane, and two

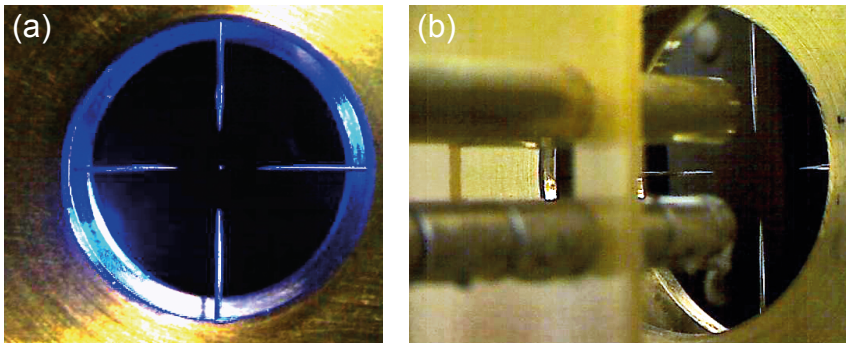

Figure 7.1.: Quadrupole needle trap. (a) A single lycopodium spore trapped in the needle trap with a tip-to-tip distance of 5 mm. (b) An additional segmented linear trap facilitates loading.

brass plates in front of and behind the needles, creating the static potential in the axial direction. The trap is similar to the linear end-cap trap presented in section 4.1.1, but the axial trap extension is compressed to a single point. The holes in the brass plates are large enough to use the full numerical aperture of 0.7 of a microscope objective with a working distance of 6 mm (Mitutoyo, Plan Apo 100x) to collect light from a particle in the trap center. Initial tests with lycopodium spores with an assumed diameter of 30 µm [338] and 5 µm silica microspheres show promising results. Unfortunately, the chance for stable injection from the electrospray is very low, due to a shallow trap potential. Nevertheless, confinement of single particles is possible by using a segmented linear trap in line with the needle trap, as shown in figure 7.1(b). Particles are injected into the linear trap as usual and transferred to the needle trap at the end. A similar technique has been demonstrated for pushing 0.44 µm sized polystyrene spheres from a linear to a planar trap [94]. In addition to the complex loading scheme, the needle trap lacks the possibility to characterize and store more than one particle at a time. But, it indicates that other (improved) trap types can be designed and used to levitate and study single nanoparticles containing single photon emitters. In a next step, other trap geometries should be tested, for instance two-level circuit board traps [163] or planar traps [94]. These traps can be designed to offer a large optical access, but can be segmented, and thus allow for multiple particle storage and handling, even with particle transfer through junctions [339, 340].

Trapping of nanoparticles with diameters down to a few nanometers is envisioned in the future. According to the stability condition in equation (3.18), stable confinement of smaller particles is challenging, as the decreased mass has to be met by changing other values, like the trap voltage, frequency or the particle charge. A large decrease of the trap voltage is unfavorable, as it means a drastic reduction of the pseudopotential (see equation (3.31)). Rather, increasing the trap frequency instead is recommended, but requires a change of the high-voltage amplifier. The third option is a reduction of the particle charge. This could be done by post-electrospray processes, like charge reduction by passing through an electron cloud from a filament. Alternatively, a different ionization method may be used. For instance, particles could be charged by friction and injected into the trap with a nebulizer [233] or a loudspeaker [74]. If a new ionization method is considered, it should (optimally) be applicable in vacuum, in order to avoid the transfer of particles from atmospheric pressure to vacuum, which is a complicated procedure that can often lead to particle loss. However, control over the amount of particle charge would also broaden the range of particles that can be stabilized in the trap at the same time. More sophisticated particle systems could be assembled, as long as the constituents fulfill the stability condition individually.

With the presented setup, any kind of nano- or microparticles can be investigated and manipulated, as long as they can be charged and injected. The trap allows for extensive isolation of individual particles from the environment, which may be useful in various research approaches. The absence of other materials enables the investigation of particles or systems levitated in the trap without symmetry breaking effects. The intrinsic mode structure of optical resonators and other trapped particles can be analyzed, as shown for silica microspheres and silver nanowires. Detailed studies of the influence of supporting substrates could be performed on a single particle before and after deposition from the trap. Additionally, particle handling is improved for levitated particles due to the absence of adhesion as well, which is a crucial issue for mechanical manipulation techniques on substrates. In particular, soft or organic nanoparticles could be prepared and ma-

nipulated with unmatched ease in the trap. For instance, molecules embedded in soft host matrices show interesting optical properties and may be used as photostable molecular single photon sources at room temperature [341]. First attempts from anthracene dissolved in diethyl ether and electrosprayed into the trap show promising results. Crystallization of anthracene particles from levitated liquid droplets was already observed as well as fluorescence emission from embedded dibenzoterrylene molecules. Unfortunately, crystal stability in the trap could not be ensured for more than a few seconds so far, but may be enabled in the future. Pursuing the stabilization of a single crystal with a single embedded fluorescing molecule seems to be favorable. The fragile particles could be coupled to plasmonic nanoantennas or waveguides with the developed assembly and deposition methods, which is difficult to achieve with the common scanning probe manipulation techniques. Additional control of pressure and humidity in the trap would enable stabilization of liquid droplets [342] and large biomolecules [343], expanding the potential capabilities of the trap setup to study chemical and biological processes with the tiniest amounts of substances [344, 345].

The most obvious future objective is trapping and detection of a single nanodiamond with a diameter of less than 50 nm containing one fluorescing defect center. Manipulation of the phonon spectrum of the nanocrystal is aspired in a thermally isolated particle that is stabilized in the trap in vacuum. The nanocrystal would show a high mechanical quality factor, which is ideal for studying optomechanical interactions. Optical refrigeration by an anti-Stokes process [228] can be envisioned for the nanodiamond isolated in the trap. For this, laser light red-shifted from the zero-phonon transition should be absorbed together with additional phonons nearby the NV defect center in the otherwise transparent diamond, as shown in figure 7.2. The diamond crystal should be cooled by radiative decay of the excited state photons with on-average higher energy than the incident laser. This scheme could be used to decrease the population of the phonon states and thus reduce the spectral broadening of the fluorescence emission. As a result, the radiative decay rate for emission at the zero phonon line would be enhanced, without the (typical) need for a cryostat setup. Laser cooling of solid materials has already been shown for rare-earth doped glasses and semiconductors [229], but special sample designs in combination with elaborate clamping are crucial to avoid fluorescence trapping and thermally decouple the

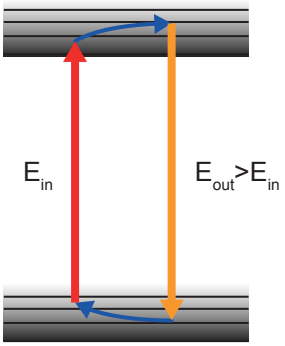

Figure 7.2.: Optical refrigeration cycle indicated in the energy level scheme of a single fluorescing defect center in an otherwise transparent diamond. Typically, emitted photons have a higher energy than absorbed photons in this anti-Stokes process (see text), which reduce the temperature of the diamond crystal.

sample from the environment, respectively. The two effects, which reduce the cooling efficiency, can be neglected for a nanocrystal levitated in a particle trap. In contrast to optical dipole traps [233, 234], fluorescence quenching and particle heating do not occur in an electric trap due to the absence of a strong trapping laser.

Last but not least, the deposition of particles or assembled systems from the trap may be improved by some sort of guided landing to increase the spatial accuracy. Using only the laser for the alignment is insufficient for exact placement on a structure, since the target disturbs the trajectory of the approaching particle by residual surface charges. This could be overcome by better control of the particle throughout the landing process, possibly through a modification of the static electric field or by additional electrodes attracting or repelling the particle towards the target point.

7.2.2. Laser-Induced Tuning of Particle Plasmon Resonances

For a complete understanding of the developed method for laser-induced tuning of individual plasmonic nanoparticles, clarification of the interplay of the involved forces is needed. The observed geometrical changes of a single gold nanoparticle in the focused laser beam are caused by optical forces. A detailed finite-element study could be used to understand the exact interplay of the radiation pressure and optical gradient force competing against gravitation and surface tension. In addition, the influence of surface effects between the particle and the supporting substrate is so far completely unknown.

Improvements of the developed tuning method may be achieved by several options. First, the experimental effort could be reduced by using the same laser for photoluminescence excitation and tuning. In the presented setup, the output power of the 457.9 nm laser line is barely strong enough for melting, and usage of the 514.5 nm laser line for both excitation and tuning is unfavorable as the associated long-pass filter in the detection path would cut off too much of the particle's photoluminescence signal. Second, the tuning range could be extended by using a variable laser wavelength, like from a tunable laser or a white light laser with a tunable optical band-pass filter, which allows following the spectral peak shift of the particle's absorption cross section, in order to keep the particle liquid without increasing the laser power. A more advanced approach may involve a precise control of the particle temperature, independent of the applied optical forces. This control could be attained by an additional heating or cooling channel. For instance, melting is not achieved for particles on the ITO-covered substrate due to an increase in heat flow away from the particle. By adjustment of the thermal conductivity of the particle environment, very high optical forces but comparatively low particle heating may enable a better control of the tuning progress and result. Third, oriented elongation of metal nanoparticles for orientation-dependent plasmon resonance tuning may be achieved by an oblique laser beam. Fourth, metal particles different from gold could be tuned with different laser wavelengths and intensities. All suggested extensions of the current work may be tested with reasonable upgrades of the presented setup and have the potential to greatly expand the usefulness and applicability of the tuning method.

The tuning method could be applied to match the plasmon resonance of a single metal nanoparticle to a nearby emitter, in order to enhance the performance of a single photon source. Such a hybrid system could be assembled from individual pre-characterized particles, like a gold nanosphere and a diamond nanocrystal containing a single NV defect center similar to the experiment shown in figure 6.15. Based on the knowledge gained

from chapter 6, now laser-induced tuning could be applied in a controlled way to one or more gold particles to set their plasmon resonances to the emission wavelength of the NV defect center. In addition, the distance between the emitters could be adjusted with the AFM to avoid coupling to dark plasmon modes reducing the quantum efficiency.

A. Material Models

Instead of using interpolated measurement data, analytical functions are often needed to describe the index of refraction of a certain material. Here, the material models used in this thesis are given.

The material models give the complex index of refraction n, which can also be expressed in terms of the relative permittivity ε_r and the relative permeability μ_r

$$n = n' + in'', \tag{A.1}$$
$$n = \sqrt{\varepsilon_r \mu_r}. \tag{A.2}$$

For a non-magnetic material μ_r equals 1 and the complex relative permittivity ε_r follows

$$\varepsilon_r = n^2, \tag{A.3}$$
$$= \varepsilon_r' + i\varepsilon_r'', \tag{A.4}$$

with

$$\varepsilon_r' = n'^2 - n''^2, \tag{A.5}$$
$$\varepsilon_r'' = 2n'n''. \tag{A.6}$$

The components of the complex refractive index can be calculated with

$$n' = \sqrt{\frac{\sqrt{\varepsilon_r'^2 + \varepsilon_r''^2} + \varepsilon_r'}{2}}, \tag{A.7}$$

$$n'' = \sqrt{\frac{\sqrt{\varepsilon_r'^2 + \varepsilon_r''^2} - \varepsilon_r'}{2}}. \tag{A.8}$$

$$\tag{A.9}$$

A.1. Silica

The index of refraction of fused silica is calculated with [346]

$$n' = \sqrt{1 + \frac{0.6961663\lambda^2}{\lambda^2 - 0.0684043^2} + \frac{0.4079426\lambda^2}{\lambda^2 - 0.1162414^2} + \frac{0.8974794\lambda^2}{\lambda^2 - 9.896161^2}}. \tag{A.10}$$

The imaginary part n'' is set to zero.

A.2. Gold

An analytical fit of the measured values [113] is used for a Drude-Lorentz model. It consists of one Drude term in combination with one or more Lorentz terms to approximate the relative permittivity of gold

$$\varepsilon(\omega) = \varepsilon_\infty - \frac{\omega_D^2}{\omega(\omega + i\gamma_D)} + \sum_j \frac{\Delta\varepsilon_j \Omega_j^2}{\Omega_j^2 - \omega(\omega + i\Gamma_j)}. \tag{A.11}$$

For the dielectric function shown in figure 2.5 a Drude term and one single Lorentz term are used. Table A.1 gives the parameters used, which are taken from [347].

	ε_∞	$\omega_D[\mathrm{s}^{-1}]$	$\gamma_D[\mathrm{s}^{-1}]$
Drude	5.9673	1.3280×10^{16}	1.0003×10^{16}
	$\Delta\varepsilon$	$\Omega[\mathrm{s}^{-1}]$	$\Gamma[\mathrm{s}^{-1}]$
Lorentz	1.09	4.0845×10^{15}	6.5885×10^{14}

Table A.1.: Parameters for the Drude-Lorentz model with a single Lorentz term to approximate the relative permittivity of gold [347].

In figure 6.10 [306] three Lorentz terms in addition to one Drude term are used. The parameters are given in table A.2

	ε_∞	$\omega_D[\mathrm{s}^{-1}]$	$\gamma_D[\mathrm{s}^{-1}]$
Drude	6.40	1.37×10^{16}	1.16×10^{14}
	$\Delta\varepsilon_j$	$\Omega_j[\mathrm{s}^{-1}]$	$\Gamma_j[\mathrm{s}^{-1}]$
Lorentz 1	1.51	4.42×10^{15}	1.54×10^{15}
Lorentz 2	1.02	5.56×10^{15}	1.83×10^{15}
Lorentz 3	0.80	6.72×10^{15}	1.79×10^{15}

Table A.2.: Parameters for the Drude-Lorentz model for gold used in the simulations of figure 6.10 [306].

B. Simple Model of a Spherical Resonator Coupled to a Tapered Optical Fiber

The intensity transmission through the coupled-cavity model shown in figure 5.26(a) and in figure B.1 is derived in this appendix. The coupling region between fiber and sphere is simplified to one point. It has four different ports where the electric field is estimated. E_1 and E_2 are the incident and the transmitted electric field in the waveguide, respectively, while their circulating equivalents in the cavity are E_3 and E_4. The transmission of the electric field across the coupling region is described by the parameter t, while the coupling between the waveguide and the cavity is given by $r = \sqrt{1 - t^2}$. The transmission constant α denotes the resonator loss.

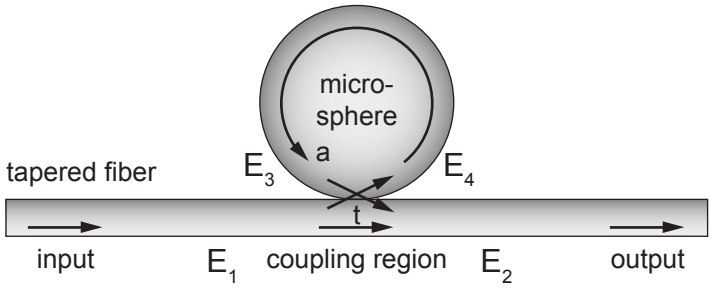

Figure B.1.: Model of the fiber-microsphere system to estimate the intensity transmission through the tapered fiber. The model geometry consists of a circular cavity coupled to a fiber waveguide. Also shown in figure 5.26(a).

B.1. Electric Field Intensities

In the frequency domain, the electric fields at the four ports of the coupling region are related by

$$E_2 = tE_1 + irE_3, \tag{B.1}$$

$$E_4 = irE_1 + tE_3. \tag{B.2}$$

After one round-trip in the cavity, the field E_4 is attenuated by the amplitude transmission $a = e^{\alpha L}$ to E_3 with a phase difference between E_3 and E_4 of $\phi = kL$, written as

$$E_3 = e^{\alpha L} e^{ikL} E_4 = a e^{i\phi} E_4, \tag{B.3}$$

with the wave number $k = \frac{2\pi}{\lambda}$ and the cavity length L, given by $L = 2\pi R$ for a circular resonator. Then, the electric field in the waveguide behind the coupling region, normalized

to the incident field, is given by

$$\frac{E_2}{E_1} = \frac{t - ae^{i\phi}}{1 - tae^{i\phi}}, \tag{B.4}$$

and the intensity transmitted through the waveguide coupled to the cavity can be calculated with

$$I_T = \left|\frac{E_2}{E_1}\right|^2 = \frac{a^2 + t^2 - 2at\cos(\phi)}{1 + a^2t^2 - 2at\cos(\phi)}. \tag{B.5}$$

The intensity inside the cavity is obtained in analogy from

$$I_C = \left|\frac{E_3}{E_1}\right|^2 = \frac{a^2r^2}{1 + a^2t^2 - 2at\cos(\phi)}. \tag{B.6}$$

B.2. Model for the Spectrum of the Halogen Lamp

The white-light emission spectrum of the halogen lamp I_L is modeled by a Gaussian function,

$$I_L \text{ (a.u.)} = \frac{A}{\sqrt{2\pi\sigma^2}} e^{-\frac{(\lambda-\mu)^2}{2\sigma^2}}, \tag{B.7}$$

with the parameters

$$A = 5 \times 10^{-3}, \tag{B.8}$$
$$\mu = 670\,\text{nm}, \tag{B.9}$$
$$\sigma = 85\,\text{nm}. \tag{B.10}$$

C. Steady-State Temperature Distribution for a Single Nanoparticle in a Focused Laser Beam

The model used to calculate the laser-induced heating of individual gold nanoparticles is explained in this appendix. The particle temperature is obtained by calculating the heat transfer to and from the particle [348]. The heat gain is determined by absorption of laser light by the particle. It is assumed that only thermal conduction reduces the heat in the particle, while free convection can be neglected here due to a very low Nusselt number [349]. As will be shown, thermal radiation is also of little impact for the final particle temperature.

The thermal diffusion equation is used to describe the temperature distribution $T(\mathbf{r})$

$$c\rho\frac{\partial T}{\partial t} = \nabla \cdot (\kappa(\mathbf{r})\nabla T(t,\mathbf{r})) + q(\mathbf{r}), \tag{C.1}$$

with c, ρ, and κ being the specific heat capacity, the density and the thermal conductivity, respectively. The heat source is given by the power density q. In the steady-state regime the temperature is constant over time and the left-hand side of equation (C.1) vanishes. The thermal conductivity is assumed to be constant inside the particle with radius R (index p) and also for the surrounding medium (index f). As a result, two equations are obtained for the different regions, written as

$$0 = \kappa_p \frac{1}{r^2}\frac{\partial}{\partial r}(r^2\frac{\partial T}{\partial r}) + q, \qquad (r < R) \tag{C.2}$$

$$0 = \kappa_f \frac{1}{r^2}\frac{\partial}{\partial r}(r^2\frac{\partial T}{\partial r}). \qquad (r > R) \tag{C.3}$$

In this step spherical coordinates are also introduced. The angle dependencies are neglected by assuming an isotropic environment with an effective thermal conductivity κ_f. The resulting one-dimensional heat conduction problem allows for an analytical treatability. The temperature distribution also has to fulfill the following constraints:

$$T \to T_0 \text{ for } r \to \infty, \tag{C.4}$$

$$T \text{ finite at } r = 0, \tag{C.5}$$

$$T(r = R - 0) = T(r = R + 0) = T_s, \tag{C.6}$$

$$\kappa_p \frac{\partial T(r = R - 0)}{\partial r} = \kappa_f \frac{\partial T(r = R + 0)}{\partial r}. \tag{C.7}$$

T_0 is the temperature of the surrounding medium far away from the particle, and T_s is the surface temperature of the particle.

The general solutions of equations (C.2) and (C.3) are

$$T(r) = -\frac{q}{6\kappa_p} r^2 - \frac{C_1}{r} + C_2, \qquad (r < R) \tag{C.8}$$

$$T(r) = -\frac{C_3}{r} + C_4, \qquad (r > R) \tag{C.9}$$

and the constants C_1 to C_4 can be derived from equations (C.4) to (C.7) to get

$$C_1 = 0, \tag{C.10}$$

$$C_2 = \frac{R^2 q}{3}\left(\frac{1}{\kappa_f} + \frac{1}{2\kappa_p}\right) + T_0, \tag{C.11}$$

$$C_3 = -\frac{R^3 q}{3\kappa_f}, \tag{C.12}$$

$$C_4 = T_0. \tag{C.13}$$

Finally, the equations for the temperature distribution are

$$T(r) = T_0 - \frac{q}{6\kappa_p} r^2 + \frac{R^2 q}{3}\left(\frac{1}{\kappa_f} + \frac{1}{2\kappa_p}\right), \qquad (r < R) \tag{C.14}$$

$$T(r) = T_0 + \frac{R^3 q}{3\kappa_f}\frac{1}{r}. \qquad (r > R) \tag{C.15}$$

The power Q of the external heat source is determined by the laser intensity I_0 and the absorption cross section of the particle C_{abs} [350] calculated by equation (2.42)

$$Q_{abs} = C_{abs} I_0. \tag{C.16}$$

From this, the power density is easily derived with the particle volume V by

$$q_{abs} = \frac{Q_{abs}}{V} = \frac{C_{abs} I_0}{\frac{4}{3}\pi R^3}. \tag{C.17}$$

Combining equation (C.15) and equation (C.17) results in the final expression for the particle's surface temperature

$$T_s = T(R) = T_0 + \frac{C_{abs} I_0}{4\pi\kappa_f R}. \tag{C.18}$$

The parameters used for this model are given in table C.1. The laser intensity I_0 is obtained from the laser power P by

$$I_0 = \frac{P}{\pi r_{spot}^2}, \tag{C.19}$$

with a diffraction-limited laser spot radius r_{spot}, calculated with the numerical aperture of the microscope objective NA and the laser wavelength λ by [351]

$$r_{spot} = 0.61\frac{\lambda}{2\,\mathrm{NA}}. \tag{C.20}$$

Parameter	Value
R	$40\,\mathrm{nm}$
P	$0.315\,\mathrm{mW}$
NA	1.4
T_0	$300\,\mathrm{K}$
κ_p	$318\,\mathrm{W\,m^{-1}\,K^{-1}}$ [348]
κ_f	$0.23\,\mathrm{W\,m^{-1}\,K^{-1}}$ [324]

Table C.1.: Parameters used for the particle heating model.

It is obvious that equation (C.17) is justified only for particles with radius $R < r_{spot}$. For larger particles, the heating power has to scale with the cross-sectional particle area that is covered by the laser spot.

To account for the presence of air and the glass substrate in the particle environment, an effective thermal conductivity of the surrounding medium κ_f is assumed from finite-element calculations of similar configurations [324].

To verify that thermal radiation can be neglected here, the Stefan-Boltzmann law [136]

$$Q_{rad} = -\epsilon\sigma_{SB}A(T_s^4 - T_0^4), \tag{C.21}$$

is used, with the Stefan-Boltzmann constant $\sigma_{SB} = 5.67 \times 10^{-8}\,\frac{\mathrm{W}}{\mathrm{m^2\,K^4}}$, the radiating surface $A = 4\pi R^2$, and the emissivity $\epsilon \in [0, 1]$, which accounts for the deviation from a perfect black body.

In the experiment, the minimum laser intensity needed to modify a spherical gold nanoparticle with a radius of $R = 40\,\mathrm{nm}$ is $8 \times 10^5\,\mathrm{W\,cm^{-2}}$. At a wavelength of 514.5 nm its absorption cross section is calculated to be $C_{abs} = 1.626 \times 10^{-14}\,\mathrm{m^2}$, giving an absorbed heating power Q_{abs} on the order of $10^{-4}\,\mathrm{W}$ (see equation (C.16)). In comparison, the power Q_{rad} radiated from a perfect black body at the melting temperature of gold ($1337\,\mathrm{K}$ [325]) into a room with a temperature of $T_0 = 300\,\mathrm{K}$ is only on the order of $10^{-9}\,\mathrm{W}$. Even with a black body temperature at the boiling point of gold ($3243\,\mathrm{K}$ [352]), the radiated power is on the order of $10^{-7}\,\mathrm{W}$, which is still three orders of magnitude smaller than the heating power. Thus, thermal radiation is insignificant in this model for the expected particle temperatures.

Abbreviations

AFM	atomic force microscope
CCD	charge-coupled device
CQED	cavity quantum electrodynamic
CROW	coupled resonant optical waveguide
DF	dark-field
EMCCD	electron multiplying CCD
ESI	electrospray ionization
FDTD	finite difference time domain
FWHM	full width at half-maximum
GND	(electrical) ground
HV	high voltage
ITO	indium tin oxide
LSP	localized surface plasmon
MOSFET	metal-oxide-semiconductor field-effect transistor
NA	numerical aperture
ND	neutral density
NSOM	near-field scanning optical microscope
NV	nitrogen vacancy
NW	nanowire
PL	photoluminescence
PSF	point spread function
QD	quantum dot
SEM	scanning electron microscope
SHV	safe high voltage
SP	surface plasmon
SPP	surface plasmon polariton
TE	transverse electric
TEM	transverse electromagnetic
THD	total harmonic distortion
TM	transverse magnetic
VP	volume plasmon
WGM	whispering-gallery mode
ZPL	zero phonon line

Bibliography

[1] Andreas W. Schell, Philip Engel, Julia F. M. Werra, Christian Wolff, Kurt Busch, and Oliver Benson. Scanning Single Quantum Emitter Fluorescence Lifetime Imaging: Quantitative Analysis of the Local Density of Photonic States. *Nano Letters*, 14(5):2623–2627, 2014.

[2] Oliver Benson. Assembly of hybrid photonic architectures from nanophotonic constituents. *Nature*, 480(7376):193–199, 2011.

[3] K. K. Nanda, S. N. Sahu, and S. N. Behera. Liquid-drop model for the size-dependent melting of low-dimensional systems. *Physical Review A*, 66(1):013208, 2002.

[4] Richard C. Tolman. The Effect of Droplet Size on Surface Tension. *The Journal of Chemical Physics*, 17(3):333, 1949.

[5] Gregory D. Scholes and Garry Rumbles. Excitons in nanoscale systems. *Nature Materials*, 5(9):683–696, 2006.

[6] Jana Olson, Sergio Dominguez-Medina, Anneli Hoggard, Lin-Yung Wang, Wei-Shun Chang, and Stephan Link. Optical characterization of single plasmonic nanoparticles. *Chemical Society Reviews*, 44(1):40–57, 2015.

[7] Arseniy I. Kuznetsov, Andrey E. Miroshnichenko, Yuan Hsing Fu, JingBo Zhang, and Boris Luk'yanchuk. Magnetic light. *Scientific Reports*, 2:492, 2012.

[8] D. J. Norris and M. G. Bawendi. Measurement and assignment of the size-dependent optical spectrum in CdSe quantum dots. *Physical Review B*, 53(24):16338, 1996.

[9] K. Lance Kelly, Eduardo Coronado, Lin Lin Zhao, and George C. Schatz. The Optical Properties of Metal Nanoparticles: The Influence of Size, Shape, and Dielectric Environment. *The Journal of Physical Chemistry B*, 107(3):668–677, 2003.

[10] Kerry J. Vahala. Optical microcavities. *Nature*, 424(6950):839–846, 2003.

[11] Celso Mello Donegá, editor. *Nanoparticles: Workhorses of Nanoscience*. Springer-Verlag, Berlin Heidelberg, 2014.

[12] E. Hutter and J. H. Fendler. Exploitation of Localized Surface Plasmon Resonance. *Advanced Materials*, 16(19):1685–1706, 2004.

[13] Andrey L. Rogach, editor. *Semiconductor Nanocrystal Quantum Dots: Synthesis, Assembly, Spectroscopy, and Applications*. Springer-Verlag, Wien, 2008.

[14] Alexios Beveratos, Rosa Brouri, Thierry Gacoin, André Villing, Jean-Philippe Poizat, and Philippe Grangier. Single Photon Quantum Cryptography. *Physical Review Letters*, 89(18):187901, 2002.

[15] M. S. Tame, K. R. McEnery, Ş. K. Özdemir, J. Lee, S. A. Maier, and M. S. Kim. Quantum plasmonics. *Nature Physics*, 9(6):329–340, 2013.

[16] Matthias D. Wissert, Birgit Rudat, Uli Lemmer, and Hans-Jürgen Eisler. Quantum dots as single-photon sources: Antibunching via two-photon excitation. *Physical Review B*, 83(11):113304, 2011.

[17] Harry A. Atwater and Albert Polman. Plasmonics for improved photovoltaic devices. *Nature Materials*, 9(3):205–213, 2010.

[18] Graham H. Carey, Ahmed L. Abdelhady, Zhijun Ning, Susanna M. Thon, Osman M. Bakr, and Edward H. Sargent. Colloidal Quantum Dot Solar Cells. *Chemical Reviews*, 115(23):12732–12763, 2015.

[19] Katherine A. Willets and Richard P. Van Duyne. Localized Surface Plasmon Resonance Spectroscopy and Sensing. *Annual Review of Physical Chemistry*, 58(1):267–297, 2007.

[20] Jeffrey N. Anker, W. Paige Hall, Olga Lyandres, Nilam C. Shah, Jing Zhao, and Richard P. Van Duyne. Biosensing with plasmonic nanosensors. *Nature Materials*, 7(6):442–453, 2008.

[21] Chi-Cheng Fu, Hsu-Yang Lee, Kowa Chen, Tsong-Shin Lim, Hsiao-Yun Wu, Po-Keng Lin, Pei-Kuen Wei, Pei-Hsi Tsao, Huan-Cheng Chang, and Wunshain Fann. Characterization and application of single fluorescent nanodiamonds as cellular biomarkers. *Proceedings of the National Academy of Sciences*, 104(3):727, 2007.

[22] Xiaohua Huang and Mostafa A. El-Sayed. Gold nanoparticles: Optical properties and implementations in cancer diagnosis and photothermal therapy. *Journal of Advanced Research*, 1(1):13–28, 2010.

[23] Xuewen He and Nan Ma. An overview of recent advances in quantum dots for biomedical applications. *Colloids and Surfaces B: Biointerfaces*, 124:118–131, 2014.

[24] Emilie Genin, Zhenghong Gao, Juan A. Varela, Jonathan Daniel, Talia Bsaibess, Isabelle Gosse, Laurent Groc, Laurent Cognet, and Mireille Blanchard-Desce. "Hyperbright" Near-Infrared Emitting Fluorescent Organic Nanoparticles for Single Particle Tracking. *Advanced Materials*, 26(14):2258–2261, 2014.

[25] Yasuhiro Shirasaki, Geoffrey J. Supran, Moungi G. Bawendi, and Vladimir Bulović. Emergence of colloidal quantum-dot light-emitting technologies. *Nature Photonics*, 7(1):13–23, 2013.

[26] P. Michler, A. Imamoğlu, M. D. Mason, P. J. Carson, G. F. Strouse, and S. K. Buratto. Quantum correlation among photons from a single quantum dot at room temperature. *Nature*, 406:968–970, 2000.

[27] F. Jelezko and J. Wrachtrup. Single defect centres in diamond: A review. *physica status solidi (a)*, 203(13):3207–3225, 2006.

[28] Sumin Choi, Brett C. Johnson, Stefania Castelletto, Cuong Ton-That, Matthew R. Phillips, and Igor Aharonovich. Single photon emission from ZnO nanoparticles. *Applied Physics Letters*, 104(26):261101, 2014.

[29] Stefan Schietinger, Michael Barth, Thomas Aichele, and Oliver Benson. Plasmon-Enhanced Single Photon Emission from a Nanoassembled Metal-Diamond Hybrid Structure at Room Temperature. *Nano Letters*, 9(4):1694–1698, 2009.

[30] A. G. Curto, G. Volpe, T. H. Taminiau, M. P. Kreuzer, R. Quidant, and N. F. van Hulst. Unidirectional Emission of a Quantum Dot Coupled to a Nanoantenna. *Science*, 329(5994):930–933, 2010.

[31] Stefan Schietinger, Tim Schröder, and Oliver Benson. One-by-One Coupling of Single Defect Centers in Nanodiamonds to High-Q Modes of an Optical Microresonator. *Nano Letters*, 8(11):3911–3915, 2008.

[32] Makoto Kuwata-Gonokami, Kenji Takeda, Hiroaki Yasuda, and Kazuhiro Ema. Laser Emission from Dye-Doped Polystyrene Microsphere. *Japanese Journal of Applied Physics*, 31(Part 2, No. 2A):L99–L101, 1992.

[33] Steven J. Oldenburg, Christine C. Genick, Keith A. Clark, and David A. Schultz. Base pair mismatch recognition using plasmon resonant particle labels. *Analytical Biochemistry*, 309(1):109–116, 2002.

[34] F. Dolde, H. Fedder, M. W. Doherty, T. Nöbauer, F. Rempp, G. Balasubramanian, T. Wolf, F. Reinhard, L. C. L. Hollenberg, F. Jelezko, and J. Wrachtrup. Electric-field sensing using single diamond spins. *Nature Physics*, 7(6):459–463, 2011.

[35] J. R. Maze, P. L. Stanwix, J. S. Hodges, S. Hong, J. M. Taylor, P. Cappellaro, L. Jiang, M. V. Gurudev Dutt, E. Togan, A. S. Zibrov, A. Yacoby, R. L. Walsworth, and M. D. Lukin. Nanoscale magnetic sensing with an individual electronic spin in diamond. *Nature*, 455(7213):644–647, 2008.

[36] Markus Gregor, Christoph Pyrlik, Rico Henze, Andreas Wicht, Achim Peters, and Oliver Benson. An alignment-free fiber-coupled microsphere resonator for gas sensing applications. *Applied Physics Letters*, 96(23):231102, 2010.

[37] Michael Barth, Stefan Schietinger, Tim Schröder, Thomas Aichele, and Oliver Benson. Controlled coupling of NV defect centers to plasmonic and photonic nanostructures. *Journal of Luminescence*, 130(9):1628–1634, 2010.

[38] B. Möller, U. Woggon, and M. V. Artemyev. Photons in coupled microsphere resonators. *Journal of Optics A: Pure and Applied Optics*, 8(4):S113–S121, 2006.

[39] D. E. Chang, C. A. Regal, S. B. Papp, D. J. Wilson, J. Ye, O. Painter, H. J. Kimble, and P. Zoller. Cavity opto-mechanics using an optically levitated nanosphere. *Proceedings of the National Academy of Sciences*, 107(3):1005–1010, 2010.

[40] Jan Gieseler, Lukas Novotny, and Romain Quidant. Thermal nonlinearities in a nanomechanical oscillator. *Nature Physics*, 9(12):806–810, 2013.

[41] C. B. Murray, D. J. Norris, and M. G. Bawendi. Synthesis and Characterization of Nearly Monodisperse CdE (E= Sulfur, Selenium, Ttellurium) Semiconductor Nanocrystallites. *Journal of the American Chemical Society*, 115(19):8706–8715, 1993.

[42] Xianmao Lu, Matthew Rycenga, Sara E. Skrabalak, Benjamin Wiley, and Younan Xia. Chemical Synthesis of Novel Plasmonic Nanoparticles. *Annual Review of Physical Chemistry*, 60(1):167–192, 2009.

[43] Manoj B. Gawande, Anandarup Goswami, Tewodros Asefa, Huizhang Guo, Ankush V. Biradar, Dong-Liang Peng, Radek Zboril, and Rajender S. Varma. Core–shell nanoparticles: synthesis and applications in catalysis and electrocatalysis. *Chemical Society Reviews*, 44(21):7540–7590, 2015.

[44] Younan Xia, Yujie Xiong, Byungkwon Lim, and Sara E. Skrabalak. Shape-Controlled Synthesis of Metal Nanocrystals: Simple Chemistry Meets Complex Physics? *Angewandte Chemie (International Edition)*, 48(1):60–103, 2009.

[45] Jonathan M. Ward, Yuqiang Wu, Krimo Khalfi, and Síle Nic Chormaic. Short vertical tube furnace for the fabrication of doped glass microsphere lasers. *Review of Scientific Instruments*, 81(7):073106, 2010.

[46] John C. Hulteen, David A. Treichel, Matthew T. Smith, Michelle L. Duval, Traci R. Jensen, and Richard P. Van Duyne. Nanosphere Lithography: Size-Tunable Silver Nanoparticle and Surface Cluster Arrays. *The Journal of Physical Chemistry B*, 103(19):3854–3863, 1999.

[47] Raghavendra Palankar, Nikolay Medvedev, Alena Rong, and Mihaela Delcea. Fabrication of Quantum Dot Microarrays Using Electron Beam Lithography for Applications in Analyte Sensing and Cellular Dynamics. *ACS Nano*, 7(5):4617–4628, 2013.

[48] A. Krüger, F. Kataoka, M. Ozawa, T. Fujino, Y. Suzuki, A. E. Aleksenskii, A. Ya. Vul', and E. Ōsawa. Unusually tight aggregation in detonation nanodiamond: Identification and disintegration. *Carbon*, 43(8):1722–1730, 2005.

[49] Sajjad Amirkhanlou, Mostafa Ketabchi, and Nader Parvin. Nanocrystalline/nanoparticle ZnO synthesized by high energy ball milling process. *Materials Letters*, 86:122–124, 2012.

[50] N. Haustrup and G. M. O'Connor. Nanoparticle Generation During Laser Ablation and Laser-Induced Liquefaction. *Physics Procedia*, 12:46–53, 2011.

[51] Tetsuya Makimura, Yasuhiko Kunii, and Kouichi Murakami. Light Emission from Nanometer-Sized Silicon Particles Fabricated by the Laser Ablation Method. *Japanese Journal of Applied Physics*, 35(Part 1, No. 9A):4780–4784, 1996.

[52] R. A. Sperling and W. J. Parak. Surface modification, functionalization and bioconjugation of colloidal inorganic nanoparticles. *Philosophical Transactions of the Royal Society A*, 368(1915):1333–1383, 2010.

[53] R. Subbiah, M. Veerapandian, and K. S. Yun. Nanoparticles: Functionalization and Multifunctional Applications in Biomedical Sciences. *Current Medicinal Chemistry*, 17(36):4559–4577, 2010.

[54] Michael W. Davidson and Mortimer Abramowitz. Optical Microscopy. In Joseph P. Hornak, editor, *Encyclopedia of Imaging Science and Technology*. John Wiley & Sons, Inc., Hoboken, NJ, USA, 2002.

[55] Bridget Ingham. X-ray scattering characterisation of nanoparticles. *Crystallography Reviews*, 21(4):229–303, 2015.

[56] Jaysen Nelayah, Mathieu Kociak, Odile Stéphan, F. Javier García de Abajo, Marcel Tencé, Luc Henrard, Dario Taverna, Isabel Pastoriza-Santos, Luis M. Liz-Marzán, and Christian Colliex. Mapping surface plasmons on a single metallic nanoparticle. *Nature Physics*, 3(5):348–353, 2007.

[57] Michael Barth, Stefan Schietinger, Sabine Fischer, Jan Becker, Nils Nüsse, Thomas Aichele, Bernd Löchel, Carsten Sönnichsen, and Oliver Benson. Nanoassembled Plasmonic-Photonic Hybrid Cavity for Tailored Light-Matter Coupling. *Nano Letters*, 10(3):891–895, 2010.

[58] Matthias Gerlach, Yury P. Rakovich, and John F. Donegan. Radiation-pressure-induced mode splitting in a spherical microcavity with an elastic shell. *Optics Express*, 15(6):3597–3606, 2007.

[59] Yongjun Bao, Bin Zhao, Xinyu Tang, Dongjie Hou, Jian Cai, Shan Tang, Junsong Liu, Fei Wang, and Tian Cui. Tuning surface plasmon resonance by the plastic deformation of Au nanoparticles within a diamond anvil cell. *Applied Physics Letters*, 107(20):201909, 2015.

[60] Jianbo Zeng, Fusheng Zhao, Ming Li, Chien-Hung Li, T. Randall Lee, and Wei-Chuan Shih. Morphological control and plasmonic tuning of nanoporous gold disks by surface modifications. *J. Mater. Chem. C*, 3(2):247–252, 2015.

[61] David G. Grier. A revolution in optical manipulation. *Nature*, 424(6950):810–816, 2003.

[62] Pavel Zemánek, Alexandr Jonáš, Libor Šrámek, and Miroslav Liška. Optical trapping of nanoparticles and microparticles by a Gaussian standing wave. *Optics Letters*, 24(21):1448–1450, 1999.

[63] Masao Takamoto, Feng-Lei Hong, Ryoichi Higashi, and Hidetoshi Katori. An optical lattice clock. *Nature*, 435(7040):321–324, 2005.

[64] D. Foresti, M. Nabavi, M. Klingauf, A. Ferrari, and D. Poulikakos. Acoustophoretic contactless transport and handling of matter in air. *Proceedings of the National Academy of Sciences*, 110(31):12549–12554, 2013.

[65] Adam E. Cohen and W. E. Moerner. Method for trapping and manipulating nanoscale objects in solution. *Applied Physics Letters*, 86(9):093109, 2005.

[66] Samuel Earnshaw. On the Nature of the Molecular Forces which regulate the Constitution of the Luminiferous Ether. *Transactions of the Cambridge Philosophical Society*, 7:97–112, 1842.

[67] Lowell S. Brown and Gerald Gabrielse. Geonium theory: Physics of a single electron or ion in a Penning trap. *Reviews of Modern Physics*, 58(1):233–311, 1986.

[68] Wolfgang Paul. Electromagnetic traps for charged and neutral particles. *Reviews of Modern Physics*, 62(3):531–540, 1990.

[69] http://www.nobelprize.org/nobel_prizes/physics/laureates/1989/. The Nobel Prize in Physics, 1989. Accessed 10 April 2015.

[70] W. Neuhauser, M. Hohenstatt, P. E. Toschek, and H. Dehmelt. Localized visible Ba^+ mono-ion oscillator. *Physical Review A*, 22(3):1137, 1980.

[71] Erhard Fischer. Die dreidimensionale Stabilisierung von Ladungsträgern in einem Vierpolfeld. *Zeitschrift für Physik*, 156(1):1–26, 1959.

[72] R. F. Wuerker, H. Shelton, and R. V. Langmuir. Electrodynamic Containment of Charged Particles. *Journal of Applied Physics*, 30(3):342, 1959.

[73] H. Winter and H. W. Ortjohann. Simple demonstration of storing macroscopic particles in a ''Paul trap''. *American Journal of Physics*, 59(9):807, 1991.

[74] Stephan Schlemmer, Jens Illemann, Stefan Wellert, and Dieter Gerlich. Nondestructive high-resolution and absolute mass determination of single charged particles in a three-dimensional quadrupole trap. *Journal of Applied Physics*, 90(10):5410, 2001.

[75] J. C. Bergquist, D. J. Wineland, Wayne M. Itano, Hamid Hemmati, H.-U. Daniel, and G. Leuchs. Energy and Radiative Lifetime of the $5d^9\ 6s^2\ ^2D_{5/2}$ State in Hg II by Doppler-Free Two-Photon Laser Spectroscopy. *Physical Review Letters*, 55(15):1567, 1985.

[76] S. Arnold and L. M. Folan. Fluorescence spectrometer for a single electrodynamically levitated microparticle. *Review of Scientific Instruments*, 57(9):2250, 1986.

[77] Th. Sauter, R. Blatt, W. Neuhauser, and P. E. Toschek. 'Quantum Jumps' Observed in the Fluorescence of a Single Ion. *Optics Communications*, 60(5):287–292, 1986.

[78] H. S. Margolis, G. P. Barwood, G. Huang, H. A. Klein, S. N. Lea, K. Szymaniec, and P. Gill. Hertz-Level Measurement of the Optical Clock Frequency in a Single $^{88}Sr^+$ Ion. *Science*, 306(5700):1355–1358, 2004.

[79] T. Rosenband, D. B. Hume, P. O. Schmidt, C. W. Chou, A. Brusch, L. Lorini, W. H. Oskay, R. E. Drullinger, T. M. Fortier, J. E. Stalnaker, S. A. Diddams, W. C. Swann, N. R. Newbury, W. M. Itano, D. J. Wineland, and J. C. Bergquist. Frequency Ratio of Al^+ and Hg^+ Single-Ion Optical Clocks; Metrology at the 17th Decimal Place. *Science*, 319(5871):1808–1812, 2008.

[80] C. W. Chou, D. B. Hume, J. C. J. Koelemeij, D. J. Wineland, and T. Rosenband. Frequency Comparison of Two High-Accuracy Al^+ Optical Clocks. *Physical Review Letters*, 104(7):070802, 2010.

[81] J. I. Cirac and P. Zoller. Quantum computations with cold trapped ions. *Physical Review Letters*, 74(20):4091, 1995.

[82] C. Monroe, D. M. Meekhof, B. E. King, W. M. Itano, and D. J. Wineland. Demonstration of a Fundamental Quantum Logic Gate. *Physical Review Letters*, 75(25):4714, 1995.

[83] D. Kielpinski, C. Monroe, and D. J. Wineland. Architecture for a large-scale ion-trap quantum computer. *Nature*, 417(6890):709–711, 2002.

[84] K. Pyka, J. Keller, H. L. Partner, R. Nigmatullin, T. Burgermeister, D. M. Meier, K. Kuhlmann, A. Retzker, M. B. Plenio, W. H. Zurek, A. del Campo, and T. E. Mehlstäubler. Topological defect formation and spontaneous symmetry breaking in ion Coulomb crystals. *Nature Communications*, 4:2291, 2013.

[85] Rainer Blatt and David Wineland. Entangled states of trapped atomic ions. *Nature*, 453(7198):1008–1015, 2008.

[86] P. Schindler, M. Müller, D. Nigg, J. T. Barreiro, E. A. Martinez, M. Hennrich, T. Monz, S. Diehl, P. Zoller, and R. Blatt. Quantum simulation of dynamical maps with trapped ions. *Nature Physics*, 9(6):361–367, 2013.

[87] J. D. Prestage, G. J. Dick, and L. Maleki. New ion trap for frequency standard applications. *Journal of Applied Physics*, 66(3):1013–1017, 1989.

[88] C. A. Schrama, E. Peik, W. W. Smith, and H. Walther. Novel miniature ion traps. *Optics Communications*, 101(1-2):32–36, 1993.

[89] S. R. Jefferts, C. Monroe, E. W. Bell, and D. J. Wineland. Coaxial-resonator-driven rf (Paul) trap for strong confinement. *Physical Review A*, 51(4):3112, 1995.

[90] Zheng Ouyang, Guangxiang Wu, Yishu Song, Hongyan Li, Wolfgang R. Plass, and R. Graham Cooks. Rectilinear Ion Trap: Concepts, Calculations, and Analytical Performance of a New Mass Analyzer. *Analytical Chemistry*, 76(16):4595–4605, 2004.

[91] L. Deslauriers, S. Olmschenk, D. Stick, W. K. Hensinger, J. Sterk, and C. Monroe. Scaling and Suppression of Anomalous Heating in Ion Traps. *Physical Review Letters*, 97(10):103007, 2006.

[92] Dieter Gerlich. Ion-Neutral Collisions in a 22-Pole Trap at Very Low Energies. *Physica Scripta*, T59:256–263, 1995.

[93] S. Seidelin, J. Chiaverini, R. Reichle, J. J. Bollinger, D. Leibfried, J. Britton, J. H. Wesenberg, R. B. Blakestad, R. J. Epstein, D. B. Hume, W. M. Itano, J. D. Jost, C. Langer, R. Ozeri, N. Shiga, and D. J. Wineland. Microfabricated Surface-Electrode Ion Trap for Scalable Quantum Information Processing. *Physical Review Letters*, 96(25):253003, 2006.

[94] C. E. Pearson, D. R. Leibrandt, W. S. Bakr, W. J. Mallard, K. R. Brown, and I. L. Chuang. Experimental investigation of planar ion traps. *Physical Review A*, 73(3):032307, 2006.

[95] Robert Maiwald, Dietrich Leibfried, Joe Britton, James C. Bergquist, Gerd Leuchs, and David J. Wineland. Stylus ion trap for enhanced access and sensing. *Nature Physics*, 5(8):551–554, 2009.

[96] Stephan Link and Mostafa A. El-Sayed. Spectral Properties and Relaxation Dynamics of Surface Plasmon Electronic Oscillations in Gold and Silver Nanodots and Nanorods. *The Journal of Physical Chemistry B*, 103(40):8410–8426, 1999.

[97] Jeffrey M. McMahon, George C. Schatz, and Stephen K. Gray. Plasmonics in the ultraviolet with the poor metals Al, Ga, In, Sn, Tl, Pb, and Bi. *Physical Chemistry Chemical Physics*, 15:5415–5423, 2013.

[98] Gururaj V. Naik, Vladimir M. Shalaev, and Alexandra Boltasseva. Alternative Plasmonic Materials: Beyond Gold and Silver. *Advanced Materials*, 25(24):3264–3294, 2013.

[99] M. Valden, X. Lai, and D. W. Goodman. Onset of Catalytic Activity of Gold Clusters on Titania with the Appearance of Nonmetallic Properties. *Science*, 281(5383):1647–1650, 1998.

[100] Hugh H. Richardson, Zackary N. Hickman, Alexander O. Govorov, Alyssa C. Thomas, Wei Zhang, and Martin E. Kordesch. Thermooptical Properties of Gold Nanoparticles Embedded in Ice: Characterization of Heat Generation and Melting. *Nano Letters*, 6(4):783–788, 2006.

[101] Lev Dykman and Nikolai Khlebtsov. Gold nanoparticles in biomedical applications: recent advances and perspectives. *Chemical Society Reviews*, 41(6):2256–2282, 2012.

[102] Sergei Kühn, Ulf Håkanson, Lavinia Rogobete, and Vahid Sandoghdar. Enhancement of Single-Molecule Fluorescence Using a Gold Nanoparticle as an Optical Nanoantenna. *Physical Review Letters*, 97(1):017402, 2006.

[103] Markus Pfeiffer, Klas Lindfors, Christian Wolpert, Paola Atkinson, Mohamed Benyoucef, Armando Rastelli, Oliver G. Schmidt, Harald Giessen, and Markus Lippitz. Enhancing the Optical Excitation Efficiency of a Single Self-Assembled Quantum Dot with a Plasmonic Nanoantenna. *Nano Letters*, 10(11):4555–4558, 2010.

[104] Vincenzo Giannini, Antonio I. Fernández-Domínguez, Susannah C. Heck, and Stefan A. Maier. Plasmonic Nanoantennas: Fundamentals and Their Use in Controlling the Radiative Properties of Nanoemitters. *Chemical Reviews*, 111(6):3888–3912, 2011.

[105] Michelle Duval Malinsky, K. Lance Kelly, George C. Schatz, and Richard P. Van Duyne. Nanosphere Lithography: Effect of Substrate on the Localized Surface Plasmon Resonance Spectrum of Silver Nanoparticles. *The Journal of Physical Chemistry B*, 105(12):2343–2350, 2001.

[106] Craig F. Bohren and Donald R. Huffman. *Absorption and Scattering of Light by Small Particles*. John Wiley & Sons, Inc., New York, 1983.

[107] Stefan A. Maier. *Plasmonics: Fundamentals and Applications*. Springer, New York, 2007.

[108] J. M. Pitarke, V. M. Silkin, E. V. Chulkov, and P. M. Echenique. Theory of surface plasmons and surface-plasmon polaritons. *Reports on Progress in Physics*, 70(1):1–87, 2007.

[109] Gustav Mie. Beiträge zur Optik trüber Medien, speziell kolloidaler Metallösungen. *Annalen der Physik*, 330(3):377–445, 1908.

[110] Lord Rayleigh. The problem of the whispering gallery. *Philosophical Magazine Series 6*, 20(120):1001–1004, 1910.

[111] Valery V. Nesvizhevsky, Alexei Yu. Voronin, Robert Cubitt, and Konstantin V. Protasov. Neutron whispering gallery. *Nature Physics*, 6(2):114–117, 2010.

[112] Kerry Vahala, editor. *Optical Microcavities*. Number 5 in Advanced Series in Applied Physics. World Scientific Publishing, Singapore, 2004.

[113] P. B. Johnson and R. W. Christy. Optical Constants of the Noble Metals. *Physical Review B*, 6(12):4370, 1972.

[114] Erwin Kretschmann. Die Bestimmung optischer Konstanten von Metallen durch Anregung von Oberflächenplasmaschwingungen. *Zeitschrift für Physik*, 241(4):313–324, 1971.

[115] Andreas Otto. Excitation of Nonradiative Surface Plasma Waves in Silver by the Method of Frustrated Total Reflection. *Zeitschrift für Physik*, 216(4):398–410, 1968.

[116] Harald Ditlbacher, Andreas Hohenau, Dieter Wagner, Uwe Kreibig, Michael Rogers, Ferdinand Hofer, Franz R. Aussenegg, and Joachim R. Krenn. Silver Nanowires as Surface Plasmon Resonators. *Physical Review Letters*, 95(25):257403, 2005.

[117] Lucía B. Scaffardi and Jorge O. Tocho. Size dependence of refractive index of gold nanoparticles. *Nanotechnology*, 17(5):1309–1315, 2006.

[118] Jeff W. Lichtman and José-Angel Conchello. Fluorescence microscopy. *Nature Methods*, 2(12):910–919, 2005.

[119] Erich E. Hoover and Jeff A. Squier. Advances in multiphoton microscopy technology. *Nature Photonics*, 7(2):93–101, 2013.

[120] S. Yue, M. N. Slipchenko, and J.-X. Cheng. Multimodal nonlinear optical microscopy. *Laser & Photonics Reviews*, 5(4):496–512, 2011.

[121] Joseph R. Lakowicz. *Principles of Fluorescence Spectroscopy*. Springer, New York, 3rd edition, 2006.

[122] Jung-Hyun Lee, Ismael J. Gomez, Valerie B. Sitterle, and J. Carson Meredith. Dye-labeled polystyrene latex microspheres prepared via a combined swelling-diffusion technique. *Journal of Colloid and Interface Science*, 363(1):137–144, 2011.

[123] J. Walker. Optical absorption and luminescence in diamond. *Reports on Progress in Physics*, 42(10):1605–1659, 1979.

[124] Marcus W. Doherty, Neil B. Manson, Paul Delaney, Fedor Jelezko, Jörg Wrachtrup, and Lloyd C.L. Hollenberg. The nitrogen-vacancy colour centre in diamond. *Physics Reports*, 528(1):1–45, 2013.

[125] Nikolai Gaponik. Transmission electron microscope image of diamond nanocrystals kindly provided by Prof. Dr. Nikolai Gaponik, Technische Universität Dresden, 2007.

[126] Igor Aharonovich, Andrew D. Greentree, and Steven Prawer. Diamond photonics. *Nature Photonics*, 5(7):397–405, 2011.

[127] F. C. Waldermann, P. Olivero, J. Nunn, K. Surmacz, Z. Y. Wang, D. Jaksch, R. A. Taylor, I. A. Walmsley, M. Draganski, P. Reichart, A. D. Greentree, D. N. Jamieson, and S. Prawer. Creating diamond color centers for quantum optical applications. *Diamond & Related Materials*, 16(11):1887–1895, 2007.

[128] Sébastien Pezzagna, Detlef Rogalla, Dominik Wildanger, Jan Meijer, and Alexander Zaitsev. Creation and nature of optical centres in diamond for single-photon emission—overview and critical remarks. *New Journal of Physics*, 13(3):035024, 2011.

[129] T. Gaebel, M. Domhan, C. Wittmann, I. Popa, F. Jelezko, J. Rabeau, A. Greentree, S. Prawer, E. Trajkov, P. R. Hemmer, and J. Wrachtrup. Photochromism in single nitrogen-vacancy defect in diamond. *Applied Physics B*, 82(2):243–246, 2006.

[130] Adam Gali, Maria Fyta, and Efthimios Kaxiras. Ab initio supercell calculations on nitrogen-vacancy center in diamond: Electronic structure and hyperfine tensors. *Physical Review B*, 77(15):155206, 2008.

[131] L. J. Rogers, S. Armstrong, M. J. Sellars, and N. B. Manson. Infrared emission of the NV centre in diamond: Zeeman and uniaxial stress studies. *New Journal of Physics*, 10(10):103024, 2008.

[132] S. H. Xin, P. D. Wang, Aie Yin, C. Kim, M. Dobrowolska, J. L. Merz, and J. K. Furdyna. Formation of self-assembling CdSe quantum dots on ZnSe by molecular beam epitaxy. *Applied Physics Letters*, 69(25):3884, 1996.

[133] Margaret A. Hines and Philippe Guyot-Sionnest. Synthesis and Characterization of Strongly Luminescing ZnS-Capped CdSe Nanocrystals. *The Journal of Physical Chemistry*, 100(2):468–471, 1996.

[134] B. O. Dabbousi, J. Rodriguez-Viejo, F. V. Mikulec, J. R. Heine, H. Mattoussi, R. Ober, K. F. Jensen, and M. G. Bawendi. (CdSe)ZnS Core-Shell Quantum Dots: Synthesis and Characterization of a Size Series of Highly Luminescent Nanocrystallites. *The Journal of Physical Chemistry B*, 101(46):9463–9475, 1997.

[135] Alexandre R. Loukanov, Ceco D. Dushkin, Karolina I. Papazova, Andrey V. Kirov, Miroslav V. Abrashev, and Eiki Adachi. Photoluminescence depending on the ZnS shell thickness of CdS/ZnS core-shell semiconductor nanoparticles. *Colloids and Surfaces A: Physicochemical and Engineering Aspects*, 245(1-3):9–14, 2004.

[136] Wolfgang Demtröder. *Experimentalphysik 3.* Springer-Verlag, Berlin Heidelberg, 2005.

[137] G. Morello, M. De Giorgi, S. Kudera, L. Manna, R. Cingolani, and M. Anni. Temperature and Size Dependence of Nonradiative Relaxation and Exciton-Phonon Coupling in Colloidal CdTe Quantum Dots. *The Journal of Physical Chemistry C*, 111(16):5846–5849, 2007.

[138] Haiguang Zhao, Hongyan Liang, François Vidal, Federico Rosei, Alberto Vomiero, and Dongling Ma. Size Dependence of Temperature-Related Optical Properties of PbS and PbS/CdS Core/Shell Quantum Dots. *The Journal of Physical Chemistry C*, 118(35):20585–20593, 2014.

[139] D. J. Douglas. Linear Quadrupoles in Mass Spectrometry. *Mass Spectrometry Reviews*, 28(6):937–960, 2009.

[140] D. Leibfried, R. Blatt, C. Monroe, and D. Wineland. Quantum dynamics of single trapped ions. *Reviews of Modern Physics*, 75(1):281–324, 2003.

[141] Josef Meixner and Friedrich Wilhelm Schäfke. *Mathieusche Funktionen und Sphäroidfunktionen.* Springer-Verlag, Berlin Heidelberg, 1954.

[142] Milton Abramowitz and Irene A. Stegun. *Handbook of Mathematical Functions: With Formulas, Graphs, and Mathematical Tables.* Dover Publications, New York, 1970.

[143] John David Jackson. *Classical Electrodynamics.* John Wiley & Sons, Inc., New York London Sydney, 1962.

[144] H. G. Dehmelt. Radiofrequency Spectroscopy of Stored Ions I: Storage. In D. R. Bates and I. Estermann, editors, *Advances in Atomic and Molecular Physics*, volume 3, pages 53–72. Elsevier, 1968.

[145] Dieter Gerlich. Inhomogeneous RF Fields: A Versatile Tool for the Study of Processes with Slow Ions. In Cheuk-Yiu Ng, Michael Baer, Ilya Prigogine, and Stuart A. Rice, editors, *Advances in Chemical Physics*, volume 82, pages 1–176. John Wiley & Sons, Inc., Hoboken, NJ, USA, 1992.

[146] D. Gerlich. Molecular Ions and Nanoparticles in RF and AC traps. *Hyperfine Interactions*, 146(1-4):293–306, 2003.

[147] F. G. Major and H. G. Dehmelt. Exchange-Collision Technique for the rf Spectroscopy of Stored Ions. *Physical Review*, 170(1):91–107, 1968.

[148] Ralph G. DeVoe. Power-Law Distributions for a Trapped Ion Interacting with a Classical Buffer Gas. *Physical Review Letters*, 102(6):063001, 2009.

[149] H. Leuthner and G. Werth. Buffer-gas-cooled ion clouds in a classical Paul trap: superimposed stability diagrams and trapping capacity investigations. *Applied Physics B*, 114(1-2):89–98, 2014.

[150] Wolfgang Demtröder. *Experimentalphysik 1.* Springer-Verlag, Berlin Heidelberg, 2006.

[151] Michael Nasse and Christopher Foot. Influence of background pressure on the stability region of a Paul trap. *European Journal of Physics*, 22(6):563, 2001.

[152] Peter Albrecht. The Runge-Kutta Theory in a Nutshell. *SIAM Journal on Numerical Analysis*, 33(5):1712–1735, 1996.

[153] H. C. Nägerl, W. Bechter, J. Eschner, F. Schmidt-Kaler, and R. Blatt. Ion strings for quantum gates. *Applied Physics B: Lasers and Optics*, 66(5):603–608, 1998.

[154] M. G. Raizen, J. M. Gilligan, J. C. Bergquist, W. M. Itano, and D. J. Wineland. Ionic crystals in a linear Paul trap. *Physical Review A*, 45(9):6493–6501, 1992.

[155] I. Waki, S. Kassner, G. Birkl, and H. Walther. Observation of Ordered Structures of Laser-Cooled Ions in a Quadrupole Storage Ring. *Physical Review Letters*, 68(13):2007, 1992.

[156] Stephan A. Schulz, Ulrich Poschinger, Frank Ziesel, and Ferdinand Schmidt-Kaler. Sideband cooling and coherent dynamics in a microchip multi-segmented ion trap. *New Journal of Physics*, 10(4):045007, 2008.

[157] W. Schnitzler, N. M. Linke, R. Fickler, J. Meijer, F. Schmidt-Kaler, and K. Singer. Deterministic Ultracold Ion Source Targeting the Heisenberg Limit. *Physical Review Letters*, 102(7):070501, 2009.

[158] D. J. Berkeland, J. D. Miller, J. C. Bergquist, W. M. Itano, and D. J. Wineland. Minimization of ion micromotion in a Paul trap. *Journal of Applied Physics*, 83(10):5025, 1998.

[159] M. E. Poitzsch, J. C. Bergquist, W. M. Itano, and D. J. Wineland. Cryogenic linear ion trap for accurate spectroscopy. *Review of Scientific Instruments*, 67(1):129–134, 1996.

[160] M. Drewsen and A. Brøner. Harmonic linear Paul trap: Stability diagram and effective potentials. *Physical Review A*, 62(4):045401, 2000.

[161] Christian Schneider, Martin Enderlein, Thomas Huber, Stephan Dürr, and Tobias Schaetz. Influence of static electric fields on an optical ion trap. *Physical Review A*, 85(1):013422, 2012.

[162] G. R. Janik, J. D. Prestage, and L. Maleki. Simple analytic potentials for linear ion traps. *Journal of Applied Physics*, 67(10):6050, 1990.

[163] Q. A. Turchette, D. Kielpinski, B. E. King, D. Leibfried, D. M. Meekhof, C. J. Myatt, M. A. Rowe, C. A. Sackett, C. S. Wood, W. M. Itano, C. Monroe, and D. J. Wineland. Heating of trapped ions from the quantum ground state. *Physical Review A*, 61(6):063418, 2000.

[164] F. Schmidt-Kaler, H. Häffner, S. Gulde, M. Riebe, G. P. T. Lancaster, T. Deuschle, C. Becher, W. Hänsel, J. Eschner, C. F. Roos, and R. Blatt. How to realize a universal quantum gate with trapped ions. *Applied Physics B: Lasers and Optics*, 77(8):789–796, 2003.

[165] G. E. Lee-Whiting and L. Yamazaki. Semi-analytical calculations for circular quadrupoles. *Nuclear Instruments and Methods*, 94(2):319–332, 1971.

[166] F. v. Busch and W. Paul. Über nichtlineare Resonanzen im elektrischen Massenfilter als Folge von Feldfehlern. *Zeitschrift für Physik*, 164(5):588–594, 1961.

[167] Y. Wang, J. Franzen, and K. P. Wanczek. The non-linear resonance ion trap. Part 2. A general theoretical analysis. *International Journal of Mass Spectrometry and Ion Processes*, 124(2):125–144, 1993.

[168] A. Drakoudis, M. Söllner, and G. Werth. Instabilities of ion motion in a linear Paul trap. *International Journal of Mass Spectrometry*, 252(1):61–68, 2006.

[169] Alexander Kuhlicke, Klaus Palis, and Oliver Benson. Broadband linear high-voltage amplifier for radio frequency ion traps. *Review of Scientific Instruments*, 85(11):114707, 2014.

[170] Alexander Kuhlicke. *Einfang und Untersuchung von Nanopartikeln in einer Paul-Falle*. Diplomarbeit, Humboldt-Universität zu Berlin, 2007.

[171] W. W. Macalpine and R. O. Schildknecht. Coaxial Resonators with Helical Inner Conductor. *Proceedings of the IRE*, 47(12):2099–2105, 1959.

[172] D. Gandolfi, M. Niedermayr, M. Kumph, M. Brownnutt, and R. Blatt. Compact radio-frequency resonator for cryogenic ion traps. *Review of Scientific Instruments*, 83(8):084705, 2012.

[173] Holger Müller. Fast high-voltage amplifiers for driving electro-optic modulators. *Review of Scientific Instruments*, 76(8):084701, 2005.

[174] C. Koçum. Digitally gain controlled linear high voltage amplifier for laboratory applications. *Review of Scientific Instruments*, 82(8):084702, 2011.

[175] Ulrich Tietze, Christoph Schenk, and Eberhard Gamm. *Electronic Circuits: Handbook for Design and Application*. Springer-Verlag, Berlin Heidelberg, 2007.

[176] F. V. Hunt and R. W. Hickman. On Electronic Voltage Stabilizers. *Review of Scientific Instruments*, 10(1):6, 1939.

[177] Daniel Axelrod. Total Internal Reflection Fluorescence Microscopy in Cell Biology. *Traffic*, 2(11):764–774, 2001.

[178] Richard W. Cole, Tushare Jinadasa, and Claire M. Brown. Measuring and interpreting point spread functions to determine confocal microscope resolution and ensure quality control. *Nature Protocols*, 6(12):1929–1941, 2011.

[179] Jean-Baptiste Sibarita. Deconvolution Microscopy. In Jens Rietdorf, editor, *Microscopy Techniques*, number 95 in Advances in Biochemical Engineering, pages 201–243. Springer-Verlag, Berlin Heidelberg, 2005.

[180] Eugene Hecht. *Optik*. Oldenbourg Verlag, München Wien, 3. edition, 2001.

[181] Günter Hildenbrand. Röntgenoptik und Röntgenmikroskopie. *Fortschritte der Physik*, 4(1-2):1–32, 1956.

[182] O. Scherzer. The Theoretical Resolution Limit of the Electron Microscope. *Journal of Applied Physics*, 20(1):20, 1949.

[183] P. E. Batson, N. Dellby, and O. L. Krivanek. Sub-ångstrom resolution using aberration corrected electron optics. *Nature*, 418(6898):617–620, 2002.

[184] Robert H. Webb. Confocal optical microscopy. *Reports on Progress in Physics*, 59(3):427, 1996.

[185] U. Dürig, D. W. Pohl, and F. Rohner. Near-field optical-scanning microscopy. *Journal of Applied Physics*, 59(10):3318, 1986.

[186] E. Betzig, P. L. Finn, and J. S. Weiner. Combined shear force and near-field scanning optical microscopy. *Applied Physics Letters*, 60(20):2484, 1992.

[187] Y. Cai, W.-P. Peng, S.-J. Kuo, Y. T. Lee, and H.-C. Chang. Single-Particle Mass Spectrometry of Polystyrene Microspheres and Diamond Nanocrystals. *Analytical Chemistry*, 74(1):232–238, 2002.

[188] Soohyung Park, Younjoo Lee, and Yeonjin Yi. Vacuum-integrated electrospray deposition for highly reliable polymer thin film. *Review of Scientific Instruments*, 83(10):105106, 2012.

[189] F. Paschen. Ueber die zum Funkenübergang in Luft, Wasserstoff und Kohlensäure bei verschiedenen Drucken erforderliche Potentialdifferenz. *Annalen der Physik*, 273(5):69–96, 1889.

[190] W. Zhang, T. S. Fisher, and S. V. Garimella. Simulation of ion generation and breakdown in atmospheric air. *Journal of Applied Physics*, 96(11):6066, 2004.

[191] Michael A. Lieberman and Allan J. Lichtenberg. *Principles of Plasma Discharges and Materials Processing*. John Wiley & Sons, Inc., New York, 1994.

[192] E. M. Bazelyan and Y. P. Raizer. *Spark discharge*. CRC Press, Boca Raton, New York, 1998.

[193] V. G. Kher and V. G. Ayachit. Increase of breakdown voltage of a low pressure A.C. discharge in air with frequencies from 20 to 15000 Hz. *Physica*, 30(4):702–712, 1964.

[194] H. B. Smith, C. Charles, and R. W. Boswell. Breakdown behavior in radio-frequency argon discharges. *Physics of Plasmas*, 10(3):875, 2003.

[195] Edmond de Hoffmann and Vincent Stroobant. *Mass Spectrometry: Principles and Applications*. John Wiley & Sons Ltd., The Atrium, Southern Gate, Chichester, West Sussex, 3rd edition, 2007.

[196] John B. Fenn, Matthias Mann, Chin Kai Meng, Shek Fu Wong, and Craig M. Whitehouse. Electrospray Ionization for Mass Spectrometry of Large Biomolecules. *Science*, 246(4926):64–71, 1989.

[197] C. S. Ho, C. W. K. Lam, M. H. M. Chan, R. C. K. Cheung, L. K. Law, L. C. W. Lit, K. F. Ng, M. W. M. Suen, and H. L. Tai. Electrospray Ionisation Mass Spectrometry: Principles and Clinical Applications. *The Clinical Biochemist Reviews*, 24(1):3, 2003.

[198] Min-Zong Huang, Cheng-Hui Yuan, Sy-Chyi Cheng, Yi-Tzu Cho, and Jentaie Shiea. Ambient Ionization Mass Spectrometry. *Annual Review of Analytical Chemistry*, 3(1):43–65, 2010.

[199] http://www.nobelprize.org/nobel_prizes/chemistry/laureates/2002/. The Nobel Prize in Chemistry, 2002. Accessed 10 April 2015.

[200] John B. Fenn. Electrospray Wings for Molecular Elephants (Nobel Lecture). *Angewandte Chemie International Edition*, 42(33):3871–3894, 2003.

[201] Alfonso M. Gañán-Calvo. Cone-Jet Analytical Extension of Taylor's Electrostatic Solution and the Asymptotic Universal Scaling Laws in Electrospraying. *Physical Review Letters*, 79(2):217, 1997.

[202] Paul Kebarle and Liang Tang. From Ions in Solution to Ions in the Gas Phase. *Analytical Chemistry*, 65(22):972A–986A, 1993.

[203] C. N. Ryan, K. L. Smith, and J. P. W. Stark. Characterization of multi-jet electrospray systems. *Journal of Aerosol Science*, 51:35–48, 2012.

[204] Denis Duft, Tobias Achtzehn, Rene Müller, Bernd A. Huber, and Thomas Leisner. Coulomb fission: Rayleigh jets from levitated microdroplets. *Nature*, 421(6919):128–128, 2003.

[205] Paul Kebarle and Udo H. Verkerk. Electrospray: From ions in solution to ions in the gas phase, what we know now. *Mass Spectrometry Reviews*, 28(6):898–917, 2009.

[206] James N. O'Shea, John B. Taylor, Janine C. Swarbrick, Graziano Magnano, Louise C. Mayor, and Karina Schulte. Electrospray deposition of carbon nanotubes in vacuum. *Nanotechnology*, 18(3):035707, 2007.

[207] Janine C. Swarbrick, J. Ben Taylor, and James N. O'Shea. Electrospray deposition in vacuum. *Applied Surface Science*, 252(15):5622–5626, 2006.

[208] Bon Ki Ku and Sang Soo Kim. Electrohydrodynamic spraying characteristics of glycerol solutions in vacuum. *Journal of Electrostatics*, 57(2):109–128, 2003.

[209] M. Block, A. Drakoudis, H. Leuthner, P. Seibert, and G. Werth. Crystalline ion structures in a Paul trap. *Journal of Physics B: Atomic, Molecular and Optical Physics*, 33(11):L375, 2000.

[210] R. Casdorff and R. Blatt. Ordered Structures and Statistical Properties of Ion Clouds Stored in a Paul Trap. *Applied Physics B*, 45(3):175–182, 1988.

[211] H. Landa, B. Reznik, J. Brox, M. Mielenz, and T. Schaetz. Structure, dynamics and bifurcations of discrete solitons in trapped ion crystals. *New Journal of Physics*, 15(9):093003, 2013.

[212] Alexander Kuhlicke, Andreas W. Schell, Joachim Zoll, and Oliver Benson. Nitrogen vacancy center fluorescence from a submicron diamond cluster levitated in a linear quadrupole ion trap. *Applied Physics Letters*, 105(7):073101, 2014.

[213] Marcel W. Grüneberg. *Entwurf und Aufbau einer Paul-Falle für das F-Praktikum*. Diplomarbeit, Humboldt-Universität zu Berlin, Berlin, 2011.

[214] D. A. Tabor, V. Rajagopal, Y.-W. Lin, and B. Odom. Suitability of linear quadrupole ion traps for large Coulomb crystals. *Applied Physics B*, 107(4):1097–1104, 2012.

[215] K. Okada, M. Wada, T. Takayanagi, S. Ohtani, and H. A. Schuessler. Characterization of ion Coulomb crystals in a linear Paul trap. *Physical Review A*, 81(1):013420, 2010.

[216] Alexander Kuhlicke, Antonio Rylke, and Oliver Benson. On-Demand Electrostatic Coupling of Individual Precharacterized Nano- and Microparticles in a Segmented Paul Trap. *Nano Letters*, 15(3):1993–2000, 2015.

[217] G. Binnig, C. F. Quate, and Ch. Gerber. Atomic Force Microscope. *Physical Review Letters*, 56(9):930, 1986.

[218] L. Gross, F. Mohn, N. Moll, P. Liljeroth, and G. Meyer. The Chemical Structure of a Molecule Resolved by Atomic Force Microscopy. *Science*, 325(5944):1110–1114, 2009.

[219] Franz J. Giessibl. Advances in atomic force microscopy. *Reviews of Modern Physics*, 75(3):949, 2003.

[220] T. Junno, K. Deppert, L. Montelius, and L. Samuelson. Controlled manipulation of nanoparticles with an atomic force microscope. *Applied Physics Letters*, 66(26):3627–3629, 1995.

[221] Andreas W. Schell, Günter Kewes, Tim Schröder, Janik Wolters, Thomas Aichele, and Oliver Benson. A scanning probe-based pick-and-place procedure for assembly of integrated quantum optical hybrid devices. *Review of Scientific Instruments*, 82(7):073709, 2011.

[222] Qiulin Ma, Lei Huang, Zhixiong Guo, and Tobias Rossmann. Spectral shift response of optical whispering-gallery modes due to water vapor adsorption and desorption. *Measurement Science and Technology*, 21(11):115206, 2010.

[223] Simin Mehrabani, Philip Kwong, Malancha Gupta, and Andrea M. Armani. Hybrid microcavity humidity sensor. *Applied Physics Letters*, 102:241101, 2013.

[224] Tindaro Ioppolo and M. Volkan Ötügen. Pressure tuning of whispering gallery mode resonators. *Journal of the Optical Society of America B*, 24(10):2721–2726, 2007.

[225] Andreas W. Schell, Alexander Kuhlicke, Günter Kewes, and Oliver Benson. 'Flying Plasmons': Fabry-Pérot Resonances in Levitated Silver Nanowires. *ACS Photonics*, 2017.

[226] Markus Gregor, Alexander Kuhlicke, and Oliver Benson. Soft-landing and optical characterization of a preselected single fluorescent particle on a tapered optical fiber. *Optics Express*, 17(26):24234–24243, 2009.

[227] A. Albrecht, A. Retzker, F. Jelezko, and M. B. Plenio. Coupling of nitrogen vacancy centres in nanodiamonds by means of phonons. *New Journal of Physics*, 15(8):083014, 2013.

[228] Richard I. Epstein and Mansoor Sheik-Bahae, editors. *Optical Refrigeration: Science and Applications of Laser Cooling of Solids*. Wiley-VCH, Weinheim, 2009.

[229] Mansoor Sheik-Bahae and Richard I. Epstein. Optical refrigeration. *Nature Photonics*, 1(12):693–699, 2007.

[230] Jun Zhang, Dehui Li, Renjie Chen, and Qihua Xiong. Laser cooling of a semiconductor by 40 kelvin. *Nature*, 493(7433):504–508, 2013.

[231] Michael Geiselmann, Mathieu L. Juan, Jan Renger, Jana M. Say, Louise J. Brown, F. Javier García de Abajo, Frank Koppens, and Romain Quidant. Three-dimensional optical manipulation of a single electron spin. *Nature Nanotechnology*, 8(3):175–179, 2013.

[232] Viva R. Horowitz, Benjamín J. Alemán, David J. Christle, Andrew N. Cleland, and David D. Awschalom. Electron spin resonance of nitrogen-vacancy centers in optically trapped nanodiamonds. *Proceedings of the National Academy of Sciences*, 109(34):13493, 2012.

[233] Levi P. Neukirch, Jan Gieseler, Romain Quidant, Lukas Novotny, and A. Nick Vamivakas. Observation of nitrogen vacancy photoluminescence from an optically levitated nanodiamond. *Optics Letters*, 38(16):2976, 2013.

[234] Levi P. Neukirch, Eva von Haartman, Jessica M. Rosenholm, and A. Nick Vamivakas. Multi-dimensional single-spin nano-optomechanics with a levitated nanodiamond. *Nature Photonics*, 9(10):653–657, 2015.

[235] V. M. Acosta, E. Bauch, M. P. Ledbetter, C. Santori, K.-M. C. Fu, P. E. Barclay, R. G. Beausoleil, H. Linget, J. F. Roch, F. Treussart, S. Chemerisov, W. Gawlik, and D. Budker. Diamonds with a high density of nitrogen-vacancy centers for magnetometry applications. *Physical Review B*, 80(11):115202, 2009.

[236] F. Jelezko, C. Tietz, A. Gruber, I. Popa, A. Nizovtsev, S. Kilin, and J. Wrachtrup. Spectroscopy of Single N-V Centers in Diamond. *Single Molecules*, 2(4):255, 2001.

[237] Abbas Mohtashami and A. Femius Koenderink. Suitability of nanodiamond nitrogen–vacancy centers for spontaneous emission control experiments. *New Journal of Physics*, 15(4):043017, 2013.

[238] R. G. Brewer, R. G. DeVoe, and R. Kallenbach. Planar ion microtraps. *Physical Review A*, 46(11):R6781, 1992.

[239] Erik W. Streed, Andreas Jechow, Benjamin G. Norton, and David Kielpinski. Absorption imaging of a single atom. *Nature Communications*, 3:933, 2012.

[240] Mark Scalf, Michael S. Westphall, and Lloyd M. Smith. Charge Reduction Electrospray Mass Spectrometry. *Analytical Chemistry*, 72(1):52–60, 2000.

[241] J. R. Rabeau, S. T. Huntington, A. D. Greentree, and S. Prawer. Diamond chemical-vapor deposition on optical fibers for fluorescence waveguiding. *Applied Physics Letters*, 86(13):134104, 2005.

[242] Tim Schröder, Andreas W. Schell, Günter Kewes, Thomas Aichele, and Oliver Benson. Fiber-Integrated Diamond-Based Single Photon Source. *Nano Letters*, 11(1):198–202, 2011.

[243] William L. Barnes, Alain Dereux, and Thomas W. Ebbesen. Surface plasmon subwavelength optics. *Nature*, 424(6950):824–830, 2003.

[244] Xiaohao Xu, Chang Cheng, Hongbao Xin, Hongxiang Lei, and Baojun Li. Controllable orientation of single silver nanowire using two fiber probes. *Scientific Reports*, 4:3989, 2014.

[245] Lianming Tong, Vladimir D. Miljković, and Mikael Käll. Alignment, Rotation, and Spinning of Single Plasmonic Nanoparticles and Nanowires Using Polarization Dependent Optical Forces. *Nano Letters*, 10(1):268–273, 2010.

[246] Zijie Yan, Justin E. Jureller, Julian Sweet, Mason J. Guffey, Matthew Pelton, and Norbert F. Scherer. Three-Dimensional Optical Trapping and Manipulation of Single Silver Nanowires. *Nano Letters*, 12(10):5155–5161, 2012.

[247] Peter J. Pauzauskie, Aleksandra Radenovic, Eliane Trepagnier, Hari Shroff, Peidong Yang, and Jan Liphardt. Optical trapping and integration of semiconductor nanowire assemblies in water. *Nature Materials*, 5(2):97–101, 2006.

[248] Lina Cao, Rene A. Nome, Jason M. Montgomery, Stephen K. Gray, and Norbert F. Scherer. Controlling Plasmonic Wave Packets in Silver Nanowires. *Nano Letters*, 10(9):3389–3394, 2010.

[249] Daniel Hofstetter and Robert L. Thornton. Theory of loss measurements of Fabry-Perot resonators by Fourier analysis of the transmission spectra. *Optics Letters*, 22(24):1831–1833, 1997.

[250] Marco Allione, Vasily V. Temnov, Yuri Fedutik, Ulrike Woggon, and Mikhail V. Artemyev. Surface Plasmon Mediated Interference Phenomena in Low-Q Silver Nanowire Cavities. *Nano Letters*, 8(1):31–35, 2008.

[251] Timur Shegai, Vladimir D. Miljković, Kui Bao, Hongxing Xu, Peter Nordlander, Peter Johansson, and Mikael Käll. Unidirectional Broadband Light Emission from Supported Plasmonic Nanowires. *Nano Letters*, 11(2):706–711, 2011.

[252] Stefan Kuhn, Peter Asenbaum, Alon Kosloff, Michele Sclafani, Benjamin A. Stickler, Stefan Nimmrichter, Klaus Hornberger, Ori Cheshnovsky, Fernando Patolsky, and Markus Arndt. Cavity-Assisted Manipulation of Freely Rotating Silicon Nanorods in High Vacuum. *Nano Letters*, 15(8):5604–5608, 2015.

[253] M. Bhattacharya. Rotational cavity optomechanics. *Journal of the Optical Society of America B*, 32(5):B55, 2015.

[254] Yoshihiko Arita, Michael Mazilu, and Kishan Dholakia. Laser-induced rotation and cooling of a trapped microgyroscope in vacuum. *Nature Communications*, 4:2374, 2013.

[255] Jan Gieseler, Romain Quidant, Christoph Dellago, and Lukas Novotny. Dynamic relaxation of a levitated nanoparticle from a non-equilibrium steady state. *Nature Nanotechnology*, 9(5):358–364, 2014.

[256] J. Millen, T. Deesuwan, P. Barker, and J. Anders. Nanoscale temperature measurements using non-equilibrium Brownian dynamics of a levitated nanosphere. *Nature Nanotechnology*, 9(6):425–429, 2014.

[257] Rutger Thijssen, Tobias J. Kippenberg, Albert Polman, and Ewold Verhagen. Plasmomechanical Resonators Based on Dimer Nanoantennas. *Nano Letters*, 15(6):3971–3976, 2015.

[258] David Solis, Jr., Wei-Shun Chang, Bishnu P. Khanal, Kui Bao, Peter Nordlander, Eugene R. Zubarev, and Stephan Link. Bleach-Imaged Plasmon Propagation (BlIPP) in Single Gold Nanowires. *Nano Letters*, 10(9):3482–3485, 2010.

[259] Barbara Wild, Lina Cao, Yugang Sun, Bishnu P. Khanal, Eugene R. Zubarev, Stephen K. Gray, Norbert F. Scherer, and Matthew Pelton. Propagation Lengths and Group Velocities of Plasmons in Chemically Synthesized Gold and Silver Nanowires. *ACS Nano*, 6(1):472–482, 2012.

[260] Zhang-Kai Zhou, Min Li, Zhong-Jian Yang, Xiao-Niu Peng, Xiong-Rui Su, Zong-Suo Zhang, Jian-Bo Li, Nam-Chol Kim, Xue-Feng Yu, Li Zhou, Zhong-Hua Hao, and Qu-Quan Wang. Plasmon-Mediated Radiative Energy Transfer across a Silver Nanowire Array *via* Resonant Transmission and Subwavelength Imaging. *ACS Nano*, 4(9):5003–5010, 2010.

[261] Limin Tong, Rafael R. Gattass, Jonathan B. Ashcom, Sailing He, Jingyi Lou, Mengyan Shen, Iva Maxwell, and Eric Mazur. Subwavelength-diameter silica wires for low-loss optical wave guiding. *Nature*, 426(6968):816–819, 2003.

[262] Joel Villatoro and David Monzón-Hernández. Fast detection of hydrogen with nano fiber tapers coated with ultra thin palladium layers. *Optics Express*, 13(13):5087–5092, 2005.

[263] Lei Zhang, Fuxing Gu, Jingyi Lou, Xuefeng Yin, and Limin Tong. Fast detection of humidity with a subwavelength-diameter fiber taper coated with gelatin film. *Optics Express*, 16(17):13349–13353, 2008.

[264] F. Warken, E. Vetsch, D. Meschede, M. Sokolowski, and A. Rauschenbeutel. Ultra-sensitive surface absorption spectroscopy using sub-wavelength diameter optical fibers. *Optics Express*, 15(19):11952–11958, 2007.

[265] M. Sumetsky, Y. Dulashko, and A. Hale. Fabrication and study of bent and coiled free silica nanowires: Self-coupling microloop optical interferometer. *Optics Express*, 12(15):3521–3531, 2004.

[266] Yongmin Jung, Gilberto Brambilla, and David J. Richardson. Broadband single-mode operation of standard optical fibers by using a sub-wavelength optical wire filter. *Optics Express*, 16(19):14661–14667, 2008.

[267] Tomáš Čižmár, Martin Šiler, Mojmír Šerý, Pavel Zemánek, Veneranda Garcés-Chávez, and Kishan Dholakia. Optical sorting and detection of submicrometer objects in a motional standing wave. *Physical Review B*, 74(3):035105, 2006.

[268] Jingyi Lou, Limin Tong, and Zhizhen Ye. Modeling of silica nanowires for optical sensing. *Optics Express*, 13(6):2135–2140, 2005.

[269] K. P. Nayak, P. N. Melentiev, M. Morinaga, Fam Le Kien, V. I. Balykin, and K. Hakuta. Optical nanofiber as an efficient tool for manipulating and probing atomic fluorescence. *Optics Express*, 15(9):5431–5438, 2007.

[270] Lars Liebermeister, Fabian Petersen, Asmus v. Münchow, Daniel Burchardt, Juliane Hermelbracht, Toshiyuki Tashima, Andreas W. Schell, Oliver Benson, Thomas Meinhardt, Anke Krueger, Ariane Stiebeiner, Arno Rauschenbeutel, Harald Weinfurter, and Markus Weber. Tapered fiber coupling of single photons emitted by a deterministically positioned single nitrogen vacancy center. *Applied Physics Letters*, 104(3):031101, 2014.

[271] V. B. Braginsky, M. L. Gorodetsky, and V. S. Ilchenko. Quality-factor and nonlinear properties of optical whispering-gallery modes. *Physics Letters A*, 137(7,8):393–397, 1989.

[272] T. J. Kippenberg, A. L. Tchebotareva, J. Kalkman, A. Polman, and K. J. Vahala. Purcell-Factor-Enhanced Scattering from Si Nanocrystals in an Optical Microcavity. *Physical Review Letters*, 103(2):027406, 2009.

[273] Paul E. Barclay, Charles Santori, Kai-Mei Fu, Raymond G. Beausoleil, and Oskar Painter. Coherent interference effects in a nano-assembled diamond NV center cavity-QED system. *Optics Express*, 17(10):8081, 2009.

[274] Jonathan M. Ward, Danny G. O'Shea, Brian J. Shortt, Michael J. Morrissey, Kieran Deasy, and Síle G. Nic Chormaic. Heat-and-pull rig for fiber taper fabrication. *Review of Scientific Instruments*, 77(8):083105, 2006.

[275] Fedja Orucevic, Valérie Lefèvre-Seguin, and Jean Hare. Transmittance and near-field characterization of sub-wavelength tapered optical fibers. *Optics Express*, 15(21):13624–13629, 2007.

[276] Hidenori Konishi, Hideki Fujiwara, Shigeki Takeuchi, and Keiji Sasaki. Polarization-discriminated spectra of a fiber-microsphere system. *Applied Physics Letters*, 89(12):121107, 2006.

[277] Gilberto Brambilla, Vittoria Finazzi, and David J. Richardson. Ultra-low-loss optical fiber nanotapers. *Optics Express*, 12(10):2258–2263, 2004.

[278] Yannick K. Lizé, Eric C. Mägi, Vahid G. Ta'eed, Jeremy A. Bolger, Paul Steinvurzel, and Benjamin J. Eggleton. Microstructured optical fiber photonic wires with subwavelength core diameter. *Optics Express*, 12(14):3209–3217, 2004.

[279] Markus Gregor. *Fiber Taper-Coupled Microresonators for Applications in Sensing and Quantum Optics*. Dissertation, Humboldt-Universität zu Berlin, Berlin, 2012.

[280] Ioannis D. Chremmos and Nikolaos K. Uzunoglu. Integral equation analysis of scattering by a spherical microparticle coupled to a subwavelength-diameter wire waveguide. *Journal of the Optical Society of America A*, 23(2):461–467, 2006.

[281] Jacques Bures and René Ghosh. Power density of the evanescent field in the vicinity of a tapered fiber. *Journal of the Optical Society of America A*, 16(8):1992–1996, 1999.

[282] S. W. Harun, K. S. Lim, C. K. Tio, K. Dimyati, and H. Ahmad. Theoretical analysis and fabrication of tapered fiber. *Optik*, 124(6):538–543, 2013.

[283] Ming Cai, Oskar Painter, and Kerry J. Vahala. Observation of Critical Coupling in a Fiber Taper to a Silica-Microsphere Whispering-Gallery Mode System. *Physical Review Letters*, 85(1):74, 2000.

[284] Brent E. Little, Sai T. Chu, and H. A. Haus. Track changing by use of the phase response of microspheres and resonators. *Optics Letters*, 23(12):894–896, 1998.

[285] Yiping Han, Loic Méès, Gerard Gouesbet, Zhensen Wu, and Gerard Gréhan. Resonant spectra of a deformed spherical microcavity. *Journal of the Optical Society of America B*, 23(7):1390–1397, 2006.

[286] Fam Le Kien, S. Dutta Gupta, V. I. Balykin, and K. Hakuta. Spontaneous emission of a cesium atom near a nanofiber: Efficient coupling of light to guided modes. *Physical Review A*, 72(3):032509, 2005.

[287] Fam Le Kien and K. Hakuta. Cavity-enhanced channeling of emission from an atom into a nanofiber. *Physical Review A*, 80(5):053826, 2009.

[288] E. Knill, R. Laflamme, and G. J. Milburn. A scheme for efficient quantum computation with linear optics. *Nature*, 409(6816):46–52, 2001.

[289] Pieter Kok, W. J. Munro, Kae Nemoto, T. C. Ralph, Jonathan P. Dowling, and G. J. Milburn. Linear optical quantum computing with photonic qubits. *Reviews of Modern Physics*, 79(1):135–174, 2007.

[290] D. K. Armani, T. J. Kippenberg, S. M. Spillane, and K. J. Vahala. Ultra-high-Q toroid microcavity on a chip. *Nature*, 421(6926):925–928, 2003.

[291] M. Cai, O. Painter, K. J. Vahala, and P. C. Sercel. Fiber-coupled microsphere laser. *Optics Letters*, 25(19):1430–1432, 2000.

[292] Hideki T. Miyazaki, Hiroshi Miyazaki, Kazuo Ohtaka, and Tomomasa Sato. Photonic band in two-dimensional lattices of micrometer-sized spheres mechanically arranged under a scanning electron microscope. *Journal of Applied Physics*, 87(10):7152–7158, 2000.

[293] Christiane Höppener, Zachary J. Lapin, Palash Bharadwaj, and Lukas Novotny. Self-Similar Gold-Nanoparticle Antennas for a Cascaded Enhancement of the Optical Field. *Physical Review Letters*, 109(1):017402, 2012.

[294] Davy Gérard, Alexis Devilez, Heykel Aouani, Brian Stout, Nicolas Bonod, Jérôme Wenger, Evgeny Popov, and Hervé Rigneault. Efficient excitation and collection of single-molecule fluorescence close to a dielectric microsphere. *Journal of the Optical Society of America B*, 26(7):1473–1478, 2009.

[295] Pascal Anger, Palash Bharadwaj, and Lukas Novotny. Enhancement and Quenching of Single-Molecule Fluorescence. *Physical Review Letters*, 96(11):113002, 2006.

[296] T. Mukaiyama, K. Takeda, H. Miyazaki, Y. Jimba, and M. Kuwata-Gonokami. Tight-Binding Photonic Molecule Modes of Resonant Bispheres. *Physical Review Letters*, 82(23):4623–4626, 1999.

[297] S. Götzinger, L. de S. Menezes, O. Benson, D. V. Talapin, N. Gaponik, H. Weller, A. L. Rogach, and V. Sandoghdar. Confocal microscopy and spectroscopy of nanocrystals on a high-Q microsphere resonator. *Journal of Optics B: Quantum and Semiclassical Optics*, 6(2):154–158, 2004.

[298] Hiroharu Tamaru, Hitoshi Kuwata, Hideki T. Miyazaki, and Kenjiro Miyano. Resonant light scattering from individual Ag nanoparticles and particle pairs. *Applied Physics Letters*, 80(10):1826–1828, 2002.

[299] Sebastian P. Scheeler, Stefan Mühlig, Carsten Rockstuhl, Shakeeb Bin Hasan, Simon Ullrich, Frank Neubrech, Stefan Kudera, and Claudia Pacholski. Plasmon Coupling in Self-Assembled Gold Nanoparticle-Based Honeycomb Islands. *The Journal of Physical Chemistry C*, 117(36):18634–18641, 2013.

[300] Michael Geiselmann, Renaud Marty, Jan Renger, F. Javier García de Abajo, and Romain Quidant. Deterministic Optical-Near-Field-Assisted Positioning of Nitrogen-Vacancy Centers. *Nano Letters*, 14(3):1520–1525, 2014.

[301] Hoon Cha, Jun Hee Yoon, and Sangwoon Yoon. Probing Quantum Plasmon Coupling Using Gold Nanoparticle Dimers with Tunable Interparticle Distances Down to the Subnanometer Range. *ACS Nano*, 8(8):8554–8563, 2014.

[302] Christopher M. Galloway, Mark P. Kreuzer, Srdjan S. Aćimović, Giorgio Volpe, Manuel Correia, Steffen B. Petersen, Maria Teresa Neves-Petersen, and Romain Quidant. Plasmon-Assisted Delivery of Single Nano-Objects in an Optical Hot Spot. *Nano Letters*, 13(9):4299–4304, 2013.

[303] W. Rechberger, A. Hohenau, A. Leitner, J. R. Krenn, B. Lamprecht, and F. R. Aussenegg. Optical properties of two interacting gold nanoparticles. *Optics Communications*, 220(1-3):137–141, 2003.

[304] N. Stefanou and A. Modinos. Impurity bands in photonic insulators. *Physical Review B*, 57(19):12127–12133, 1998.

[305] Amnon Yariv, Yong Xu, Reginald K. Lee, and Axel Scherer. Coupled-resonator optical waveguide: a proposal and analysis. *Optics Letters*, 24(11):711–713, 1999.

[306] Alexander Kuhlicke, Stefan Schietinger, Christian Matyssek, Kurt Busch, and Oliver Benson. In Situ Observation of Plasmon Tuning in a Single Gold Nanoparticle during Controlled Melting. *Nano Letters*, 13(5):2041–2046, 2013.

[307] Ren-Min Ma, Rupert F. Oulton, Volker J. Sorger, Guy Bartal, and Xiang Zhang. Room-temperature sub-diffraction-limited plasmon laser by total internal reflection. *Nature Materials*, 10(2):110–113, 2011.

[308] M. A. Noginov, G. Zhu, A. M. Belgrave, R. Bakker, V. M. Shalaev, E. E. Narimanov, S. Stout, E. Herz, T. Suteewong, and U. Wiesner. Demonstration of a spaser-based nanolaser. *Nature*, 460(7259):1110–1112, 2009.

[309] T. Wenzel, J. Bosbach, A. Goldmann, F. Stietz, and F. Träger. Shaping nanoparticles and their optical spectra with photons. *Applied Physics B*, 69(5-6):513–517, 1999.

[310] Anton Plech, Vassilios Kotaidis, Maciej Lorenc, and Johannes Boneberg. Femtosecond laser near-field ablation from gold nanoparticles. *Nature Physics*, 2(1):44–47, 2006.

[311] S. Link, C. Burda, B. Nikoobakht, and M. A. El-Sayed. Laser-Induced Shape Changes of Colloidal Gold Nanorods Using Femtosecond and Nanosecond Laser Pulses. *The Journal of Physical Chemistry B*, 104(26):6152–6163, 2000.

[312] A. Podlipensky, A. Abdolvand, G. Seifert, and H. Graener. Femtosecond laser assisted production of dichroitic 3d structures in composite glass containing Ag nanoparticles. *Applied Physics A*, 80(8):1647–1652, 2005.

[313] A. Stalmashonak, A. Podlipensky, G. Seifert, and H. Graener. Intensity-driven, laser induced transformation of Ag nanospheres to anisotropic shapes. *Applied Physics B*, 94(3):459–465, 2009.

[314] A. V. Podlipensky, V. Grebenev, G. Seifert, and H. Graener. Ionization and photomodification of Ag nanoparticles in soda-lime glass by 150 fs laser irradiation: a luminescence study. *Journal of Luminescence*, 109(3-4):135–142, 2004.

[315] Qingfeng Zhang, Nicolas Large, Peter Nordlander, and Hui Wang. Porous Au Nanoparticles with Tunable Plasmon Resonances and Intense Field Enhancements for Single-Particle SERS. *The Journal of Physical Chemistry Letters*, 5(2):370–374, 2014.

[316] Cynthia Vidal, Dong Wang, Peter Schaaf, Calin Hrelescu, and Thomas A. Klar. Optical Plasmons of Individual Gold Nanosponges. *ACS Photonics*, 2(10):1436–1442, 2015.

[317] Terukazu Kosako, Yutaka Kadoya, and Holger F. Hofmann. Directional control of light by a nano-optical Yagi–Uda antenna. *Nature Photonics*, 4(5):312–315, 2010.

[318] Martin Böhmer and Jörg Enderlein. Orientation imaging of single molecules by wide-field epifluorescence microscopy. *Journal of the Optical Society of America B*, 20(3):554–559, 2003.

[319] Shiuan-Yeh Chen, Jack J. Mock, Ryan T. Hill, Ashutosh Chilkoti, David R. Smith, and Anne A. Lazarides. Gold Nanoparticles on Polarizable Surfaces as Raman Scattering Antennas. *ACS Nano*, 4(11):6535–6546, 2010.

[320] E. Dulkeith, T. Niedereichholz, T. A. Klar, J. Feldmann, G. von Plessen, D. I. Gittins, K. S. Mayya, and F. Caruso. Plasmon emission in photoexcited gold nanoparticles. *Physical Review B*, 70(20):205424, 2004.

[321] David Keller. Reconstruction of STM and AFM images distorted by finite-size tips. *Surface Science*, 253(1):353–364, 1991.

[322] Jens Niegemann, Michael König, Kai Stannigel, and Kurt Busch. Higher-order time-domain methods for the analysis of nano-photonic systems. *Photonics and Nanostructures - Fundamentals and Applications*, 7(1):2–11, 2009.

[323] K. Busch, M. König, and J. Niegemann. Discontinuous Galerkin methods in nanophotonics. *Laser & Photonics Reviews*, 5(6):773–809, 2011.

[324] Kenji Setoura, Yudai Okada, Daniel Werner, and Shuichi Hashimoto. Observation of Nanoscale Cooling Effects by Substrates and the Surrounding Media for Single Gold Nanoparticles under CW-Laser Illumination. *ACS Nano*, 7(9):7874–7885, 2013.

[325] Kenji Koga, Tamio Ikeshoji, and Ko-ichi Sugawara. Size- and Temperature-Dependent Structural Transitions in Gold Nanoparticles. *Physical Review Letters*, 92(11):115507, 2004.

[326] Ph. Buffat and J.-P. Borel. Size effect on the melting temperature of gold particles. *Physical Review A*, 13(6):2287, 1976.

[327] T. Castro, R. Reifenberger, E. Choi, and R. P. Andres. Size-dependent melting temperature of individual nanometer-sized metallic clusters. *Physical Review B*, 42(13):8548, 1990.

[328] Keir C. Neuman and Steven M. Block. Optical trapping. *Review of Scientific Instruments*, 75(9):2787, 2004.

[329] Karel Svoboda and Steven M. Block. Optical trapping of metallic Rayleigh particles. *Optics Letters*, 19(13):930–932, 1994.

[330] Poul Martin Hansen, Vikram Kjøller Bhatia, Niels Harrit, and Lene Oddershede. Expanding the Optical Trapping Range of Gold Nanoparticles. *Nano Letters*, 5(10):1937–1942, 2005.

[331] Kenji Setoura, Yudai Okada, and Shuichi Hashimoto. CW-laser-induced morphological changes of a single gold nanoparticle on glass: observation of surface evaporation. *Physical Chemistry Chemical Physics*, 16(48):26938–26945, 2014.

[332] Toon Coenen, Ernst Jan R. Vesseur, Albert Polman, and A. Femius Koenderink. Directional Emission from Plasmonic Yagi–Uda Antennas Probed by Angle-Resolved Cathodoluminescence Spectroscopy. *Nano Letters*, 11(9):3779–3784, 2011.

[333] Mario Hentschel, Daniel Dregely, Ralf Vogelgesang, Harald Giessen, and Na Liu. Plasmonic Oligomers: The Role of Individual Particles in Collective Behavior. *ACS Nano*, 5(3):2042–2050, 2011.

[334] M. B. Cortie, N. Stokes, and A. McDonagh. Plasmon resonance and electric field amplification of crossed gold nanorods. *Photonics and Nanostructures - Fundamentals and Applications*, 7(3):143–152, 2009.

[335] Baptiste Auguié, José Lorenzo Alonso-Gómez, Andrés Guerrero-Martínez, and Luis M. Liz-Marzán. Fingers Crossed: Optical Activity of a Chiral Dimer of Plasmonic Nanorods. *The Journal of Physical Chemistry Letters*, 2(8):846–851, 2011.

[336] Jiafang Li, Siyun Liu, Ye Liu, Fei Zhou, and Zhi-Yuan Li. Anisotropic and enhanced absorptive nonlinearities in a macroscopic film induced by aligned gold nanorods. *Applied Physics Letters*, 96(26):263103, 2010.

[337] A. Stalmashonak, G. Seifert, and H. Graener. Spectral range extension of laser-induced dichroism in composite glass with silver nanoparticles. *Journal of Optics A: Pure and Applied Optics*, 11(6):065001, 2009.

[338] Z. Živcová, E. Gregorová, and W. Pabst. Porous alumina ceramics produced with lycopodium spores as pore-forming agents. *Journal of Materials Science*, 42(20):8760–8764, 2007.

[339] R. B. Blakestad, C. Ospelkaus, A. P. VanDevender, J. M. Amini, J. Britton, D. Leibfried, and D. J. Wineland. High-Fidelity Transport of Trapped-Ion Qubits through an X -Junction Trap Array. *Physical Review Letters*, 102(15):153002, 2009.

[340] Kenneth Wright, Jason M. Amini, Daniel L. Faircloth, Curtis Volin, S. Charles Doret, Harley Hayden, C.-S. Pai, David W. Landgren, Douglas Denison, Tyler Killian, Richart E. Slusher, and Alexa W. Harter. Reliable transport through a microfabricated X-junction surface-electrode ion trap. *New Journal of Physics*, 15(3):033004, 2013.

[341] C. Toninelli, K. Early, J. Bremi, A. Renn, S. Götzinger, and V. Sandoghdar. Near-infrared single-photons from aligned molecules in ultrathin crystalline films at room temperature. *Optics Express*, 18(7):6577–6582, 2010.

[342] A. D. Ward, M. Zhang, and O. Hunt. Broadband Mie scattering from optically levitated aerosol droplets using a white LED. *Optics Express*, 16(21):16390, 2008.

[343] Erik W. Streed. Unfolding Large Biomolecules. *arXiv:1211.3168*, 2012.

[344] Robert M. Lorenz, J. Scott Edgar, Gavin D. M. Jeffries, Yiqiong Zhao, David McGloin, and Daniel T. Chiu. Vortex-Trap-Induced Fusion of Femtoliter-Volume Aqueous Droplets. *Analytical Chemistry*, 79(1):224–228, 2007.

[345] Sadao Ota, Hiroaki Kitagawa, and Shoji Takeuchi. Generation of Femtoliter Reactor Arrays within a Microfluidic Channel for Biochemical Analysis. *Analytical Chemistry*, 84(15):6346–6350, 2012.

[346] I. H. Malitson. Interspecimen Comparison of the Refractive Index of Fused Silica. *Journal of the Optical Society of America*, 55(10):1205–1208, 1965.

[347] Alexandre Vial, Anne-Sophie Grimault, Demetrio Macías, Dominique Barchiesi, and Marc Lamy de la Chapelle. Improved analytical fit of gold dispersion: Application to the modeling of extinction spectra with a finite-difference time-domain method. *Physical Review B*, 71(8):085416, 2005.

[348] Michael I. Tribelsky, Andrey E. Miroshnichenko, Yuri S. Kivshar, Boris S. Luk'yanchuk, and Alexei R. Khokhlov. Laser Pulse Heating of Spherical Metal Particles. *Physical Review X*, 1(2):021024, 2011.

[349] James R. Welty, Charles E. Wicks, Robert E. Wilson, and Gregory L. Rorrer, editors. *Fundamentals of Momentum, Heat, and Mass Transfer*. John Wiley & Sons, Inc., Hoboken, NJ, USA, 5th edition, 2008.

[350] Guillaume Baffou, Romain Quidant, and F. Javier García de Abajo. Nanoscale Control of Optical Heating in Complex Plasmonic Systems. *ACS Nano*, 4(2):709–716, 2010.

[351] Wolfgang Demtröder. *Experimentalphysik 2*. Springer-Verlag, Berlin Heidelberg, 2006.

[352] Yiming Zhang, Julian R. G. Evans, and Shoufeng Yang. Corrected Values for Boiling Points and Enthalpies of Vaporization of Elements in Handbooks. *Journal of Chemical & Engineering Data*, 56(2):328–337, 2011.

List of Own Work

Publications in Peer-Reviewed Journals

The following articles, which have been published by the author in peer-reviewed journals, form the basis of this thesis:

- A. W. Schell, **A. Kuhlicke**, G. Kewes, and O. Benson, 'Flying Plasmons': Fabry-Pérot Resonances in Levitated Silver Nanowires, *ACS Photonics* (2017)
- **A. Kuhlicke**, A. Rylke, and O. Benson, On-Demand Electrostatic Coupling of Individual Precharacterized Nano- and Microparticles in a Segmented Paul Trap, *Nano Letters* 15, 1993-2000 (2015)
- **A. Kuhlicke**, A. W. Schell, J. Zoll, and O. Benson, Nitrogen vacancy center fluorescence from a submicron diamond cluster levitated in a linear quadrupole ion trap, *Applied Physics Letters* 105, 073101 (2014)
- **A. Kuhlicke**, K. Palis, and O. Benson, Broadband linear high-voltage amplifier for radio frequency ion traps, *Review of Scientific Instruments* 85, 114707 (2014)
- **A. Kuhlicke**, S. Schietinger, C. Matyssek, K. Busch, and O. Benson, In Situ Observation of Plasmon Tuning in a Single Gold Nanoparticle during Controlled Melting, *Nano Letters* 13, 2041-2046 (2013)
- M. Gregor, **A. Kuhlicke**, and O. Benson, Soft-landing and optical characterization of a preselected single fluorescent particle on a tapered optical fiber, *Optics Express* 17, 24234-24243 (2009)

Additional publications have been submitted, which are not part of this thesis:

- H. L. Partner, J. Zoll, **A. Kuhlicke**, and O. Benson, Printed-circuit-board linear Paul trap for manipulating single nano- and microparticles, submitted (2017)
- G. Kewes, K. Herrmann, R. Rodríguez-Oliveros, **A. Kuhlicke**, O. Benson, and K. Busch, Limitations of Particle-Based Spasers, *Physical Review Letters* 118, 237402 (2017)
- G. Kewes, R. Rodríguez-Oliveros, K. Höfner, **A. Kuhlicke**, O. Benson, and K. Busch, A fully nanoscopic dielectric laser, *arXiv*:1412.4549 (2014)

Conferences Contributions

The following conference contributions have been made by the author.

Talks

- **A. Kuhlicke**, A. W. Schell, J. Zoll, H. Partner, and O. Benson, Observation of Nitrogen Vacancy Center Fluorescence from Levitated Diamonds, DPG Frühjahrstagung Berlin 2015, HL 63.7
- **A. Kuhlicke**, S. Schietinger, C. Matyssek, K. Busch, and O. Benson, Plasmon Resonance Tuning of a Single Gold Nanoparticle by Controlled Melting, DPG Frühjahrstagung Berlin 2014, Q 23.4
- **A. Kuhlicke**, G. Kewes, S. Schietinger, C. Matyssek, K. Busch, and O. Benson, Laser-Induced Plasmon Resonance Tuning of a Single Gold Nanoparticle & Assembly of HIOS with a Linear Paul Trap, HIOS Young Researcher Workshop 2013, Rheinsberg
- **A. Kuhlicke**, M. Gregor, and O. Benson, Soft-Landing of Preselected Single Nanoparticles on Optical Fiber Tapers for Spectroscopy and Detection, Frontiers in Optics 2009/Laser Science XXV, FWE4 , San Jose, CA
- **A. Kuhlicke**, M. Gregor, and O. Benson, Detection and Spectroscopy of Preselected Microparticles Soft-Landed on Optical Fibre Tapers, IONS-6 Glasgow 2009
- **A. Kuhlicke**, M. Gregor, and O. Benson, Detection and Spectroscopy of Preselected Single Nanoparticles Soft-Landed on Optical Fibre Tapers, DPG Frühjahrstagung Hamburg 2009, Q 57.2
- **A. Kuhlicke**, S. Schietinger, and O. Benson, Optical Spectroscopy On Nanoparticles in a Linear Paul Trap, DPG Frühjahrstagung Regensburg 2007, CPP 27.5

Posters

- **A. Kuhlicke**, S. Schietinger, and O. Benson, Optical Observation of Symmetry Change in a Single Gold Nanoparticle by Melting, IONS-13 Zürich 2013
- **A. Kuhlicke**, S. Schietinger, and O. Benson, Optical Spectroscopy On Trapped Nanoparticles, DPG Frühjahrstagung Darmstadt 2008, Q 50.2
- **A. Kuhlicke**, S. Schietinger, and O. Benson, Trapping Single Nanoparticles, International Workshop on Spin and Optoelectronics, Berlin 2007

Supervision of Students

- Joachim Zoll, Konstruktion, Fertigung und Charakterisierung einer Paulfalle zum Einfangen von Nanodiamanten, bachelor thesis, 2014
- Antonio Rylke, Einfang und Kopplung von Mikroresonatoren in einer linearen Paulfalle, bachelor thesis, 2013
- Marcel Grüneberg, Entwurf und Aufbau einer Paul-Falle für das F-Praktikum, master thesis, 2011
- Philipp Meixner, Einfang und Transport von Nanopartikeln in photonischen Kristallfasern, bachelor thesis, 2010
- Tarlan Vezirov, Design und Test eines Mikroskopobjektivs für Vakuumanwendungen, bachelor thesis, 2008

List of Figures

List of Tables

Danksagung

An dieser Stelle möchte ich mich bei den wichtigsten Menschen bedanken, die mich während meiner langen Promotionszeit unterstützt haben.

Prof. Oliver Benson ist sicherlich als erster zu nennen, da er mir die Möglichkeit für diese Dissertation gab. Ohne seine Zuversicht und seine Geduld hätte ich die letztendlich doch erfolgreichen Projekte nicht durchführen können.

Ebenfalls undenkbar wäre das Zustandekommen dieser Arbeit ohne Klaus Palis. Dank seiner Arbeit, vor allem zu den Hochspannungsverstärkern, konnten die Paul-Fallen überhaupt nur betrieben werden. Die zahlreichen gemeinsamen Stunden in der Elektronikwerkstatt möchte ich nicht missen.

Erst als Betreuer meiner Diplomarbeit, später als Kollege ist mir Stefan Schietinger vor allem ein guter Freund geworden. Seine Leidenschaft und Kreativität im Labor haben mir stets neue Perspektiven eröffnet und mich von Anfang an die Freude an der experimentellen Arbeit gelehrt.

Mit Markus Gregor, Rico Henze, Günter Kewes, Gesine Steudle, Michael Barth und Andrea Mazzei durfte ich mir zeitweilig nicht nur die Labore sondern auch die Büros teilen. Ihre Hilfsbereitschaft in allen Belangen, aber auch die unzähligen Diskussionen haben dafür gesorgt, dass sich die Arbeit nie nach Arbeit angefühlt hat, sondern immer wie ein spannendes Projekt unter Freunden.

Benjamin Sprenger hatte stets eine offene Tür für mich. Er hat mir gezeigt, dass es bei einer guten Kaffeepause nicht in erster Linie auf den Kaffee ankommt.

Ich wünschte Heather Partner wäre früher zu meinem Experiment hinzugekommen. Wir hätten eine ganze Menge bewegen können. So blieb mir Ihre fundierte Beratung und ihre Freundschaft.

Meinen Studenten Joachim Zoll, Antonio Rylke, Marcel Grüneberg, Philipp Meixner und Tarlan Vezirov danke ich für ihre Arbeit, die sie während ihrer Abschlußarbeiten bei mir erbracht haben. Es war mir stets eine große Freude, sie auf ihrem Studienweg begleiten zu dürfen.

Allen Nanos und Qoms möchte ich für die tolle Zeit an der Uni danken.

Für das Korrekturlesen einzelner Kapitel bzw. der ganzen Arbeit bedanke ich mich bei Ben, Günter und Andreas Schell sowie ganz besonders bei Heather.

Mein größter Dank geht zum Schluß an meine Familie, die mich all die Jahre unterstützt und mir den Rücken freigehalten hat. Meinen Eltern danke ich für den Zuspruch und den hilfreichen, aber immer angenehmen Druck. Meiner Frau Ines und meinen beiden Kindern Charlotte und Johann danke ich für ihre Geduld und das Vertrauen in meine Fähigkeiten.

Selbständigkeitserklärung

Hiermit erkläre ich, dass ich die vorliegende Arbeit selbständig und nur unter Verwendung der angegebenen Literatur und Hilfsmittel angefertigt habe.
Ich habe mich anderweitig nicht um einen Doktorgrad beworben und besitze einen solchen auch nicht.
Die dem Verfahren zugrunde liegende Promotionsordnung der Mathematisch-Natur-wissenschaftlichen Fakultät der Humboldt-Universität zu Berlin habe ich zur Kenntnis genommen.

Berlin, den 17. Mai 2017 Alexander Kuhlicke